

**STUDY OF DROP-ON-DEMAND INKJET
PRINTING TECHNOLOGY WITH APPLICATION
TO ORGANIC LIGHT-EMITTING DIODES**

ZHOU JINXIN

(M.Eng., B.Eng.)



**A THESIS SUBMITTED
FOR THE DEGREE OF DOCTOR OF PHILOSOPHY
DEPARTMENT OF MECHANICAL ENGINEERING
NATIONAL UNIVERSITY OF SINGAPORE**

2010

ACKNOWLEDGEMENTS

There are really quite a few persons that have assisted in the realization of my Ph.D. thesis work. First of all, I send my deep appreciation to my supervisors, Prof. Jerry Fuh Ying Hsi and A/Prof. Loh Han Tong, for their valuable guidance, scientific advice and strong encouragement throughout the entire duration of my research. This Ph.D. degree and dissertation would not have been possible without their generous support during the most critical stage of my doctoral program. A special thanks goes to Prof. Wong Yoke San for his valuable comments and suggestions which helped improving the advancement of my research. Your ideas and our discussions have been very inspiring. Thanks for your time and encouraging input.

I would like to thank Prof. Chua Soo Jin for his contribution and support from IMRE on my research. I would also like to thank Mr. Jeffrey Gray for his technical advice and assistance from IMRE. I am thankful to Dr. William Birch in IMRE for providing me with the useful knowledge on surface science and the related measurements.

Thanks to all the people in the CIPMAS Lab, especially Mr. Ng Yuan Song who was my junior project team member, for their making me feel welcome, for their useful discussions and writings on the research, and for their entertaining conversations over coffee. Finally I am grateful to my family and close friends for their blessings and moral support to give me courage and patience to face the obstacles in life.

TABLE OF CONTENTS

ACKNOWLEDGEMENTS	I
TABLE OF CONTENTS	II
SUMMARY	VII
LIST OF TABLES	IX
LIST OF FIGURES	XI

CHAPTER 1

INTRODUCTION	1
1.1 Background	1
1.2 Research Motivation	4
1.3 Research Objectives and Scope	6
1.4 Organization of Thesis	8

CHAPTER 2

LITERATURE REVIEW	9
2.1 Introduction	9
2.2 OLED Structure and Operation	11
2.2.1 Single Layer Devices	11
2.2.2 Multiple Layer Devices	14
2.3 Materials Used in OLEDs	17

2.3.1	Conjugated Small Organic Molecules	18
2.3.2	Conducive Conjugated Polymers	22
2.3.3	Conducting Polymer - PEDOT:PSS	27
2.3.4	Electrodes - Anode and Cathode	30
2.4	Fabrication Techniques	32
2.4.1	Thermal Vacuum Evaporation	33
2.4.2	Spin-Coating	35
2.4.3	Doctor Blade Coating	36
2.4.4	Screen Printing	37
2.4.5	Inkjet Printing	39

CHAPTER 3

INDIUM-TIN-OXIDE	(ITO)	SUBSTRATE	SURFACE
TREATMENT			52
3.1	Introduction		52
3.1.1	Introduction to Surface Wettability		53
3.1.2	Review of Surface Treatment and Related Wettability		60
3.2	Experimental Procedures		63
3.2.1	Equipment and Materials		63
3.2.2	Surface Modification of ITO Substrates		65
3.2.3	Contact Angle Measurement Procedures		68
3.3	Results and Discussion		73

3.3.1 Contact Angles and Surface Energies of Modified ITO Substrates	73
3.3.2 Contact Angle Hysteresis of Modified ITO Substrates	79
3.3.3 Ageing Effect of Modified ITO Surface Wettability	81
3.4 Conclusion	83

CHAPTER 4

INKJET PRINTING: FABRICATION AND CHARACTERIZATION OF OLEDS

4.1 Introduction	85
4.2 Experimental Procedures	87
4.2.1 ITO Substrate Surface Preparation Process	87
4.2.2 Drop-on-Demand Inkjet Printing of PEDOT:PSS	100
4.2.3 Design and Fabrication of P-OLED Devices	109
4.3 Results and Discussion	118
4.3.1 ITO Surface Patterning	118
4.3.2 Drop-on-Demand Inkjet Printing of PEDOT:PSS	119
4.3.3 Characterization of P-OLED Devices	127
4.4 Conclusion	135

CHAPTER 5

CHARACTERIZATION OF SINGLE MICRODROPLET DRYING BEHAVIOR

138

5.1 Introduction	138
5.2 Overview of Drop Spreading and Drying	139
5.2.1 Drop Impact and Spreading	139
5.2.2 Drop Drying Behavior	141
5.3 Experimental	149
5.3.1 Equipment	149
5.3.2 Materials	149
5.4 Results and Discussion	150
5.4.1 Profile of Printed Droplets after Drying	150
5.4.2 Variations of Drop Profile Properties with Substrate Temperature	159
5.4.3 Drop Dispensing	163
5.5 Conclusion	167
CHAPTER 6	
REPRESENTATION AND MAPPING OF DRIED DROPLET PROFILES	169
6.1 Introduction	169
6.2 Model of Radial Basis Function Networks	170
6.2.1 Basic Theory	170
6.2.2 Training of Radial Basis Function Networks	174
6.3 Normalization of Experimental Data	177
6.4 Results and Discussion	181

6.4.1 Representation and Mapping of Dried Droplet Profiles	182
6.4.2 Evaluation of Generated RBFN Models	188
6.5 Conclusion	195
CHAPTER 7	
CONCLUSIONS AND FUTURE WORK	196
7.1 Conclusions	196
7.2 Future Work	201
BIBLIOGRAPHY	205
PUBLICATIONS	229
APPENDIX	A.1
A. Taguchi Design of Experiments in Optimization of Inkjet Printing Drop Ejection Parameters	A.1

SUMMARY

This thesis aims to further investigate the application of drop-on-demand (DoD) inkjet printing technology in the fabrication of organic light-emitting diode (OLED) devices. Three areas of work related to OLED and inkjet printing were performed and addressed as follows.

Firstly, surface wettability and surface degradation of indium-tin-oxide (ITO) glass substrates for OLED devices have been characterized by contact angle measurements after five different surface treatments - two dry treatments (UV-Ozone and Oxygen-Plasma) and three wet treatments (Alkaline, Neutral and Organic). It is found that dry surface treatments are generally more efficient than wet surface treatments for removing hydrocarbon contamination with positive surface modification. Furthermore, Oxygen-Plasma dry treatment possesses slower surface degradation than UV-Ozone dry treatment. The results achieved better the existing results reported by other researchers.

Secondly, polymeric OLED (P-OLED) devices with a hole transport layer of conductive polymer poly(3,4-ethylenedioxythiophene):poly(styrenesulfonate) (PEDOT:PSS) at two inkjet printing resolutions have been fabricated in comparison with the P-OLED of spin-coated PEDOT:PSS layer. Inkjet printing demonstrates to be able to achieve better P-OLED device performance than spin-coating under some

controlled conditions, as it is found that more effective surface contact areas of inkjet printed functional film exist in between adjacent layers, which may balance and enhance interactions between the hole and electron charge carriers to improve the performance of final devices.

Thirdly, in-depth study on characteristics of inkjet printed droplet features after drying have been conducted from the two aspects of experiment and modeling. The experiment work makes significant findings on the influence of substrate temperature on the drying shape of single printed droplets, which are Gaussian shape, transition shape, and ring-like shape corresponding to different drying temperature range. The results also imply that the droplet morphology can be controlled for the selected drop dispensing by the substrate temperature. The modeling work deals with the shape representation and mapping of dried droplets to drying temperatures. Radial basis function network (RBFN) is the first to be employed to map the droplet shape. It evaluates both Gaussian and thin-plate spline (TPS) RBFN methods. It concludes that the former works well only for a lower temperature range less than 50°C, and the latter shows a better mapping and estimation across the entire range of drying temperature. With the successful shape representation and mapping, it would enable future researches to set desirable drop printing parameters for the required droplet shape that forms in practice.

LIST OF TABLES

Table 3.1: Sources of thermodynamic contact angle hysteresis.	58
Table 3.2: Summary of contact angles reported from the literature.	62
Table 3.3: Summary of the average sessile contact angles and surface energies.	75
Table 3.4: Summary of the average advancing contact angles.	76
Table 3.5: Summary of the average receding contact angles.	76
Table 3.6: Summary of contact angle hysteresis.	80
Table 4.1: Parameter setting for the Oxygen-Plasma treatment.	98
Table 4.2: Brief specifications for Litrex 80.L inkjet printing system performance.	101
Table 4.3: Brief specifications of Spectra SX3 print-head.	103
Table 4.4: Brief characteristics of PEDOT:PSS (Baytron® P VP CH 8000).	105
Table 4.5: Parameters for voltage pulse profile used in printing PEDOT:PSS.	107
Table 4.6: Parameters for the thermal evaporation system Edwards Auto 306.	114
Table 4.7: Brief information of the P-OLED device performances.	131
Table 5.1: Brief characteristics of PEDOT:PSS (Baytron® P VP CH 8000).	150
Table 6.1: Summary of dried droplet profiles with temperature used for training RBFN.	179
Table 6.2: Summary of dried droplet profiles with temperature used for evaluating RBFN.	180
Table 6.3: Characteristics and comparison of Gaussian and TPS RBFN training.	186
Table 6.4: Procedure for estimation of dried droplet profile at given temperature.	189

Table 6.5: Characteristics and comparison of Gaussian and TPS RBFN estimation. 191

Table 6.6: Procedure for estimation of temperature at given dried droplet profile. 193

Table 6.7: Characteristics and comparison of Gaussian and TPS RBFN estimation. 194

Table A.1: $L16(2^{15})$ array used for Taguchi design of experiments. A.4

Table A.2: Level settings of the main factors for Taguchi design of experiments. A.4

Table A.3: Taguchi design of experiments with 3 replications and randomization. A.6

LIST OF FIGURES

Figure 2.1: Examples of OLED displays in consumer products.	10
Figure 2.2: Basic structure of a single layer OLED.	12
Figure 2.3: Working principle of an OLED device.	12
Figure 2.4: An actual example for the single layer OLED device.	14
Figure 2.5: A multiple layer OLED device.	16
Figure 2.6: Schematic of one more complex OLED device.	16
Figure 2.7: Molecular structure of copper phthalocyanine (CuPc).	19
Figure 2.8: Molecular structures of HTL materials: N,N'-bis(3-methylphenyl)-N,N'-diphenyl-benzidine (TPD, $T_g = 63^\circ\text{C}$) and N,N'-di(naphthalen-1-yl)-N,N'-diphenyl-benzidine (NPB, $T_g = 98^\circ\text{C}$).	20
Figure 2.9: Small molecular guest dye emitter: 5,6,11,12-tetraphenylnaphthacene (Rubrene).	20
Figure 2.10: Molecular structure of tris(8-hydroxyquinolato) aluminum (Alq_3 , $T_g = 174^\circ\text{C}$).	21
Figure 2.11: Overview of some applications of conductive conjugated polymers.	22
Figure 2.12: Chemical structures of some most essential conductive conjugated polymers: polyacetylene (PA), poly(p-phenylene) (PPP), poly(p-phenylene vinylene) (PPV), polythiophene (PT), polypyrrole (PPy), and polyaniline (PANI).	24
Figure 2.13: Main chemical structure of the conducting polymer polyaniline (PANI).	26

Figure 2.14: Molecular structure of PEDOT:PSS.	27
Figure 2.15: Molecular structures of glycerol (boiling point = 290°C), sorbitol (boiling point = 295°C), and N-methyl-2-pyrrolidone (NMP, boiling point = 202°C).	29
Figure 2.16: Principle of organic small molecules deposition by thermal vacuum evaporation.	33
Figure 2.17: Schematic representation of doctor blade coating.	36
Figure 2.18: A schematic of typical process for screen printing. The screen is patterned using a photo emulsion.	37
Figure 2.19: Layout of the different inkjet printing technologies.	40
Figure 2.20: Binary deflection C-IJP system.	41
Figure 2.21: Multiple deflection C-IJP system.	41
Figure 2.22: Streams of continuous droplets from a C-IJP process.	42
Figure 2.23: Schematic of the DoD-IJP process.	43
Figure 2.24: Droplets from a DoD-IJP process.	43
Figure 2.25: Roof-shooter thermal inkjet mechanism layout.	44
Figure 2.26: Side-shooter thermal inkjet mechanism layout.	44
Figure 2.27: Drop formation within the ink chamber of a thermal inkjet device.	45
Figure 2.28: Different modes that a piezoelectric plate can deform.	46
Figure 2.29: Bend mode piezoelectric inkjet system.	46
Figure 2.30: Push mode piezoelectric inkjet system.	47
Figure 2.31: Shear mode piezoelectric inkjet system.	47
Figure 2.32: Squeeze mode inkjet using a piezo-ceramic cylinder and a glass tube.	48

- Figure 3.1: Different surface energy components and contact angle of a liquid droplet. 55
- Figure 3.2: Advancing contact angle (θ_a) and receding contact angle (θ_r) of a liquid droplet on a tilted substrate. 56
- Figure 3.3: Set-up of the goniometer showing the drop deposited onto the sample on the sample stage. 68
- Figure 3.4: Sample and sample stage. 68
- Figure 3.5: Syringe and plunger system used to deposit the one micro-liter droplet onto the sample. 68
- Figure 3.6: Software screen view of a projected sessile drop use for the measurement of sessile contact angles. 70
- Figure 3.7: Software screen view showing the cross-hair that is used to target the sessile drop for measurement and the tangents for measuring the angle at both ends of the drop. 70
- Figure 3.8: Entire goniometer set-up is tilted with the sample, in order to capture images for the measurement of advancing and receding contact angles. 71
- Figure 3.9: As the entire goniometer set-up including the camera tilts together with the sample, it is able to capture the projected image of a tilted drop and measure it the same way as an un-tilted sessile drop. The left-end of the droplet gives the advancing contact angles and the right-end of the droplet gives the receding contact angles. 71
- Figure 3.10: Graphical representation of the various sessile contact angles and surface energies for different surface treatment processes. 75

Figure 3.11: Summary of all three types of contact angles in the relative positions for different surface treatment processes.	77
Figure 3.12: Summary of a qualitative variation of contact angles for different surface treatment processes.	77
Figure 3.13: Ageing effect of UV-Ozone treated ITO surface wettability.	81
Figure 3.14: Ageing effect of Oxygen-Plasma treated ITO surface wettability.	82
Figure 3.15: Contact angle variation on Oxygen-Plasma freshly-treated ITO surface.	83
Figure 4.1: Basic P-OLED device structure being investigated in this research.	86
Figure 4.2: Flow chart of the entire ITO surface preparation process.	88
Figure 4.3: Spin-coater (Model: CEE 100).	88
Figure 4.4: Hotplate (Model: HP-150).	89
Figure 4.5: Karl Suss Mask & Bond Aligner MA8/BA6.	89
Figure 4.6: Trion Sirius reactive ion etching (RIE) system.	90
Figure 4.7: Olympus BX60 metallurgical microscope.	90
Figure 4.8: KLA-Tencor Surface Profiler P-10.	91
Figure 4.9: Spin speed curve used in the spin-coating of photoresist AZ 5214-E.	93
Figure 4.10: (a) Shadow-mask used for UV curing of samples ($100\times 100\text{mm}^2$) in the photolithography process; (b) Top view of a $25\times 25\text{mm}^2$ ITO substrate after patterned, and the black strips are where the ITO remains.	95
Figure 4.11: Summary of processes and parameters for ITO surface preparation.	99
Figure 4.12: Litrex 80.L drop-on-demand (DoD) inkjet printing system.	100

Figure 4.13: Gantry arm holding the print-head assembly.	100
Figure 4.14: Mounted print-head assembly.	100
Figure 4.15: Print-head assembly.	100
Figure 4.16: Spectra SX3 print-head.	102
Figure 4.17: Profile of voltage pulse signal used to control piezoelectric print-head.	103
Figure 4.18: WYKO NT1100 optical profiling system.	104
Figure 4.19: Microscopic image of consistent printed droplets.	107
Figure 4.20: PEDOT:PSS layer printed on patterned ITO substrate.	108
Figure 4.21: Vacuum oven (VWR 1415M-2).	110
Figure 4.22: Thermal evaporation system (Edwards Auto 306).	110
Figure 4.23: OLED current-voltage-luminance (I - V - L) measurement instrument.	111
Figure 4.24: Spin speed curve used in the spin-coating of MEH-PPV.	112
Figure 4.25: MEH-PPV layer spin-coated on PEDOT:PSS layer.	113
Figure 4.26: Shadow mask for the thermal evaporation.	114
Figure 4.27: Thermal evaporation of LiF, Ca and Ag as the cathode electrode.	115
Figure 4.28: Schematic diagram of the fabrication of a P-OLED device.	117
Figure 4.29: Various locations on a patterned ITO substrate showing reasonably sharp and clear features under an optical microscope.	119
Figure 4.30: Bitmap images for sample pattern printing on photo paper.	120
Figure 4.31: Photographs for PEDOT:PSS pattern printing on photo paper.	120
Figure 4.32: Optical image of inkjet printed PEDOT:PSS dots on the ITO substrate.	

	122
Figure 4.33: 3D image of single drop at room temperature.	122
Figure 4.34: Top-down view and 2D cross-sectional profile at room temperature.	122
Figure 4.35: 3D image and 2D profile of PEDOT:PSS single line printed at 450dpi.	123
Figure 4.36: 3D image and 2D profile of PEDOT:PSS single line printed at 720dpi.	124
Figure 4.37: Schematic of the droplet overlapping for 450dpi.	125
Figure 4.38: Schematic of the droplet overlapping for 720dpi.	126
Figure 4.39: Schematic structure of 4 diodes P-OLED device.	127
Figure 4.40: Pictures of a 4 diodes P-OLED device: (a) ITO side facing downwards; (b) ITO side facing up with cathode layers on the top.	128
Figure 4.41: Characteristic of current density-voltage for P-OLED devices.	129
Figure 4.42: Characteristic of luminance-voltage for P-OLED devices.	129
Figure 4.43: Characteristic of luminous efficiency-voltage for P-OLED devices.	130
Figure 4.44: Characteristic of luminous power efficiency-voltage for P-OLED devices.	130
Figure 4.45: Schematic of effective surface contact area for inkjet printed films.	134
Figure 5.1: Different stages of the drop spreading process on a substrate.	140
Figure 5.2: ‘Ring’ formation due to outward flow of solute particles to the boundary.	141
Figure 5.3: An increment of evaporation viewed in a drop cross-section.	142

Figure 5.4: Images of the resulting deposit under three evaporation conditions.	143
Figure 5.5: Effect of drying condition on thickness and luminescence of blue light-emitting polymer films.	148
Figure 5.6: (a) 3D image at 25°C; (b) Top-down view & 2D cross-sectional profile at 25°C.	151
Figure 5.7: (a) 3D image at 30°C; (b) Top-down view & 2D cross-sectional profile at 30°C.	152
Figure 5.8: (a) 3D image at 35°C; (b) Top-down view & 2D cross-sectional profile at 35°C.	152
Figure 5.9: (a) 3D image at 40°C; (b) Top-down view & 2D cross-sectional profile at 40°C.	152
Figure 5.10: (a) 3D image at 45°C; (b) Top-down view & 2D cross-sectional profile at 45°C.	153
Figure 5.11: (a) 3D image at 50°C; (b) Top-down view & 2D cross-sectional profile at 50°C.	153
Figure 5.12: (a) 3D image at 55°C; (b) Top-down view & 2D cross-sectional profile at 55°C.	154
Figure 5.13: (a) 3D image at 60°C; (b) Top-down view & 2D cross-sectional profile at 60°C.	154
Figure 5.14: Summary of the variation of droplet shape with substrate temperature.	155
Figure 5.15: Schematic showing a liquid flow in the evaporation rate distribution theory.	

	156
Figure 5.16: Variation of droplet width with substrate temperature.	159
Figure 5.17: Variation of droplet center height with substrate temperature.	160
Figure 5.18: Variation of droplet edge angle with substrate temperature.	162
Figure 5.19: Linear fittings of the droplet width and height with substrate temperature after drying in Gaussian Stage.	164
Figure 5.20: Variations of dried droplet properties in Transition Stage: (a) Drops keep similar height after drying; (b) Droplet width and edge angle vary in the inverse direction.	165
Figure 5.21: An example of dried single line with sharp edge at 45°C in Transition Stage: (a) Top-down view; (b) 3D image.	166
Figure 5.22: Linear relation of the droplet width with temperature in Ring-Like Stage.	166
Figure 6.1: Architecture of a generalized radial basis function network.	171
Figure 6.2: Schematic of function profiles for Gaussian and thin-plate spline.	173
Figure 6.3: Plot of all normalized dried droplet Profiles.	181
Figure 6.4: Convergence of EM algorithm for RBFN training from data set T7.	183
Figure 6.5: RMSE of the network with different number of RBFs.	184
Figure 6.6: Shape representation and mapping using both Gaussian and TPS RBFN.	186
Figure 6.7: Shape estimation using both Gaussian and TPS RBFN.	190
Figure A.1: Schematic flow of methodology based on Taguchi design of experiments	

for data collection and analysis.

A.3

CHAPTER 1

INTRODUCTION

1.1 Background

Using organic materials for light-emitting diodes (LED) is fascinating due to their vast variety and the relative ease of controlling their composition to tune their properties through chemical means. Due to the promising attributes of organic light-emitting diodes (OLED) for applications in flat panel displays, research and development efforts in the field of plastic electronics are increasing dramatically. The ease of fabrication, wide-viewing angle, mechanical flexibility, transparency and excellent scalability are some of the attractive features of such devices. Especially, the flexible and transparent nature of OLED allows for new applications to emerge, such as portable electronics, roll-up and see-through displays.

Compared to a liquid crystal display (LCD) used in many computer screens today, one of the largest benefits of an OLED display is that OLEDs do not require a backlight to function. They are self-luminous and do not require backlighting, diffusers, polarizer or any of the other supporting electronics that are commonly used in LCDs^[1-2]. This eliminates the need for bulky and environmentally undesirable mercury lamps and yields a thinner, lighter, more versatile and more compact display. They draw far less power and can be used with small portable devices. Hence, they will be able to last for

a longer period of time with the same amount of battery power. Their low power consumption provides for maximum efficiency and helps minimize heat and electrical interference to other electronic devices. However, degradation of OLED working materials has limited their use ^[3].

One basic OLED cell structure consists of a few thin organic layers, sandwiched between two electrode layers. When an external voltage is applied to the cell, the active organic layer produces visible light. The first OLED was made in 1965 by Helfrich and Schneider ^[4] using an anthracene crystal. But it was only in 1987, when Tang and Van Slyke ^[5] in Eastman Kodak Company reported a *small molecular* OLED (SM-OLED) consisting of a bi-layer thin film via vapor deposition process, to achieve a substantial advance towards a practical organic electroluminescence technology. This is also the rudiment model for present OLEDs. Their work showed that amorphous or nearly amorphous active materials, through simple fabrication procedures such as sublimation, were adequate to realize stable devices using small direct-current (DC) voltages (~10V). These results raised worldwide research interest in organic materials for LED research. In 1990, the research group Burroughes *et al* ^[6] in Cambridge University announced *conjugated polymer* OLEDs (P-OLED), with the same light emission mechanism but with different two polymers, that successfully developed a new display technology. Conjugated polymers have an intrinsic advantage over small organic molecules due to their better mechanical properties, easy fabrication techniques, flexibility and cost effectiveness. Many renowned

companies such as Seiko-Epson, Eastman-Kodak, Cambridge Display Technology (CDT), Sony, and Samsung are exploring for the possible applications of these conjugated polymers.

Generally, SM-OLEDs are patterned and produced via vacuum deposition methods. However, for roll-to-roll based processing, such vacuum deposition methods are relatively expensive, time consuming, and offer a limited scope of pattern shape and dimension. In contrast, as conjugated polymer materials used in P-OLEDs are solution processable, this means that P-OLED devices can be made in a very flexible and cheap way. In fact, although P-OLED lags SM-OLED development by a few years, in terms of efficiency and lifetime, it is still more promising because of their easier production techniques, such as spin-coating (or solution-casting) through photolithography processes ^[7], screen printing ^[8-9] and inkjet printing ^[7, 10-14], which do not require vacuum environment. Spin-coating is a simple and cost effective method. However, material wastage is very high and it can normally be used to produce monochrome displays only. Screen printing technique requires a physical entity through which a given pattern is transferred to the underlying substrate. This entity (i.e. stencil for screen printing) must be changed when a new pattern is needed. Moreover, it relies on contacting the substrate during the printing process, which may be undesirable in some cases. Among all these polymer deposition techniques, inkjet printing is potentially the most low-cost and a high throughput approach ^[15] with maskless and non-contact fabrication advantages.

Drop-on-demand (DoD) inkjet printing as a member of inkjet printing family is an additive manufacturing process which “direct-writes” or dispenses materials directly onto a substrate to build up a specimen part drop by drop. Over the past decade, this technology has come to be viewed as a precision micro-dispensing tool, in addition to its huge success with color printing. It is capable of precise deposition of pico-liter (pL) volumes at high rates, even onto non-planar surfaces. A high resolution of about 15 μ m diameter dispensed droplets (\sim 2pL in volume) with high generation rates of up to 30kHz can be obtained ^[16]. Currently, a variety of materials has been deposited by DoD inkjet printing including ceramics, metals, organic semiconducting materials, and biopolymers ^[17]. In the development of OLEDs, drop-on-demand inkjet printing technology has been used to deposit polymer layers on the top of a given anode ^[10-12], or to print poly(3,4-ethylenedioxythiophene):poly(styrenesulfonate) (PEDOT:PSS) and/or electroluminescent polymers in a pixel array on a circuit ^[13-14]. This promises a low cost, maskless, and non-contact approach to fabricate potentially delicate features in a virtually limitless selection of patterns.

1.2 Research Motivation

Since inkjet printing technology was applied in the OLED fabrication, with its inherent manufacturing advantages, inkjet printing has been becoming the next most sought-after method for the production of organic electronics. Across the globe, quite a large number of research institutes and companies involved in the display industry

have reported the fabrication of OLED devices by drop-on-demand inkjet printing to high resolution and large screen sizes. However, any manufacturing details or insights into the finer points of inkjet printing and relevant operating parameters have still not been revealed, to say nothing of much less their influence on OLED device performance. Therefore, in this research, aspects of OLED fabrication using piezoelectric DoD inkjet printing will be investigated under experiments. In some areas, statistical analysis will be used to examine experimental results in order to obtain a better understanding of the behavior of this versatile technique.

Upon impact of an ejected droplet from an inkjet printing machine, surface properties of the substrate other than impact mechanics of the droplet plays an important role in the spreading, solidification and dried character of the droplets. Surface characteristics of OLED substrates are normally modified during the preparation processes. When the inkjet printed layer is printed onto these substrates, these processes will have an influence on the droplet as it initially forms on the surface. It will also have an effect on the interfacial properties between the substrate and the printed layer. These variations will in turn affect performance of complete P-OLED devices to various degrees. In this research, some aspects of the substrate preparation process will be fine tuned and related surface characteristics produced will be also investigated.

Inkjet printing technique requires depositing solutions to have low viscosity ^[18]. A drying droplet sometimes deposits its solute as a ring stain under some printing

conditions. The stain marks the circumference of the droplet before drying. This ring formation is considered to be one of different drying behaviors after inks are ejected from print head onto a substrate. Different drying outcome may affect the performance of final OLED devices as it produces different surface morphologies of printed thin films. Non-uniform surface formation would retard the advancement of inkjet printing technique in fabrication of some electronic devices. In this research, inkjet printed drying features will be characterized to various aspects such that results could be considered as a reference to achieve thin films with desired surface morphology after drying, and may have potential to be applied in the modeling analysis of drop drying.

1.3 Research Objectives and Scope

In order to understand the working principle of inkjet printing, its capabilities, performance characteristics and related controlling parameters, a commercial drop-on-demand inkjet printing machine is used in our studies. In inkjet printing processes, we will develop an understanding of some important aspects relating to P-OLED and their processing methodology. This will provide the preliminary ground work for ways to achieve a P-OLED with more predictable performance and for drop-on-demand inkjet printing technology itself. Three objectives targeted have been set out as follows:

(1) To conduct a study of substrate surface characteristics after surface treatment is

used in OLED to determine what improvement takes place in its surface wettability.

- (2) To examine the performance of OLED fabricated by means of drop-on-demand inkjet printing technology and to compare with spin-coated OLED devices.
- (3) To investigate and characterize drop-on-demand inkjet printed droplet features after drying in relation to the substrate temperature.

Correspondingly, the research scope has been recognized as below:

- (1) For the first objective, the research scope aims:
 - To characterize different surface treatments to OLED substrates in surface wettability by contact angle measurement
 - To investigate surface ageing effect of processed OLED substrates
- (2) For the second objective, the research scope aims:
 - To build OLED devices introduced with drop-on-demand inkjet printing process
 - To examine electrical and optical properties in terms of current density-voltage characteristic and voltage-luminance characteristic
 - To examine power efficiency of OLED devices
 - To compare device performance of inkjet-printed OLEDs with spin-coated OLEDs
- (3) For the third objective, the research scope aims:
 - To characterize drying behavior of inkjet printed conductive polymer drops

on the hydrophilic substrate

- To conduct shape representation and mapping of dried droplet profiles with drying temperature

1.4 Organization of Thesis

In this thesis, Chapter 2 conducts a literature review on the development and investigation on OLED devices and their fabrication technologies. As the first step to building a device, substrate surface treatment and related surface characteristics are explored in Chapter 3. Following it, Chapter 4 presents fabrication and performance characteristics of the complete OLED device introduced with inkjet printing process. Meanwhile, OLED device fabricated under standard processes by spin-coating has also been built as comparison with the inkjet printing device. In order to obtain an understanding of the formation of different thin film surface morphology, Chapter 5 characterizes the drying behavior of inkjet printed conductive polymer drops on the hydrophilic substrate, and then Chapter 6 investigates shape representation and mapping of dried droplet profiles with drying temperature by making use of radial basis function network methods. Finally, Chapter 7 draws the conclusions by discussing achievements and limitations of the research presented in the thesis. Some suggestions for future work are also proposed.

CHAPTER 2

LITERATURE REVIEW

2.1 Introduction

Organic light-emitting diode (OLED) devices present a subject of interest to a large number of researchers and industries due to their promising attributes for applications in flat panel displays. The fascination with these devices is due to their advantages of relative ease of fabrication and low fabrication cost, lack of need for backlighting, flexibility, transparency and scalability. OLEDs were first introduced in 1987 by Tang and Van Slyke ^[5] (Eastman Kodak) with efficient electroluminescence in a double-layer thin film device, based on sublimed small molecules and was known as small molecular OLEDs (SM-OLEDs). Within three years, Burroughes *et al* ^[6] developed long chain conjugated polymer based OLEDs (P-OLEDs) based on a single active organic semiconductor layer. Since then, great advancements have been made, most notably in the improvement of full-color capability, luminance efficiency, and device lifetime. Significant progress in the reliability of OLEDs, especially the operational lifetime, has been made since the late 1980s. For instance, OLEDs with an estimated operational lifetime of 35 000 hours have been reported, with a starting brightness of 200cd/m² ^[19]. In fact, reports of more than 40 000 hours of continuous OLED operation have also appeared ^[20]. An acceptable lifetime for portable displays is currently around 10 000 ~ 15 000 hours at 100 ~ 150cd/m².

Over the past few years, OLEDs have begun to make the transition from the laboratory to the market. It is now possible to buy devices such as car stereos, cell phones, and digital cameras where the display is based on OLEDs (Figure 2.1). Great efforts are being directed to the creation of larger displays, and prototypes of 13- to 17-inch displays have recently been demonstrated. Commercially, up till now most passive matrix displays can only display diagonals up to 3.8 inches. Meanwhile prototypes of larger demonstrators with display diagonals of up to 40 inches have also been announced in Press Releases by Seiko-Epson (2004) and Samsung (2005). However, despite all the advances made thus far, there is still much room for improvement, especially in the areas of material selection, device optimization, and lifetime.



Figure 2.1: Examples of OLED displays in consumer products.

2.2 OLED Structure and Operation

2.2.1 Single Layer Devices

2.2.1.1 Basic Structure

The basic structure of a typical bottom-emitting monolayer OLED under direct-current (DC) bias voltage is shown in Figure 2.2 ^[21]. The total thickness of functional layers is just a few hundred nanometers. It consists of the following parts [22-23].

- **Substrate** (clear plastic, glass or metal foil) - The substrate is used to support and also protect OLED devices.
- **Anode** (transparent) - The anode removes electrons or adds electron ‘holes’ when a current flows through the device.
- **Emissive Layer / Light-Emitting Layer** - This layer is made of organic molecular or polymeric active materials where holes from the anode and electrons from the cathode meet and recombine when an external voltage is applied; this is where light is emitted.
- **Cathode** (may or may not be transparent depending on the type of OLED) - The cathode injects electrons when a current flows through the device.

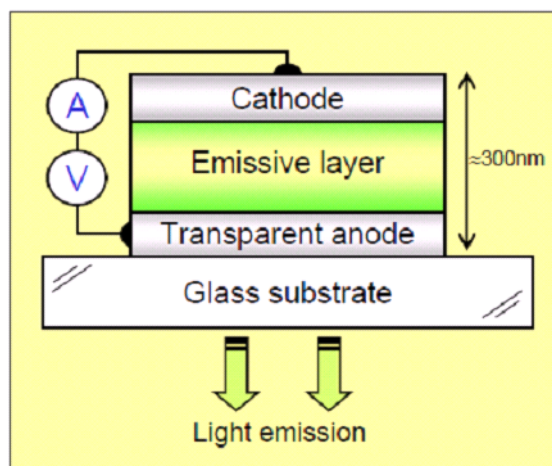


Figure 2.2: Basic structure of a single layer OLED ^[21].

2.2.1.2 Device Working Principle

OLEDs work on the principle of *electroluminescence* which is defined as the electrically driven emission of light from non-crystalline organic materials. When an external voltage is applied to the electrodes, the top electrode (cathode) injects electrons into OLED organic layers while the bottom electrode (anode) injects holes as shown in Figure 2.3 ^[24].

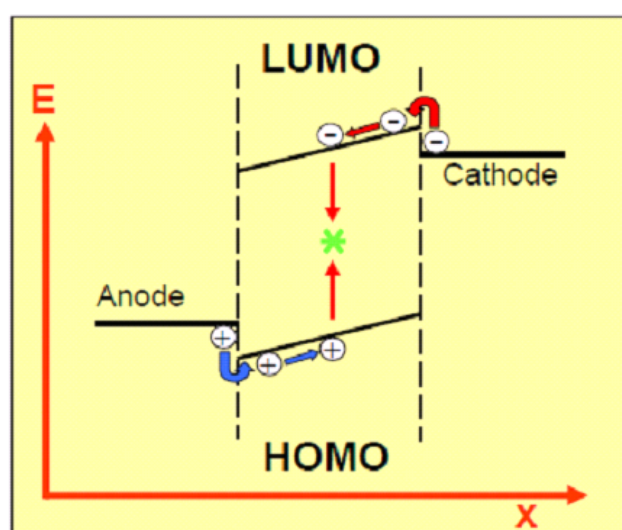


Figure 2.3: Working principle of an OLED device ^[24].
LUMO stands for the **Lowest Unoccupied Molecular Orbital**.
HOMO stands for the **Highest Occupied Molecular Orbital**.

The detailed processes are described as follows:

Step 1. The battery or power supply of the device containing OLED applies a bias voltage across an OLED device.

Step 2. An electrical current flows from the cathode to the anode through organic layers (an electrical current is a flow of electrons).

i) Electrons from the cathode are injected into the lowest unoccupied molecular orbital (LUMO) energy level in the emissive layer and held at excited states.

ii) The anode removes electrons from the organic layer. This is equivalent to giving hole charge carriers to the organic layer. Holes from the anode are injected into the highest occupied molecular orbital (HOMO) energy level in the emissive layer and held at excited states.

Step 3. In the emissive layer, electrons meet hole charge carriers.

i) When an electron finds an electron hole, the electron fills the hole, that is, the recombination process occurs.

ii) When this happens, the electron gives up energy in the form of a photon of light. This phenomenon is called *electroluminescence*.

Step 4. OLED devices emit visible light.

Step 5. The color of the light depends on the type of organic molecule in the emissive layer.

Step 6. The intensity or brightness of the light depends on the amount of external electrical current applied. The higher the applied current, the brighter the

OLED.

In addition, work function is the minimum amount of energy required to cause an electron to be emitted from the surface of a material. For OLED devices, work function of the cathode metal is usually low to facilitate efficient electron injection into the active material while the work function of the semi-transparent anode is preferably high ^[23].

2.2.2 Multiple Layer Devices

An actual example of a single layer OLED device is given in Figure 2.4 ^[25]. Indium-tin-oxide (ITO) is used as the transparent anode and calcium (Ca) as the metallic cathode. An electroluminescent conjugated polymer material poly(*p*-phenylene vinylene) (PPV) is used to form the emissive layer.

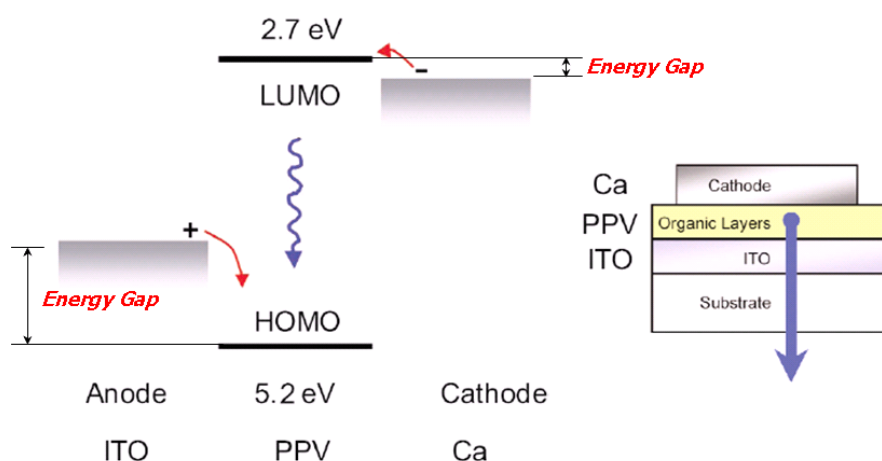
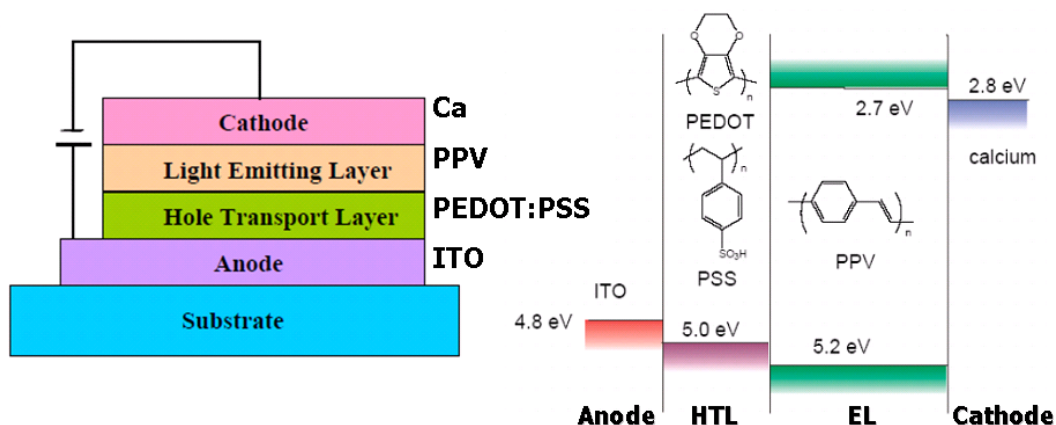
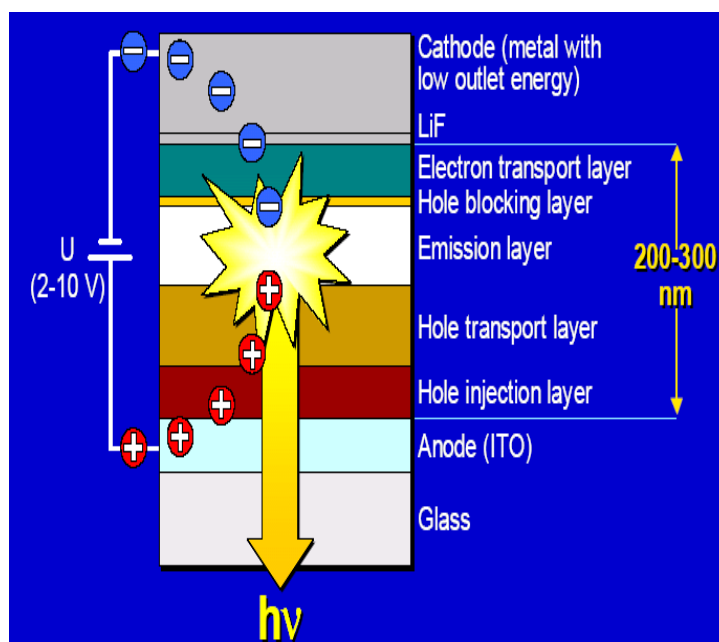


Figure 2.4: An actual example for the single layer OLED device ^[25].

From the illustration in the previous subsection, hole charge carriers from the ITO anode surface have to overcome an energy barrier before jumping into the HOMO energy level. Meanwhile, electrons from the Ca cathode also have to overcome an energy barrier before jumping into the LUMO energy level. In order to increase device performance such as efficacy, lifetime and etc., decreasing these energy gaps is a viable and relatively preferable approach. For this purpose, adding some extra intermediate layers into the device is an effective way, resulting in a so-called multiple-layer structure device as shown in Figure 2.5 ^[26].

Figure 2.5 shows a multilayer device structure with an additional polymer poly(3,4-ethylenedioxythiophene):poly(styrenesulfonate) (PEDOT:PSS) hole transport layer (HTL) in between the ITO anode and PPV emissive layer. As can be seen from the right hand side of the figure, the HTL layer can balance the energy barrier required for the transition of holes. If there is no HTL layer, holes from ITO anode jumping into the emissive layer (EL) need to overcome 0.4eV energy barrier. But now the energy gap can be reduced by 50%. This is one of the advantages of introducing an additional organic layer.

Figure 2.5: A multiple layer OLED device ^[26].Figure 2.6: Schematic of one more complex OLED device ^[25].

Indeed, most organic materials used in thin film LEDs do not transport both carrier types (i.e. electrons and holes) with comparable carrier mobilities. Generally, there is a large disparity between electron and hole mobilities ^[23]. Thus, the efficiency of a device might be low. Figure 2.6 shows an example of a more complex multilayer device ^[25]. Other than additional HTL layer, there are many other extra intermediate layers such as hole injection layer (HIL) to enhance the injection of holes from the

anode, electron transport layer (ETL) to increase electron movement, etc. A hole blocking layer (HBL) could also be introduced between EL and ETL layers to block holes from moving into the ETL before combining with an electron to give off light. Obviously, the selection of materials and structures of the different layers are designed to improve device lifetime, efficiency and reduce degradation during service. Moreover, in practice there is no clear function limit for the different layers. Some layer of thin film materials used in OLEDs usually exhibits multiple functions instead of only one specific function. For example, a PEDOT:PSS layer often acts as a HJL layer and a HTL layer as well. Generally speaking, those additional layers will have positive functions as follows:

- (1) To reduce energy gaps between different thin film layers such that electrons and holes can transit easily from one layer to the other.
- (2) To enhance the injection of charge carriers in the materials.
- (3) To balance electron and hole mobilities to improve the probability of recombination within the emissive layer.

2.3 Materials Used in OLEDs

Huge efforts have made great progress in the development of small molecular based organic ^[27-29] and polymeric ^[30-31] electroluminescent materials used in OLEDs. These two classes of materials have similar physical properties, and devices made from both exhibit comparable performance characteristics. However, thin film formation

processes, purification, and patterning methods for the two classes of materials are quite different. Small molecular based organic films are generally deposited by the thermal evaporation in a high vacuum environment, while polymer films are formed by solution-based methods such as spin-coating and inkjet printing. To date, the complete list of materials that have been incorporated in OLEDs is too large to provide in this section. The following highlights some of the materials that have drawn considerable attention.

2.3.1 Conjugated Small Organic Molecules

As mentioned before, inspired by the search for light-emitting devices based on organic crystals such as anthracene^[32], a significant breakthrough in achieving high electrical efficiency OLEDs using small molecular based organic materials is the discovery of a double-layered heterostructural OLED reported by Kodak scientists^[5] in 1987. Undoubtedly, SM-OLED device construction, device engineering and, particularly, new materials design continue to drive advances in this field. In the following sections, some typical small molecular organic materials appropriate for inclusion into the particular functional layers in SM-OLEDs will be described. However, with the addition of new layers of new materials with new functions, any review that attempts to cover such a rapidly developing area will be outdated even before it is published.

To enhance carrier injection at the interface between anode and organic layer, a hole injection or transport layer with optimized low HOMO energy levels is often introduced. As shown in Figure 2.7, a thin layer (10 ~ 15nm) of copper phthalocyanine (CuPc) is widely applied in organic thin film transistors, solar cells and OLEDs due to its good chemical and thermal stability^[33]. In SM-OLEDs, due to the lower ionization energy (4.7eV) than the ITO (4.8 ~ 5.2eV) anode, this CuPc layer can significantly enhance the concentration and mobility of hole carriers and thus the hole injection efficiency and device stability can be improved.

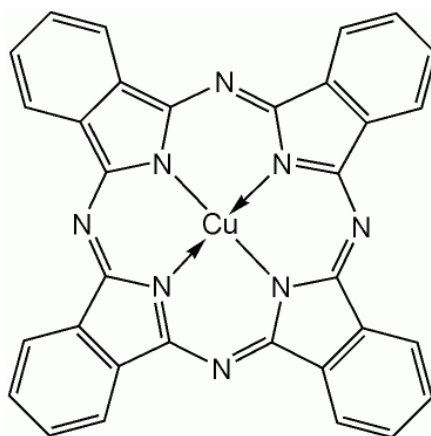


Figure 2.7: Molecular structure of copper phthalocyanine (CuPc).

Among the layers in SM-OLEDs, the hole transport layer (HTL) generally improves hole mobility and often has the lowest glass transition temperature (T_g). In some situations, such as the thermal deposition of cathode or the device encapsulation process, it is necessary to apply a relatively high temperature ($>85^\circ\text{C}$), a low T_g causes inter-diffusion between the HTL and the adjacent organic layer, and then leads to an increasing device operating voltage and may even damage the final product. Therefore, when designing HTL materials, the selection of high T_g value is critical.

At present, N,N'-bis(3-methylphenyl)-N,N'-diphenyl-benzidine (TPD, Figure 2.8) has been used extensively as the HTL. It has a relatively low T_g value ($\sim 63^\circ\text{C}$), and thus it may cause a failure of OLED when depositing the cathode at high temperature as it recrystallizes^[34]. However, its recrystallization may be suppressed by adding a guest molecule, such as 5,6,11,12-tetraphenylnaphthalene (Rubrene)^[34] in Figure 2.9. Rubrene is a prominent emitting molecule that emits red light. When incorporated as a guest in hosts such as TPD, it yields bright red OLEDs and the device lifetime can be greatly enhanced. In this case holes and electrons may recombine in the Rubrene and result in red light emission from it.

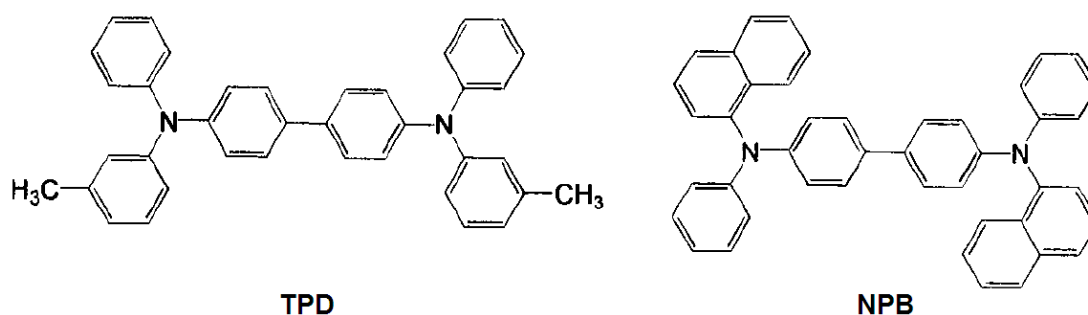


Figure 2.8: Molecular structures of HTL materials:
N,N'-bis(3-methylphenyl)-N,N'-diphenyl-benzidine (TPD, $T_g = 63^\circ\text{C}$) and
N,N'-di(naphthalen-1-yl)-N,N'-diphenyl-benzidine (NPB, $T_g = 98^\circ\text{C}$).

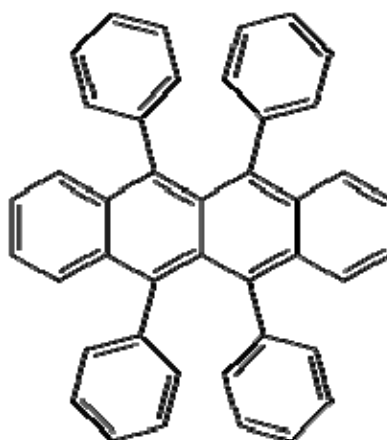


Figure 2.9: Small molecular guest dye emitter:
5,6,11,12-tetraphenylnaphthalene (Rubrene).

Another widely used HTL material N,N'-di(naphthalen-1-yl)-N,N'-diphenyl-benzidine (NPB, Figure 2.8) is very similar to TPD in chemical structure. However, NPB gives a better thermal stability of the HTL, and has been shown to significantly enhance the stability of the SM-OLEDs, apparently due to the considerably higher T_g value of NPB (98°C) as compared to TPD, which has the T_g value of only 63°C [34].

In OLEDs, the layer deposited on the anode would generally be using a good hole injection or transport material, providing HIL or HTL. Similarly, the organic layer in contact with the cathode would be the optimized electron transporting layer (ETL) to improve the electron transport properties in order to enhance the device performance. Although many new and improved ETL materials have been discovered [35-36], the most commonly used material in ETL is still tris(8-hydroxyquinolato) aluminum (Alq_3) [5] as shown in Figure 2.10.

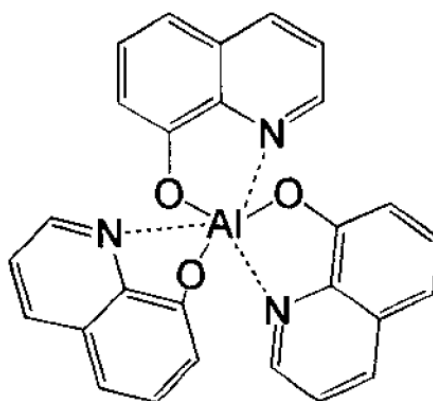


Figure 2.10: Molecular structure of tris(8-hydroxyquinolato) aluminum (Alq_3 , $T_g = 174^\circ\text{C}$).

It is worth pointing out that Alq_3 is also commonly used as an emitting molecule, which emits light in the green with a broad emission peak at 530nm. Alq_3 is a metal

chelate compound, and has excellent thermal stability ($T_g = 174^\circ\text{C}$) to form thin films by thermal evaporation methods. Thermally sublimed Alq_3 films have a microcrystalline structure with an average grain size smaller than 50nm [37]. Modifications on the chemical structure of Alq_3 have been attempted to improve its quantum efficiency, thermal stability, and thin film morphology [27].

2.3.2 Conducive Conjugated Polymers

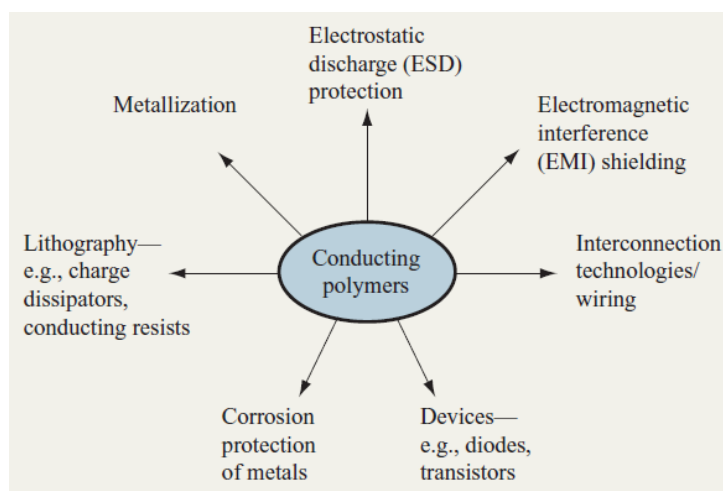


Figure 2.11: Overview of some applications of conducive conjugated polymers [38].

Conjugated polymers in the undoped and doped conducting state have potential applications at all levels of microelectronics (see Figure 2.11) [38]. Conducive conjugated polymers are effective in discharging layers as well as conducting resists in electron beam lithography. They have applications in metallization of plated through-holes for printed circuit board (PCB) and potential applications in electromagnetic interference (EMI) shielding. They provide excellent electrostatic discharge (ESD) protection for packages and housings of electronic components, and

excellent corrosion protection for metals. They are also applied in electronic devices and interconnection technologies.

As a matter of fact, conjugated polymers are not very conductive in their pure form. In order to obtain a conducting state, charge carriers have to be introduced via chemical doping to decrease the band gap of the conjugated polymer. The conductivities of doped conjugated polymers are usually increased by many orders of magnitude higher than their undoped counterparts.

Since the first metallic conductivities in conjugated polymers polyacetylene (PA, Figure 2.12) emerged in 1977 ^[39], the development of electrically conductive polymers has been quite rapid. In 1980, doped poly(*p*-phenylene) (PPP) was demonstrated as a base structure for the highly conducting polymer complexes ^[40]. The chemical structures of some of the most essential conjugated polymers, such as poly(*p*-phenylene vinylene) (PPV), polythiophene (PT), polypyrrole (PPy), and polyaniline (PANI) are shown in Figure 2.12.

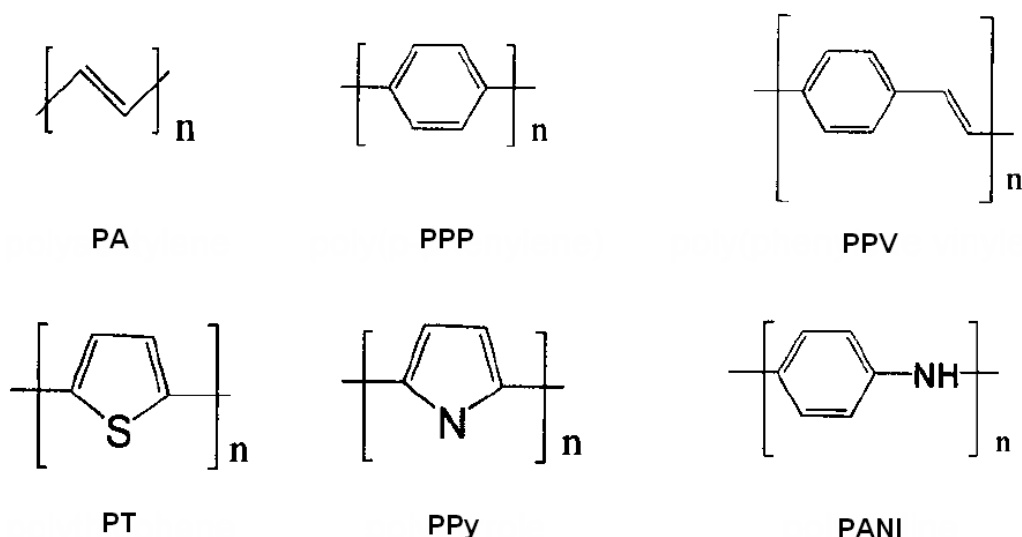


Figure 2.12: Chemical structures of some most essential conductive conjugated polymers: polyacetylene (PA), poly(*p*-phenylene) (PPP), poly(*p*-phenylene vinylene) (PPV), polythiophene (PT), polypyrrole (PPy), and polyaniline (PANI).

PPV and its soluble derivatives like poly(2-methoxy-5-(2'-ethyl-hexyloxy)-*p*-phenylene vinylene) (MEH-PPV) have excellent electroluminescent properties [6, 41-43]. Extensive studies on the chemical morphology and optical properties of the polymer films have been reported in the literature, however, with less work on the charge carrier transport studies. The relationship between the charge carrier transport and polymer film morphology [44-45] is important in the design of OLEDs, laser diodes [46], and thin film transistors [47]. The change in optical properties depending on the processing conditions results in the change in the OLED device efficiency [48-51].

Among the materials shown in Figure 2.12, PPV and PT are considered to be more environmentally stable than PPy and PANI, and therefore more suitable for the solution processing from a variety of organic solvents. For example, as one of the first

electroluminescent conjugated polymers, PPV was utilized in a single layer OLED, which emitted yellow-green light ^[6]. By adding the side chain of electron donors or electron acceptors, the energy band gap determining emission color and solubility of polymers can be easily modified. Generally, electron donors shift luminescence to the lower energy (red-shift, such as MEH-PPV) and electron acceptors shift it to higher energy (blue-shift) ^[52-53]. The stability of conductive polymers is a critical issue for technical applications. PPy, PT, and their derivatives have shown more stable conductivities than PA at room temperature or higher temperatures. However, the relatively poor lifetime of PT-based electroluminescent materials P-OLED inhibits their commercialization ^[34].

The conjugated polymer PANI (Figure 2.12) has been demonstrated as a good hole injection material for P-OLEDs, which increases the device stability ^[54-56]. In addition, this layer reduces oxidation of the active emissive layers which is caused by oxygen diffusion from the ITO anode. PANI can be polymerized in one of the following three doped forms ^[57]: (1) Leucoemeraldine (white), (2) Emeraldine (green or blue), and (3) Pernigraniline (blue). Figure 2.13 shows the main chemical structure of PANI, where reduced and oxidized states of PANI are represented by the index of m and n , respectively. Leucoemeraldine (LB) is the fully reduced form of PANI, obtained when $m = 1$ and $n = 0$. Pernigraniline (PB), the complete oxidization state of PANI, is obtained when $m = 0$ and $n = 1$. The Emeraldine (EB) form of PANI is either neutral or doped corresponding to $m = 0.5$ and $n = 0.5$. EB is considered as the most useful

form of PANI due to its high stability at room temperature and the fact that it is electrically conducting upon doping.

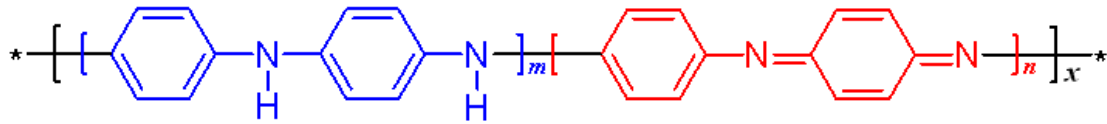


Figure 2.13: Main chemical structure of the conducting polymer polyaniline (PANI). x is the degree of polymerization. Reduced and oxidized states of PANI are represented respectively by the index of m and n with the relation of $m + n = 1$, corresponding to different PANI forms: (1) Leucoemeraldine (LB, $m = 1$, $n = 0$), (2) Emeraldine (EB, $m = 0.5$, $n = 0.5$), and (3) Pernigraniline (PB, $m = 0$, $n = 1$)^[57].

Bayer AG researchers developed an inherently conductive conjugated polymer, poly(3,4-ethylenedioxythiophene) (PEDOT) doped with water soluble poly(styrenesulfonate) (PSS)^[58-59], which has been commercially available as PEDOT:PSS Baytron/Clevios P series. PEDOT:PSS is electro-chemically stable and moderately transparent with a high electrical conductivity ($\sim 10\text{S/cm}$) and a high charge carrier mobility. The work function of PEDOT:PSS is relatively high ($\sim 5.0\text{eV}$). PEDOT:PSS has been widely demonstrated as a hole injection/transport layer^[59-63] or an anode^[64-65] in OLEDs.

It should be noted that by using polymer based materials, the device fabrication can be simplified by using solution processing techniques. Such techniques include not only spin-coating, but also printing methods, such as screen printing^[8-9] and inkjet printing^[10-14]. In addition, by using polymer solution-based processes, it is possible to overlie most of surface defects or surface inhomogeneity of the ITO anode. One of the greatest concerns of using PEDOT on the surface of the ITO anode is its acid nature

(i.e. pH = 1 ~ 2 in Baytron/Clevios P series) ^[66-67]. To meet a variety of applications, Bayer AG formulated several PEDOT:PSS dispersions with different particle sizes, ratios of PEDOT to PSS, and electrical resistivity ^[68-70]. Conducting polymer PEDOT:PSS is still introduced at length in the next Section 2.3.3.

2.3.3 Conducting Polymer - PEDOT:PSS

Poly(3,4-ethylenedioxythiophene):poly(styrenesulfonate) (PEDOT:PSS) were first synthesized by the Bayer AG research group in the late 1980s and became one of the most successful conjugated polymers to be developed and studied ^[59]. The structure of PEDOT:PSS is shown in Figure 2.14.

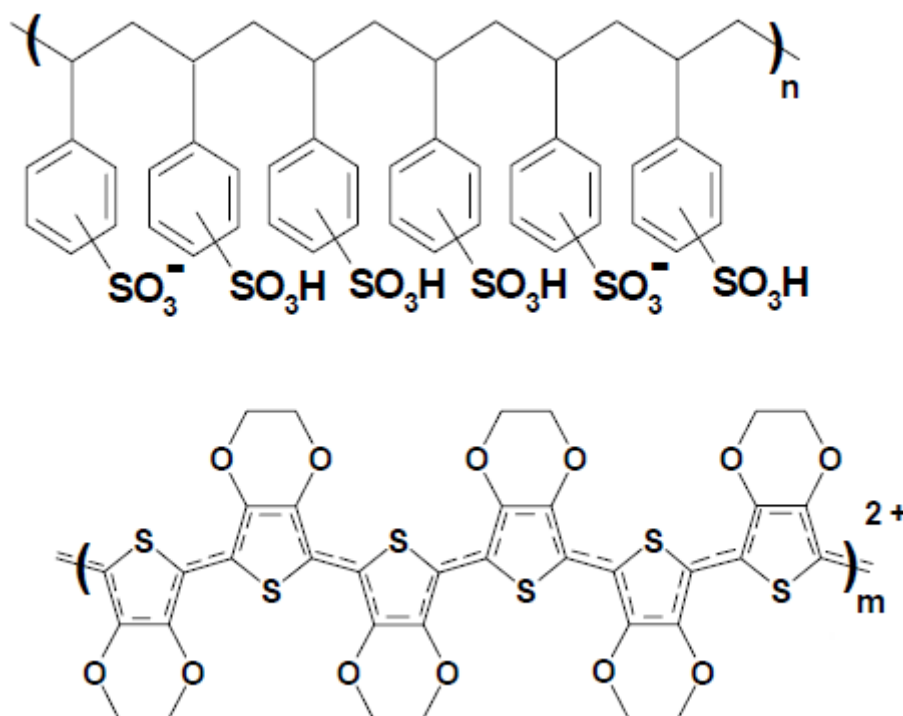


Figure 2.14: Molecular structure of PEDOT:PSS ^[70-72].

PEDOT has been prepared by standard oxidative chemical or electrochemical polymerization methods [73-74]. PEDOT itself is found to be highly conductive (400 ~ 600S/cm) [59], highly transparent [58], electrochemically stable [75], and thermally stable (up to 230°C) [76] in thin oxidized films. Unfortunately, the processing ability of PEDOT itself is very poor because it is an insoluble polymer. This drawback can be overcome by polymerizing it in combination with a water-soluble polyelectrolyte PSS [77]. The resulting PEDOT:PSS is dark blue, electro-chemically stable, moderately transparent with high electrical conductivity (1 ~ 10S/cm) [78], and also has excellent film forming properties.

PEDOT:PSS has drawn considerable attention for industrial and laboratory applications from biology to engineering [79], including antistatic coatings in photographic films (Agfa) [53], electrochromic displays [75, 80-84], organic transistors [85-87], organic resistor-capacitor (RC) filter circuits [88], organic sensor-transistor [89], all-polymer capacitors [90], a hole injection/transport layer [60-63] or anode [64-65] of OLED devices, and a hole collection layer in organic photovoltaic devices [91-93].

It is worth pointing out that the addition of PSS units significantly reduces the conductivity of pure PEDOT, as PSS over-oxidizes around one third of PEDOT units and acts partially as an insulator [59]. When the PEDOT:PSS dispersion (for instance, 0.5wt% of PEDOT doped with 0.8wt% of PSS in Baytron/Clevios P series) is coated on a substrate, polymer chains are most likely found in a high degree of disorder and

then a grain-like microstructure film. Within the grains, PEDOT and PSS species are surrounded by an insulating PSS-rich ‘shell’, which is on the order of ~3nm thick [94].

Since conjugated polymers are generally polycrystalline materials, the bulk conductivity is decided by the properties on the intra-chain and inter-chain transport of charge carriers in the polymer. This usually creates a strong dependence between the conductivity and the film morphology of the polymer. Recent studies have shown that the conductivity of PEDOT:PSS films is considerably increased by adding high-boiling liquid solvents, such as glycerol [64-65, 95-96], sorbitol [97], and N-methyl-pyrrolidone (NMP) [98] (Figure 2.15) during the solution processing, followed by a heat treatment as an annealing process. This improvement is due to the changes in the PEDOT:PSS film morphology induced by the addition of the solvent.

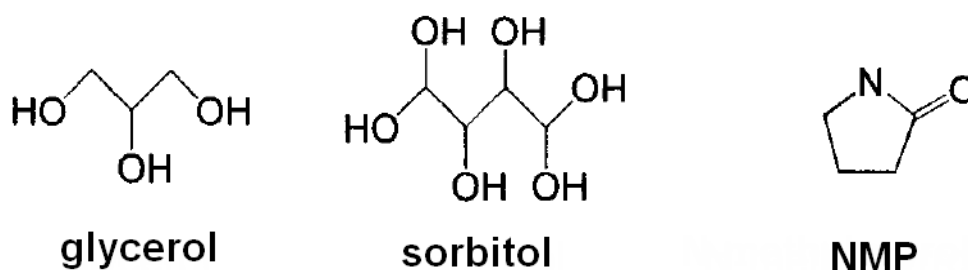


Figure 2.15: Molecular structures of glycerol (boiling point = 290°C), sorbitol (boiling point = 295°C), and N-methyl-2-pyrrolidone (NMP, boiling point = 202°C).

It should be noted that the film morphology, chemical and physical structure can be strongly influenced by a variety of post-deposition treatments such as annealing [65, 99]. Furthermore, Jonsson *et al* [100] reported that the ratio of PEDOT to PSS in the surface region of the film was increased by a factor of 2 to 3, when the dispersion was mixed with high boiling solvents. This would indicate that some of the excess PSS was

removed from the surface during the formation of PEDOT:PSS film, enhancing the connectivity of the conducting regions in the film and thus increasing the bulk conductivity of the film.

2.3.4 Electrodes - Anode and Cathode

2.3.4.1 Indium-Tin-Oxide (ITO) Anode

In OLED applications, at least one of the electrodes must be optically transparent to allow light to exit the device towards the viewer. By far the most commonly used transparent anode material is indium-tin-oxide (ITO). As mentioned in Section 2.2.1.2, it is better to use a material with higher work function as an anode for OLED devices. ITO has a relatively high work function with high transparency in the visible regime, as well as an acceptable surface resistance ($10 \sim 270\Omega/\square$). It can be deposited on various substrates such as glass, metal foil and flexible plastic.

ITO substrates should be carefully prepared since any contaminant deposits or defects from the substrate handling or cleaning will result in poor device performances. The work function of ITO is strongly influenced by an oxidative surface treatment. It appears that the work function of ITO films (Φ_{ITO}) is raised by as much as 0.5eV with rich oxygen content ^[101]. It was also found that increased Φ_{ITO} tends to enhance device brightness, efficiency and device reliability, while reducing the necessary driving voltage. Hence several procedures for increasing the oxygen content of ITO

surface have been developed. One common process is ultraviolet (UV) ozone treatment, in which the ITO film is exposed to ozone ambience produced by a UV lamp^[102]. Oxygen plasma treatment is another effective way widely used to improve surface properties of the ITO anode^[103-104]. Other procedures involve partial etching of the ITO in aqua regia^[105] or plasma etching^[106]. However, for some special cases, such as flexible display applications, the ITO thin film exhibits a poor ability of deflection and is found to develop cracks upon repeated flexing, thus lose conductivity. To avoid these problems, polymeric anodes, such as polyaniline (PANI)^[107] or PEDOT:PSS^[64-65] have been reported as alternate materials, despite possessing a higher surface resistance ($280 \sim 2\,000\Omega/\square$) than that of ITO.

2.3.4.2 Cathode Materials

Many metals have been used as a cathode. The choice of the metal cathode and its composition has a significant effect on device performance and stability. In general, organic materials have a higher hole mobility than electron mobility^[23]. Along with other factors, the high hole mobility, and large electron injection barrier leads to an unbalanced electron and hole charge density in the recombination zone at the ETL-HTL interface. This unbalance has a negative effect on the device external quantum efficiency. One way to enhance the external quantum efficiency is to increase the number of injected electrons. This can be achieved by decreasing the barrier height between the work function of the metal cathode and the LUMO energy

of the ETL.

OLEDs can have cathodes based on metals (or alloys) with low work function (Φ) such as calcium (Ca, $\Phi_{\text{Ca}} = 2.87\text{eV}$), aluminum (Al, $\Phi_{\text{Al}} = 4.3\text{eV}$) or magnesium(Mg)-silver(Ag) alloy $\text{Mg}_{0.9}\text{Ag}_{0.1}$ (for Mg, $\Phi_{\text{Mg}} = 3.66\text{eV}$)^[34] deposited either by thermal or e-beam evaporation method. However, very low work function metals like Ca themselves exhibit a high chemical reactivity with organic mediums and atmosphere. This chemical reactivity easily leads to the oxidation of the cathode layer^[108]. Thus, a small amount of Ag is commonly co-evaporated with Mg to improve the sticking coefficient and the chemical stability of the overall cathode. Other efficient electron-injecting cathode structures such as a bilayer of lithium fluoride (LiF) and Al^[109-110], mixed layers of alkali halide and metal, or alkali halide and organic material^[111] have been demonstrated. OLEDs using such cathode structures show higher external quantum efficiency and light output (at a given voltage) than similar devices with cathodes based on Al ($\Phi_{\text{Al}} = 4.3\text{eV}$), Ag ($\Phi_{\text{Ag}} = 4.3\text{eV}$), or copper (Cu, $\Phi_{\text{Cu}} = 4.7\text{eV}$).

2.4 Fabrication Techniques

One of the major challenges that the OLED industry is facing, is to uniformly deposit the organic materials accurately in a well controlled fashion uniformly onto the substrate in order to obtain the desired pixels and patterns. This section provides a

brief overview of popular existing OLED deposition methods. They are thermal vacuum evaporation of the small molecular organic layers in SM-OLEDs and solution-based or wet-coating techniques of the polymer layers in P-OLEDs including: spin-coating, doctor blade coating, screen printing and inkjet printing, of which inkjet printing technique is the major topic of our concern.

2.4.1 Thermal Vacuum Evaporation

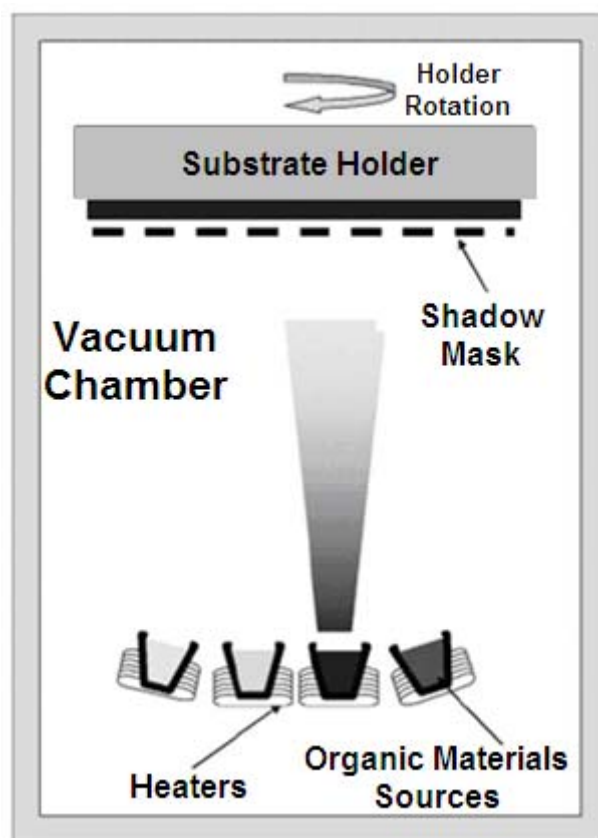


Figure 2.16: Principle of organic small molecules deposition by thermal vacuum evaporation ^[112].

Figure 2.16 shows a layout of a thermal vacuum evaporation for the deposition of organic small molecules. Thermal vacuum evaporation involves the evaporation of

small molecule organic powders placed within crucibles, which are heated to between 100°C to 500°C under vacuum. As shown in Figure 2.16, a thin shadow-mask of between 20 to 100µm thick is placed above the crucibles with the substrate set directly above it ^[112]. This mask bears holes representing the pixel pattern. The mask is shifted by one pixel to deposit the next set of pixels once the material of one color is deposited. For industrial purpose, each material is deposited in a different chamber. Accuracy and handling of large shadow-masks are among the main concerns and limitations of this technique, as alignment of substrate and mask should be done with a precision of ±5µm.

This process takes place within a vacuum environment of about 10⁻⁶ mbar or better. However, it has been observed that the performance of devices may be affected significantly by residual gases in the chamber. Broms *et al* ^[113] found that the performance of OLEDs in which a calcium film was deposited as the cathode in a high vacuum system of ~10⁻⁶ mbar was far better than that deposited under ultra high vacuum of 10⁻¹⁰ mbar. Apparently, this is due to the formation of an oxide layer between the top organic layer and the cathode metal. This led to the deliberate introduction of an aluminum oxide buffer layer by Li *et al* ^[114].

One of the main advantages of this technique is that it enables the fabrication of multilayer devices in which the thickness of each layer can be easily controlled. Furthermore, 2D combinatorial arrays of OLEDs, in which two parameters such as

thickness and composition may be systematically varied across the array, can be easily achieved in a single deposition process ^[115-117].

2.4.2 Spin-Coating

Spin-coating is well-studied and much employed deposition process in inorganic semiconductor industry, where it is mostly deployed to deposit organic photoresist on silicon wafers. It is also a popular method for forming polymeric films for OLEDs. The process is simple. Immediately after loading an excess amount of solution onto the substrate, the substrate is rotated at a high speed (generally 500 ~ 3000rpm) and the fluid solution is spread by the centrifugal force. The resulting film characteristics depend on such parameters as the spin time, the spin speed, the spin plate temperature, the solvent evaporation rate and the rheological properties of the fluid to be spun. It is possible to obtain very thin and homogeneous films using appropriate materials in this deposition method. Although it is a convenient method, only a very small amount of the polymer in the solution, remains as the final film, but more than 99% of the solution is spun off.

Undoubtedly, most of the solutions utilized in OLED fabrication are based on conjugated polymers, which have their own unique morphology. Research reports proved that these polymer morphologies (including aggregation) have a pronounced effect on device optical and electrical properties ^[48-49, 118]. Conjugated polymer

morphology can be greatly influenced by the processing conditions, such as organic solvents, spin-coating speeds, solute concentrations, and drying conditions. Spin-coating technique cannot be used on flexible substrates without special care, and cannot be used on roll-to-roll based substrates. These drawbacks increase the fabrication cost and hinder large-scale applications of spin-coating.

2.4.3 Doctor Blade Coating

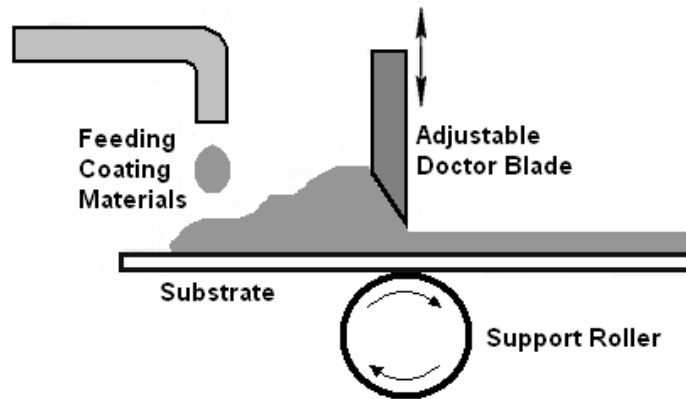


Figure 2.17: Schematic representation of doctor blade coating.

Doctor blade coating is usually used to produce thicker films. This coating is schematic shown in Figure 2.17. Where doctor blade coating uses a blade fixed slightly above the substrate, the coating blade consists of a core steel bar with wires wrapped around to give more control during film formation. The coating blade is placed near the edge of the substrate with a sufficient amount of solution wetting the substrate. Continuous films are formed by moving either the blade or the substrate over the sample. The gap between the blade and the substrate plays a dominant role in

determining the thickness of the film. Physical properties of the ink, such as surface tension, and viscosity, along with drying environment, have a great influence on the film uniformity. For the large area coating of thin films, the doctor blade coating process of conjugated polymers (PEDOT:PSS and MEH-PPV) were demonstrated by Ouyang *et al* ^[119] with high uniformity and over thickness ranges from 30 ~ 80nm.

2.4.4 Screen Printing

Screen printing is a well-known, solution-based, patterning technique. The process involves pushing polymer ink through threads (normally made from polymer) of a screen which form a cross-mesh pattern defined by the screen mesh (number of threads per inch) and the thickness of the thread, as shown in Figure 2.18.

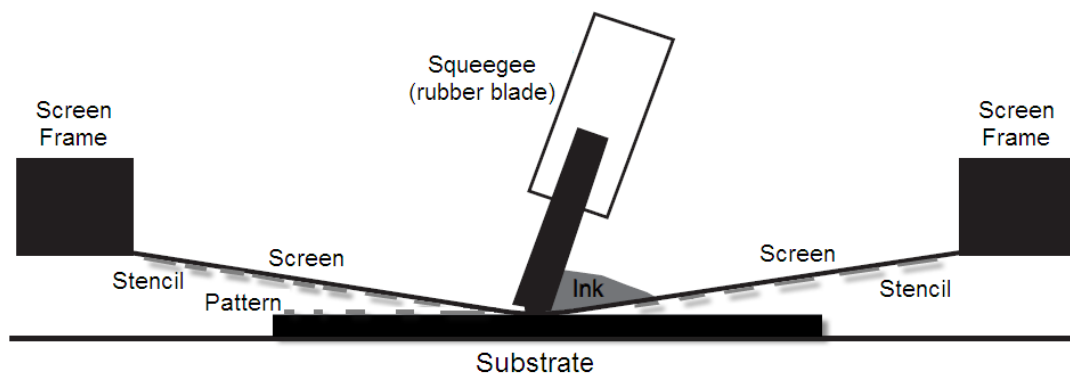


Figure 2.18: A schematic of typical process for screen printing. The screen is patterned using a photo emulsion ^[120].

The most common way to create the stencil is to use a photo emulsion which hardens when exposed to UV light. The emulsion is used to cover the parts of the screen (attached to a frame) which are not supposed to let any ink pass through to form the

‘negative’ image. The ‘positive’ image will be the uncovered areas of the screen, which allows ink to pass through it and thus be transferred onto the substrate. The ‘negative’ image formed by the emulsion is usually created by first covering the entire screen with the photo emulsion and then covering parts of the screen with the ‘positive’ image while exposing it to UV light. The ‘positive’ image, used to protect the parts of the emulsion against the UV light, must be entirely opaque. The unexposed emulsion can then be washed off the screen while the hardened emulsion stays on to form the stencil. Having prepared the screen, the printing procedure will then proceed as follows. The screen and its frame are placed above the substrate, either directly in contact with the substrate or a few millimeters above it. Then the ink is transferred from the top side of the screen to the substrate by pressing it through the screen with a squeegee, which is simply a rubber blade. Since no ink can pass through the areas covered by emulsion, the ‘positive’ image will be printed on to the substrate.

Screen printing has been used by the printed circuit industry to resolutions down to 50 μm ; however, the practical limitations are above 100 μm due to the edge and alignment effects in printing organic light-emitting displays. Since materials are deposited only where desired, screen printing can minimize a great amount of waste. Furthermore, it allows relatively high speed patterning over a large area with a resolution below 75 μm . Fabricating thin films in OLEDs using screen printing, was first demonstrated by Pardo *et al* ^[8] from the University of Arizona in 2000. To control film thickness and film uniformity, the most important parameters are the

concentration of the solution, the mesh count of the screen, and the distance between the screen and substrate^[9, 121]. This simple and inexpensive technique provides a great potential for low cost and high-throughput fabrication of OLEDs, especially in such applications, signs, lights, and low-information content displays.

2.4.5 Inkjet Printing

Inkjet printing is a familiar method for printing ink on absorbent paper or photo paper. Inkjet technology has the advantages of simplicity, high throughputs, and speed. A desktop computer can directly control the delivery of pico-liter volume of liquids in flexible precise patterns. Therefore, inkjet printing does not consume significant amount of material as is the case with spin-coating. It promises a low cost, maskless and even non-contact approach to generate potentially varying patterns on a given delicate substrate. A large number of different inkjet printing technologies and methods have been invented and developed by different companies and researchers. Figure 2.19 shows a fundamental layout of the different inkjet printing technologies. Some of the more commonly used methods will be given a brief introduction. Basically, inkjet printing is categorized into the continuous and the drop-on-demand modes in operation.

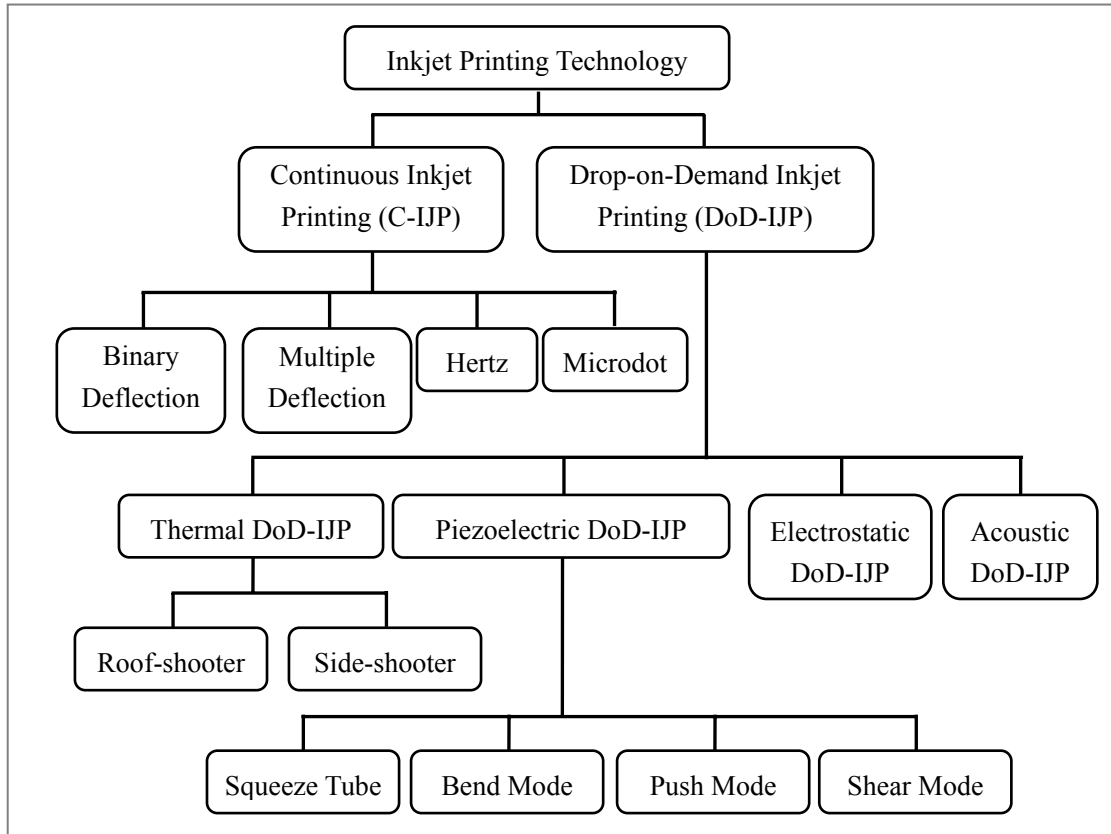


Figure 2.19: Layout of the different inkjet printing technologies.

2.4.5.1 Continuous Inkjet Printing Technologies

By applying a pressure wave profile to a nozzle orifice, the ink stream can be broken into droplets of uniform size and spacing. A continuous inkjet printing (C-IJP) can dispense 20 to 500 μm size droplets at rates of up to 1MHz. With proper control of the drop forming mechanisms, an electric charge can be induced on the drops selectively as the continuous ink stream breaks up. When the droplets pass through an electric field, those uncharged droplets drift into a catcher for recirculation and those that are charged will be deflected onto the substrate to form a pattern^[122]. C-IJP is classified as binary or multiple deflection modes depending on the drop deflection methodology.

In a binary deflection system shown in Figure 2.20, the charged droplets are allowed to deposit onto the substrate, while the uncharged drops are collected in a catcher for recirculation.

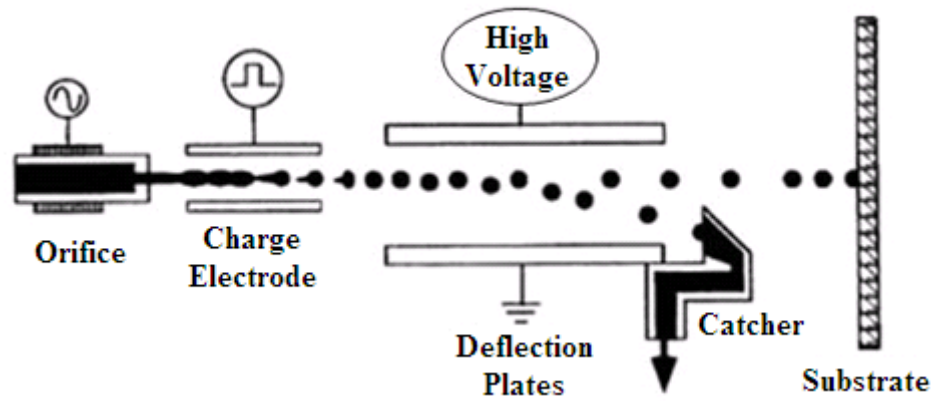


Figure 2.20: Binary deflection C-IJP system ^[123].

In a multiple deflection system shown in Figure 2.21, droplets are charged and deflected onto the substrate at different levels. The uncharged droplets drift into a catcher for recirculation. Using this approach, a small image swath can be printed by a single nozzle. Figure 2.22 shows streams of droplets from a C-IJP process.

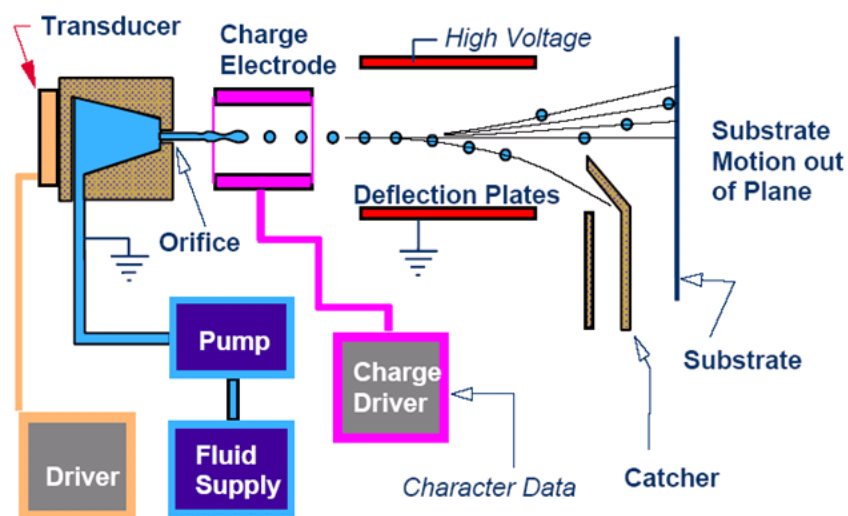


Figure 2.21: Multiple deflection C-IJP system ^[122].

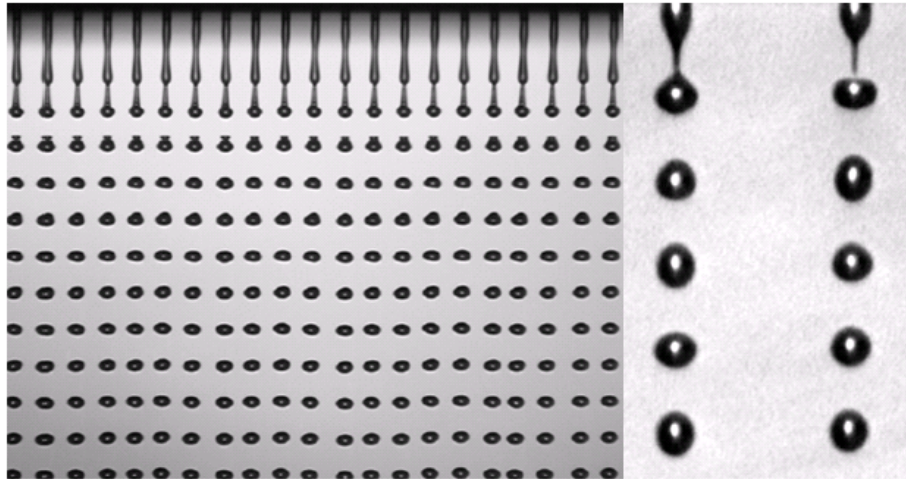


Figure 2.22: Streams of continuous droplets from a C-IJP process ^[122].

2.4.5.2 Drop-on-Demand Inkjet Printing Technologies

A drop-on-demand inkjet printing (DoD-IJP) device ejects liquid droplets only when they are required at the particular location on the substrate ^[124]. DoD principle eliminates the need for drop charging and a drop deflection system, as well as the unreliability of the ink recirculation system required by C-IJP. Currently, most of the industrial and research interest in inkjet printing are in the DoD methods. DoD mode inkjet technology can dispense 15 to 150 μm size droplets at rates of between 0 to 25kHz ^[122]. Depending on the mechanism during the drop formation process, DoD-IJP can be classified into four main types of thermal, piezoelectric, electrostatic and acoustic. Most DoD-IJP systems in the market are using the thermal or the piezoelectric principles. Figure 2.23 shows the schematic layout of a DoD-IJP process. Regardless of the type of transducers used, the basic working mechanisms of the DoD process are similar. Figure 2.24 shows the droplets from a DoD-IJP process. A continuous stream is not found in this process to produce droplets.

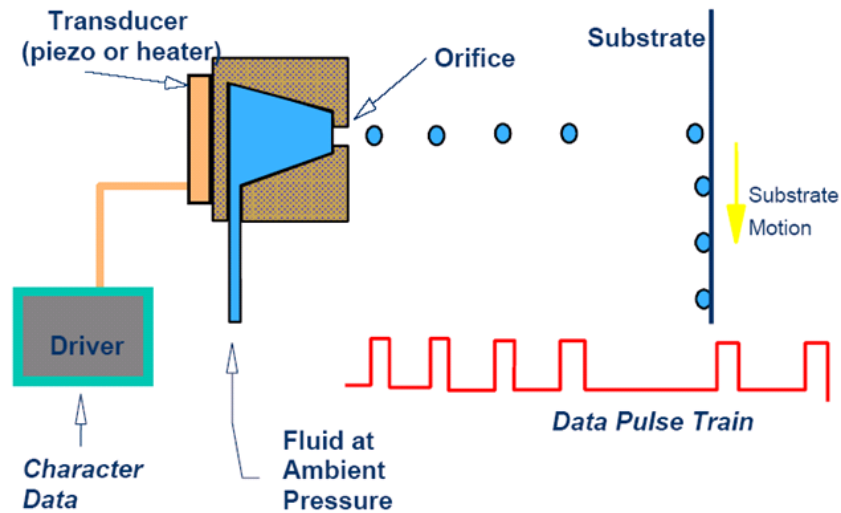


Figure 2.23: Schematic of the DoD-IJP process ^[122].

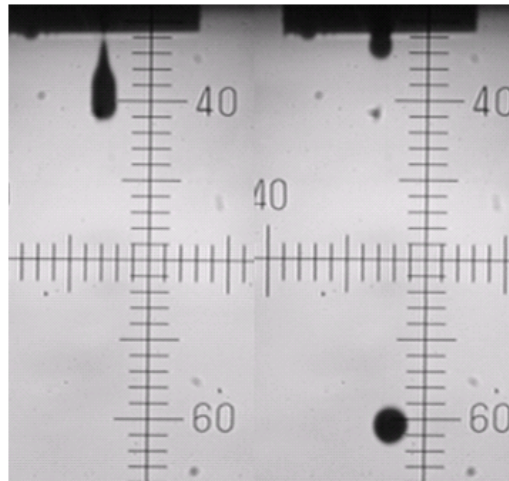


Figure 2.24: Droplets from a DoD-IJP process ^[122].

(1) Thermal Inkjet Technologies

In thermal IJP, droplets are ejected from the nozzle due to cavitation of a water vapor bubble on the top surface of a small heater located near the nozzle. IJP print-heads can be built at low cost with high nozzle packing density due to the simplicity of a thermal jet print-head design and its semiconductor compatible fabrication process. Thermal IJP was not the first IJP method to be implemented on a commercial product. However, it is one of the highly successful methods, especially for graphic-arts

applications and home and office desktop printers. Depending on the way its mechanism is structured, a thermal inkjet can be a roof-shooter (Figure 2.25) with an orifice located on the top of the heater or a side-shooter (Figure 2.26) with an orifice located on a side near the heater.

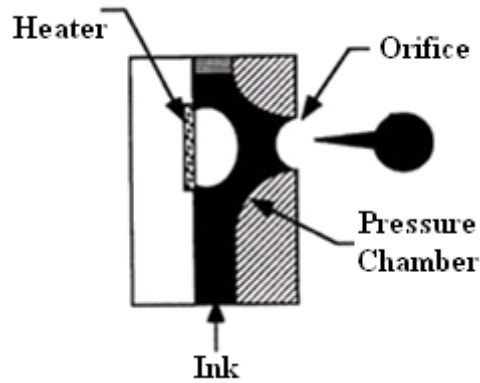


Figure 2.25: Roof-shooter thermal inkjet mechanism layout ^[123].

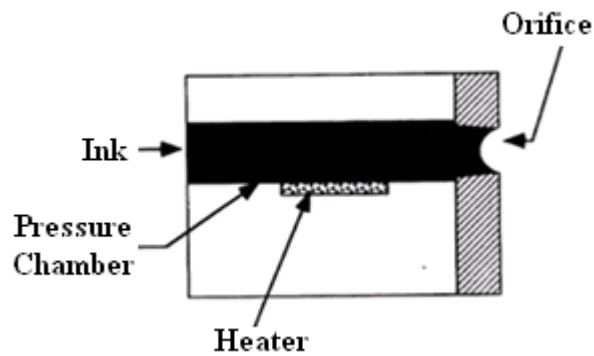


Figure 2.26: Side-shooter thermal inkjet mechanism layout ^[123].

In Figure 2.27, we see the drop formation process within the ink chamber of a thermal inkjet device.

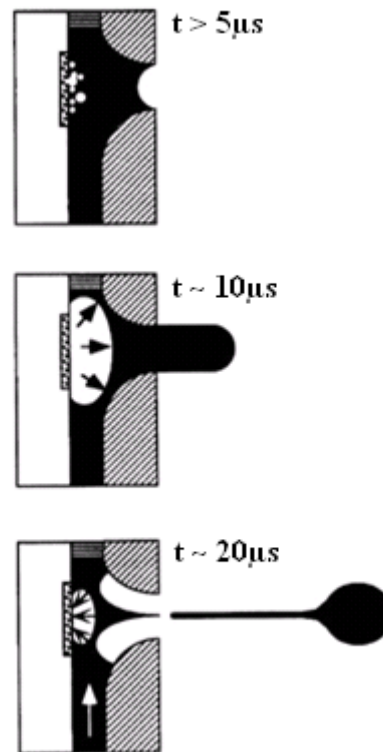


Figure 2.27: Drop formation within the ink chamber of a thermal inkjet device ^[123].

(2) Piezoelectric Inkjet Printing Technologies

In piezoelectric IJP, the underlying principle of operation is the creation of acoustic waves in the fluid column by a piezoelectric actuator. The application of a voltage pulse to the piezoelectric element causes mechanical motion of this element, which generates a pressure wave that ejects droplets. Under proper shaping of the stimulating pulse to the piezoelectric element, it leads to a controlled ejection of single droplets onto the feature substrate. Depending on the piezoelectric element's deformation mode as shown in Figure 2.28, piezoelectric inkjet technology falls into four different categories: bend, push, shear, and squeeze.

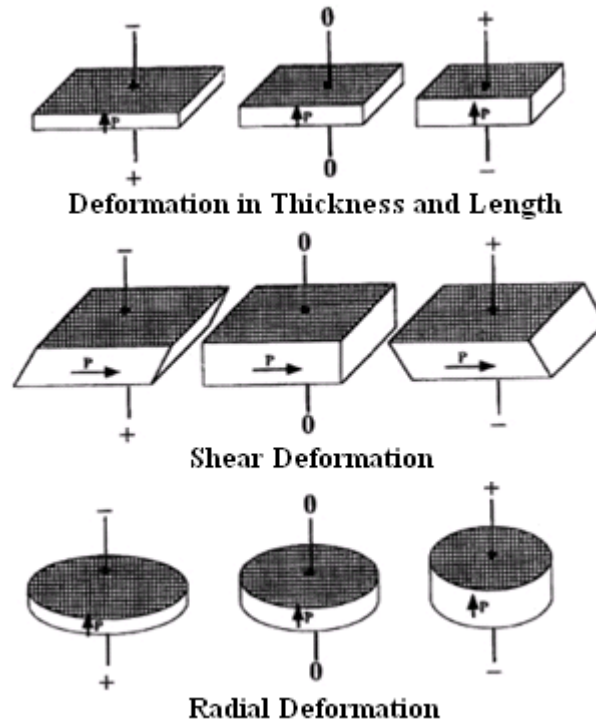


Figure 2.28: Different modes that a piezoelectric plate can deform ^[123].

In a bend mode inkjet design shown in Figure 2.29, the piezo-ceramic plates are bonded to the diaphragm. This forms an array of bi-laminar electromechanical transducers used to eject the ink droplets ^[123].

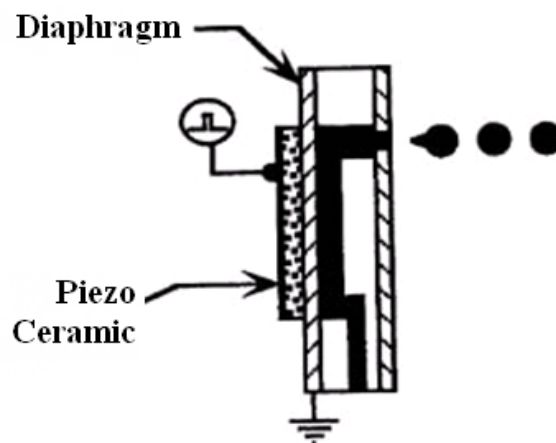


Figure 2.29: Bend mode piezoelectric inkjet system ^[123].

For a push mode inkjet as shown in Figure 2.30, a piezo-ceramic rod pushes against

the ink to eject the droplets, as it expands.

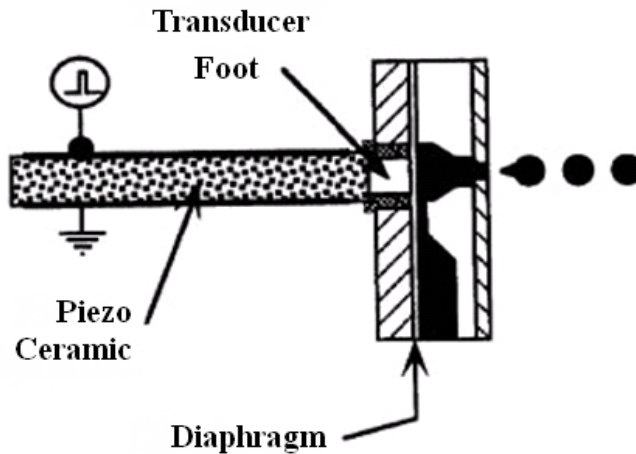


Figure 2.30: Push mode piezoelectric inkjet system ^[123].

In both the bend and push mode inkjet systems, electric field generated between electrodes is parallel with the polarization of the piezoelectric material. However, in a shear mode inkjet, the electric field is perpendicular to the polarization of the piezoelectric driver as shown in Figure 2.31. The shear action deforms the piezoelectric slice against the ink to eject droplets. For this design, the piezoelectric element forms an active part of the wall in the ink chamber. Hence, interaction between ink and piezo-element is one of the features of a shear-mode inkjet system.

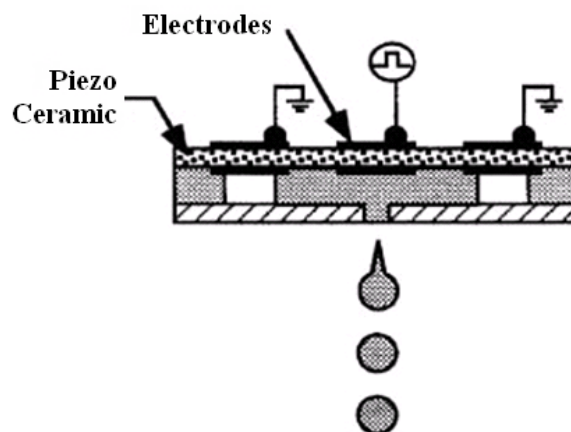


Figure 2.31: Shear mode piezoelectric inkjet system ^[123].

A squeeze-mode inkjet can be designed such that a thin tube of piezo-ceramic surrounds a glass nozzle, a piezo-ceramic tube cast in plastic that encloses the ink channel or a piezo-ceramic block with a number of fluid channels machined directly into it ^[124]. Figure 2.32 shows an example of a squeeze mode inkjet, where the cylindrical piezo-ceramic transducer surrounds a thin-walled glass tube.

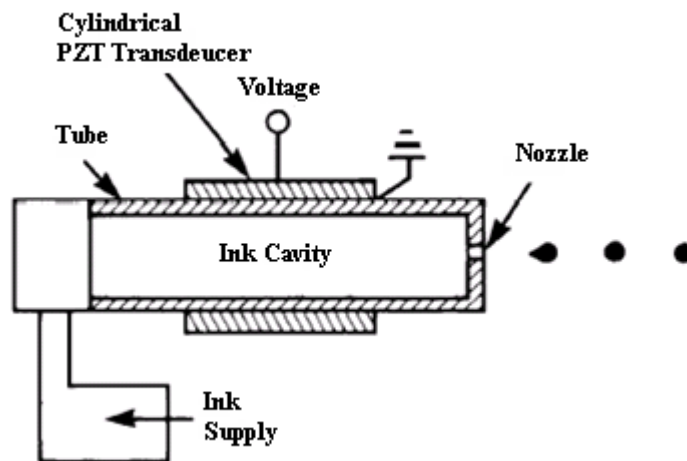


Figure 2.32: Squeeze mode inkjet using a piezo-ceramic cylinder and a glass tube ^[125].

In theory, piezoelectric elements can come into direct contact with the ink solution. However, in practical applications, a thin diaphragm separates the piezoelectric driver and the ink. This is incorporated to prevent any undesirable interactions between the ink and the piezoelectric material.

2.4.5.3 Inkjet Printing of Materials and Devices

In recent years, inkjet printing has been used in a variety of fields including ceramics, metals, organic semiconductors and biopolymers. Efforts to dispense materials by IJP

have been reviewed recently by Calvert^[17]. A few reported applications of the inkjet technique include the printing of hole-based interconnections in all-polymer thin film transistor (TFT) circuits^[87], the printing of all-polymer field-effect transistors^[126], and the printing of capacitors^[88]. For applications in polymer OLEDs, inkjet printing has been used to deposit a patterned polymer layer on the top of a given anode^[10-12], or to deposit the PEDOT:PSS or electroluminescent polymers as a pixel array on a circuit, which was pre-patterned via photolithography^[13-14]. Dielectric layers and organic compounds, including photoresists^[127], self-assembled mono-layers^[128], semiconducting polymer such as MEH-PPV^[129] and organic nano-particles^[130] have been patterned by inkjet printing with the resolution range of 100µm below.

Garnett and Ginley characterized the electrical and morphological properties of inkjet printed PEDOT:PSS films^[131]. They found that their films had lower sheet resistivity than spin-coated reference films and suggested that the technique itself provides a better mixing of PEDOT and PSS in the film.

Much of the reported work on inkjet printing of conjugated polymers have been carried out using rather advanced inkjet equipments^[126, 132-133]. However, some research groups have chosen a different approach and are using simple desktop printers as their tools for device fabrication. Liu *et al* succeeded in constructing an all inkjet polymer field-effect transistors^[126]. A few years earlier, the same group of researchers inkjet printed fully functional RC circuits with a commercial Epson Stylus

color 480 SXU printer with a mounted piezoelectric print head^[88, 90].

Inkjet printing comes in handy as an electrode patterning tool. As an example, Yoshika and Jabbour^[134-135] used a modified HP 5550 thermal desktop inkjet printer to print PEDOT:PSS on glass substrates. Patterns were designed in Microsoft Power Point software. The black ink cartridge had been filled with PEDOT:PSS dispersion, so the sheet resistivity of the films could be controlled by the luminosity values of the patterns from the software. Sirringhaus *et al*^[85] inkjet printed the gate, the source and the drain electrodes of their historically important first all-polymer thin film transistor, using PEDOT:PSS as polymeric electrode material. The semiconducting and the insulating layers of this device were spin-coated onto the substrate. In 2005, Sele and Sirringhaus *et al*^[136] succeeded in building polymeric field-effect transistors with channel lengths less than 100nm using an innovative technique called self-aligned inkjet printing.

As the organic layers can be deposited directly as an array of pixels, there is vast potential of it being used for the direct patterning of displays. Currently, this technique is being utilized for the development of high information content (HIC) displays by many companies including Cambridge Display Technology (CDT), Seiko-Epson, Toshiba and Philips etc. Samsung in 2005 demonstrated display prototypes deposited using inkjet printing, ranging in size of up to 40 inches. It should be noted that across the globe, there are now more than a handful of research institutes

and companies involved in the display industry, which have reported the fabrication of P-OLED displays to high resolutions and large screen sizes. However, a literature survey has not revealed any manufacturing details or insights into the finer points of inkjet printing and relevant operating parameters. Therefore research on the inkjet printing applied in OLEDs is still necessary in order to have a better understanding of the behavior of this versatile technique. In fact, inkjet printing technologies in application of polymer electronics, OLED devices and solar cells etc. have been gathering much more attention by manufacturers.

CHAPTER 3

INDIUM-TIN-OXIDE (ITO) SUBSTRATE SURFACE TREATMENT

3.1 Introduction

A large number of transparent conducting oxides are known and these include tin oxide, indium oxide, zinc oxide and their combinations. However, the anode of organic light-emitting diodes (OLEDs) is in the majority a thin layer (~100nm to 200nm) of indium-tin-oxide (ITO) or fluorinated-tin-oxide (FTO) ^[137-140]. ITO is a common substrate used in many applications such as OLEDs, photovoltaic devices and flat-panel displays like liquid crystal displays (LCDs) ^[141]. It has attracted much of an interest for these applications due to its widespread availability, unique characteristics of high electrical conductivity, high optical transmittance over the visible wavelength region or transparency (better than 90% at 550nm), excellent adhesion to glass substrates, stable chemical properties, and the ease with which it can be patterned ^[137-140]. ITO thin films with different optical and electrical properties required for different purposes are produced industrially and reproducibly using reactive thermal evaporation deposition or magnetron sputtering ^[137]. They can be easily patterned by photolithographic techniques, which are currently been used widely for device fabrication.

For OLEDs, ITO substrate surface properties are extremely important because these displays depend on the charge carrier injection through the interface formed with another OLED material layer which is in direct contact with the ITO substrate. As surface wettability, which is one direct and crucial measurement of surface properties, has a great influence on the final OLED performance, a better understanding of the effect of different surface processing techniques on the ITO surface is highly desirable for the purpose of device applications.

3.1.1 Introduction to Surface Wettability

3.1.1.1 Surface Energy and Contact Angle

As mentioned, surface wettability of ITO substrates plays an important role for enhancing the performance of OLED devices. Furthermore, for inkjet printing purposes, wettability of the surface by the printed droplets on impact is one of the main concerns. Spreading of these droplets after initial impact, which determines the final dried droplet shape and profile, is also apparently closely related to the surface wettability of the substrates. These will have an impact on the different aspects of the ITO surface and interface, as well as the performance of final devices.

Surface properties of any solid substrate are a direct result of intermolecular forces within the solid. *Surface energy* quantifies the disruption of intermolecular bonds that occurs when a surface is created. In the physics of solids, surfaces must be

intrinsically less energetically favorable than the bulk of a material; otherwise there would be a driving force for surfaces to be created such that the surface of a solid possesses additional free energy. *Surface energy* may therefore be defined as the excess energy at the surface of a material compared to the bulk. For a liquid, the *surface tension*, which is the force per unit length, is usually used and it is analogous to the surface energy for a solid. Due to the reduced molecular mobility in a solid, this free energy is not directly measurable and must be probed with indirect techniques such as *contact angle measurements* ^[142]. With regard to the prediction of its wetting and adhesion properties, the surface energy of a solid material is of considerable interest. It is a useful indication of both surface wettability and adhesion, and can be applied in many technical processes such as quality control procedures found in industries.

By measuring the contact angle of a liquid deposited on a solid, we can obtain a quantitative measurement of surface wettability, which enables us to determine its surface free energy. *Contact angle* is the angle at which a liquid/vapour interface meets the solid surface (see Figure 3.1). Contact angle is specific for any given system and is determined by the interactions across the three interfaces. It should be noted that contact angle is not limited to a liquid/vapour interface meeting the solid surface, and it is equally applicable to the interface of two liquids or two vapours although this is not typical. Contact angle plays the role of a boundary condition. The smaller the contact angle, the better the surface wettability and the higher the surface energy.

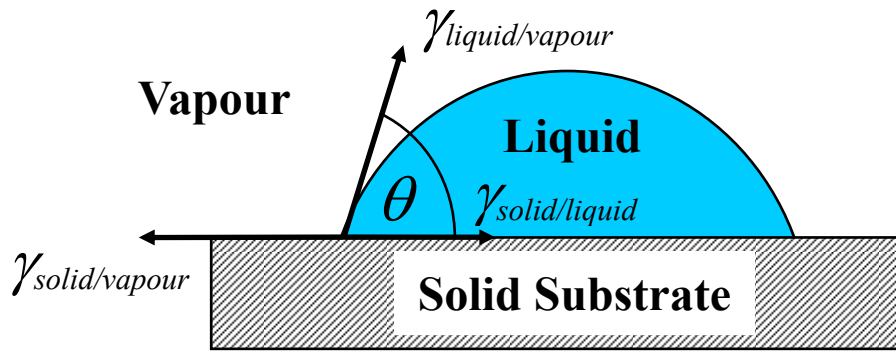


Figure 3.1: Different surface energy components and contact angle of a liquid droplet.

The different components of surface energy between a solid substrate, a liquid and the surrounding environment for a liquid droplet, together with the contact angle at the three phase boundaries are as shown in Figure 3.1. The contact angle (θ) is established by a force balance between the surface energy of the solid substrate ($\gamma_{solid/vapour}$), the surface tension of the liquid droplet ($\gamma_{liquid/vapour}$) and the interface energy between the substrate and the liquid ($\gamma_{solid/liquid}$). This relationship is given by the famous Young's equation ^[143-145]:

$$\cos \theta = \frac{\gamma_{solid/vapour} - \gamma_{solid/liquid}}{\gamma_{liquid/vapour}} \quad (3.1)$$

From the above equation, the cosine value of the contact angle is used within the calculations. Actual contact angle is then explored to indicate the degree of surface wettability. The better surface wettability is available at the lower contact angle. However, for this contact angle to have any physical significance, we must also investigate its cosine value.

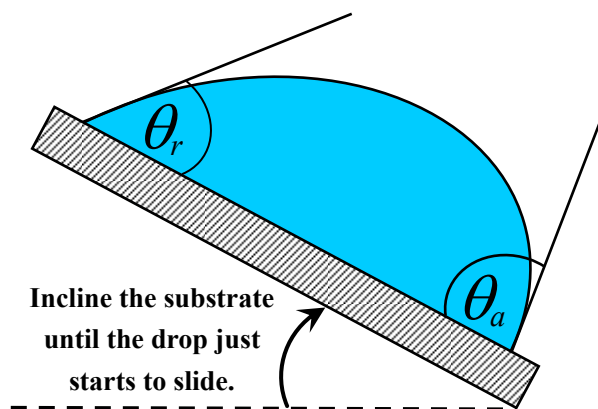


Figure 3.2: Advancing contact angle (θ_a) and receding contact angle (θ_r) of a liquid droplet on a tilted substrate.

In addition, three different contact angles can be measured when a sessile drop is deposited on a solid substrate. In Figure 3.1, the contact angles obtained are for a substrate that is held at the horizontal position. This is normally the contact angle that is referred to in the literature. For differentiation purposes in this thesis, we shall call it the *sessile contact angle* (θ). When the substrate is tilted as shown in Figure 3.2 and the liquid drop just starts to slide down the substrate, two other *dynamic contact angles* can be obtained. They are known respectively as the *advancing contact angle* (θ_a) at the advancing edge of the droplet and the *receding contact angle* (θ_r) at the receding ‘tail’ of the same droplet. θ_a and θ_r are the two reproducible and reliable contact angle values that may be published. When looking at a model of a heterogeneous surface, the advancing angle reflects the characteristics of the low-energy portion of the surface, while the receding angle reflects the characteristics of the high-energy portion of the surface. The sessile contact angle will always lie somewhere between the advancing and receding contact angles. Correspondingly, the advancing and receding contact angles define the maximum and minimum contact

angles respectively.

For an ideal surface that is wetted by a pure liquid, contact angle theory predicts one and only one thermodynamically stable contact angle. In the real world, however, the ideal surface is rarely found. To fully characterize any surface, therefore, it is important to measure both advancing and receding contact angles and report their difference as the *contact angle hysteresis*.

3.1.1.2 Contact Angle Hysteresis

The difference between the maximum (advancing) and minimum (receding) contact angle values, θ_a and θ_r , is referred to as the *contact angle hysteresis* (H). However, this difference is often not a simple subtraction of θ_a from θ_r . In practice, the contact angle hysteresis is simply calculated by subtracting the measured θ_a with the measured θ_r , given by:

$$H = \theta_a - \theta_r \quad (3.2)$$

One can thus say that the hysteresis is the range of stable apparent contact angles that can be measured for the system. From the Young's equation, we can also define hysteresis H in terms of their cosine values given by the following equation:

$$H = \cos \theta_r - \cos \theta_a \quad (3.3)$$

This is usually used for the formula derivations in theory.

Contact angle hysteresis is a result of the presence of energy barriers at the edge of the liquid droplet as it starts to slide. These barriers arise from surface heterogeneity, roughness, adsorption, desorption, deformation, liquid properties, and/or inter-diffusion ^[142]. There are two sources of so-called *thermodynamic contact angle hysteresis* - surface roughness and surface heterogeneity. These represent the two most common of all sources of contact angle hysteresis in real-world surfaces. Table 3.1 below is a summary of the two primary sources of true contact angle hysteresis ^[146].

Table 3.1: Sources of thermodynamic contact angle hysteresis ^[146].

General Assumption	Specific Assumption	Effect on Contact Angle Hysteresis (H)
Smooth Surface	Surface must be smooth at the 0.1 μm to 0.5 μm level.	H increases with increasing surface roughness (θ_a increases and θ_r decreases with increasing surface roughness).
Homogenous Surface	Surface must be homogeneous at the 0.1 μm level and above.	θ_a dependent on low energy phase; θ_r dependent on high energy phase.

For a surface that is perfectly smooth and compositionally homogeneous, theory suggests that there is no hysteresis and a liquid droplet will start to slide down this surface at the slightest tilt of the substrate. A liquid droplet deposited on a surface will move easily if hysteresis is small and with great difficulty if hysteresis is large. If a droplet moves easily, it also means that the surface is fairly uniform. Otherwise, it means that the surface is patchy and non-uniform. This indication of surface characteristics is why a great deal of research has gone into analysis of the significance of contact angle hysteresis.

Any pristine surface exposed to ambient air will absorb hydrocarbon molecules from the atmosphere. This is known as *surface degradation* or *ageing effect* and all contact angle measurements should be carried out before this occurs, unless we are interested in the surface degradation or ageing behavior with respect to time. Hydrocarbon molecules are strongly absorbed by higher energy surfaces, such as metals and metal oxides. They are one major source of contamination reducing surface wettability and uniformity. This is similar to organic contaminant that is left behind due to an inappropriate cleaning process or a cleaning process that has not been carried out properly. Surfaces with a full coverage of organic molecules will have a contact angle of between 50° and 90°. For ITO surfaces, a partial contamination will give a patchy surface, with bare ITO patches (areas of high surface energy that pin the receding tail of a sliding droplet; decreasing θ_r) and organic contaminants (areas of low surface energy that pin an advancing liquid front; increasing θ_a) that gives rise to a higher contact angle hysteresis.

In the OLED application, Kim *et al* ^[142] reported some results on contact angle hysteresis and surface energy of ITO substrates treated using different procedures and measured using contact angles. They found that both contact angle hysteresis and surface energy depended strongly on the surface treatment procedures, and oxygen plasma treatment induced the highest surface energy. They concluded that this improves the interface formation with polymers and hence the device performance.

3.1.2 Review of Surface Treatment and Related Wettability

From literature survey, studies have been reported on modifying the surface properties of ITO substrates. Various treatment processes leading to different surface properties have been investigated. These processes include mechanical, wet, dry and combined treatments. Mechanical treatments include rubbing with different materials like paper or Teflon ^[142]. Wet treatments are related with the use of liquids or solutions, including ultrasonic degreasing ^[137-138, 141-142], hydrochloric acid (HCl) treatment ^[138], RCA ($\text{NH}_4\text{OH}:\text{H}_2\text{O}_2 = 1:4$) ^[137, 142], and aqua regia ($\text{HNO}_3:\text{HCl} = 1:3$) ^[137, 141-142]. Dry treatments are without any liquids or solutions, inclusive of oxygen plasma ^[138, 141-142] and argon plasma ^[141-142]. Combined treatments include aqua regia followed by oxygen plasma ^[142] or oxygen plasma followed by aqua regia ^[142].

The various surface treatment processes of the ITO substrate can modify its electronic and transport properties such as work function, carrier concentration, surface conductivity, and charge carrier (hole and electron) injection characteristics. They can also influence its morphological properties such as surface roughness, hardness and interface structure, its physicochemical properties such as surface energy and polarity, and its optical properties such as transparency ^[138-139, 141]. Since the various surface treatment procedures have an effect on the ITO surface properties, they will also have an effect on the performance properties of complete OLED devices built using substrates modified by one of these processes. Performance properties that would possibly be affected include luminescent lifetime, efficiency, brightness and driving

voltage ^[138-139, 141]. Zhong *et al* ^[138, 141] concluded that the surface wetting properties of ITO substrates have a direct impact on the performance of polymeric OLED (P-OLED) devices. It was suggested that the electronic and transport properties of the ITO anodes are not the only factors of importance affecting device performance ^[141]. Hence, studies on ITO substrate surface modifications and the enhancement of its wetting properties is very important for P-OLED device characteristics.

From the literature, contact angles that were achieved using various surface cleaning and modification process are summarized and tabulated in Table 3.2. Some of the literature gives only advancing and receding contact angles (θ_a and θ_r), whereas in others, sessile contact angles (θ) are given. However, we can make a very rough estimation of the sessile contact angle from the advancing and receding contact angles using the following formula:

$$\cos \theta = \frac{\cos \theta_a + \cos \theta_r}{2} \quad (3.4)$$

It should be noted that this is not done here as we only need a rough idea of what values of contact angles other researchers have achieved. The testing liquid that was used in contact angle measurement is distilled water. For most processes, the actual procedural steps were not given in the literature, and only the name and type of process is known to us. Hence, processes with the same name within the table may have some differences in the way they are actually been carried out.

Table 3.2: Summary of contact angles reported from the literature.

Surface Treatment Classification	Surface Treatment Processes	Advancing Contact Angle (°)	Sessile Contact Angle (°)	Receding Contact Angle (°)	Reference No.
Mechanical Process	Paper Rubbing	57.8		26.5	[142]
	Teflon Rubbing	53.8		22.5	[142]
Wet Process	Ultrasonic Degreasing	42.5		18.1	[142]
	RCA Protocol without Isopropyl Alcohol	45.3		19.8	[142]
	Aqua Regia	70.2		30.2	[142]
	Ultrasonic Degreasing		74.0		[137]
	RCA Protocol with Isopropyl Alcohol		47.0		[137]
	Aqua Regia		34.6		[137]
	Ultrasonic Degreasing		64.6		[138]
	Hydrochloric Acid		82.0		[138]
	Ultrasonic Degreasing		46.7		[141]
	Aqua Regia		73.6		[141]
Dry Process	Oxygen Plasma	28.6		12.3	[142]
	Argon Plasma	96.5		49.3	[142]
	Oxygen Plasma		30.7		[138]
	Oxygen Plasma		20.1		[141]
	Argon Plasma		37.3		[141]
Combined Process	Aqua Regia + Oxygen Plasma	37.7		18.0	[142]
	Oxygen Plasma + Aqua Regia	53.8		21.3	[142]

3.2 Experimental Procedures

The equipment, materials, surface treatment processes, contact angle measurement procedures and experimental setups are documented and presented in this section.

3.2.1 Equipment and Materials

Given below in two separate sections are the list of equipment and materials that have been used for this portion of the work.

3.2.1.1 Equipment

(1) For the wet surface treatment processes (Alkaline, Organic and Neutral described in the next Section 3.2.2), an ultrasonic cleaner (Branson Ultrasonic Cleaner; Model: 3510E-DTH) supplied by Branson Ultrasonic Co. was used.

(2) For the UV-Ozone drying surface treatment process, a UV-Ozone surface treatment system (UVO-Cleaner; Model: 42-220) supplied by Jelight Company Inc. was used as shown in Figure.

(3) For the Oxygen-Plasma drying surface treatment process, an oxygen-plasma cleaner (Sirius RIE Etch System) supplied by Trion Technology Inc. was used.

(4) For the measurement of contact angles, a contact angle goniometer (CAG) (Rame-Hart CAG (NRL); Model: 100-00; SN: 2165) supplied by Rame-Hart

Instrument Co. was used.

(5) For the dispensing of the water droplet onto the ITO substrates, a set of syringe (50L Gastight High Performance Micro Syringe; Part No.: 80965), needle (Removable-type needles; Part No.: 7770-01) and plunger (Repeating Dispenser; Part No.:83700) system supplied by Hamilton Company was used.

3.2.1.2 Materials

(1) The ITO-coated glass substrates were supplied by Merck Display Technologies Inc. The ITO layer is deposited on sodalime polished glass that comes in a size and thickness of $200 \times 200 \times 0.7 \text{mm}^3$ with a sheet resistance of $11.7 \Omega/\square$.

(2) The de-ionized (DI) water was produced in-house by a Labconco Co. machine - WaterPro PS Polishing Station 90005-00. This DI water is free of ions, has a resistivity of $18.2 \text{M}\Omega/\text{cm}$ and a surface tension of 72.4mN/m . However, the monitor device measuring conductivity does not measure hydrocarbon content. An extra filtration step which is found in this machine is needed to produce organic-free pure water.

(3) For the Alkaline wet surface treatment process, the alkaline treatment agent Deconex was supplied by Borer Chemie AG.

(4) For the Organic wet surface treatment process, both Acetone and Isopropyl Alcohol (IPA) in use were supplied by Honeywell International Inc.

(5) For the Neutral wet surface treatment process, the near neutral treatment agent Decon Neutracon was supplied by Decon Laboratories Ltd.

3.2.2 Surface Modification of ITO Substrates

Two different sets of the FIVE surface treatment processes, wet and dry cleanings, have been used in this research to modify the surface of ITO substrates. They are namely the three wet treatment methods of Alkaline, Organic and Neutral and the two dry treatment methods of UV-Ozone and Oxygen-Plasma.

3.2.2.1 Wet Treatment Methods

(1) Alkaline Treatment Process

- Rinse ITO substrates with DI water
- Warm-up ultrasonic bath with 2% (by weight) Deconex in DI water to 50°C
- Degas this solution for 10mins
- Ultrasonic clean with samples immersed in this solution for 5mins
- Rinse three times with DI water (replace with fresh DI water for each time)
- Ultrasonic clean with samples immersed in DI water for 15mins at 50°C

- Rinse three times with DI water
- Immerse in DI water for 20mins
- Rinse three times with DI water

(2) Organic Treatment Process

- Rinse ITO substrates with DI water
- Ultrasonic clean in Acetone for 45mins
- Rinse three times with DI water
- Ultrasonic clean in IPA for 45mins
- Rinse three times with DI water
- Warm-up ultrasonic bath with samples in DI water to 50°C
- Ultrasonic clean for 10mins
- Rinse three times with DI water

(3) Neutral Treatment Process

- Rinse ITO substrates with DI water
- Warm-up ultrasonic bath with 2% (by weight) Neutracon in DI water to 50°C
- Degas this solution for 10mins
- Ultrasonic clean with samples immersed in this solution for 7mins
- Rinse three times with DI water
- Ultrasonic clean with samples immersed in DI water for 15mins at 50°C
- Rinse three times with DI water

- Immerse in DI water for 20mins
- Rinse three times with DI water

3.2.2.2 Dry Treatment Methods

(1) UV-Ozone Treatment Process

- Wipe aluminum foil with IPA
- Wipe ITO substrates with IPA
- Put substrates on aluminum foil and place foil into UV-Ozone treatment system
- UV-Ozone treats for 10mins
- Remove substrates and wrap in the same aluminum foil

(2) Oxygen-Plasma Treatment Process

- Wipe ITO substrates with IPA
- Place substrates into Oxygen-Plasma reactive ion etching (RIE) machine with the following parameter settings:
 - Pressure Set: 250 mTorr
 - RIE RF Power Set: 100 Watt
 - O₂ Flow-Rate Set: 10 sccm (standard cubic centimeters per minute)
 - Process Time Set: 600 seconds
 - Base Pressure Read: 50 mTorr
- Remove the substrates and wrap in aluminum foil

3.2.3 Contact Angle Measurement Procedures

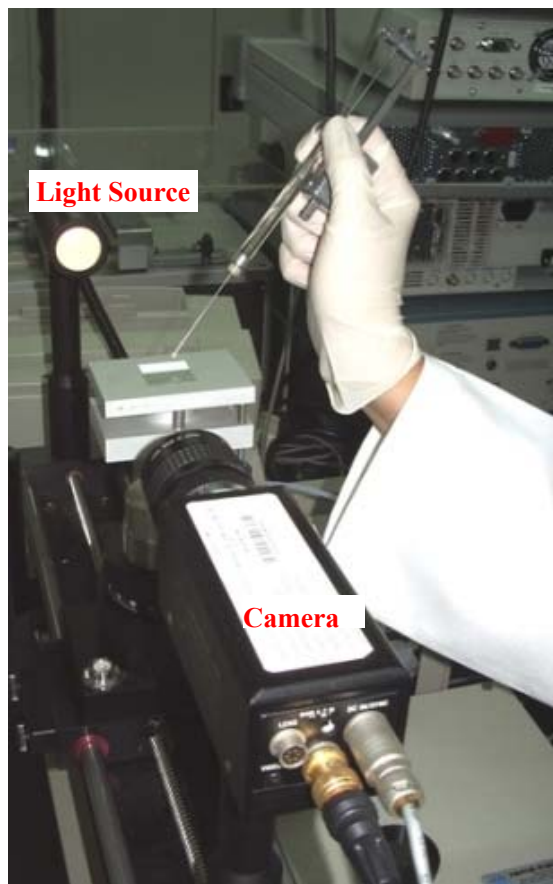


Figure 3.3: Set-up of the goniometer showing the drop deposited onto the sample on the sample stage. The camera and light-source found on the two sides of the sample stage is used to capture the projected drop image for measurement purposes.

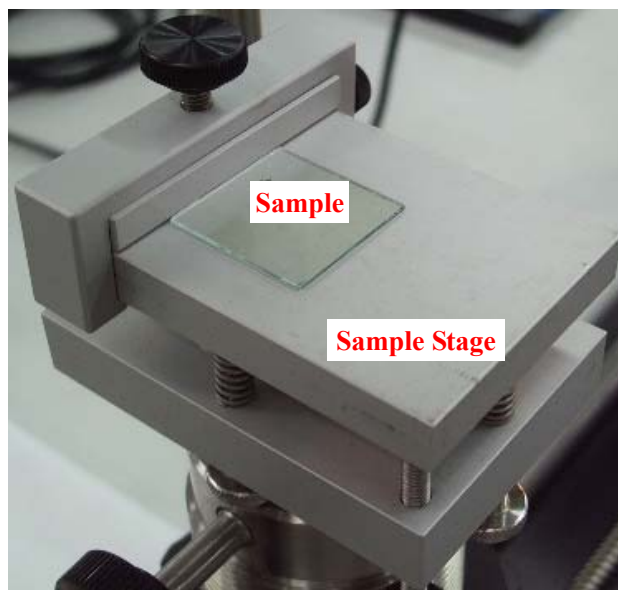


Figure 3.4: Sample and sample stage.



Figure 3.5: Syringe and plunger system used to deposit the one micro-liter droplet onto the sample. The needle tip is suggested to be flat-ended and not a tapered sharp point.

Contact angles are measured by the sessile drop technique, using a contact angle goniometer with a built-in inclinable setup at room temperature in ambient air as shown in Figure 3.3. All three types of contact angle (CA), sessile CA, advancing CA and receding CA, were measured for freshly treated samples of the wet surface treatment. However for the dry surface treatment, due to extremely low contact angles

($\sim 0^\circ$) observed on freshly treated samples, their surface degradation or ageing behavior with respect to time was probed using only sessile CA. The freshly treated substrates are left in a general air-conditioned laboratory environment, not under direct airflow, for 90 minutes with contact angle readings taken at appropriate intervals. There are also no measurable values of advancing CA and receding CA for corresponding freshly treated samples. At angles close to 0° , the drop will slide the moment the stage is tilted. Therefore, advancing CA and receding CA which are both close to 0° do not give a measurable contact angle hysteresis. It should be pointed out that care has been taken to minimize the effect of human influence such as sneezing, coughing and dust on the substrates during all measurements. The experimenters wore proper experiment attire such as lab-coat, face mask and sterile gloves.

In the actual measurement, an ITO substrate is placed onto the sample stage, as shown in Figure 3.4, of the contact angle goniometer and a DI water drop of $1\mu\text{L}$ (DI water from (2) of Section 3.2.1.2) is deposited onto the substrate using the syringe and plunger system as shown in Figure 3.5. A projected image of the liquid droplet, as shown in Figure 3.6, was captured using the camera. The sessile CA was measured directly and instantaneously through the built-in software that comes with the contact angle goniometer. In Figure 3.7, we can see the droplet in the viewing screen of the software with cross-hair shown for targeting the drop to be measured and tangents for the angle at both ends of the droplet. The final sessile CA value is the mean of the angle at these two ends. For the measurement of sessile CA, it is important that the

measurement is carried out within 30 seconds of the drop being deposited onto the substrate. If not, the measurement would not be accurate as the drop would have started to evaporate and the sessile CA would tend towards the receding CA, giving a smaller value. The reported values in this thesis are the average of 10 drops placed and measured on 5 different ITO substrates of $25 \times 25 \text{mm}^2$ for each surface treatment process.

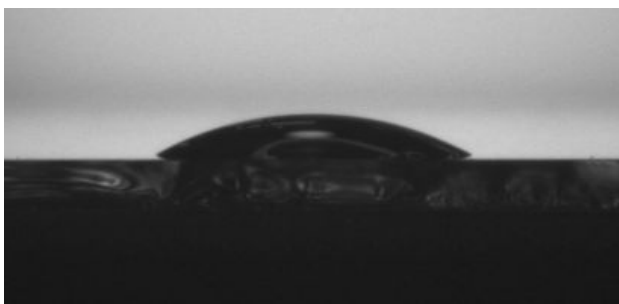


Figure 3.6: Software screen view of a projected sessile drop use for the measurement of sessile contact angles.

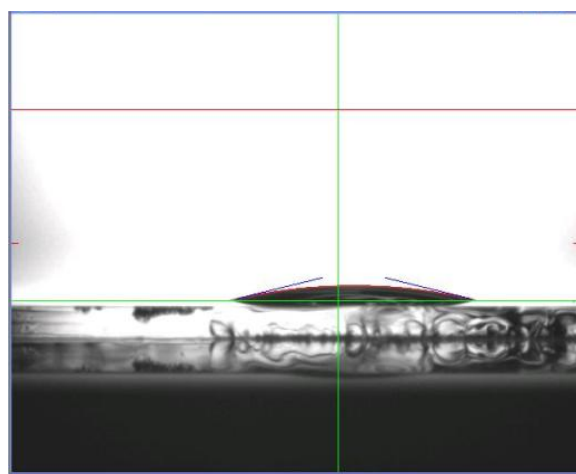


Figure 3.7: Software screen view showing the cross-hair that is used to target the sessile drop for measurement and the tangents for measuring the angle at both ends of the drop.

For the measurement of advancing and receding CAs, the set-up is tilted as shown in Figure 3.8 together with the sample until the liquid droplet begins to move. When the liquid droplet just starts to move, we take a measurement. Again, the projected drop image is captured as shown in

Figure 3.9 and the advancing and receding CAs will be measured by the software. The reported values in this thesis are the average of 5 drops placed and measured on 5

different $25 \times 25 \text{ mm}^2$ ITO substrates for each surface treatment process.



Figure 3.8: Entire goniometer set-up is tilted with the sample, in order to capture images for the measurement of advancing and receding contact angles.

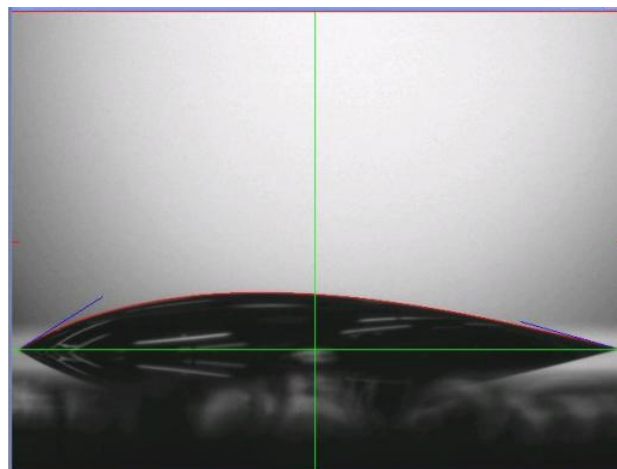


Figure 3.9: As the entire goniometer set-up including the camera tilts together with the sample, it is able to capture the projected image of a tilted drop and measure it the same way as an un-tilted sessile drop. The left-end of the droplet gives the advancing contact angles and the right-end of the droplet gives the receding contact angles.

For the advancing and receding CAs, bigger droplets are used. The bigger size is required just to give the droplet enough weight to slide down the sample. Due to these bigger droplets, we are sometimes unable to fit the entire projected image into a single viewing screen (screen size fixed). Hence, we have to take a measurement of the advancing CA and then move the sample stage for the camera to capture the receding CA. From experience, it is generally easier to measure the advancing CA first followed by the receding CA. For this measurement, the time within which the measurement has to be made is not 30 seconds upon depositing the droplet. The

30-second count should start from the critical moment when the drop starts to slide. Strictly speaking, the measurement should be made when the drop is on the point of but not yet sliding. From experience, this would take some practice to achieve.

Measuring the sessile CA of sessile drops is a quick and simple way of obtaining a reference to the quality of the surface concerned. This is a fairly robust way of surface quality control on a production line, where measurements have to be quick and easy. The deviation of this contact angle on a uniform surface should be less than $\pm 1^\circ$. It is worth pointing out that the sessile CA of a surface can be anywhere between the advancing CA and receding CA, and it appears to be a coincidence that it is a reproducible measurement.

The advancing and receding CAs are the two extremes of the contact angles for a particular surface and they are the only two angles that will always be reproducible and reliable at approximately the same two values. In fact, advancing CA and receding CA are considered as the only physically significant values for surface wettability measurements in certain publications. However, they are difficult and time consuming to measure and very sensitive to any surface roughness and heterogeneities. Due to this fact, the allowable deviations for these two angles are between $\pm 5^\circ$ to 8° . Furthermore, they are seldom if ever used for normal quality control checks for surfaces on a production line or other purposes that requires a quick reference result.

3.3 Results and Discussion

In this section, we report sessile, advancing and receding contact angles that are measured from DI water droplets deposited on ITO substrates modified using different surface treatment processes. We also present the contact angle hysteresis of these treated ITO substrates. For those processes producing too low contact angles close to 0°, surface degradation or ageing effect of these freshly treated ITO substrates with respect to time is documented. The evaluation of contact angles, hysteresis and ageing allows us to better understand the surface of these substrates and possible modifications by these treatment processes.

3.3.1 Contact Angles and Surface Energies of Modified ITO Substrates

As introduced in Section 3.1.1.1, the surface energy of the solid substrate ($\gamma_{solid/vapour}$), the surface tension of the liquid droplet ($\gamma_{liquid/vapour}$) and the interface energy between the solid and the liquid ($\gamma_{solid/liquid}$) satisfy a thermodynamic force balance relationship - the Young's equation (Equation (3.1)). From it, we can write its another form as:

$$\gamma_{solid/liquid} = \gamma_{solid/vapour} - \gamma_{liquid/vapour} \cos \theta \quad (3.5)$$

where θ is the contact angle between the solid substrate and liquid drop. In order to evaluate $\gamma_{solid/vapour}$ of a given solid substrate using the contact angles of a single test liquid, Kwok and Neumann^[147] proposed one of surface equations of state for solid-liquid interfacial tensions to describe the correlation between contact angle θ ,

$\gamma_{liquid/vapour}$ and $\gamma_{solid/vapour}$ as:

$$\gamma_{solid/liquid} = \gamma_{liquid/vapour} + \gamma_{solid/vapour} - 2\sqrt{\gamma_{liquid/vapour}\gamma_{solid/vapour}} e^{-\beta(\gamma_{liquid/vapour} - \gamma_{solid/vapour})^2} \quad (3.6)$$

Solving Equation (3.6) with Young's Equation (3.5) gives:

$$\cancel{\gamma_{solid/vapour}} - \gamma_{liquid/vapour} \cos \theta = \gamma_{liquid/vapour} + \cancel{\gamma_{solid/vapour}} - 2\sqrt{\gamma_{liquid/vapour}\gamma_{solid/vapour}} e^{-\beta(\gamma_{liquid/vapour} - \gamma_{solid/vapour})^2} \quad (3.7)$$

Finally, rearranging the above equation yields:

$$\cos \theta + 1 = 2 \sqrt{\frac{\gamma_{solid/vapour}}{\gamma_{liquid/vapour}}} e^{-\beta(\gamma_{liquid/vapour} - \gamma_{solid/vapour})^2} \quad (3.8)$$

where β is an experimentally determined constant. Referred to the article [147], β is determined to be $0.0001247(\text{mJ}/\text{m}^2)^{-2}$. Thus from experimental contact angles and liquid surface tensions, the solid surface energies can be obtained by solving Equation (3.8) using a numerical iterative process.

Table 3.3 summarizes the sessile contact angle and surface energy results for the 5 different surface treatment processes with Figure 3.10 showing them in a graphical manner for better visualization. Note that the column labeled as $\cos(\theta)$ is simply the cosine value of the sessile contact.

Table 3.3: Summary of the average sessile contact angles and surface energies.
(Note that surface energy of the solid substrate is calculated by Equation (3.8).)

Surface Treatment Process	Average Sessile Contact Angle, θ ($^{\circ}$)	Standard Deviation	$\cos(\theta)$	Surface Energy, $\gamma_{solid/vapour}$ (mJ/m^2)
UV-Ozone	$\sim 0 \pm 0$	0	1	72.4
Oxygen-Plasma	$\sim 0 \pm 0$	0	1	72.4
Alkaline	8.6 ± 1.3	1.3	0.989	71.6
Neutral	54.1 ± 0.7	0.7	0.587	51.0
Organic	55.0 ± 4.0	4.0	0.578	50.5

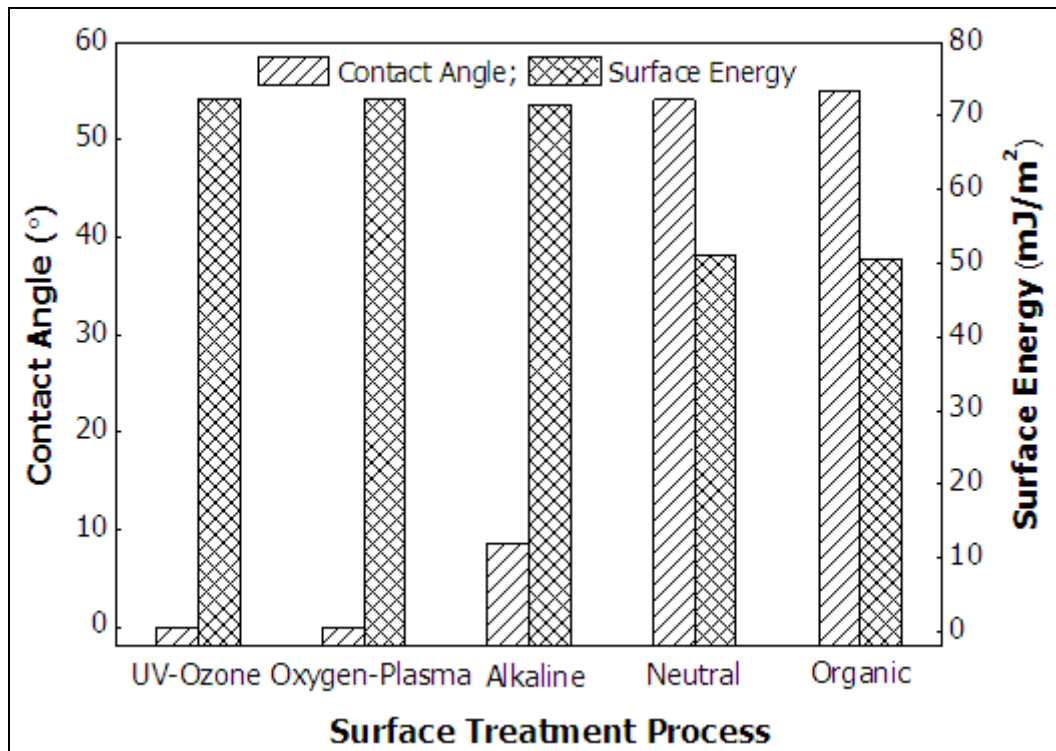


Figure 3.10: Graphical representation of the various sessile contact angles and surface energies for different surface treatment processes.

Table 3.4 summarizes the results of the advancing contact angle for the 5 processes.

Table 3.5 summarizes the corresponding results of the receding contact angle.

Similarly, columns labeled as $\cos(\theta_a)$ and $\cos(\theta_r)$ are the cosine values of the average advancing and average receding contact angles, respectively.

Table 3.4: Summary of the average advancing contact angles.

Surface Treatment Process	Average Advancing Contact Angle, θ_a ($^\circ$)	Standard Deviation	$\cos(\theta_a)$
UV-Ozone	$\sim 0 \pm 0$	0	1
Oxygen-Plasma	$\sim 0 \pm 0$	0	1
Alkaline	35 ± 2.0	2.0	0.822
Neutral	64.1 ± 1.4	1.4	0.437
Organic	65.0 ± 3.0	3.0	0.430

Table 3.5: Summary of the average receding contact angles.

Surface Treatment Process	Average Receding Contact Angle, θ_r ($^\circ$)	Standard Deviation	$\cos(\theta_r)$
UV-Ozone	$\sim 0 \pm 0$	0	1
Oxygen-Plasma	$\sim 0 \pm 0$	0	1
Alkaline	3.3 ± 1.0	1.0	0.998
Neutral	23.4 ± 0.8	0.8	0.917
Organic	29.6 ± 1.3	1.3	0.870

Figure 3.11 is the summary of the relative positions of all the three types of contact angles with a qualitative summary of the variation of contact angles for different surface treatment processes as shown in Figure 3.12.

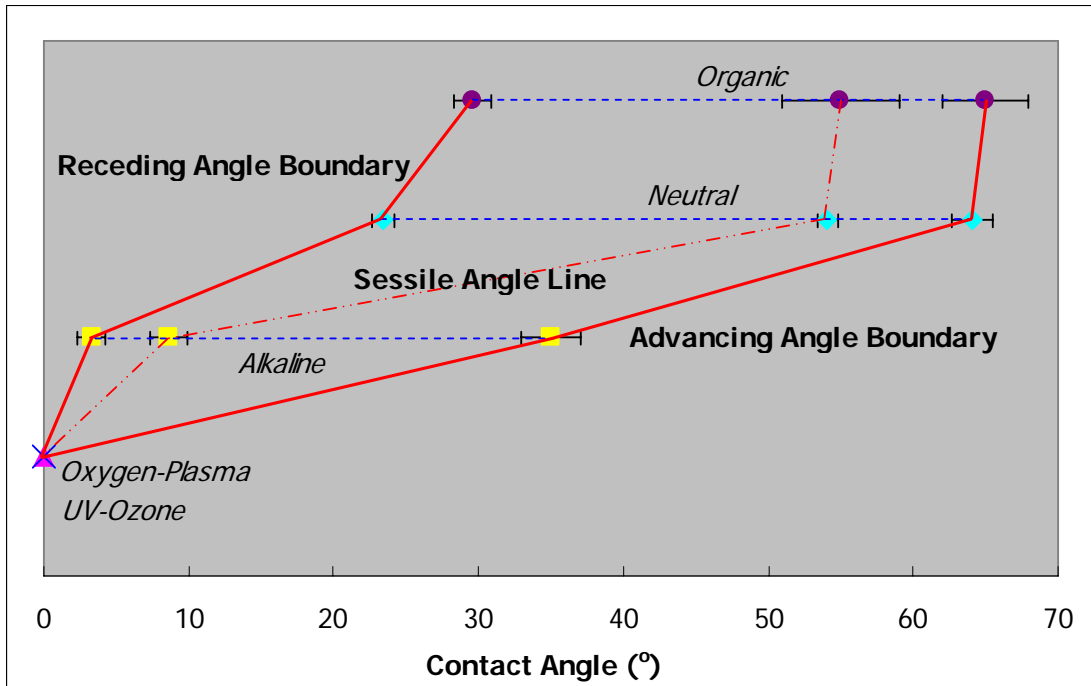


Figure 3.11: Summary of all three types of contact angles in the relative positions for different surface treatment processes.

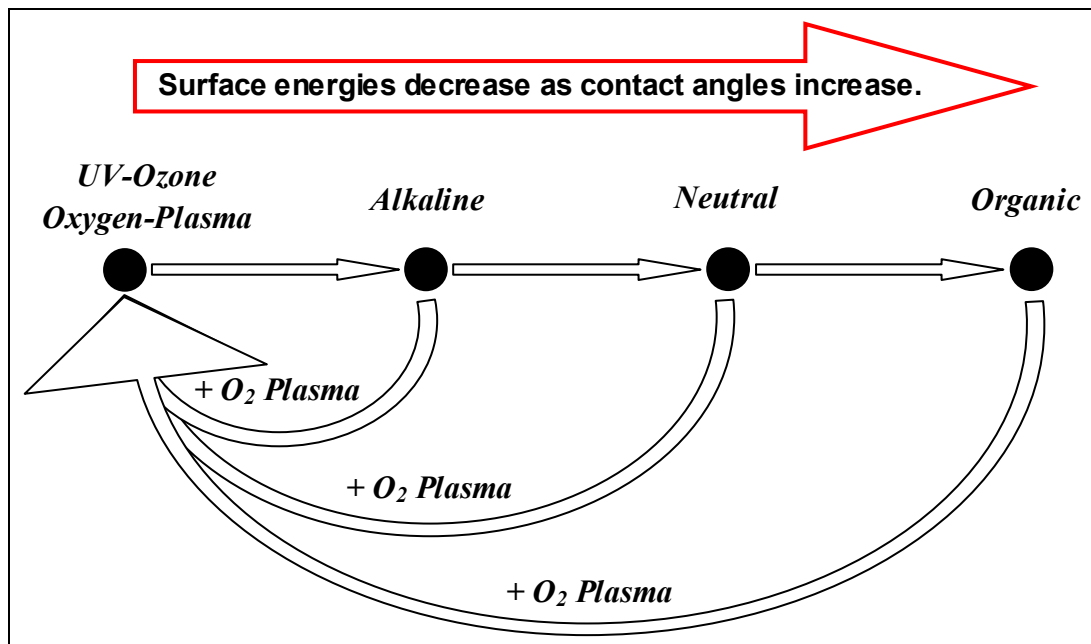


Figure 3.12: Summary of a qualitative variation of contact angles for different surface treatment processes. (Note that O_2 Plasma is Oxygen-Plasma for short.)

From Table 3.3 to Table 3.5 and Figure 3.11, it can be seen that for the dry treatment processes of UV-Ozone and Oxygen-Plasma, contact angles turn out to be quite close

to 0° , meaning that the surface is very hydrophilic and that it is fully wetting to water. The other processes from the wet treatment cleaning procedures do not give better results as illustrated in Figure 3.12. Alkaline treatment process with its low values for all three contact angles θ , θ_a and θ_r gives a better cleaned surface over both Neutral and Organic processes. Furthermore, due to the small difference between their cosine values for contact angles θ , θ_a and θ_r , it may be inferred by examining contact angles alone that the Neutral and Organic treatment processes produce a similar surface hydrophobicity.

The main source of re-contamination of a freshly cleaned surface comes from atmospheric hydrocarbons and other organic molecules. The high contact angle results show that the Neutral and Organic treatment processes are inadequate in removing them. In fact, the Organic process is only able to dissolve any microscopic grease or gross dirt on the ITO substrate surface. It leaves behind randomly adsorbed organic molecules that will result in a patchy and non-uniform surface. The Alkaline process seems to be doing better. The low sessile and receding contact angles indicate a mostly clean surface, with the higher advancing contact angle indicating that a few small patches of organic contamination are left behind. An Alkali solution has the ability to gently etch the ITO surface and remove hydrocarbons. However, this could slightly produce a rougher surface and alter the surface composition. For the UV-Ozone and Oxygen-Plasma processes, these processes introduce oxygen and increase the oxygen content of the surface, while ‘burning’ away hydrocarbon

molecules. These increase the uniformity of the surface and remove contamination from the ITO substrate, producing a hydrophilic surface.

Investigating the standard deviation of these three types of contact angles, it can be seen that Organic treatment process has the largest deviation. This shows that the Organic cleaned surface is non-uniform in the microscale level and that droplets deposited on different positions of these surface met with different degrees of cleanliness. Hence, other than a surface that is not devoid of organic contaminants, we also have a non-uniform surface. This is to be expected as contamination is generally a random phenomenon. The Alkali process has the next largest deviation. For the Neutral process, its standard deviation is the smallest amongst the wet processes, showing that it produces one of the most uniform surfaces. However, due to its high contact angles, if we assume that a perfectly-cleaned ITO surface is fully wetting to water, we conclude that even though this process gives a uniform surface, it cannot remove all of the organic contaminants.

3.3.2 Contact Angle Hysteresis of Modified ITO Substrates

Table 3.6 summarizes the results of contact angle hysteresis for all the surface treatment processes. There is no hysteresis for freshly cleaned substrates using the dry treatment processes, as the contact angles are both 0° and a slight tilt of the substrate will result in sliding of the droplet. Any advancing and receding contact angles that

can possibly be measured are close to 0° and the difference between them is negligible. Hence, we can only calculate hysteresis for the three wet cleaning processes.

Table 3.6: Summary of contact angle hysteresis.

(Note that H_1 is calculated by Equation (3.2) and H_2 calculated by Equation (3.3). Advancing and receding contact angles are denoted as θ_a and θ_r , respectively.)

Surface Treatment Process	Contact Angle Hysteresis, $H_1 = \theta_a - \theta_r$ ($^\circ$)	Contact Angle Hysteresis, $H_2 = \cos\theta_r - \cos\theta_a$
UV-Ozone	0	0
Oxygen-Plasma	0	0
Alkaline	31.7	0.176
Neutral	40.7	0.480
Organic	35.4	0.440

From the results, it can be seen that the Neutral and Organic processes give a higher contact angle hysteresis. This means that the treated surface is possibly rougher and definitely more heterogeneous, with organic contaminants consisting of low surface energy regions that stop the advancing water contact line, and the bared ITO surface making up high surface energy regions that pin the receding water contact line. These two processes seem to give a fairly similar surface, judging solely by the comparison of their contact angle hysteresis. However, since hysteresis is very sensitive to surface properties, other factors that we do not know about may be involved. What is actually happening on the surface in terms of its roughness and composition would require a detailed mapping of the exposed surface chemistry and surface roughness.

3.3.3 Ageing Effect of Modified ITO Surface Wettability

The contact angles for freshly cleaned ITO substrates using the dry surface treatment processes of UV-Ozone and Oxygen-Plasma is 0° . Cleaned surfaces when left in the atmosphere can be re-contaminated quickly by atmospheric hydrocarbon molecules. Hence, for these two dry processes that give us better initial results, their surface ageing properties with respect to time were measured in conditions stated in Section 3.2.3. Figure 3.13 and Figure 3.14 show the ageing characteristics of ITO surface wettability after UV-Ozone and Oxygen-Plasma treatment processes, respectively.

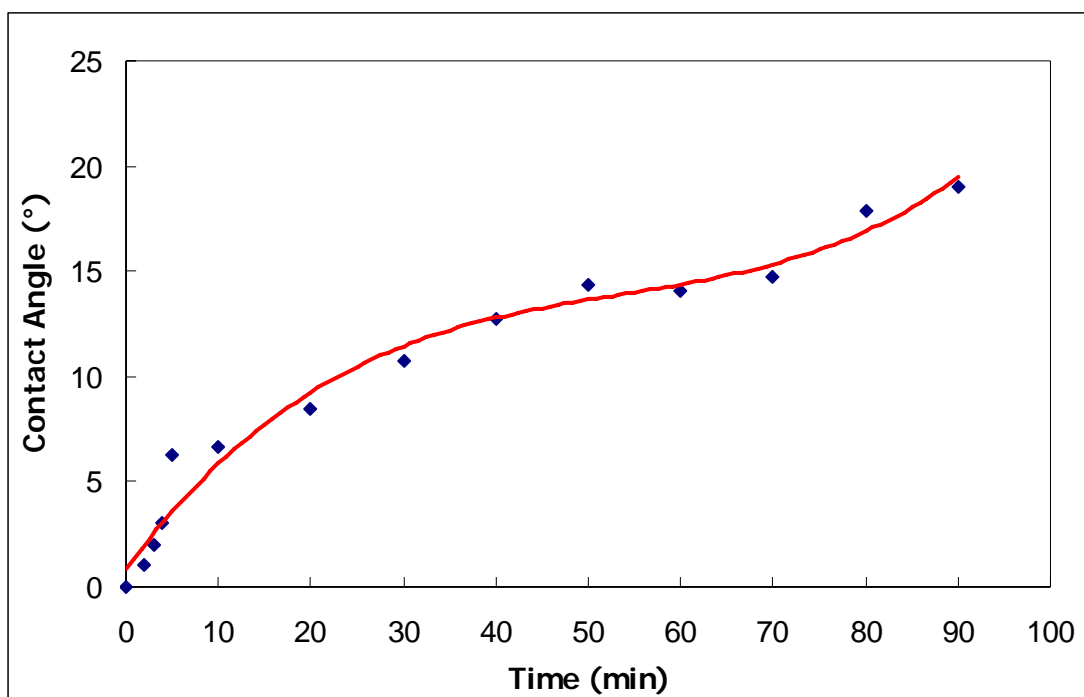


Figure 3.13: Ageing effect of UV-Ozone treated ITO surface wettability.

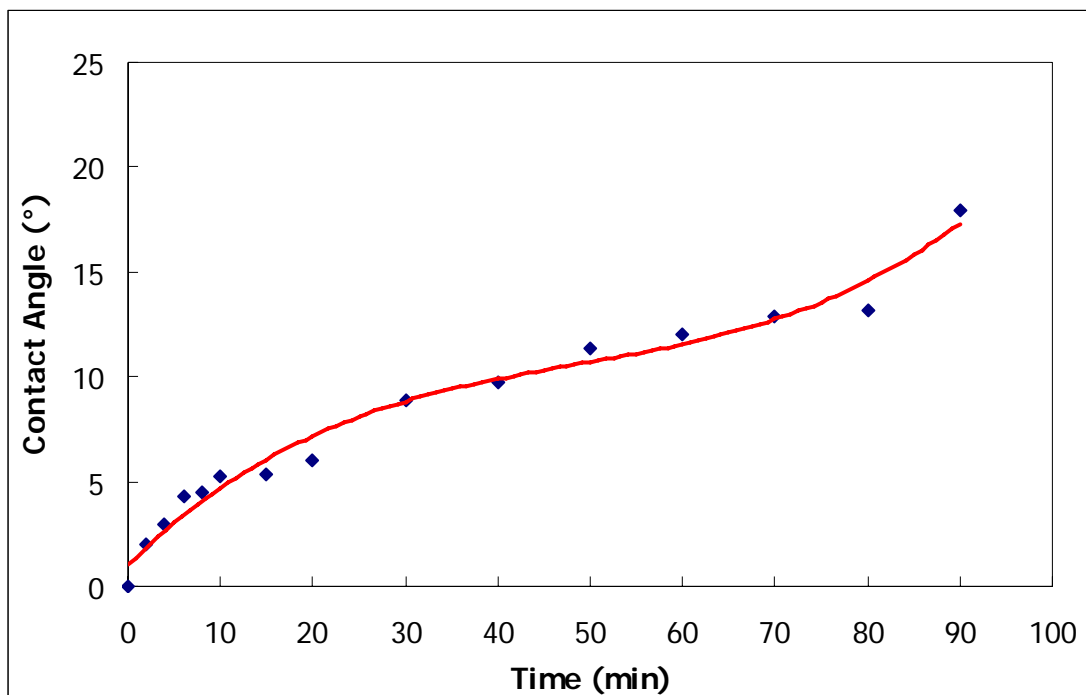


Figure 3.14: Ageing effect of Oxygen-Plasma treated ITO surface wettability.

From the above two figures, it can be seen that the general trend of re-contamination of the ITO substrates by atmospheric contaminants follows a similar behavior. Moreover, re-contamination occurs very quickly and within 5 minutes, the contact angles for both UV-Ozone and Oxygen-Plasma processes have risen by around 6.5° and 3.5° respectively. Figure 3.15 gives an actual example of the variation of contact angles within the initial 4 minutes on a freshly cleaned ITO substrate using Oxygen-Plasma surface treatment. This is sufficient to tell us that if we do not have the means to maintain a freshly cleaned surface at its initial conditions, then it is important that it should be used immediately after surface treatment and exposure to atmospheric air.

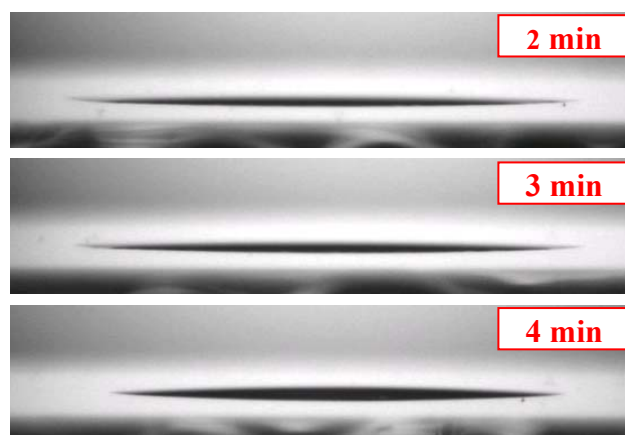


Figure 3.15: Contact angle variation on Oxygen-Plasma freshly-treated ITO surface.

From the comparison of Figure 3.13 and Figure 3.14, it can also be seen that the Oxygen-Plasma process seems to be the better dry treatment process. Other than the 0° contact angle that is achievable, its surface also degrades slower than that of the UV-Ozone process. Uniform wettability of the substrate is a key performance attribute because uniform wetting behavior of the deposited droplets result in a uniform deposited film on it. Ambient contamination is generally random, often resulting in a non-uniform substrate surface and non-uniform wetting behavior of deposited droplets. Control over this randomness is quite difficult and hence, the earlier recommendation that freshly cleaned surfaces is to be used at the earliest opportunity.

3.4 Conclusion

We have investigated and compared the contact angles that can be obtained on ITO substrates using different surface treatment processes. Generally, the dry treatment processes are more efficient than the wet treatment processes for removing

hydrocarbon contamination and making the surface wettable. The wet processes tend to produce surfaces that are not fully hydrophilic and non-uniform. The dry processes on the other hand produce surfaces that are fully hydrophilic (around zero contact angle) and fairly uniform (around zero contact angle hysteresis). This is an important advantage when printing droplets that require uniform substrate wettability.

When left in the air, freshly cleaned ITO surfaces using dry surface treatment processes can be re-contaminated quickly by atmospheric hydrocarbons. The surface degradation (ageing effect) has then been characterized with respect to time for UV-Ozone and Oxygen-Plasma dry surface treatment. Oxygen-Plasma process shows a better performance for surface treatment. Other than high surface wettability and uniformity, its surface also degrades slower than that of the UV-Ozone process. Hence for our work, we selected the Oxygen-Plasma process as the standard cleaning and modification for ITO substrates. Furthermore, from the results under our processes and proper experimental controls, surface wettability achieved is generally better than those reported by other researchers as reviewed in Section 3.1.2.

CHAPTER 4

INKJET PRINTING: FABRICATION AND CHARACTERIZATION OF OLEDs

4.1 Introduction

Inkjet printing is a familiar method for printing inks onto absorbent paper or photo paper. Inkjet technology has the advantages of being simple, fast, and high throughputs. In recent years, inkjet printing has been used in a wide range of materials such as metals, organic semiconductors and biopolymers ^[17]. For applications in organic light-emitting diode (OLED) devices, inkjet printing has been used to directly deposit poly(3,4-ethylenedioxythiophene):poly(styrenesulfonate) (PEDOT:PSS) or electroluminescent polymers as a pixel array on a substrate ^[13-14], which is pre-patterned by photolithography.

In this research the designed structure of the polymer-based organic light-emitting diode (P-OLED) device shown in Figure 4.1 is being investigated. The investigation will be done on certain aspects of such a device. It consists of a silicon dioxide (SiO₂) glass substrate and an indium-tin-oxide (ITO) anode that has undergone a surface preparation process. PEDOT:PSS is used as the hole transport layer, followed by the active emissive layer of polymer material - poly(2-methoxy-5-(2'-ethyl-hexyloxy)-*p*-phenylene vinylene) (MEH-PPV). Other

layers include a lithium fluoride (LiF) layer acting as an electron injection modifier to modify the properties of electron injection and a cathode of calcium (Ca) with a cap layer of silver (Ag) to protect the layer of Ca against oxidation. The ITO layer is pre-coated on the SiO₂ glass substrate as received. As for the fabrication of such a structure, the hole transport layer will be printed by drop-on-demand using inkjet printing technique. The emissive layer is spin-coated. The LiF layer and the cathode are deposited by vacuum evaporation, as it is difficult or impossible to get the inks of these materials that are solution processed.

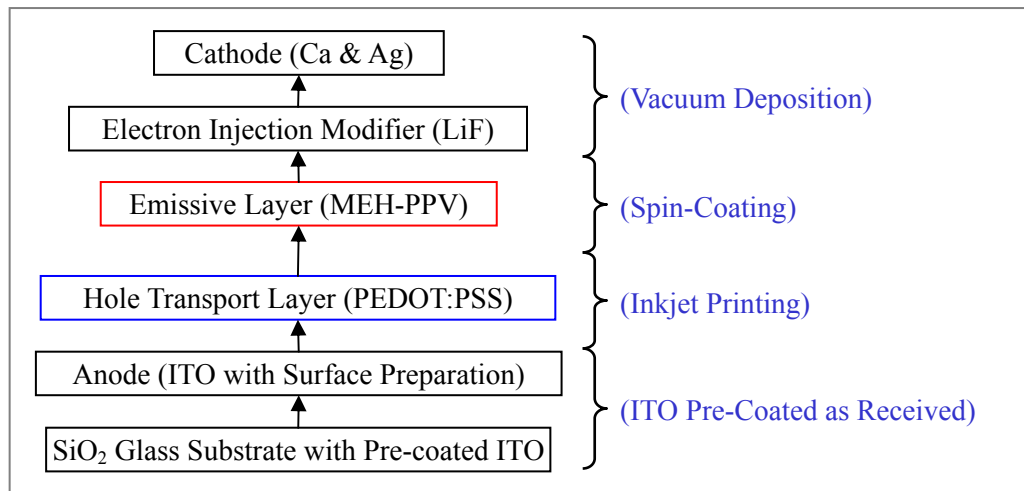


Figure 4.1: Basic P-OLED device structure being investigated in this research.

This chapter presents the work associated with the set-up of an inkjet printer system for the production of P-OLED devices with ITO substrates. Firstly, the surface patterning and modification of ITO substrates along with the chemicals used are described. Next the complete inkjet printer system and the direct deposition of PEDOT:PSS conductive polymer by inkjet printing method are introduced. Next, the detailed design and fabrication processes of P-OLED devices on the ITO substrate are presented. In the final section of this chapter, the characterizations of complete

P-OLED devices both with inkjet printed PEDOT:PSS layer and with spin-coated PEDOT:PSS layer are described and compared.

4.2 Experimental Procedures

4.2.1 ITO Substrate Surface Preparation Process

Before completed P-OLED devices can be made, the ITO surface had to be pre-patterned into a required design for subsequent layers to be added on. In this work, a 4-diode P-OLED display pattern was used and the surface patterning procedures were similar to standard photolithography processes. In this section, the process steps carried out and their parameters will be reported.

The flow chart showing the various steps that are involved in the ITO surface preparation process are illustrated in Figure 4.2. The chart shows all the steps from which the ITO substrates are first received till they are patterned and ready for printing. The as-received ITO coated glass substrates are put through an initial cleaning process to remove any surface organic contaminants, after which, a standard photolithography process using positive photoresist and the relevant etching chemicals is carried out to pattern the substrate. This substrate is then treated with oxygen plasma surface treatment to remove any remaining photoresist residues and prepare the surface for the printing process.

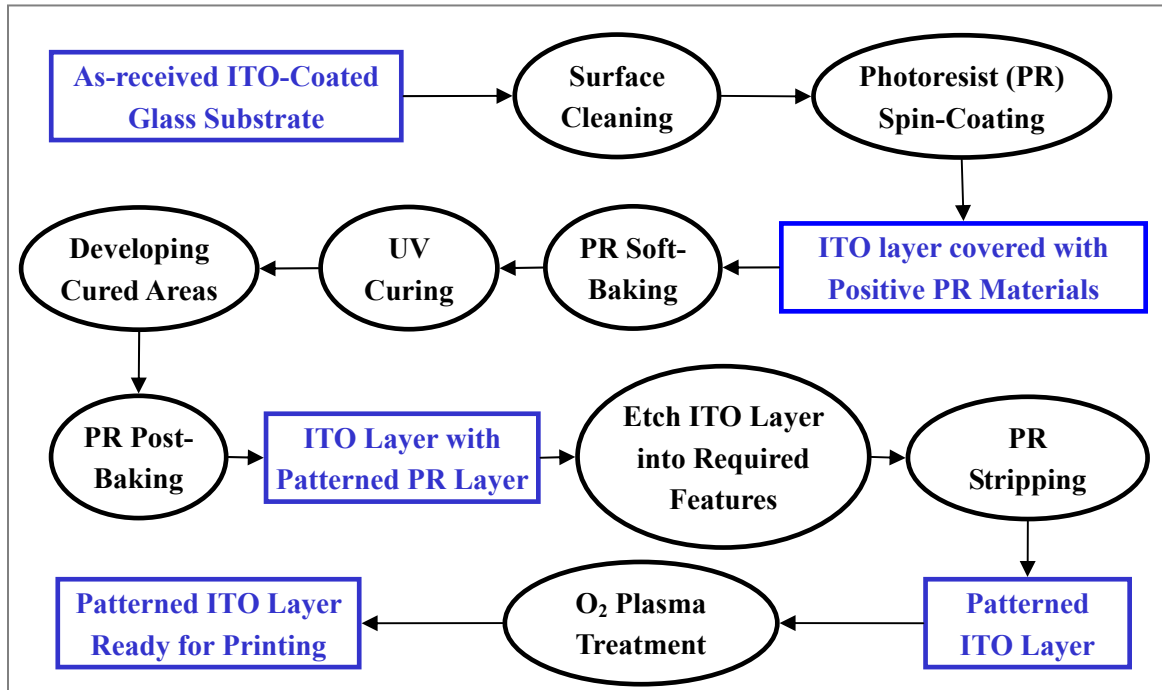


Figure 4.2: Flow chart of the entire ITO surface preparation process.

4.2.1.1 Equipment

- (1) The spin-coater (Model: CEE 100) used in the spin-coating of the photoresist or other materials is supplied by Brewer Science.



Figure 4.3: Spin-coater (Model: CEE 100).

- (2) The hotplate (Model: HP-150) used for baking of the photoresist materials is

supplied by Sawatzki Technology.



Figure 4.4: Hotplate (Model: HP-150).

(3) Photolithography equipment (Model: Karl Suss Mask & Bond Aligner, MA8/BA6)

used in the curing of the photoresist materials is supplied by SUSS MicroTec.



Figure 4.5: Karl Suss Mask & Bond Aligner MA8/BA6.

(4) The oxygen plasma etching system (Model: Trion Sirius Reactive Ion Etching (RIE)

System) used in the cleaning and modification of the surface just before the printing process is supplied by Trion Technology.



Figure 4.6: Trion Sirius reactive ion etching (RIE) system.

(5) The optical microscope (Model: Olympus BX60 Metallurgical Microscope) used for general observation of the patterned surface is supplied by Olympus America Inc.

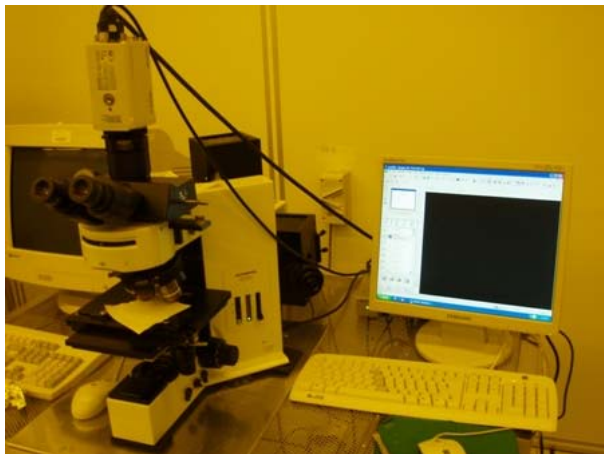


Figure 4.7: Olympus BX60 metallurgical microscope.

(6) The surface profiler (Model: KLA-Tencor P-10 Surface Profiler) used for thickness measurements of the photoresist and ITO coating is supplied by KLA-Tencor Co.



Figure 4.8: KLA-Tencor Surface Profiler P-10.

4.2.1.2 Materials

(1) The ITO-coated glass substrates were supplied by Merck Display Technologies Inc. The ITO layer is deposited on sodalime polished glass that comes in a size and thickness of $200 \times 200 \times 0.7 \text{ mm}^3$ with a sheet resistance of $11.7 \Omega/\square$.

(2) The surface cleaning agents (Acetone and Isopropyl Alcohol (IPA)) used in initially wiping and cleaning surface are supplied by Honeywell International Inc.

(3) The positive photoresist (AZ 5214-E) material is supplied by Clariant Co.

(4) The developer (AZ Developer) used in developing the UV-cured photoresist is supplied by Clariant Co.

(5) The etching agent (Hydrobromic Acid 48% or HBr) used in etching of the ITO

layer is supplied by Thermo Fisher Scientific Inc.

(6) The stripping agent (Acetone) used in removing the remaining uncured photoresist is supplied by Honeywell International Inc.

4.2.1.3 Processes and Parameters

(1) Surface Cleaning of As-received ITO Glass Substrate

The as-received ITO coated glass substrate (200×200mm²) was cut into 4 equal pieces of size of 100×100mm² and then put through an initial cleaning process to remove any surface various contaminants. The procedures for the cleaning process as follows:

- Wipe ITO substrate with IPA to ensure to remove all visible particles and stains.
- Ultrasonic clean in Acetone for 45mins at room temperature
- Rinse thrice with de-ionized (DI) water
- Ultrasonic clean in IPA for 45mins at room temperature
- Rinse thrice with DI water and blow dry using the nitrogen gun

(2) Spin Coating of Photoresist Material

A positive photoresist (AZ 5214-E) was used for spin coating in the standard photolithography process. After cleaning, the substrate was placed into the spin coater and a sufficient amount of photoresist was dropped onto it. The spin coater was programmed to increase its speed steadily from stationary to 500rpm (revolutions per

minute) with an acceleration of 500r/s for a total time of 5 seconds. Then, the speed was increased to 4000rpm with an acceleration of 1000r/s for a total time of 30 seconds. The spin speed curve was shown in Figure 4.9.

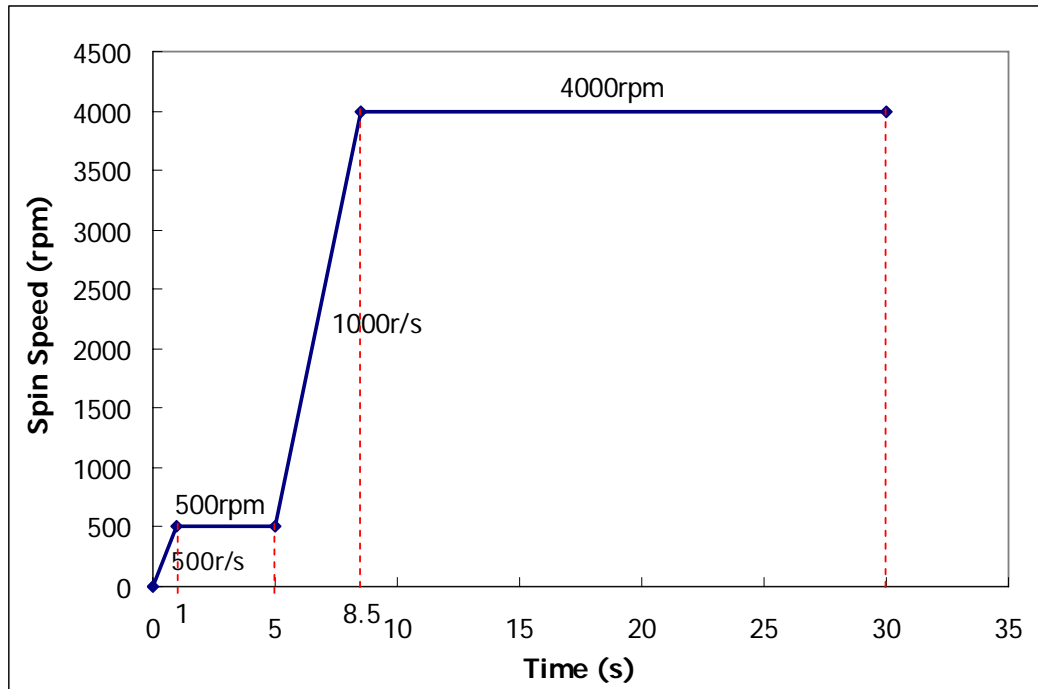


Figure 4.9: Spin speed curve used in the spin-coating of photoresist AZ 5214-E.

From observation, a higher speed is desirable during spin-coating as the final photoresist layer is thinner and solvents can be baked out of it more easily. However, spinning at this high speed for too long will cause photoresist to build up at the edges, causing a thicker edge that may be harder to remove later in the photolithography process. Thus, a proper trade-off must be made.

(3) Soft Baking of Photoresist

After the photoresist was spun on, the substrate was immediately baked directly on a hotplate for 2mins at 95°C to ensure that it was completely dry. This is known as *soft*

baking, an initial baking phase to harden the photoresist material before conducting ultraviolet curing and other developing steps.

During baking, the substrate should not be covered with any objects, such as glass beakers or petri dishes of any sort, as solvents will not be able to escape effectively from the photoresist. The photoresist will also not be able to cross-link and harden properly. This can result in problems in later processes, as the resulting photoresist will be relatively soft and can be removed easily.

(4) Ultraviolet (UV) Curing of Photoresist

After the soft baking, the substrate was subjected to UV radiation curing to be able to acquire the desired pattern of the ITO layer in the following processes. The photoresist used here is positive photoresist, meaning that areas that are exposed to the UV light will 'break-down' and be removed in the subsequent process. For a negative photoresist, the opposite happens and areas that are exposed will cross-link to form the pattern. A shadow mask as shown in Figure 4.10 (a) was used for this process. This mask is able to pattern one $100\times 100\text{mm}^2$ ITO substrate into nine $25\times 25\text{mm}^2$ ITO substrates with four diodes each. The substrate was held in contact with the underside of the mask using tape and then placed into the mask aligner for curing. The substrate was exposed to UV light for 12 seconds at a constant power of 900watt using the Karl Suss Mask Aligner MA8/BA6. As positive photoresist was used here, after being exposed to the UV light, the black strips will be where

photoresist materials will remain after the developing process and the desired pattern is generated.

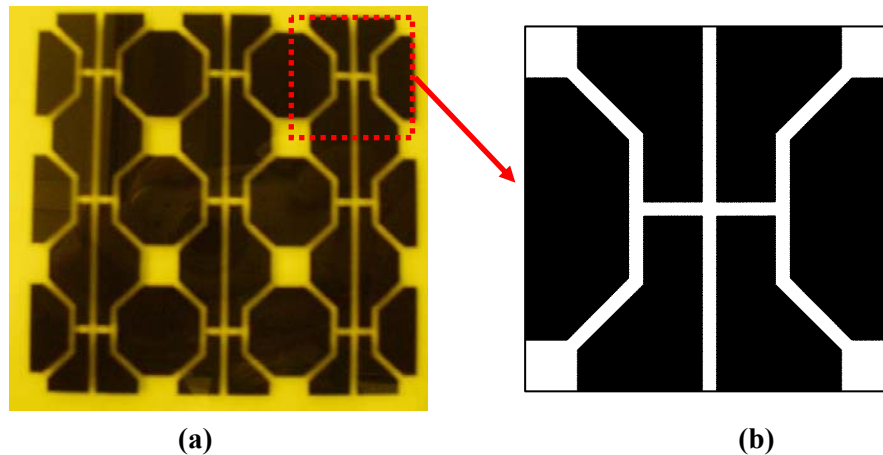


Figure 4.10: (a) Shadow-mask used for UV curing of samples ($100\times 100\text{mm}^2$) in the photolithography process; (b) Top view of a $25\times 25\text{mm}^2$ ITO substrate after patterned, and the black strips are where the ITO remains.

During curing, exposure intensity has a strong influence on the exposure time of the photoresist. In order to ensure the same exposure intensity for all the samples, it is important to maintain a constant lamp-to-sample distance. If UV lamp degrades over time due to usage, it will take a longer time to expose the photoresist to the UV radiation. On the contrary, if a new UV lap is used, the exposure time may be shorter.

(5) Chemical Developing of Photoresist

After the UV curing process to cure the undesired photoresist, the substrate was developed using a chemical known as AZ Developer to remove the cured photoresist. This is known as the developing process. The substrate was developed for 20 ~ 25 seconds in the solution of AZ Developer and DI water with the volume ratio of 2:1, and then rinsed with DI water for one minute. The final product of this step was a

substrate surface with the photoresist layer having the pattern as required.

(6) Post Baking of Photoresist

After the developing process, the substrate with its patterned photoresist layer was subjected to another baking process directly on the hotplate known as *post baking*. This process lasted for 1min at a temperature of 110°C. Alternatively, post baking can also be carried out in the oven for 10mins at a temperature of 120°C. The purpose is to harden the photoresist further in order to withstand the subsequent step of etching the ITO surface into the required pattern.

(7) Chemical Etching of ITO Surface

After the final post baking process, the ITO surface was etched into the required pattern using hydrobromic acid (HBr). The substrate was immersed in the acid for 8mins at room temperature, and then rinsed with DI water for at least 30secs. For faster etching, the substrate could be immersed in the HBr at a higher temperature of 40°C for only 2 to 3 minutes. The required ITO pattern was protected under the hardened photoresist and the unprotected areas were removed. The samples should be constantly observed under optical microscope to ensure complete etching. The photoresist that had been protecting the ITO beneath it would be removed in the next process known as photoresist stripping.

(8) Chemical Stripping of Remaining Photoresist

After the ITO surface had been patterned, the photoresist layer on top would be removed with a chemical (Acetone) in a process known as stripping. At room temperature, the samples were immersed in Acetone with ultrasonic agitating if possible. The samples should be also constantly observed under optical microscope to ensure complete elimination of the masked photoresist. Finally, we would get the ITO surface in the pattern as shown in Figure 4.10, in which the black strips are where ITO will remain to form conductive electrodes for the polymer diodes.

(9) Dicing of ITO Glass Substrates

As only a $25\times 25\text{mm}^2$ ITO substrate in this research is used to fabricate P-OLED devices, the patterned $100\times 100\text{mm}^2$ ITO glass needs an additional dicing process to be cut into $25\times 25\text{mm}^2$ substrates before use. The final practical ITO substrates were shown in Figure 4.10 (b).

(10) Oxygen-Plasma Treatment of Patterned ITO Substrate

After the patterning and dicing processes, the substrates were put through an oxygen-plasma treatment to simultaneously remove any residual contaminants and modify the surface property of the substrates. According to the conclusion from Chapter 3, oxygen-plasma treatment produces a well-cleaned surface with high wettability, which remains wettable (hydrophilic) for a longer time after exposure to atmospheric conditions. Furthermore, since oxygen is electronegative, it renders negative charges to the surface of ITO which may cause depletion of electrons below

the ITO surface and increases the work function of ITO ^[103-104]. The parameters used for this treatment are shown in Table 4.1, where sccm stands for standard cubic centimeters per minute. The ITO substrates were loaded onto the top chamber of the Trion RIE unit. After pumping down the pressure in the chamber to below 50mTorr, the RF power was turned on (100W), establishing a pale blue plasma. The inlet valve on the chamber was then slowly opened to let in a stream of oxygen at 30sccm, turning the plasma purplish red. The substrates were exposed to the oxygen plasma for 5 minutes. The RF power was then turned off and the chamber was vented. The substrates were subsequently removed and ready for the next step of the experiment.

Table 4.1: Parameter setting for the Oxygen-Plasma treatment.

Parameter	Setting
Pressure Set	350 mTorr
RIE RF Power Set	100 Watt
O ₂ Flow-Rate Set	30 sccm
Process Time Set	300 seconds
Base Pressure Read	≤50 mTorr

Note: sccm stands for standard cubic centimeters per minute.

Figure 4.11 summarizes a typical ITO substrate preparation process with corresponding processing parameters. It should be noted that different batches of ITO-coated glass substrates may have slightly different properties. They will behave differently when subjected to the same surface patterning process, similar to when a different machine or parameter setting is used. From experience, each new batch of glass must be tested to obtain an appropriate set of parameter settings that will result in good patterned features.

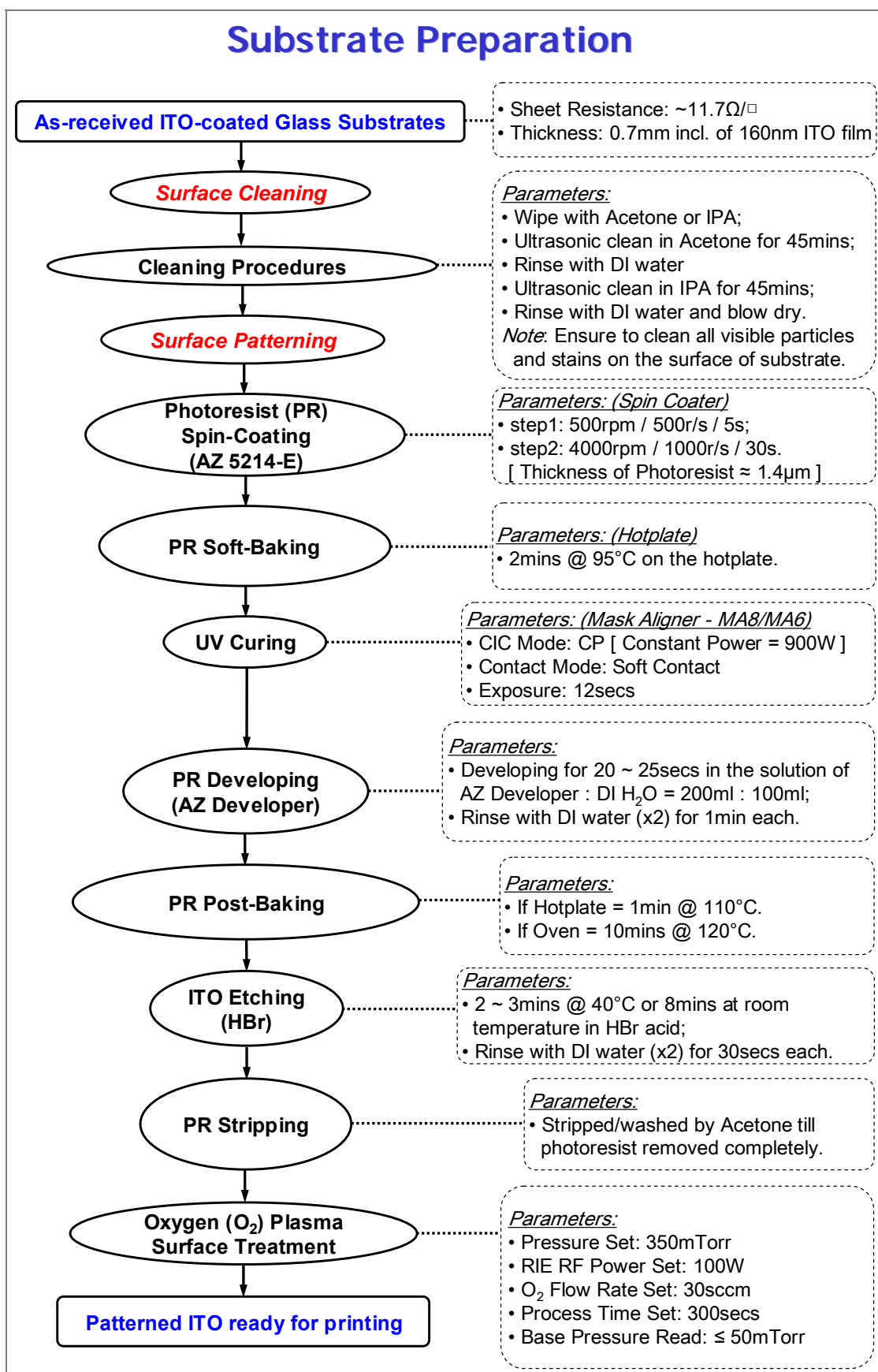


Figure 4.11: Summary of processes and parameters for ITO surface preparation.

4.2.2 Drop-on-Demand Inkjet Printing of PEDOT:PSS

4.2.2.1 Drop-on-Demand Inkjet Printing System

The equipment that was used is a Litrex 80.L DoD inkjet printing system supplied by Litrex Co. and built for research work, as shown in Figure 4.12 to Figure 4.15. This system utilizes piezoelectric DoD inkjet printing technology ejecting droplets using the deformation of piezo crystals within the dispenser under a supplied voltage pulse. It is designed to take multiple models of heads from a number of print-head manufacturers with different characteristics and resolutions ^[148].

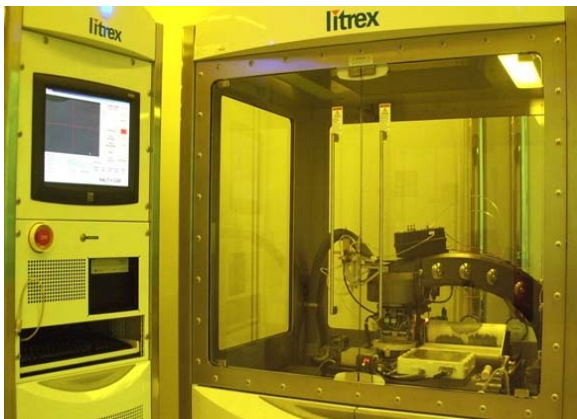


Figure 4.12: Litrex 80.L drop-on-demand (DoD) inkjet printing system.

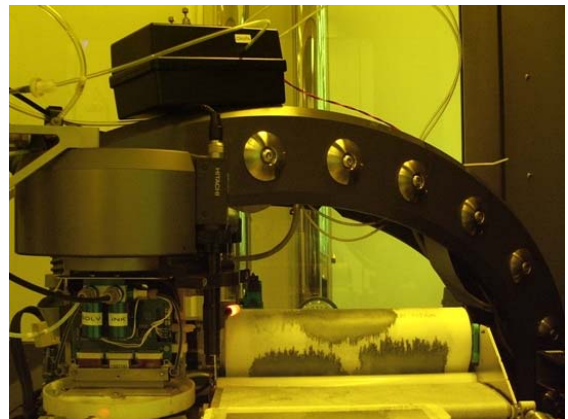


Figure 4.13: Gantry arm holding the print-head assembly.

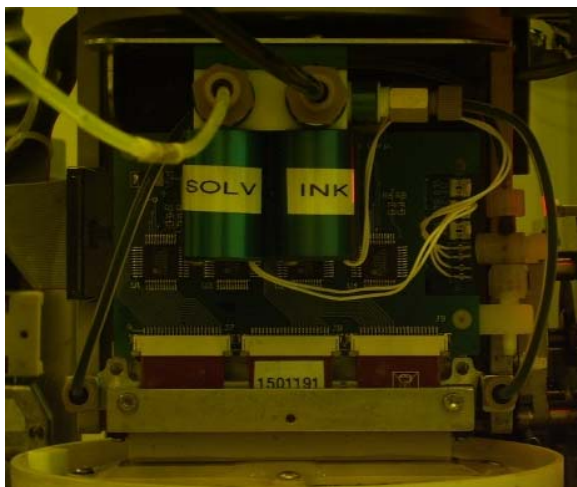


Figure 4.14: Mounted print-head assembly.

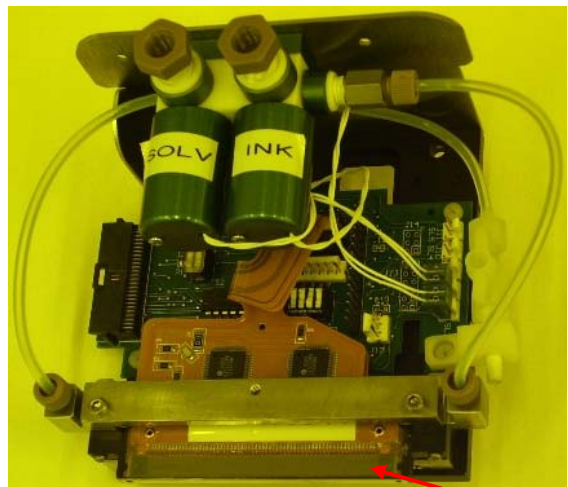


Figure 4.15: Print-head assembly.

Within the main printing compartment of this inkjet printing system is a gantry arm as shown in Figure 4.13 that holds all the print-head, materials supply lines, solvent supply lines and pressure lines over the movable XY two-axis table that holds the substrate. Figure 4.14 shows the mounted print-head assembly on the gantry arm. In Figure 4.15, we see the un-mounted print-head assembly. This is the assembly that does the actual dispensing of materials within the inkjet printer supported by the gantry arm. The print-head or nozzle bar, which will be introduced in the next section, is mounted on this assembly at the position indicated by the arrow sign. As the P-OLED production process is very sensitive to contaminants such as dust, the machine is placed within a cleanroom facility. Table 4.2 gives a summarized list of technical and performance specifications of this inkjet printing system.

Table 4.2: Brief specifications for Litrex 80.L inkjet printing system performance ^[148].

Performance		Specification
Number of Print-head Assemblies at a time		1
Maximum Substrate Dimensions		200 × 200 mm
Substrate Thickness		0.3 ~ 1.2 mm
Substrate	Rotational Adjustment Accuracy	+/- 1 μm
Positioning	Movement Accuracy	+/- 5 μm
Accuracy	Drop Placement Accuracy	+/- 25 μm
Maximum Print Speed		100 mm/s
Maximum Substrate Temperature		60 °C

4.2.2.2 Inkjet Print-Head

The print-head that was used is a Spectra SX3 (SN: 1501191) supplied by Fujifilm Dimatix Inc. as shown in Figure 4.16. It consists of a silicon nozzle plate with a non-wetting coating, and is compatible with the aggressive fluids such as PEDOT:PSS used in electronics and other fabrication applications^[149]. It is a multiple nozzle jetting assembly that has 128 nozzles in a single straight line at 508 microns between nozzles. The nozzles are controlled alternately by two electrically independent piezoelectric slices. Each slice operates 64 nozzles. Each of the piezoelectric slices can be individually controlled by their own supplied electrical pulse signal. These two individual voltage pulse signal amplitudes are known as Channel I and Channel II. If these 128 nozzles are numbered 0 to 127, the Channel I signal controls all the odd numbered nozzles and Channel II controls all the even numbered nozzles.

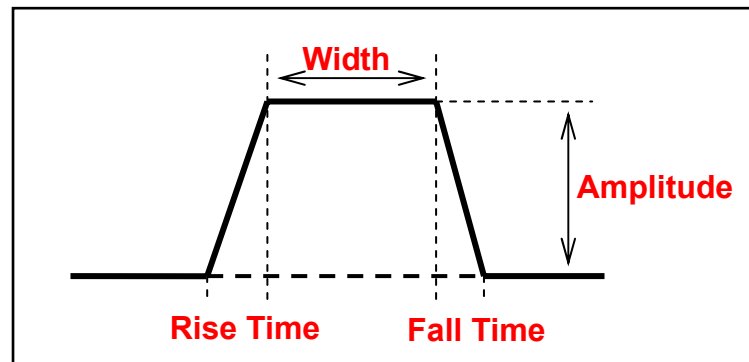


Figure 4.16: Spectra SX3 print-head.

Table 4.3 given below shows some of the technical and performance specifications of a Spectra SX3 print-head.

Table 4.3: Brief Specifications of Spectra SX3 print-head ^[149].

Performance	Specification
Number of Nozzles	128
Nozzle Spacing	508 μm
Nozzle Size	19 μm
Calibrated Drop Size	8 pico-liters (pL)
Nominal Drop Velocity	8 m/s
Maximum Operating Temperature	70 $^{\circ}\text{C}$
Maximum Operating Frequency	10 kHz

**Figure 4.17: Profile of voltage pulse signal used to control piezoelectric print-head.**

The above Figure 4.17 schematically shows a pulse profile of the voltage pulse signal used to activate the piezoelectric slices of the Spectra SX3 print-head. The Amplitude is the maximum voltage of the supplied pulse signal. The Width is the length of time for which the voltage of the supplied pulse signal is kept at its Amplitude. The Rise Time is the amount of time that the supplied signal needs to reach its Amplitude. The Fall Time is the amount of time that the supplied signal taken to go back to its original level. All the four above mentioned quantities are controllable parameters for the inkjet printing process. As stated before, each of the piezoelectric slices is controlled

by their own individually supplied pulse signal. However, only the Amplitude of these signals can be set separately in the machine. The settings of Width, Rise Time and Fall Time are shared by them. Hence, there are only 5 (not 8) individually controllable parameters: Channel I Pulse Amplitude (*CHI*), Channel II Pulse Amplitude (*CH2*), Pulse Width (*W*), Pulse Rise Time (*R*) and Pulse Fall Time (*F*).

4.2.2.3 White Light Interferometer

A white light interferometer (WYKO NT1100 Optical Profiling System) supplied by Veeco Instruments Inc. was used for the surface and cross-sectional profiling of printed features as shown in Figure 4.18.

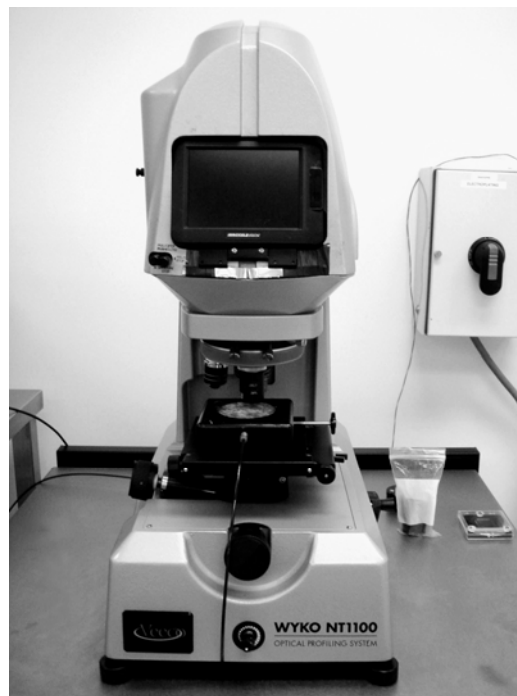


Figure 4.18: WYKO NT1100 optical profiling system.

White light interferometry (WLI) is a non-contact technique for determining

small-scale surface topography. Its working principle is to pass a beam of white light through a beam splitter, which directs the split light to the sample surface and a reference mirror respectively. When the light reflected from these two surfaces recombines, a pattern of interference fringes forms and reveals the sample surface information.

4.2.2.4 Dispensed Material

The ink used in the Litrex 80.L inkjet printing system is an aqueous dispersion of the intrinsically conductive polymer - PEDOT:PSS (Baytron[®] P VP CH 8000) supplied by H. C. Starck Inc. Summarized in Table 4.4 are some of its performance and characteristic properties.

Table 4.4: Brief characteristics of PEDOT:PSS (Baytron[®] P VP CH 8000).

Form	Odor	Color	Boiling Point T_b (°C)	Density at 20°C D_ρ (g·cm ⁻³)
Liquid	Weak/Odorless	Blue	~100	~1.0
pH at 20°C	Solid Content by Weight C_w (%)	Viscosity μ (mPa·s)	Resistivity (dry) ρ (10 ⁵ ·Ω·cm)	
1.2 ~ 1.8	2.5 ~ 3	9 ~ 20	1 ~ 3	

The formulated PEDOT:PSS ink has a solid content of approximately 2.5% by weight. This formulation is developed for the formation of thin, uniform intermediate hole transport layer (HTL) between the ITO anode and the emissive layer of P-OLED. The use of this HTL leads to significantly improved device performance by smoothening

the anode surface and facilitating hole injection and transportation. Ink properties like a small mean particle size and a narrow particle size distribution allow to create HTL with a smooth surface on the ITO anode, such that electric ‘shorts’ in the LED devices can be reduced. With the very low inherent conductivity of the polymer, the electric ‘cross-talk’ problem in devices with very small pixel size ($<10\mu\text{m}$) can be avoided [72].

4.2.2.5 Inkjet Printing of PEDOT:PSS

In order to reduce experimental errors, we have to ensure that the jetted drops from DoD inkjet printing system are consistent in drop volume, velocity and direction etc. under the same ejection conditions. Hence it is crucial to optimize the ejecting parameters to minimize deviation of drops fired from different nozzles. This is done using Taguchi methods in my preliminary work [150], wherein the part on the experimental design was described with expansion in Appendix of this thesis. Optimized single ejected PEDOT:PSS droplet has a volume of $\sim 10\text{pL}$ at around 3m/s ejection speed under optimized piezoelectric voltage pulse profile parameters as shown in Table 4.5. Figure 4.19 shows a microscopic image of consistent dried drops spread on the oxygen-plasma treated ITO glass substrate.

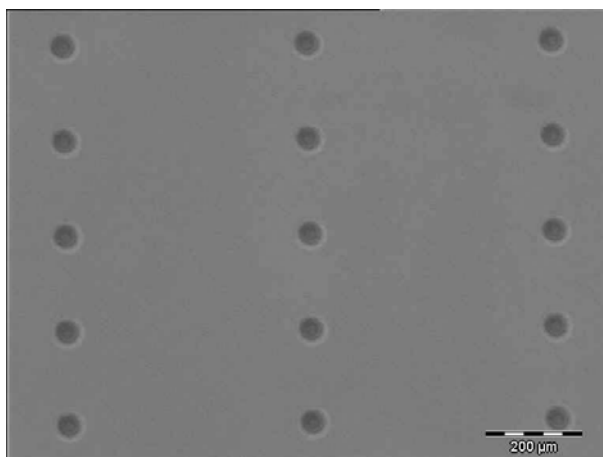
Table 4.5: Parameters for voltage pulse profile used in printing PEDOT:PSS.

Pulse Profile Parameters	Setting
Channel I Amplitude (<i>CHI</i>)	55 V
Channel II Amplitude (<i>CH2</i>)	55 V
Rise Time (<i>R</i>)	30 μ s
Width (<i>W</i>)	20 μ s
Fall Time (<i>F</i>)	20 μ s

Note:

(1) *CHI* and *CH2* have units of voltage (V);

(2) *W*, *F*, and *R* are not real time in units of microsecond (μ s), but in units defined by Litrex Co. *W* can be converted to real time in microsecond by multiplying a factor of 0.125. *F* and *R* can be converted to real time in microsecond by multiplying a factor of 0.1.

**Figure 4.19: Microscopic image of consistent printed droplets.**

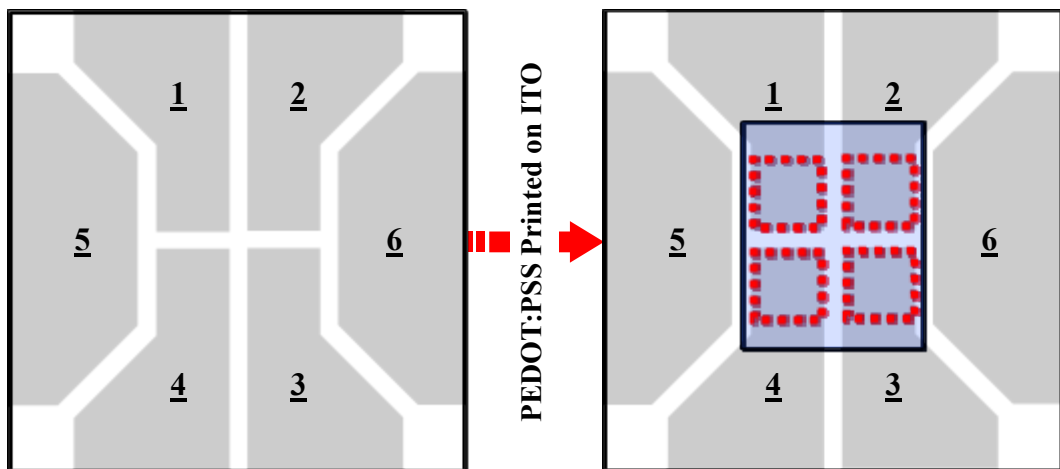
After the ITO substrate had been patterned, the Litrex 80.L inkjet system was used to print PEDOT:PSS onto the ITO side of the substrate as the hole transport layer. The temperature of the substrate was held at 25°C (room temperature) prior to inkjet printing. The DoD inkjet printing of PEDOT:PSS was held at the print speed of 16mm/s and with two different resolutions of 450dpi and 720dpi respectively. *DPI* stands for *drops per inch*, therefore 450dpi means there are 450 drops in one inch of

printed lines. The corresponding *drop pitch* which is the distance between two drops is around 56 μm and calculated by the following formula:

$$\text{Drop Pitch} = \frac{25.4 \times 10^3 \mu\text{m}}{\text{DPI}} \quad (4.1)$$

Similarly, 720dpi means there are 720 drops in one inch of printing and the corresponding drop pitch is around 35 μm .

The printed PEDOT:PSS HTL was schematically illustrated in Figure 4.20. The printed size of this layer was 9 \times 11mm², and was used to fabricate 4 diodes of 3 \times 3mm² each indicated by the dot-dashed squares. After printing, the substrate was baked in the oven for 15 minutes at 120°C.



ITO Region 1 ~ 4 - used as Anode Part

ITO Region 5 & 6 - used as Cathode Part to contact later deposited cathode layers

Solid Rectangle - PEDOT:PSS layer

Dot-dashed Squares - 4 diodes

Figure 4.20: PEDOT:PSS layer printed on patterned ITO substrate.

As a comparison, the substrate with spin-coated PEDOT:PSS layer was also fabricated and tested to compare the difference in performance of P-OLEDs between

inkjet printed and spin-coated thin films. PEDOT:PSS solution to be used was filtered with a 0.45 μm polyvinylidene fluoride (PVDF) filter and dispensed onto the oxygen-plasma treated ITO substrate, and then spin-coated at 1000rpm with an acceleration of 500r/s for a total time of 60secs to attain a thickness of around 80 μm . It should be noted that the left and right large ITO patterned regions 5 & 6 shown in Figure 4.20 are used to keep contact with deposited cathode layers. We must ensure that PEDOT:PSS does not cover any of these two ITO regions. Thus, any undesired areas of spin-coated PEDOT:PSS layer were wiped and eliminated manually by the cotton bar with DI water in our experiments. The optical microscope was used to inspect the removal of these areas. After that, the substrate was baked in the oven for 15 minutes at 120 $^{\circ}\text{C}$ similar to the inkjet printed substrates.

4.2.3 Design and Fabrication of P-OLED Devices

4.2.3.1 Equipment

(1) The spin-coater (Model: CEE 100) used in the spin-coating of organic materials is supplied by Brewer Science, as introduced in Section 4.2.1.1.

(2) The vacuum oven (Model: VWR Vacuum Oven 1415M-2) with vacuum pump and accessories used in the annealing of thin film materials is supplied by VWR International Co.



Figure 4.21: Vacuum oven (VWR 1415M-2).

(3) The thermal evaporator (Model: Edwards Auto 306 Thermal Evaporation System) used in the vacuum deposition of organic and electrode materials is supplied by BOC Edwards Co.



Figure 4.22: Thermal evaporation system (Edwards Auto 306).

(4) The Current-Voltage-Luminance (I - V - L) Measurement System with Dark Enclosure Y-Z Stage & OLED Device Holder is used in OLED performance measurement homemade by Institute of Materials Research and Engineering (IMRE).



Figure 4.23: OLED current-voltage-luminance (*I-V-L*) measurement instrument.

4.2.3.2 Materials

(1) The electroluminescent conjugated polymer used in the spin-coating of light emitting material is poly(2-methoxy-5-(2'-ethyl-hexyloxy)-*p*-phenylene vinylene) (MEH-PPV) (Model: ADS200RE) supplied by American Dye Source Inc. MEH-PPV is highly soluble in toluene and chloroform, and can be used for fabrication of light emitting displays, organic solar cells and biosensors.

(2) The powder material - Lithium Fluoride (LiF) ($\geq 99.98\%$) used in the deposition of the electron injection modifier layer is supplied by Sigma-Aldrich Co.

(3) The metal material - Calcium (Ca) ($\geq 99\%$) used in the deposition of cathode is supplied by Sigma-Aldrich Co.

(4) The metal material - Silver (Ag) ($\geq 99.99\%$) used in the deposition of the cathode capping layer is supplied by Sigma-Aldrich Co.

4.2.3.3 Processes and Parameters

(1) Spin-Coating of Electroluminescent Conjugated Polymer (MEH-PPV)

Polymer light emitting diodes were fabricated using MEH-PPV as an electroluminescent polymer. 1.3% (by weight) solution of MEH-PPV in toluene (i.e. MEH-PPV:Toluene = 1.3g:100ml) was prepared by stirring for more than 4 hours at room temperature. Approximate one milliliter of MEH-PPV solution was dropped onto the surface of one $25 \times 25 \text{mm}^2$ ITO substrate with a $0.2 \mu\text{m}$ polytetrafluoroethylene (PTFE) filter and spin-coated according to the spin speed curve shown in Figure 4.24, resulting in a $75 \mu\text{m}$ thick film which covers the PEDOT:PSS layer.

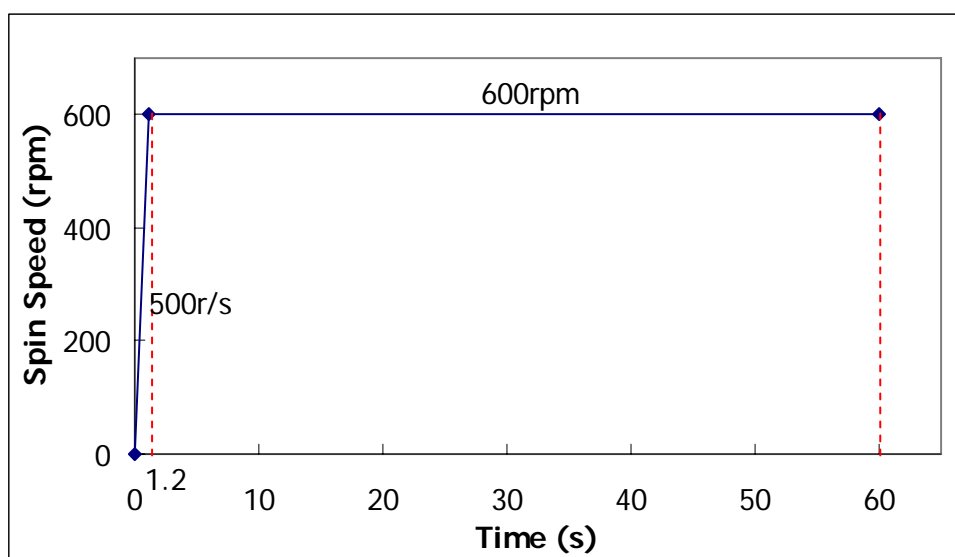
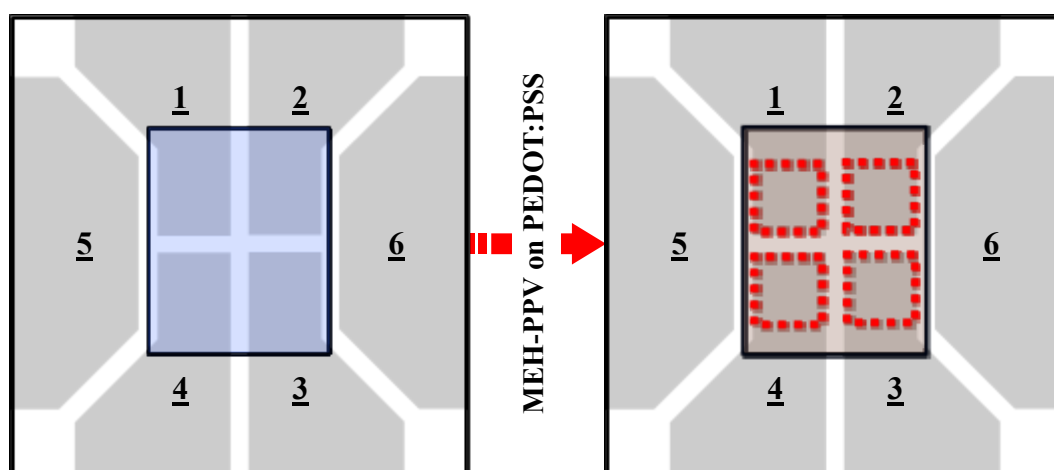


Figure 4.24: Spin speed curve used in the spin-coating of MEH-PPV.

Due to reasons similar to that of the spin-coated PEDOT:PSS layer, the undesired areas of spin-coated MEH-PPV layer were wiped and eliminated manually using the cotton bar with toluene to open contacts with ITO cathode parts, leaving a rectangular shape as shown in Figure 4.25. Regions indicated by the dot-dashed squares would later consist of 4 diodes of $3 \times 3 \text{mm}^2$ each.



ITO Region 1 ~ 4 - used as Anode Part

ITO Region 5 & 6 - used as Cathode Part to contact later deposited cathode layers

Solid Rectangles - PEDOT:PSS layer and MEH-PPV layer

Dot-dashed Squares - 4 diodes

Figure 4.25: MEH-PPV layer spin-coated on PEDOT:PSS layer.

(2) Annealing of the MEH-PPV Film

After the spin-coating of MEH-PPV, the substrate was annealed in a vacuum oven at 120°C for 30mins. Besides the vacuum oven, an oven with the purging inert gas such as nitrogen can also be used. The purpose of the annealing process is to release stress and to purge any remaining toluene for complete drying of the MEH-PPV layer.

(3) Thermal Evaporation for Cathode Electrode Layers of LiF, Ca and Ag

After the annealing process, the substrate was placed onto a shadow mask as shown in

Figure 4.26 with the ITO side facing downwards and loaded at the substrate holder of the thermal evaporator Edwards Auto 306. Each of the three materials - LiF, Ca and Ag was placed inside a 'boat' (material container) and loaded onto the turning table. After that, the bell jar of the evaporator was closed tightly and the base pressure was pumped down to 1.0×10^{-6} mBar to prepare for the vacuum deposition.

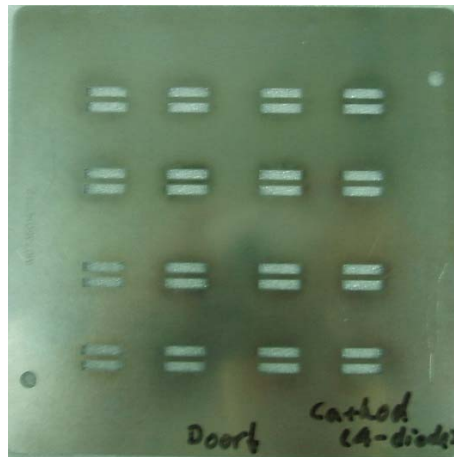


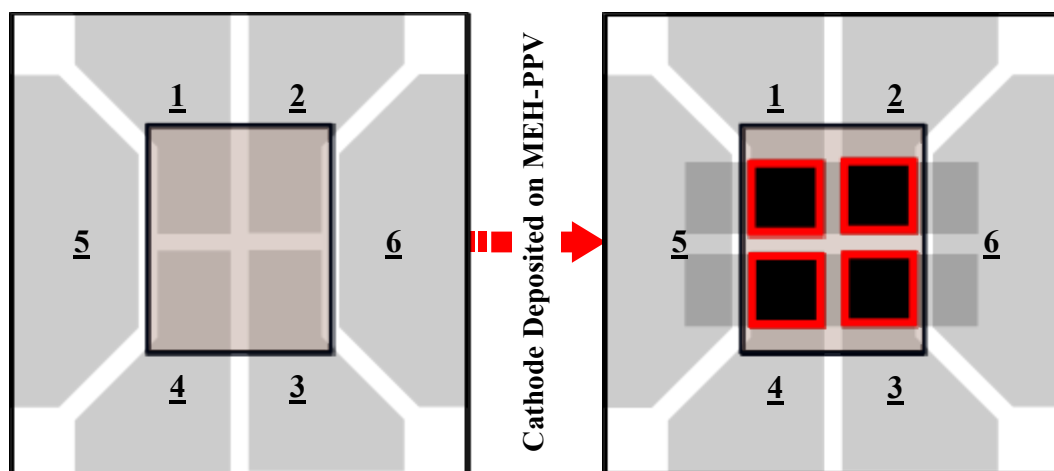
Figure 4.26: Shadow mask for the thermal evaporation.

The first material to be evaporated was LiF. Electrical current was passed through the material container and the heat generated would evaporate the material. The vapor would travel outwards in all directions and condensed on the cool substrate surface to form two $13 \times 3 \text{ mm}^2$ strips determined by the shadow mask for each $25 \times 25 \text{ mm}^2$ ITO substrate. The process was repeated with calcium and then followed by silver. The processing parameters for the three materials were shown in Table 4.6.

Table 4.6: Parameters for the thermal evaporation system Edwards Auto 306.

Film Material	Pressure (mBar)	Deposition Rate (nm/s)	Current Applied (A)	Thickness (nm)
LiF	$\leq 1 \times 10^{-6}$	0.05	2.2	0.5
Ca	$\leq 1 \times 10^{-6}$	0.2	3.0	20
Ag	$\leq 2 \times 10^{-6}$	0.2	3.3	150

Although LiF, Ca and Ag layers have their own particular functionality, without loss of generality they are here considered as a single cathode for simplicity. As shown in Figure 4.27, these three layers contacting ITO Region 5 & 6 act as cathode and ITO Region 1 ~ 4 serve as anode. The MEH-PPV layer is the active electroluminescent layer. The four P-OLED diodes with size of $3 \times 3 \text{ mm}^2$ each were formed on each ITO substrate indicated by solid black squares.



ITO Region 1 ~ 4 - used as Anode Part

ITO Region 5 & 6 - used as Cathode Part to contact later deposited cathode layers

Solid Rectangles - superposed PEDOT:PSS and MEH-PPV layers

Double Rectangular Strips - superposed cathode layers of LiF, Ca and Ag

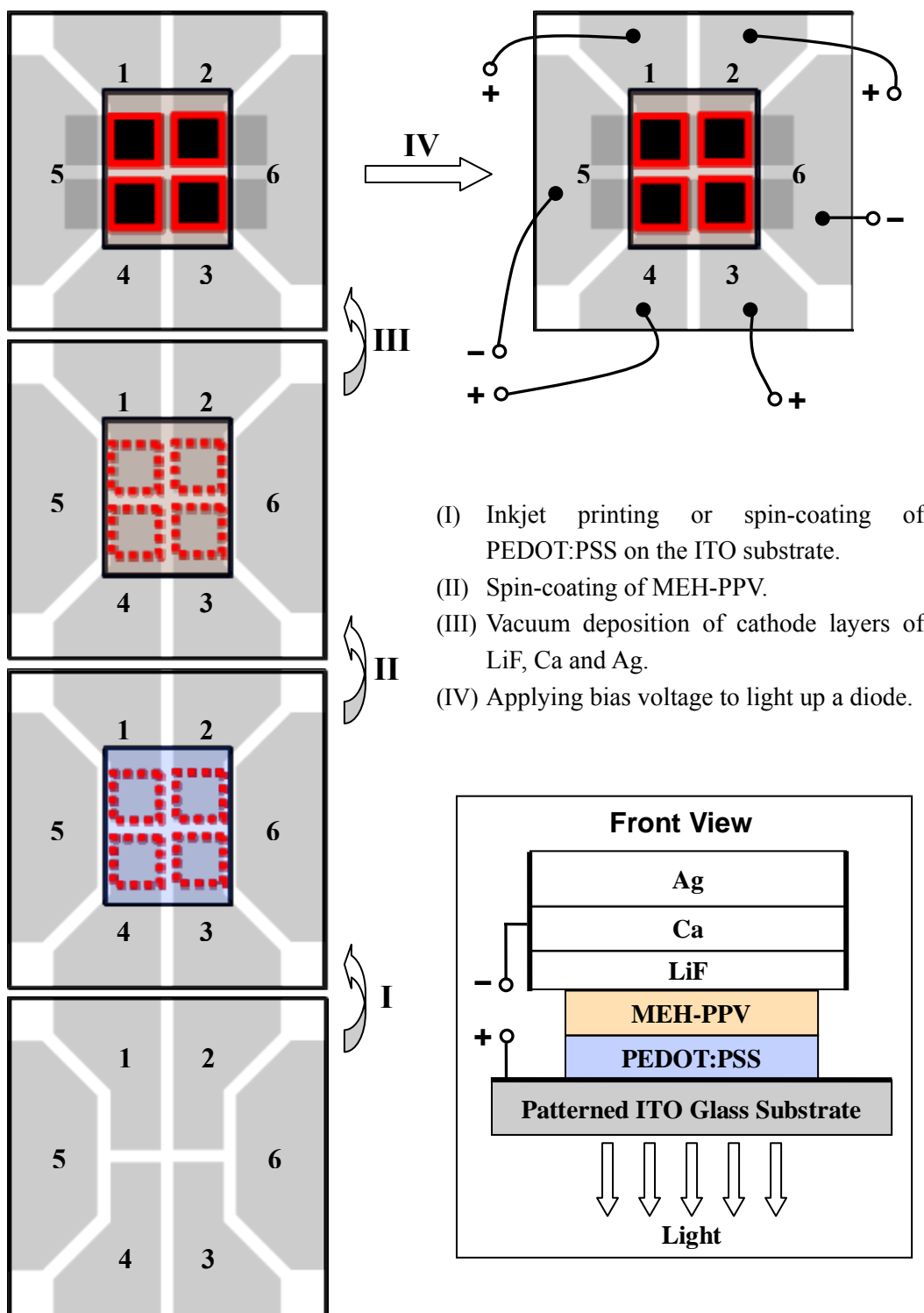
Solid Black Squares - 4 diodes

Figure 4.27: Thermal evaporation of LiF, Ca and Ag as the cathode electrode.

(4) Applying Bias Voltage to P-OLED Devices

The aforementioned complete fabrication process of a P-OLED device was illustrated in Figure 4.28. A positive bias voltage was applied to the ITO Anode Part in the sandwiched P-OLED structure: ITO | PEDOT:PSS | MEH-PPV | LiF | Ca | Ag. Electrical current was passed through the cathode layer by applying a negative bias voltage to the ITO Cathode Part. The MEH-PPV layer acts as the light emitting layer,

in which the holes and electrons from ITO and Ca, respectively, meet and recombine. The recombination of holes and electrons will form excitons which when falling to the ground state emit photons. P-OLEDs were tested on their device performance in the OLED *I-V-L* measurement instrument shown in Figure 4.23 of Section 4.2.3.1.



ITO Region 1 ~ 4: used as Anode Part;

ITO Region 5 & 6: used as Cathode Part to contact deposited cathode layers.

Figure 4.28: Schematic diagram of the fabrication of a P-OLED device.

4.3 Results and Discussion

4.3.1 ITO Surface Patterning

In this section, some results for the ITO surface patterning process are shown. Here, we are concerned only with getting a reasonably well patterned surface with sharp lines and features. Some images of the patterned surface taken under an optical microscope are shown in order to highlight what should be considered as reasonable. The results are considered acceptable when the patterns showed clear-cut lines and corners to the eye under an optical microscope. The important thing concerned is that the processes, procedures and parameters are repeatable for getting similarly reasonable results.

Figure 4.29 shows the different features on the patterned surface of an ITO substrate. Two different ITO regions were indicated on the images and we can see that all the features seem reasonably sharp and clear. This is sufficient for our purposes in this work. Also, the processes and parameters have been shown to be repeatable and relatively stable for the materials and machines that have been used. Repeated patterning of different ITO substrates has been carried out without any major problems.

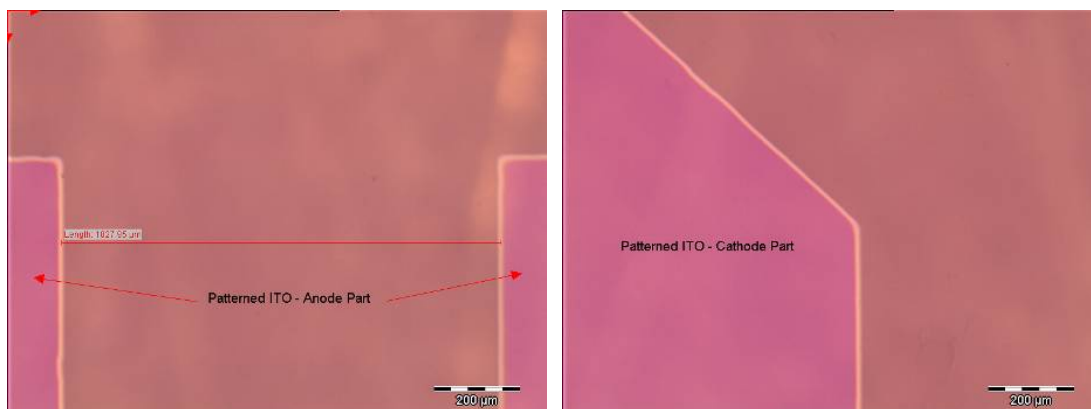


Figure 4.29: Various locations on a patterned ITO substrate showing reasonably sharp and clear features under an optical microscope.

4.3.2 Drop-on-Demand Inkjet Printing of PEDOT:PSS

4.3.2.1 Sample Pattern Printing on Photo Paper

Sample patterns consisting of common electrical components (resistors, capacitors and inductors) and also lines of different circles were printed on photo paper using sources from bitmap images as shown in Figure 4.30. Sample patterns were printed using the Litrex 80.L DoD inkjet printer in order to show its printing capabilities of the system. The patterns were printed on photo paper as photo paper has a layer of absorbing materials that ensure the ink printed will dry out very quickly, ensuring that the end results of the printing will likely be smooth and clear.

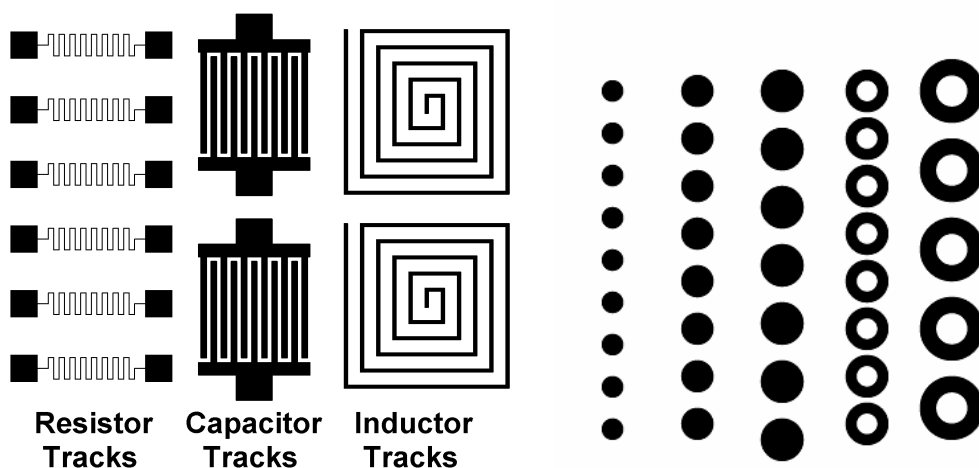


Figure 4.30: Bitmap images for sample pattern printing on photo paper.

Figure 4.31 demonstrates examples of printed electrical components and lines of circles on photo paper using Litrex inkjet printing system with PEDOT:PSS. It can be observed that the qualities of the printings are sufficiently good and accurate for our purposes. Besides, the printings are also clean and smooth without drop satellites.

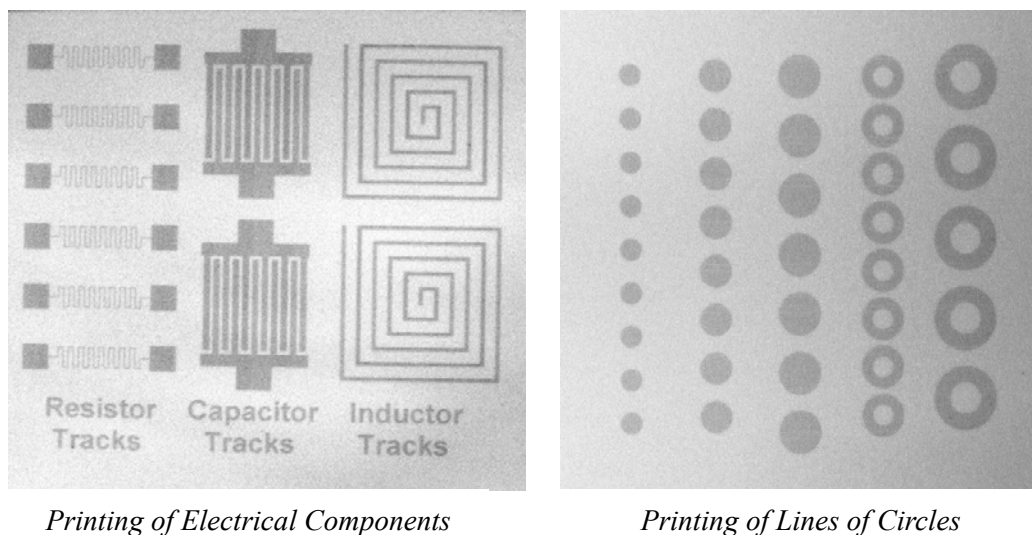


Figure 4.31: Photographs for PEDOT:PSS pattern printing on photo paper.

The printing of the electrical components indicates that the machine is very flexible as it can print very small details such as the small tracks of the resistors. The machine is

also very precise as it can print the electrical components accurately despite the complex design of the components. The printing of the different circles shows the consistency and repeatability of the machine while maintaining precise printing. For the same columns of circles, the dimensions can be seen as being consistent throughout the whole columns.

4.3.2.2 PEDOT:PSS Inkjet Printing on ITO Substrates

In order to investigate the influence of different parameters on the performance of P-OLED devices, PEDOT:PSS single lines had been printed so that the line surface topography can be investigated. The two typical printing resolutions selected for printing on the ITO substrates were 450dpi and 720dpi at room temperature of 25°C with a print speed of 16mm/s.

Firstly, we examined PEDOT:PSS individual dots printed on the ITO glass substrate under the above print speed and substrate temperature. Figure 4.32 shows a result of PEDOT:PSS drops after drying using optical microscope. The 3D shape of single drop and the cross-sectional profile through its center are shown in Figure 4.33 and Figure 4.34 respectively using white light interferometer. It can be seen that the diameter of one droplet after drying at room temperature is about 70 μ m. In addition, we found that there are different drying behaviors for such super fine drops at different ranges of substrate temperature. This will be addressed in detail in Chapter 5.

In this chapter, only different printing resolutions for the line or area formation were taken into consideration in the experiment.

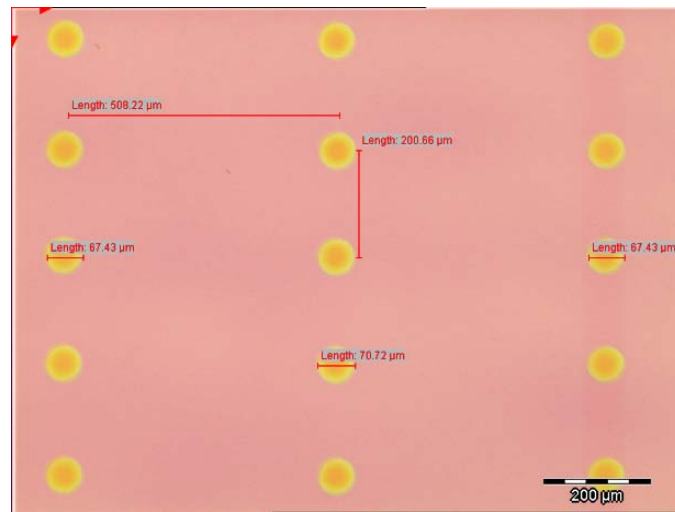


Figure 4.32: Optical image of inkjet printed PEDOT:PSS dots on the ITO substrate.

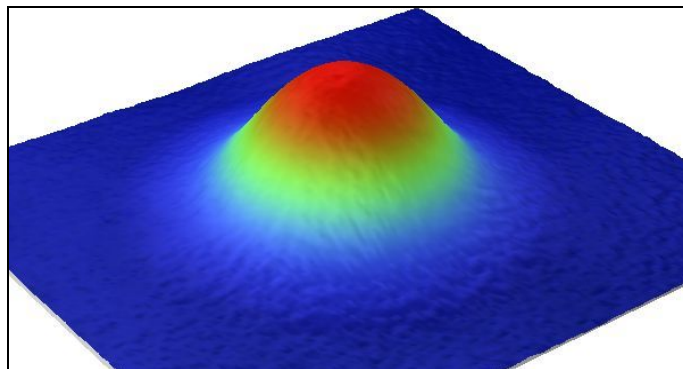


Figure 4.33: 3D image of single drop at room temperature.

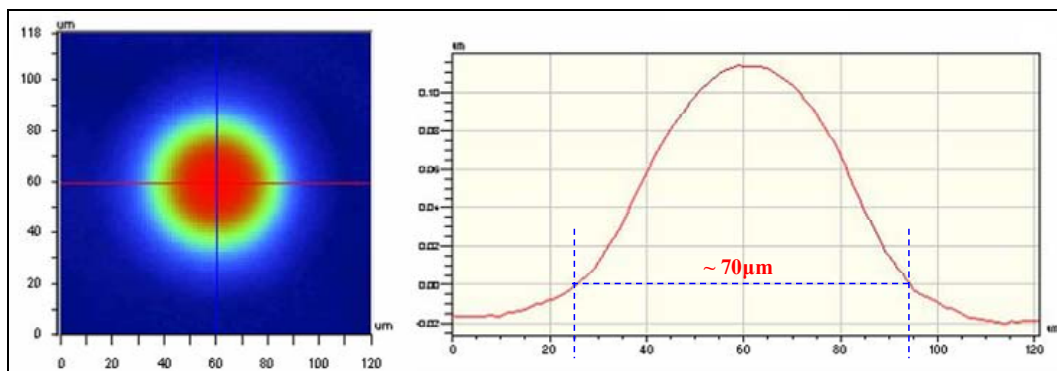
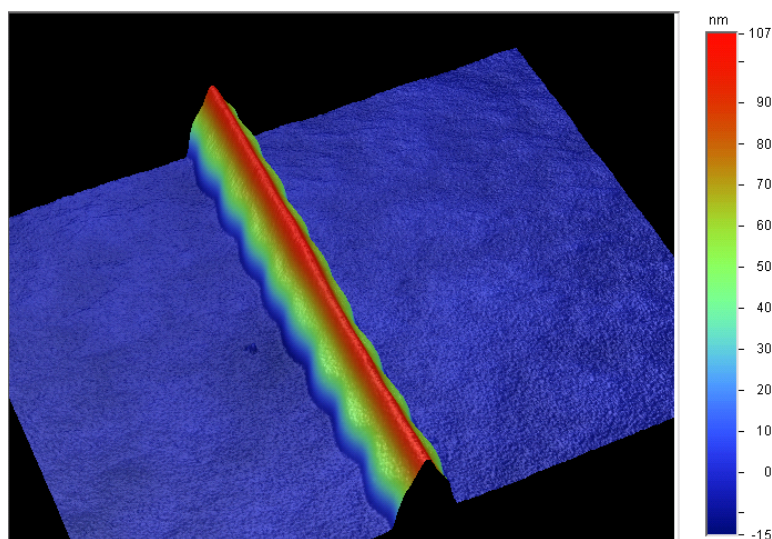


Figure 4.34: Top-down view and 2D cross-sectional profile at room temperature (Units: height in nm; width in μm).

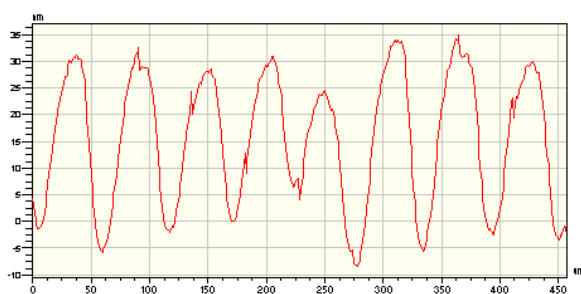
As introduced in Section 4.2.2.5, drop pitch (distance between two adjacent drops) can be simply calculated by Equation (4.1), rewritten as below:

$$\text{Drop Pitch} = \frac{25.4 \times 10^3 \mu\text{m}}{\text{DPI}}$$

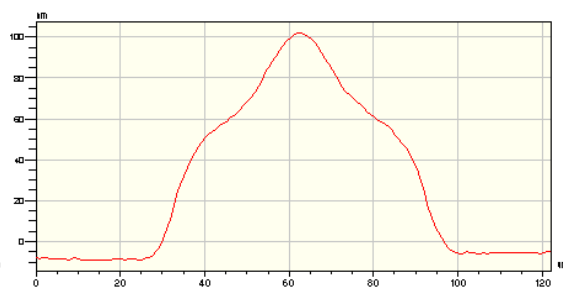
Hence, the corresponding drop pitches of 450dpi and 720dpi are around $56\mu\text{m}$ and $35\mu\text{m}$ respectively. Since PEDOT:PSS single dot has a size of $70\mu\text{m}$ after drying, drops in the single line printed under 450dpi and 720dpi must overlap each other. The following are the images for single line printing of 450dpi.



(a) 3D image of printed single line.



(b) 2D profile of the line edge.



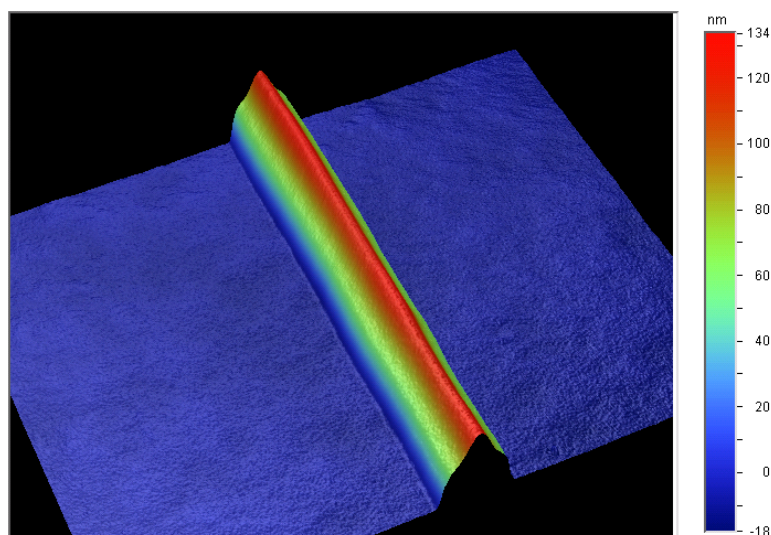
(c) 2D profile of cross section.

Figure 4.35: 3D image and 2D profile of PEDOT:PSS single line printed at 450dpi (Units: height in nm; width in μm).

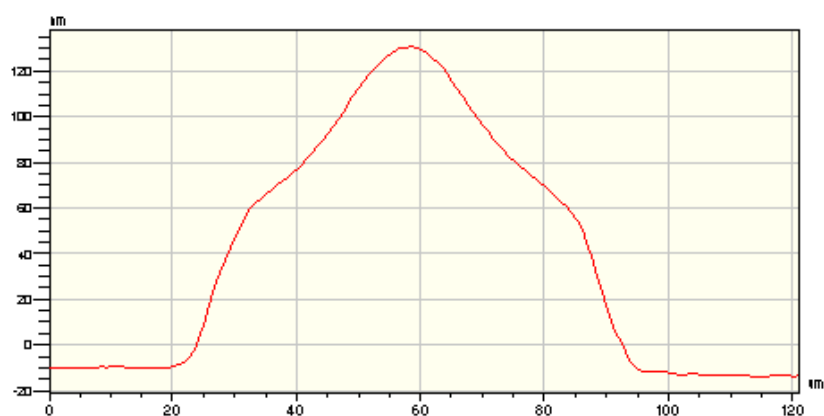
From the observation of Figure 4.35 (a) and (b), it can be seen that the edge of the

single line is not straight but quite wavy. Figure 4.35 (c) shows the profile of cross sectional view of the line. The result from Figure 4.35 (c) also shows that the height of the line is about 110nm and the surface of the line is not flat with the centre part higher than the edge.

Figure 4.36 (a) shows 3D image of a PEDOT:PSS single line printed at 720dpi after drying up, while Figure 4.36 (b) shows the cross sectional profile of the line.



(a) 3D image of printed single line.



(b) 2D profile of cross section.

Figure 4.36: 3D image and 2D profile of PEDOT:PSS single line printed at 720dpi (Units: height in nm; width in μm).

From the observation of Figure 4.36 (a), it can be seen that the edge of the single line is almost straight and smooth. The result from Figure 4.36 (b) also shows that the height of the line is about 140nm which is higher than that at 450dpi, and the surface is also not flat with the centre higher than the edge.

As for 450dpi, the edge of the line is not straight because the drop pitch is $56\mu\text{m}$ which is larger than the radius of the droplet which is about $35\mu\text{m}$. As a result, only a small fraction of a droplet overlaps with each other as illustrated in Figure 4.37 and thus the shape of the droplet is still visible along the edge of the line to make the edge become wavy as shown in Figure 4.35.

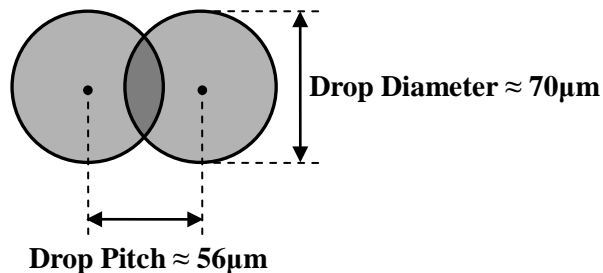


Figure 4.37: Schematic of the droplet overlapping for 450dpi.

As a comparison, for 720dpi, the edge of the single line is almost straight because the drop pitch is $35\mu\text{m}$ which is almost the same size as the radius of the droplet which is about $35\mu\text{m}$. As a result, almost each half of the droplets overlapped with each other as illustrated in Figure 4.38. As such, the shape of individual droplet is not visible along the sides of the line and thus a straight edge is formed together with the influence of surface tension as shown in Figure 4.36.

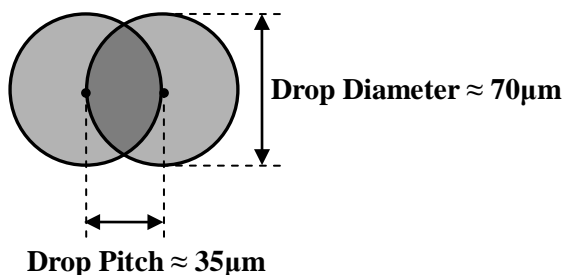


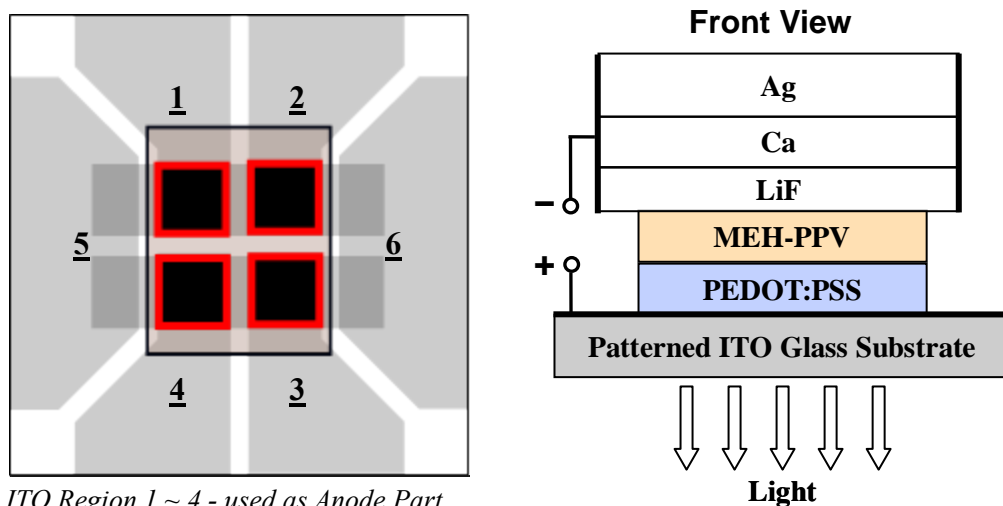
Figure 4.38: Schematic of the droplet overlapping for 720dpi.

From the results of the above images, it was found that both the single line printing for 450dpi and 720dpi have some similarities and also differences. The top surfaces of both lines are similarly not flat. This is very important as this means if the same resolutions are used to print a layer of material as compared with the spin-coated layer, the total surface area of the material will be higher due to an uneven surface. This is very critical especially for some electrical device applications as more surface area may increase *surface contact area* between two layers and thus there will be more concentration of charge carriers or more interaction between holes and electrons. As a result, the device performance will be affected depending on the level of injection and interaction between the holes and electrons.

One of the differences between the line printed at 450dpi and the line printed at 720dpi is the thickness of the line, especially at the area where the drops overlap with each other. The height of the line printed at 720dpi is higher than 450dpi as higher resolution causes more volume of materials to be printed in a line of the same length. At areas where the drops overlap with each other, the thickness for 720dpi is also higher as there is a high proportion of the drops that overlaps. This will make a

difference in device performance when these two resolutions are used to print films, as the thin film with different thickness especially at the overlapped areas will have different *effective surface contact area* with the adjacent layer of thin film and thus different concentration of holes or electrons are able to flow through the material. It should be noted that effective surface contact area here is defined as any contact area between two layers that can improve related performance effectively, such as to increase the concentration of charge carriers. However, in region where the contact area is too low or high, the properties for charge carriers are unable to be improved or even worse. Such contact area is not part of effective surface contact area.

4.3.3 Characterization of P-OLED Devices



ITO Region 1 ~ 4 - used as Anode Part

ITO Region 5 & 6 - used as Cathode Part to contact later deposited cathode layers

Solid Rectangles - superposed PEDOT:PSS and MEH-PPV layers

Double Rectangular Strips - superposed cathode layers of LiF, Ca and Ag

Solid Black Squares - 4 diodes

Figure 4.39: Schematic structure of 4 diodes P-OLED device.

The 4 diodes P-OLED device has the structure as shown in Figure 4.39 after all the processes involved in the fabrication of P-OLED were completed. The first ITO layer is patterned for a 4-diode P-OLED device and used as the electrodes. Above the ITO layer is PEDOT:PSS which function as hole transport layer (HTL). In the thesis, the HTL is inkjet printed with two different printing resolutions, namely 450dpi and 720dpi, and also spin-coated in order to investigate the effect of different parameters on the performance of the P-OLED. The MEH-PPV layer on the top of PEDOT:PSS is used as the active light-emitting layer.

The top three layers are LiF, Ca and Ag which serve as the cathode of the P-OLED device. When electrical current is connected between the ITO anode and cathode, holes and electrons will start to flow and when they interact with each other at the emissive layer, light will be produced. The two sides of an actual P-OLED are shown in the following Figure 4.40.

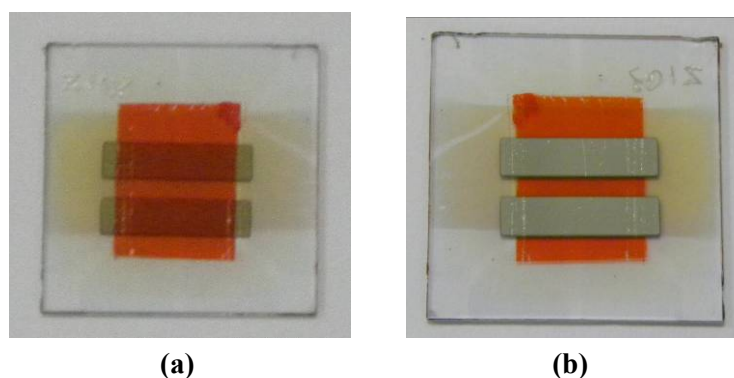


Figure 4.40: Pictures of a 4 diodes P-OLED device: (a) ITO side facing downwards; (b) ITO side facing up with cathode layers on the top.

Here, we compared the device performance of P-OLEDs with both types of PEDOT:PSS films, one fabricated by an inkjet printing method and the other by

spin-coating. Figure 4.41 to Figure 4.44 as below show the results of the current density (mA/cm^2), luminance (cd/m^2), luminous efficiency (cd/A) and luminous power efficiency (lm/W) versus applied bias voltage (V) respectively, for P-OLED devices with the PEDOT:PSS HTL deposited by inkjet printing and spin coating.

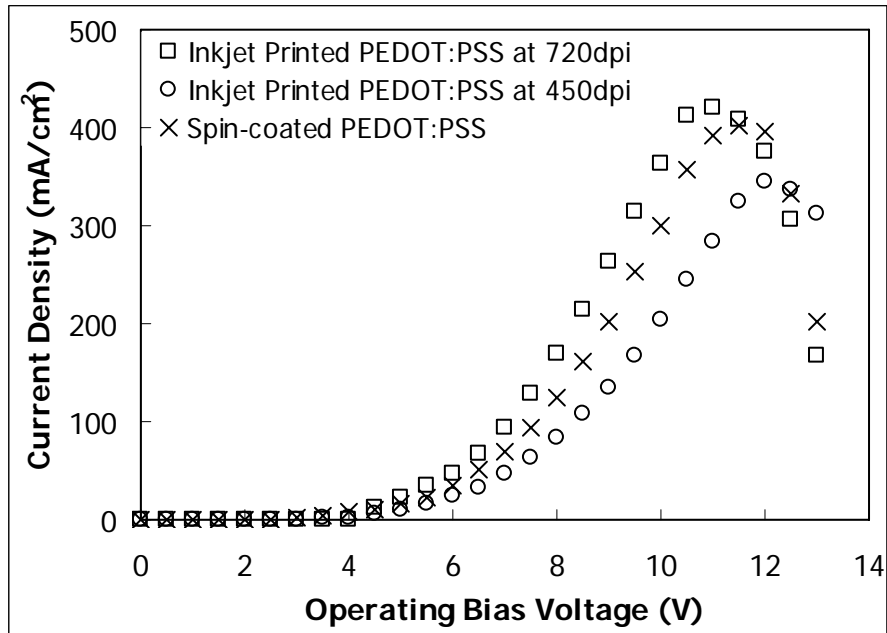


Figure 4.41: Characteristic of current density-voltage for P-OLED devices.

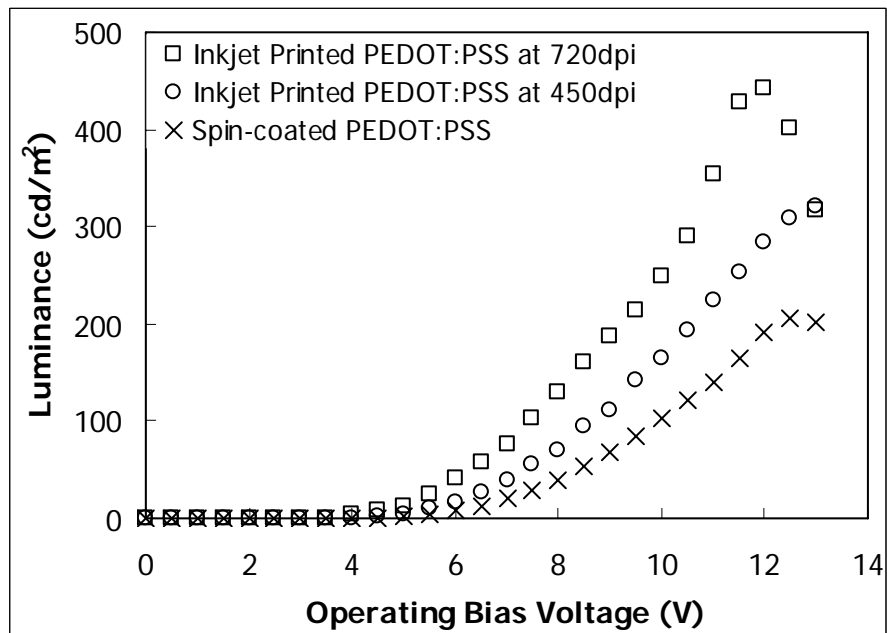


Figure 4.42: Characteristic of luminance-voltage for P-OLED devices.

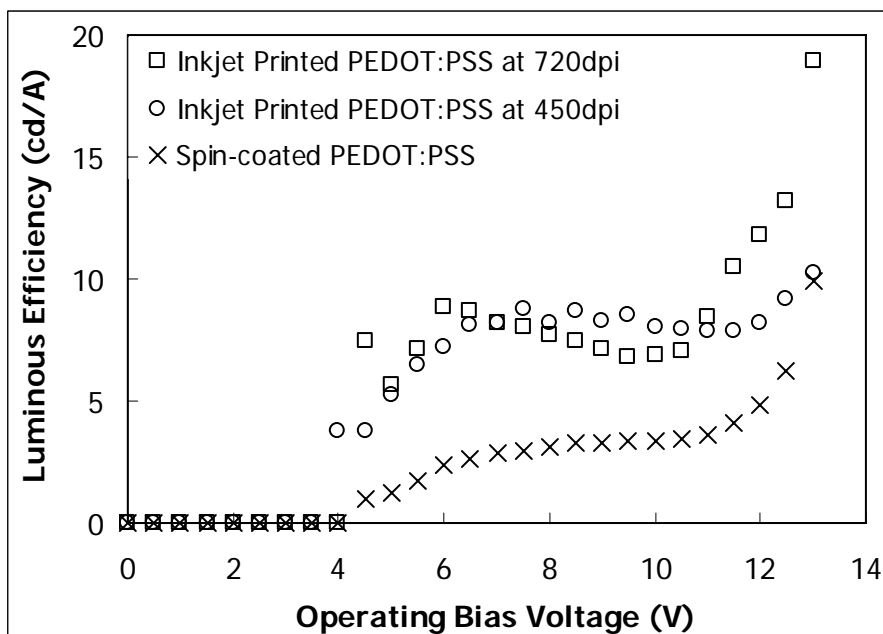


Figure 4.43: Characteristic of luminous efficiency-voltage for P-OLED devices.

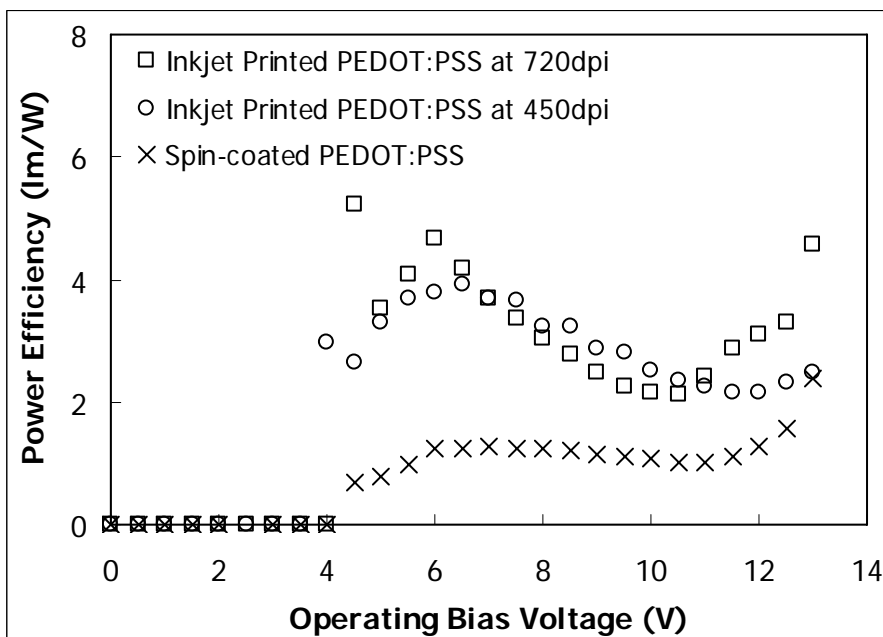


Figure 4.44: Characteristic of luminous power efficiency-voltage for P-OLED devices.

It should be pointed out that once variations of current density and luminance with operating bias voltage are accurately measured, the luminous efficiency and power

efficiency can be determined by the following expressions ^[151]:

$$\text{Luminous Efficiency (cd/A)} = \frac{\text{Luminance (cd/m}^2\text{)}}{\text{Current Density (mA/cm}^2\text{)}} \times 10 \quad (4.2)$$

$$\text{Power Efficiency (lm/A)} = \frac{\pi \times \text{Luminance (cd/m}^2\text{)}}{\text{Current Density (mA/cm}^2\text{)} \times \text{Operating Bias Voltage (V)}} \quad (4.3)$$

From the graphs, it was observed that inkjet printing appears to demonstrate better P-OLED device performance than spin-coating under some controlled conditions. At 720dpi, inkjet printing can result in higher conductivity and luminance for P-OLED as compared to spin-coating at the same applied bias voltage, similar conclusions are also observed for luminous efficiency and power efficiency. In Figure 4.41 inkjet printing at 450dpi shows lower device conductivity than spin-coating, but it still attains a higher brightness than spin-coating. This would be attributed to its higher device efficiency as shown in Figure 4.43 and Figure 4.44.

Table 4.7: Brief information of the P-OLED device performances.

Device	Turn-on Voltage at 1cd/m ² (V)	Operating Voltage at 100cd/m ² (V)	Maximum Luminance (cd/m ²)
A (720dpi Printing)	3.9	7.6	431 (at 12.0V)
B (450dpi Printing)	4.2	8.7	322 (at 13.2V)
C (Spin-Coating)	4.5	10.0	204 (at 12.9V)

Device A: ITO | inkjet printed PEDOT:PSS HTL (720dpi) | MEH-PPV | LiF | Ca | Ag
 Device B: ITO | inkjet printed PEDOT:PSS HTL (450dpi) | MEH-PPV | LiF | Ca | Ag
 Device C: ITO | spin-coated PEDOT:PSS HTL | MEH-PPV | LiF | Ca | Ag

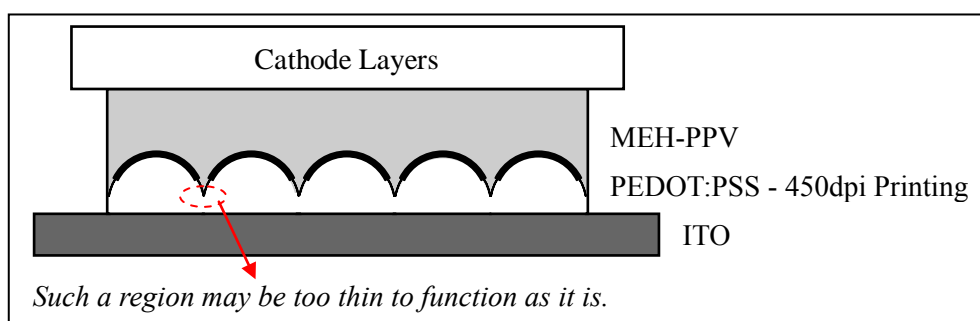
Table 4.7 summarizes some information for device performances. It can be seen that the turn-on voltage (defined as the voltage required to obtain a luminance of 1cd/m^2) for the P-OLED with inkjet printed HTL reduces to 3.9V and 4.2V for 720dpi and 450dpi respectively, while that for the P-OLED with spin-coated HTL is 4.5V. The operating voltage at a luminance of 100cd/m^2 , a level where the light can be easily seen by human eyes also attains lower values of 8.7V and 7.6V for inkjet printed HTL at 450dpi and 720dpi respectively, as compared to the value of 10.0V for spin-coated HTL. The maximum luminance is the highest achievable luminance level for the P-OLED. It was found that inkjet printing exhibits a higher luminance than spin-coating. However, at this level of luminance, OLED devices will degrade and burn off very fast due to the high operating voltage which results in a high electrical current passing through the device.

The differences in these P-OLEDs can arise from their fabrication processes. As some behaviors of a micro-liquid and its related phenomena are quite different from those of a macroscopic liquid due to the drop size effect, it is natural to infer that the properties of a dried film produced from a micro-liquid would be different from those produced from a macroscopic liquid. In the case of a spin-coated film, the film is dried during rotation of the substrate. The two dimensional structure of the film tends to be realized by centrifugal force, together with one dimensional vaporization normal to the substrate. As for inkjet printing, an inkjet printed droplet has greater freedom of material transport during the drying process and this gives it a more three dimensional

surface structure. Based on this consideration, the conductivity of the P-OLED with inkjet printed film (such as at 720dpi) can be higher than that of the P-OLED with spin-coated film. The reason is that the conductivity of the spin-coated film is mainly governed by a hopping mechanism of charge carriers between polymer chains, while intra-chain carrier transport could be taken into account in the inkjet printed film because of its three dimensional structure. Hence, for the inkjet printed film, the charge carrier concentration or injection might be enhanced which improves its conductivity.

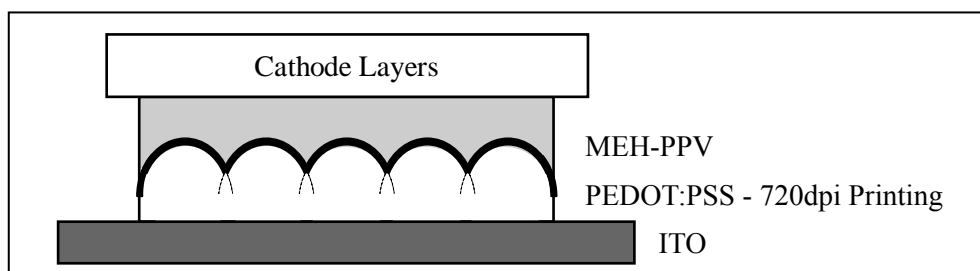
The reason P-OLEDs with inkjet printed PEDOT:PSS HTL have higher luminance might be because inkjet printed HTL is not as flat and smooth as spin-coated HTL as mentioned before. This can also be seen by examining the shape profile of printed single lines. For single line printing, the surface of the line is not flat as the centre part is higher than the edge and the line edge also likely becomes wavy. Therefore, when PEDOT:PSS HTL is printed as a region, which is actually formed by many lines, the inkjet printed HTL will also not be flat. As a result, the inkjet printed HTL will have more surface area as compared to the spin-coated HTL and thus the inkjet printed HTL will have more surface contacts with the emissive layer and increase the recombination of holes and electrons in the emissive layer. Hence, more light will be emitted for P-OLEDs with inkjet printed HTL. This is also why P-OLEDs with inkjet printed HTL just require lower operating bias voltage as compared to those with spin-coated HTL in order to obtain the same level of luminance.

Another important result is that the inkjet printed HTL at 720dpi also has a higher luminance as compared to the inkjet printed HTL at 450dpi at the same operating voltage. This may be due to the different effective contact area between the HTL and emissive layer as shown in the Figure 4.45.



(a) PEDOT:PSS is inkjet printed at 450dpi.

Effective surface contact area is indicated by heavy curve lines.



(b) PEDOT:PSS is inkjet printed at 720dpi.

Effective surface contact area is indicated by heavy curve lines.

Figure 4.45: Schematic of effective surface contact area for inkjet printed films. The inkjet printed film at 720dpi may have more effective contact area than that at 450dpi. However, surface contact area in too thick or thin regions might not improve device performance or even make it worse.

Effective surface contact area is the area where holes and electrons can recombine and emit light in the emissive layer. From the profile of the line printing, single line printed at 720dpi has a maximum height of about 140nm while single line printed at 450dpi has a maximum height of about 110nm. Moreover, single line printed at 720dpi has a higher proportion of a drop that overlapped with adjacent drop and this

leads to higher thickness at overlapped areas for 720dpi. As the thickness of inkjet printed HTL at 720dpi is higher, this might cause more holes to travel through the HTL and thus more interaction between holes and electrons at the emissive layer. As a result, more light will be produced for HTL printed at 720dpi. It should be noted that surface contact area in too thick or thin regions might not improve device performance or even make it worse. Hence the thickness of inkjet printed thin films can optimize the final device performance. Here, inkjet printing at 720dpi gives a sufficiently good example for our purpose.

4.4 Conclusion

(1) ITO Surface Patterning

For this section of the work, the patterned features that we have obtained are reasonably sharp and sufficient for our purposes. Also, the processes and parameters have been shown to be repeatable and relatively stable for the materials and machines that have been used. Repeated patterning of different ITO substrates has been carried out without any major problems.

(2) Drop-on-Demand Inkjet Printing

The Litrex 80.L is a machine that gives a lot of freedoms of control with sufficient precision and accuracy which prove to be very useful for research purposes. Important printing parameters such as resolution, temperature and voltage pulse signal can be

easily changed for research purposes. PEDOT:PSS single line printing experiment shows that by using different resolutions for DoD inkjet printing, different feature profiles and results can be achieved such as at 720dpi and 450dpi. As surface flatness for inkjet printed lines is not low, it would result in the formation of inkjet printed areas without adequately flat surface as compared to the spin-coating method. Thus for inkjet printing the total surface area of materials will be higher due to their uneven surface. This information is very important as the result can be applied to the fabrication of devices and implies why the change in printing parameters affects the final device performance.

(4) Fabrication of P-OLED Devices

During the fabrication of P-OLED devices, the same printing parameters for the PEDOT:PSS single line printing are used for the PEDOT:PSS HTL printing. This is to make sure that the effects of the parameters on the P-OLED performance can be explained using the surface morphology of inkjet printed single lines. From the comparison by the inkjet printed HTL and spin-coated HTL, it is known that inkjet printing produced better HTL properties which improve the final device performance. This is due to the inkjet printed HTL forming more surface contact area, which can balance and enhance interactions between holes and electrons and thus may emit more light. From the different printing resolutions used for the HTL inkjet printing, it is also found that P-OLEDs with inkjet printed HTL at 720dpi give better device performance than those at 450dpi due to the more effective surface contact area. This

encourages more hole carriers to flow through and therefore more recombination with electrons. In all, the inkjet printed functional film is able to produce better device performance as compared to the spin-coated film. Furthermore, the performance of the P-OLED devices can be easily manipulated by using different operating parameters of a DoD inkjet printing system such as printing resolution. However, further studies are needed to understand the in-depth mechanism behind the change in device performance characteristics upon the formation of inkjet printed films produced drop by drop.

CHAPTER 5

CHARACTERIZATION OF SINGLE MICRODROPLET DRYING BEHAVIOR

5.1 Introduction

As introduced in previous chapters, poly(3,4-ethylenedioxythiophene):poly(styrenesulfonate) (PEDOT:PSS) has been used extensively in the fabrication of electronic devices such as polymeric organic light-emitting diode (OLED) displays by drop-on-demand (DoD) inkjet printing technique. To obtain uniform thin films and printed features, we must first explore and characterize a single printed drop. In this work, the surface morphology of printed drops of ~10pL after drying will be examined and explained in a qualitative manner, which would extend the comparison with previous work described in published literature. The influence of temperature of the indium-tin-oxide (ITO) substrate on the dried profile of a single droplet that has been deposited onto it will be investigated. Our aim is to have an understanding of the drying behavior of this droplet upon impact and spreading on the substrate with respect to temperature. Dried profile of the printed droplets at different substrate temperatures may give us an insight into this behavior.

5.2 Overview of Drop Spreading and Drying

In order to obtain a good thin film with high uniformity if required, it is crucial to control the drying process. Due to size effects, the drying behavior of an inkjet printed droplet is very different from that of a macroscopic liquid such as a spin-coated film. Due to the much higher surface area per unit volume found in small droplets, such as ~10pL in volume, rapid evaporation and drying takes place, even when higher boiling-point solvents like water as compared to some organic solvents are used^[152].

5.2.1 Drop Impact and Spreading

Upon impact on a substrate, an inkjet printed droplet starts to spread. This spreading consists of an initial *spontaneous inertial (dynamic) spreading* for a short time, followed by a wet spreading for a longer period of time. A schematic of the spreading process is shown in Figure 5.1 below. The droplet expands in its radial direction and reaches a maximum diameter, D_{cmax} , just after impact. If there is excessive surface tension, D_{cmax} decreases as liquid flows back towards its center and increases its height there. This is known as *recoiling*. When the surface tension is too high, the droplet might rebound. In cases where the surface tension is very high, the droplet vibrates and repeatedly increases and decreases its diameter for several microseconds. When this energy is dissipated, the droplet settles into an almost stable shape. Such recoiling and rebounding occurs when D_{cmax}/d_0 (initial diameter of the droplet) and the contact angle are large^[153].

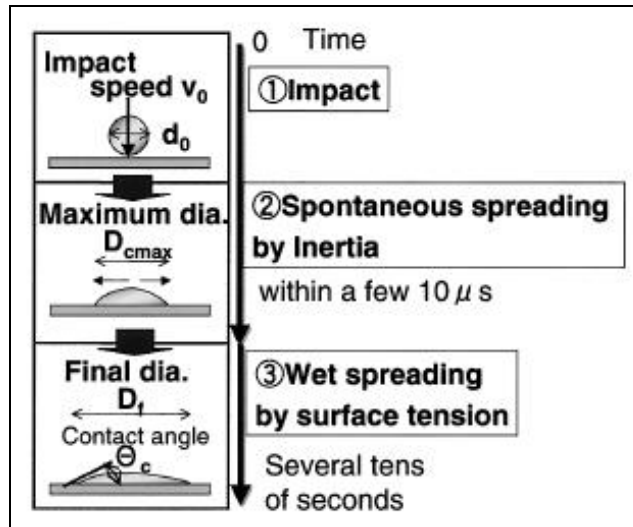


Figure 5.1: Different stages of the drop spreading process on a substrate ^[153].

After initial spreading to D_{cmax} and dissipating almost all energy, the drop spread slowly to its final equilibrium diameter with the minimum surface energy. This is known as *wet spreading*. The drop diameter asymptotically approaches its final equilibrium diameter, D_f , and its contact angle becomes stable. This phase of the spreading is much slower than the initial spontaneous spreading. Ideally, a spherical cap with the minimum surface energy will be its final profile. However, due to the contact angle differing from place to place depending on material condition, dirt and roughness, various shapes are actually seen. Hence, uniform substrate wettability is very important. Drop spreading is dependent on fluid viscosity, but the final shape is determined only by drop volume and contact angle. It does not depend on the fluid's physical properties. Hence, substrate material and treatment is very important as D_f is determined by the contact angle ^[153].

5.2.2 Drop Drying Behavior

During drying, even if the initial fluid surface is flat, we cannot be sure that the surface of the dried film is also flat. For example, when a drop of coffee is spilled on a table, the thickness of the dried coffee drop does not stay uniform. Instead, there is dark material deposited in a ‘ring’ along the drop outer boundary. This deposition of material on the outer boundary is due to a capillary action in which the contact line of the drying drop is fixed. The contact line of the drying drop is fixed because the rate of evaporation at the outer boundary is more than the rate of evaporation in the interior of the drop. To compensate for this evaporated liquid from the outer boundary, the liquid from the interior moves outward and the solute particles are also transferred to the boundary as shown in Figure 5.2.

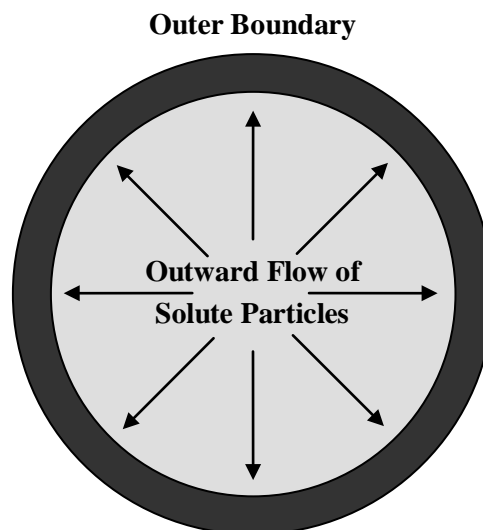


Figure 5.2: ‘Ring’ formation due to outward flow of solute particles to the boundary.

This phenomenon is known as *coffee-stain effect*. The previous brief explanation is credited to the evaporation rate distribution theory proposed by Deegan et al. ^[154] in

1997, which gives a rather satisfactory explanation of the coffee-stain effect.

5.2.2.1 The Evaporation Rate

Figure 5.3 shows a cross-sectional representation of a drop during an increment of evaporation ^[154]. The shaded portion of the drop represents the volume of liquid evaporated in a single time increment. Figure 5.3 (a) shows that the droplet would shrink due to the evaporation if there were no flow produced. However, the radius of the drop cannot shrink as its contact line with the substrate is pinned. To prevent the shrinkage, the liquid evaporated from the boundary must be refilled by an outward flow of solute particles along with the solvent, indicated by arrows in Figure 5.3 (b).

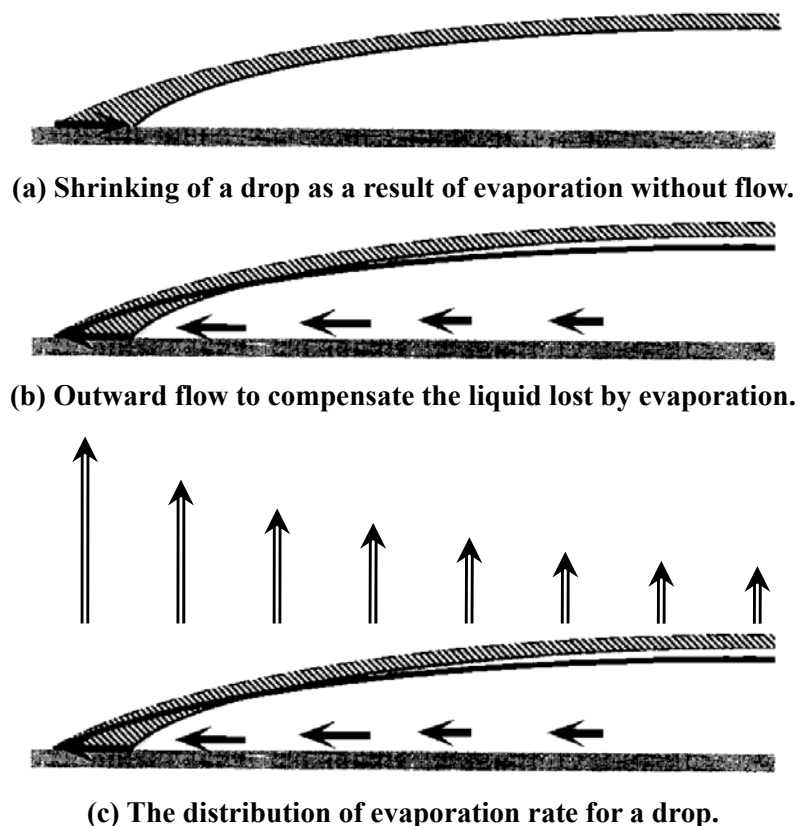


Figure 5.3: An increment of evaporation viewed in a drop cross-section ^[154].

A qualitative analysis by altering the morphology of the ring deposit was done^[155-156]. Since evaporation is the driving mechanism, different deposits can be produced by changing the evaporation rate distribution. Figure 5.4 shows the schematic of the three evaporation profiles and corresponding images of the resulting deposit. The shaded portions of drops indicate the amount of liquid removed at a given radius. In Figure 5.4 (c), when the evaporation profile is such that no liquid leaves from the boundary and no ring is formed.

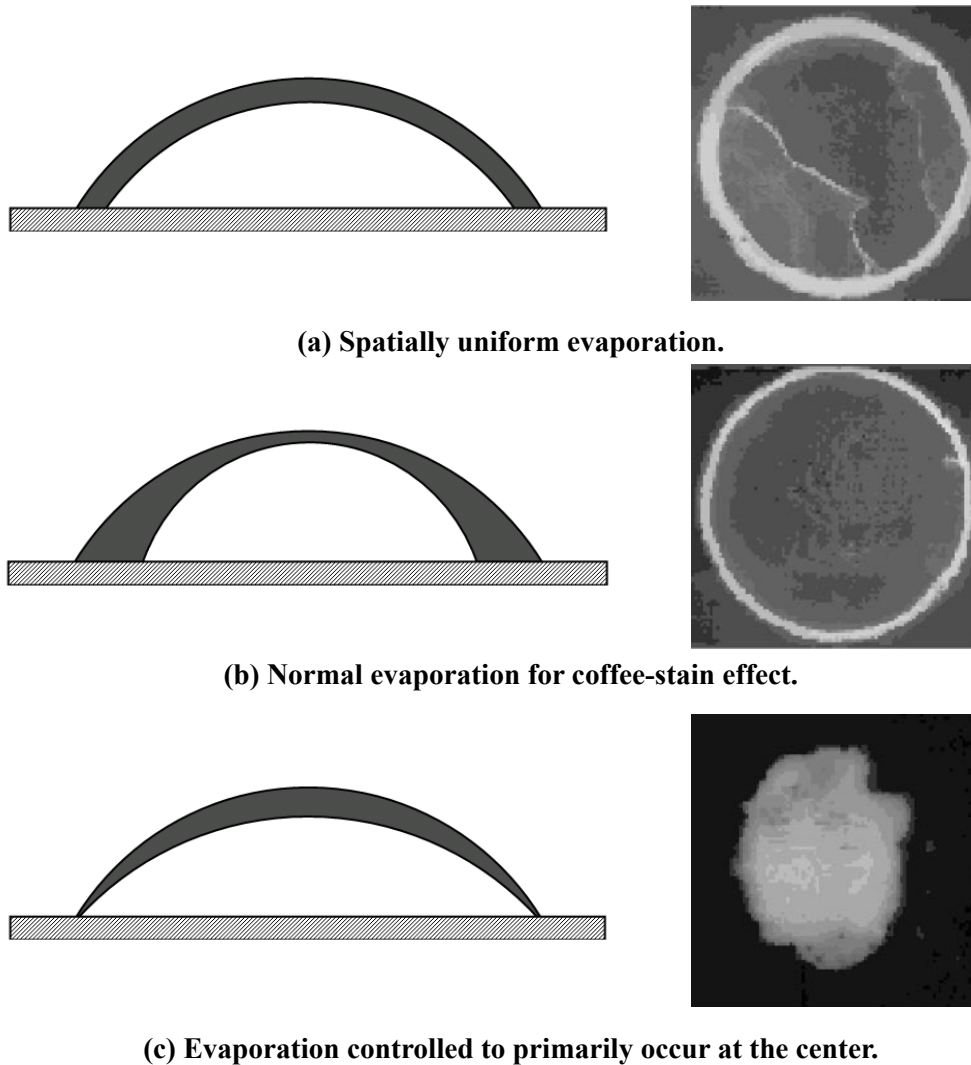


Figure 5.4: Images of the resulting deposit under three evaporation conditions^[155-156].

The outward flow of solute particles is independent of the nature of solute. The size of the solute particles should be small enough, so that sedimentation of these particles does not occur. Moreover the DoD inkjet printed droplet is so small that the surface tension is dominant and the gravitational effects are neglected. The balance of surface tension and gravitational force is accounted by the *Bond number* (Bo):

$$Bo = \frac{\rho g R h_0}{\sigma} \quad (5.1)$$

where ρ is the density of the liquid, g the gravitational constant, R the radius of the drop on the substrate, h_0 the maximum height of the drop before drying and σ the surface tension of the liquid.

5.2.2.2 Selected Factors Concerning Drop Dynamics

(1) Impact Energy of the Drop

When a drop impacts a solid surface, its spherical shape is changed into disc form due to spreading. The amount of spreading depends on the balance between driving and resisting forces. The driving force for impact spreading is the kinetic energy of the drop. The flow resistance is due to the viscosity and surface tension of the liquid^[157].

The relative magnitudes of the kinetic and surface energies can be expressed with the *Weber number*:

$$We = \frac{\rho v^2 d_0}{\sigma} \quad (5.2)$$

where ρ is the liquid density, v the impact velocity, d_0 the droplet diameter before impact and σ the surface tension. For larger Weber number ($We > 1$), the kinetic energy of the drop is able to overcome the surface tension of the liquid and thus spreading takes place. For low Weber number such as at low impact velocity, the drop does not change its shape if no wetting takes place ^[157].

(2) Drop Viscosity

The effect of viscosity on the drop spreading can be assessed by the *Reynolds number*:

$$Re = \frac{\rho v d_0}{\mu} \quad (5.3)$$

where ρ is the liquid density, v the impact velocity, d_0 the droplet diameter before impact and μ the liquid viscosity. For large Reynolds number ($Re > 4000$), the liquid has low viscosity and thus the droplet kinetic energy is large enough to overcome the viscous resistance. This leads to the spreading of the drop upon impact ^[157]. On the contrary, low Reynolds number shows that the liquid has high viscosity and the kinetic energy of the drop has minimal effect on the drop. This reduces the spreading of the drop on impact with the substrate.

(3) Drop Velocity

Drops leaving the nozzle are bound by a minimum velocity because a minimum pressure is required to overcome the pressure, P_n , developed by surface tension at the nozzle tip given by ^[158]:

$$P_n \approx \frac{2\sigma}{R_n} \quad (5.4)$$

where R_n is the radius of the nozzle and σ the surface tension of the liquid.

The pressure to overcome surface tension is generated by the inertia of the liquid drops given by ^[158]:

$$P_n \approx \rho V_d^2 \quad (5.5)$$

where ρ is the density of the liquid and V_d the velocity of the drop.

Finally if the friction in the nozzle is neglected, the typical minimum velocity of the drops as they leave the nozzle, $V_{d\min}$, can be obtained by solving the above two equations ^[158]:

$$V_{d\min} \approx \sqrt{\frac{2\sigma}{\rho R_n}} \quad (5.6)$$

(4) Drop Spreading Ratio

Drop spreading ratio is defined as the ratio of maximum spread diameter and the initial droplet diameter, given as below:

$$\text{Drop Spreading Ratio} = \frac{d_m}{d_0} \quad (5.7)$$

where d_m is the maximum diameter of the drop after spreading and d_0 the diameter of the drop before spreading.

(5) Contact Angle

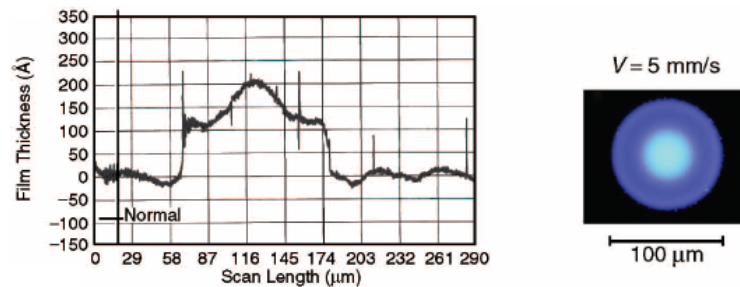
When a liquid does not spread on a substrate, a contact angle is formed which is defined as the angle between liquid-substrate interface at the contact line. A contact angle of 0° results in full wetting, while an angle less than 90° results in spreading and an angle greater than 90° indicates that the liquid tends to shrink away from the substrate. Hence oxygen-plasma surface treatment of the substrate is done before inkjet printing. This wets the surface and renders negative charge to it and thus decreases the contact angle of PEDOT:PSS drop with ITO substrate to less than 90° , as discussed at length in Chapter 3. If the influence of kinetic energy of the drop is negligible, the drop will spread due to capillarity to its equilibrium contact angle. Therefore drop spreading ratio can be considered as a function of contact angle only.

(6) Surface Tension

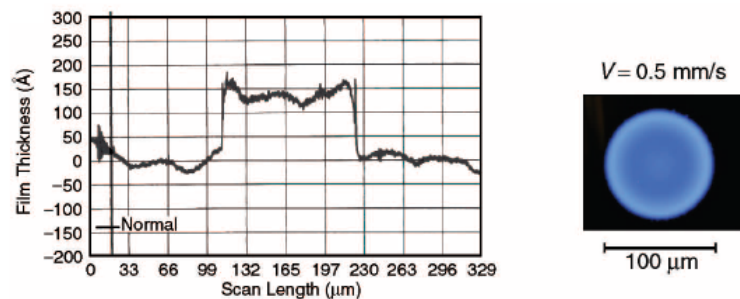
Surface tension is an internal force due to an imbalance in molecular forces that occurs at the liquid-substrate interface. The force is due to the tendency of all materials to reduce their surface area. The result of this force directs the surface wettability and contact angle between the drop and substrate. With the increase of the substrate temperature, surface tension will decrease accordingly. Hence the solute particles tend to move away from each other and then increase the deposition at the droplet perimeter.

5.2.2.3 Example for Drop Drying

An example of a drying inkjet printed droplet is provided by Shimoda et al. who varied the evaporation rate of solvent by changing the velocity of the XY-moving table that carries the substrate. The droplets that were used have a volume of $\sim 20\text{pL}$ at a standoff of 0.3mm . Figure 5.5 shows the effect of drying condition on thickness and luminescence of printed blue light-emitting polymer films. At the higher velocity of 5mm/s , polymer solute tends to stay in the center of the droplet as its evaporation time is shortened due to the faster air flow around the droplet generated by the higher velocity. Before solute has time to move to the edge, the drop has already dried. At the lower velocity of 0.5mm/s , solute is carried to the edge of the droplet forming rings as drying is slower ^[152].



(a) Higher velocity of 5mm/s : solute tends to stay in the center.



(b) Lower velocity of 0.5mm/s : solute carried to the edge.

Figure 5.5: Effect of drying condition on thickness and luminescence of blue light-emitting polymer films ^[152].

5.3 Experimental

From this section onwards, we started to explore and present the drying characteristics of the drops produced by drop-on-demand (DoD) inkjet printer. These characteristics in application of drop dispensing were discussed at the end. Equipment and materials used in the experiment were first introduced as below.

5.3.1 Equipment

(1) The DoD inkjet printer used to print drops is a Litrex 80.L inkjet printing system supplied by Litrex Co., introduced in Section 4.2.2.1 of Chapter 4.

(2) The print-head that was used is a Spectra SX3 print-head supplied by Dimatix Inc., introduced in Section 4.2.2.2 of Chapter 4.

(3) The instrument used to measure surface topography of dried droplets is a WYKO NT1100 optical profiling system produced by Veeco Instruments Inc., introduced in Section 4.2.2.3 of Chapter 4.

5.3.2 Materials

(1) The material used as ink in the Litrex 80.L inkjet printing system is an aqueous dispersion of the intrinsically conductive polymer - PEDOT:PSS (Baytron[®] P VP CH 8000) with a concentration of 2.5% by weight, supplied by H. C. Starck Inc.

Table 5.1: Brief characteristics of PEDOT:PSS (Baytron® P VP CH 8000).

Form	Odor	Color	Boiling Point T_b (°C)	Density at 20°C D_ρ (g·cm⁻³)
Liquid	Weak/Odorless	Blue	~100	~1.0
pH at 20°C	Solid Content by Weight C_w (%)		Viscosity μ (mPa·s)	Resistivity (dry) ρ (10⁵·Ω·cm)
1.2 ~ 1.8	2.5 ~ 3		9 ~ 20	1 ~ 3

(2) The substrate used in this research for actual printing of droplets was 0.7mm thick ITO coated glass with sheet resistance of 11.7Ω/□ from Merck Display Technologies Ltd. The glass substrates are cleaned and modified by oxygen-plasma surface treatment using a Trion Sirius plasma etching system before inkjet printing.

5.4 Results and Discussion

After ensuring that the jetted drops are consistent in droplet volume, velocity and direction at the same ejection conditions from Litrex 80.L DoD inkjet printer, we examined the variation of dried droplet profiles with respect to substrate temperature. The WYKO NT1100 optical profiling system based on white light interferometry (WLI) was used to capture images of these dried droplets and to analyze the relevant properties.

5.4.1 Profile of Printed Droplets after Drying

Representative images of dried droplet three-dimensional profile and two-dimensional

cross-sectional profile with a top-down view of the position where the droplets are sectioned are shown in Figure 5.6 to Figure 5.13. In order to get the two dimensional cross-sectional profile of these droplets, we took a section through their center using the WLI machine's built-in software. Any data collected is the average of at least six different droplets.

From the profile of printed droplets with respect to temperature, we can see three distinct types of effects that different temperatures can have on the profile of printed droplets. We classify these three different types of shapes that are achievable with different temperatures as: (1) Gaussian shape, (2) transition shape, and (3) ring-like shape.

5.4.1.1 Gaussian Shape

As can be inferred from the name of this type, the profiles that are obtained look like that of a simple cap. The first three temperatures of 25°C, 30°C, and 35°C give such a shape, as shown in Figure 5.6 to Figure 5.8 respectively.

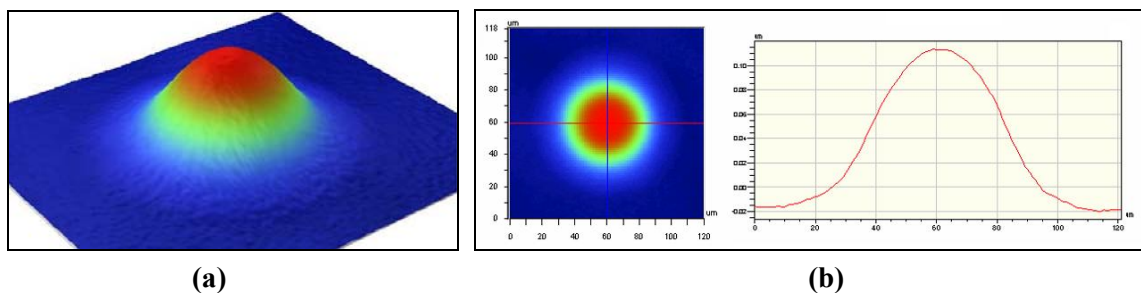


Figure 5.6: (a) 3D image at 25°C; (b) Top-down view & 2D cross-sectional profile at 25°C.

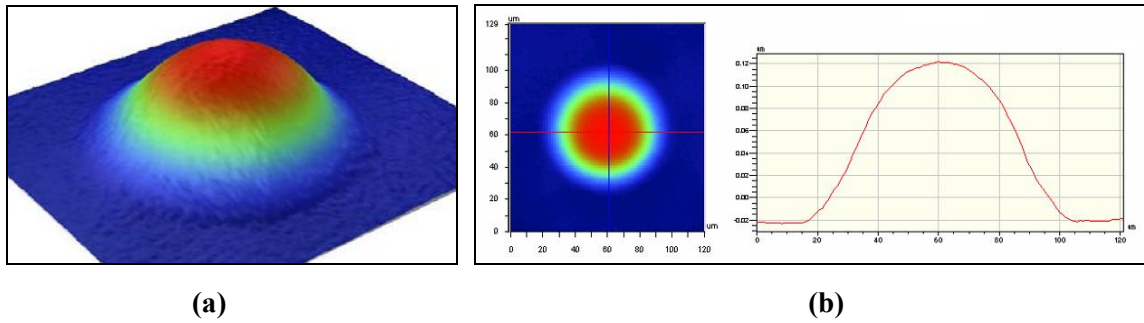


Figure 5.7: (a) 3D image at 30°C; (b) Top-down view & 2D cross-sectional profile at 30°C.

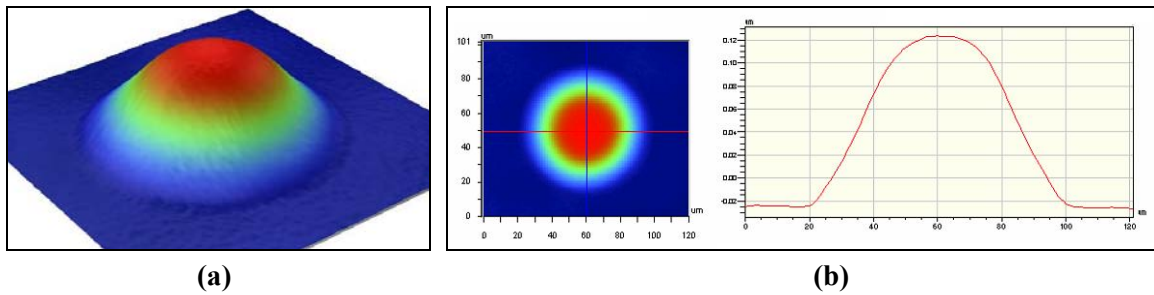


Figure 5.8: (a) 3D image at 35°C; (b) Top-down view & 2D cross-sectional profile at 35°C.

5.4.1.2 Transition Shape

As the name implies, droplet profiles that are obtained at these temperatures start to show a transition from Gaussian shape to the formation of a ring-like shape. The dried drop surface tends to become flat. Temperatures at which this takes place in the experiment are 40°C and 45°C, as shown in Figure 5.9 and Figure 5.10 respectively.

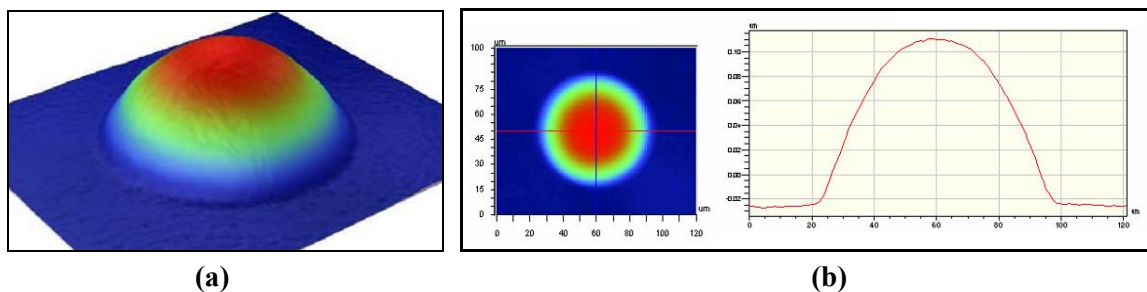


Figure 5.9: (a) 3D image at 40°C; (b) Top-down view & 2D cross-sectional profile at 40°C.

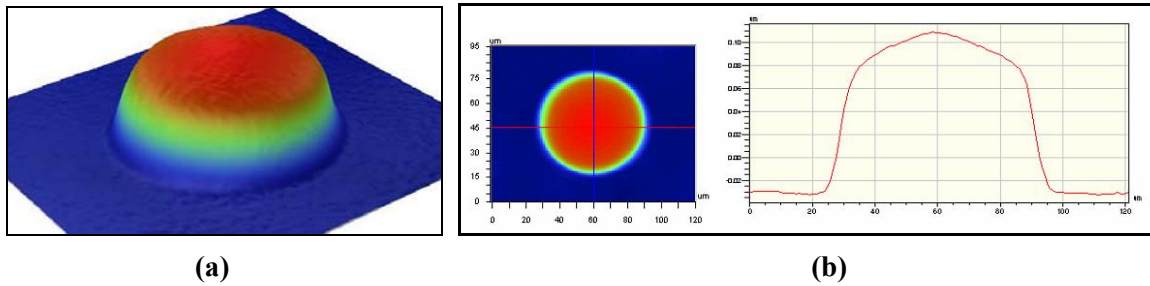


Figure 5.10: (a) 3D image at 45°C; (b) Top-down view & 2D cross-sectional profile at 45°C.

5.4.1.3 Ring-Like Shape

The droplet profiles that are obtained at these temperatures showed a distinct ring-like pattern starting to be formed with higher edges and lower centers. Temperatures at which this happens are 50°C, 55°C, and 60°C, as shown in Figure 5.11 to Figure 5.13 respectively.

In Figure 5.13, we see that part of the profile along circled vertical sections is missing. This is because the droplet wall along those sections is too steep and hence there is no reflected light. Therefore, no interference fringes are produced. This is a limitation of the optical profiler based on WLI.

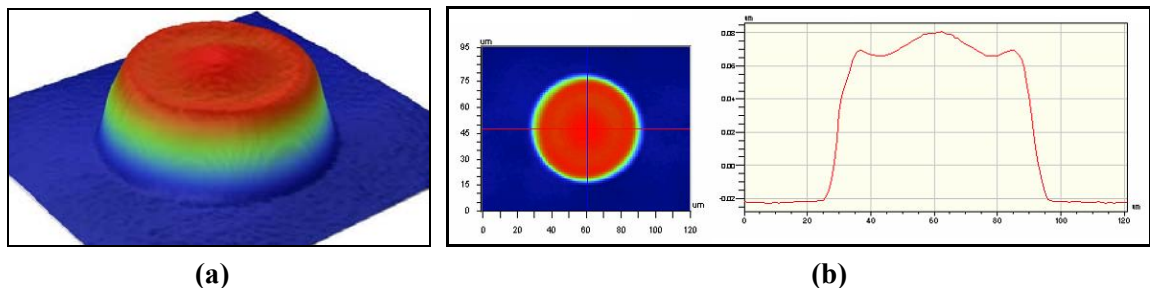


Figure 5.11: (a) 3D image at 50°C; (b) Top-down view & 2D cross-sectional profile at 50°C.

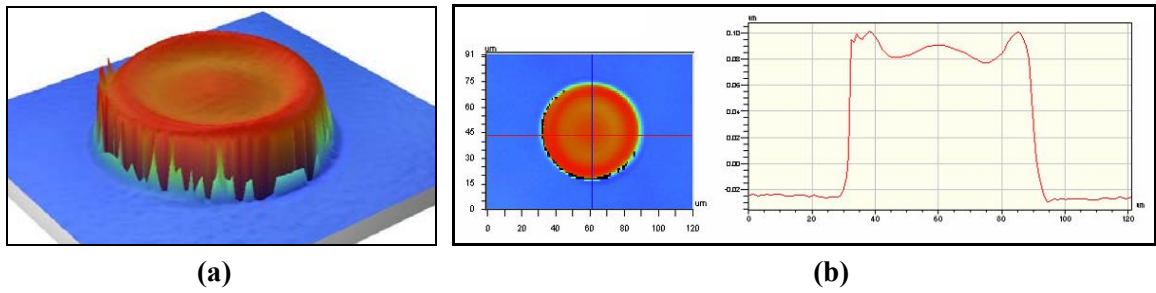


Figure 5.12: (a) 3D image at 55°C; (b) Top-down view & 2D cross-sectional profile at 55°C.

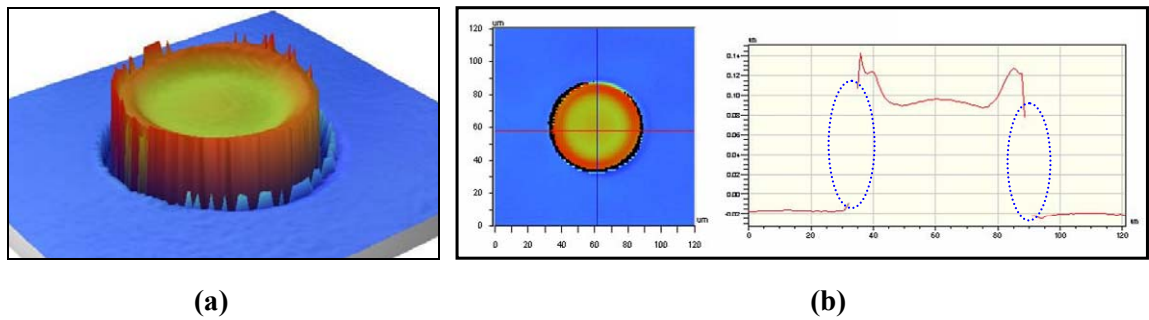


Figure 5.13: (a) 3D image at 60°C; (b) Top-down view & 2D cross-sectional profile at 60°C.

Figure 5.14 shows a summary of different droplet shapes that are achievable at different substrate temperatures. Droplet profiles are listed corresponding to substrate temperatures along the diagonal direction and three different types of dried droplet shapes are also indicated in the figure.

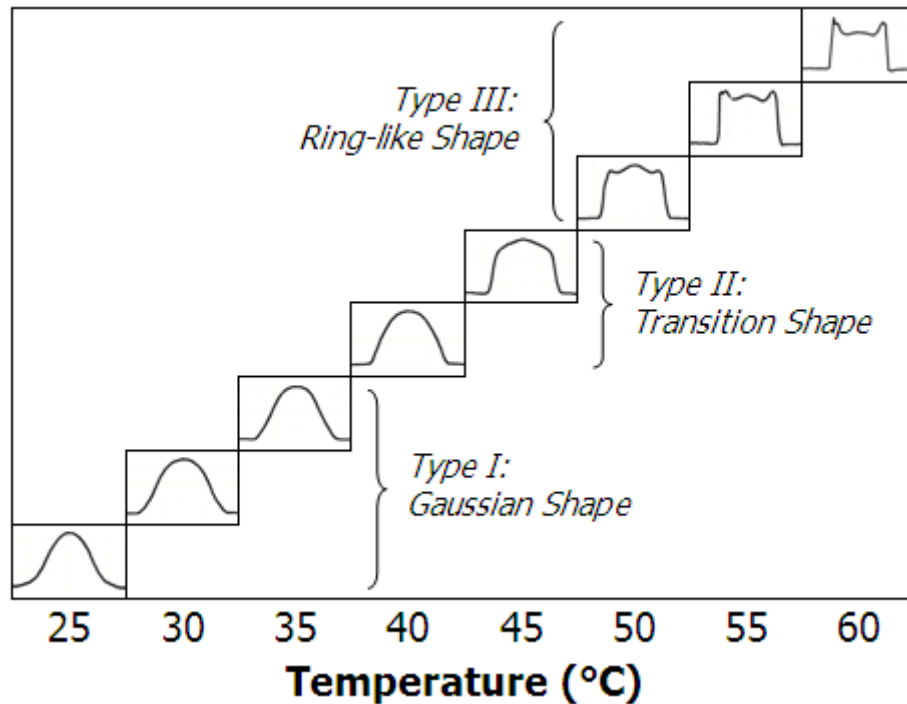


Figure 5.14: Summary of the variation of droplet shape with substrate temperature.

5.4.1.4 Coffee-Stain Effect

As mentioned in the Section 5.2.2, a so-called coffee-stain effect may produce the formation of a ring-like shape. Let's recap the evaporation rate distribution theory from Deegan et al. ^[153-156] for the explanation of this phenomenon. The theory states that an outward flow of liquid is produced in a drying drop due to the inconsistent evaporation flux distribution on a droplet surface. When droplet contact line is pinned due to the presence of surface irregularities, liquid that is removed through evaporation at the boundary must be replenished by this flow from the interior. This flow is capable of transferring the solute particles to the contact line and thus producing the high-perimeter concentration of solutes. A schematic of such a process is re-drawn in Figure 5.15.

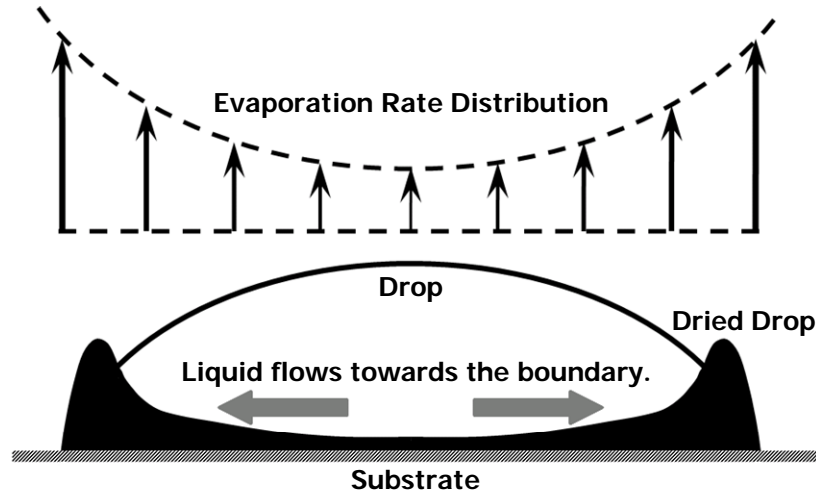


Figure 5.15: Schematic showing a liquid flow in the evaporation rate distribution theory.

5.4.1.5 A Contradiction

From the droplet profiles obtained, we can see that, at higher temperatures starting from 50°C, ring-like formation starts to take shape. This could be an observation of coffee-stain effect mentioned earlier. From what we have described earlier, we can reasonably infer that, with faster drying rate regardless of droplet size, less materials can be carried to the edge of a drying droplet. Therefore, the ring shape that is formed will become more indistinct or there is no ring formation at all, as the material does not have time to move distance to the edge before drying takes place.

For our case, as substrate temperature increases, it would mean a faster drying rate. There should be little or no movement of solutes to the edge of the droplet. Therefore, there should be little or even no ring formation and hence no coffee-stain effect. However, what we observed actually contradicts what is predicted from the

evaporation rate distribution theory and even other researcher's findings^[152]. We see that, at higher temperatures above 50°C, ring-like formation starts to take place and at low temperatures such as below 40°C, dried droplets are approximately spherical caps without the formation of rings. Furthermore, for droplets at higher temperatures, those that formed ring-like structures are thinner and more obvious. The bulk of materials are still taken up by the main body of dried droplets.

5.4.1.6 An Explanation

We are able to see the coffee-stain effect because the drop has finished the spreading stage and is transiting into its liquid equilibrium state shape. The drop then settles down to complete its drying stage. In short, the coffee-stain effect can take place only when the drop drying rate is not quite high. The rapid drying rate and the small volume of a droplet will most likely result in the droplet retaining its original shape. Murata et al. even found that small inkjet droplets dry immediately upon landing^[159]. Therefore, for droplets subjected to extremely high evaporation rate, we may get the case where the drop is dried at the moment upon impact, or the drop is dried anywhere during the spreading. Such a drop will retain the shape where it dries up.

We can imagine a process at low temperature as follows. Once a super fine drop impacts on the substrate, a splashing process occurs immediately. Materials from the droplet center accumulate at the droplet edge. After the splashing, part of the mass at

the edge flows back to the center due to gravitational force and surface tension till that drop forms a nearly spherical surface shape. This happens with the spreading of droplet, after which droplet shape will become stable during drying. Hence, in our case, a possible explanation of “ring” formation would be that droplets at higher temperatures above 50°C are dried immediately upon impact before droplet spreading or even initial inertial spreading can occur. Owing to the small size of the droplets, the evaporation rate at higher temperatures is so rapid that droplets splash and simply solidify on impact. As the splashing leads to the droplet center going down with its edge coming up, ring-like structures are then retained during the solidification.

To sum up, from the different profiles obtained at different temperatures, we dare to infer that, at lower temperatures between 25°C and 35°C, drops finish their spreading stages before drying. Hence, the profiles obtained are of Gaussian shapes. However, there is no or little occurrence of the coffee-stain effect as fine droplets are dried up before that effect could happen. At temperatures between 40°C and 45°C, we begin to see a change in shape of dried profiles. This could be due to the comparatively higher evaporation rate that prevents droplets from spreading fully before they are dried. At higher temperatures between 50°C and 60°C, we see that ring-like shapes start to form. We conclude that this is not due to the coffee-stain effect, but due to the immediate drying of impact droplet during the splashing without spreading.

5.4.2 Variations of Drop Profile Properties with Substrate Temperature

5.4.2.1 Variation of Droplet Width

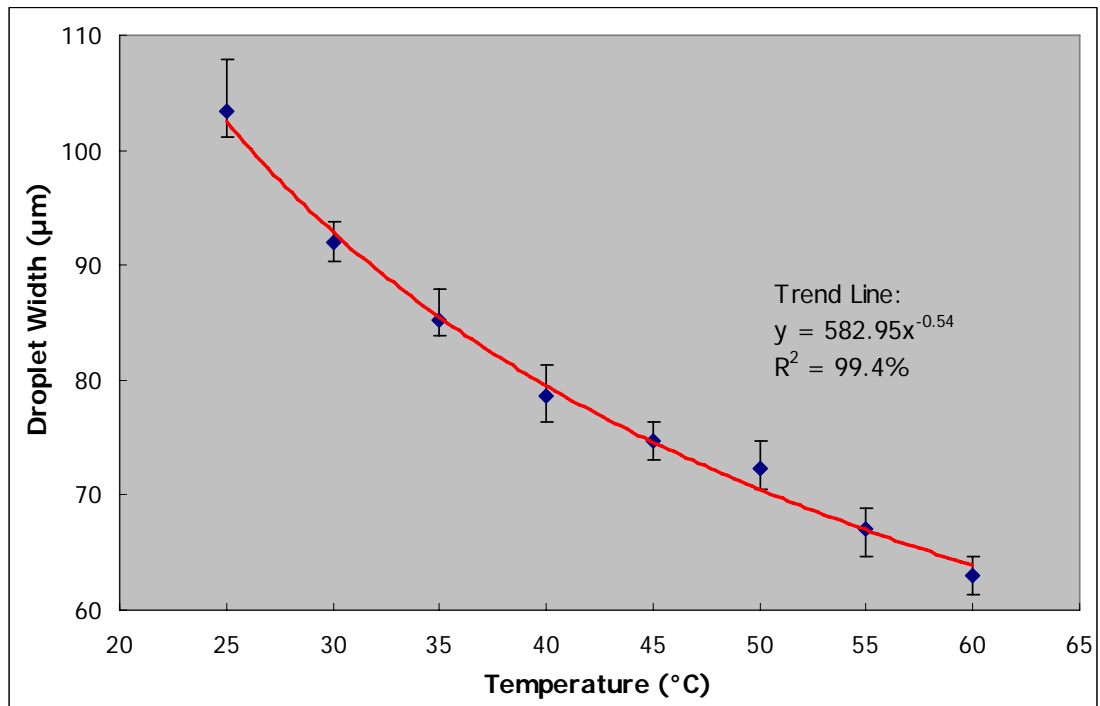


Figure 5.16: Variation of droplet width with substrate temperature.

Variation of droplet width with respect to substrate temperature is summarized and given in Figure 5.16. The width is the maximum diameter of drop spreading area after drying. The curve fitting was done and the regressed trend line of the droplet width (W) with temperature (T) follows a power function as:

$$W = 582.95T^{-0.54} \quad (5.8)$$

and $R^2 = 99.4\%$, which is very close to one, representing an excellent fit. R^2 is the coefficient of determination in statistics that will give some information about the goodness of fit of a model. In regression, R^2 is a statistical measure of how well the

regression line approximates the real data points. An R^2 of 1.0 indicates that the regression line perfectly fits the data.

From the graph, we see that droplet width decreases with respect to rise in temperature of the substrate. This can be attributed to the fact that droplet dries faster and has less time to spread due to the increase in temperature. Using the empirical analysis we can predict the width or maximum diameter of a dried droplet dispensed by inkjet printing.

5.4.2.2 Variation of Droplet Center Height

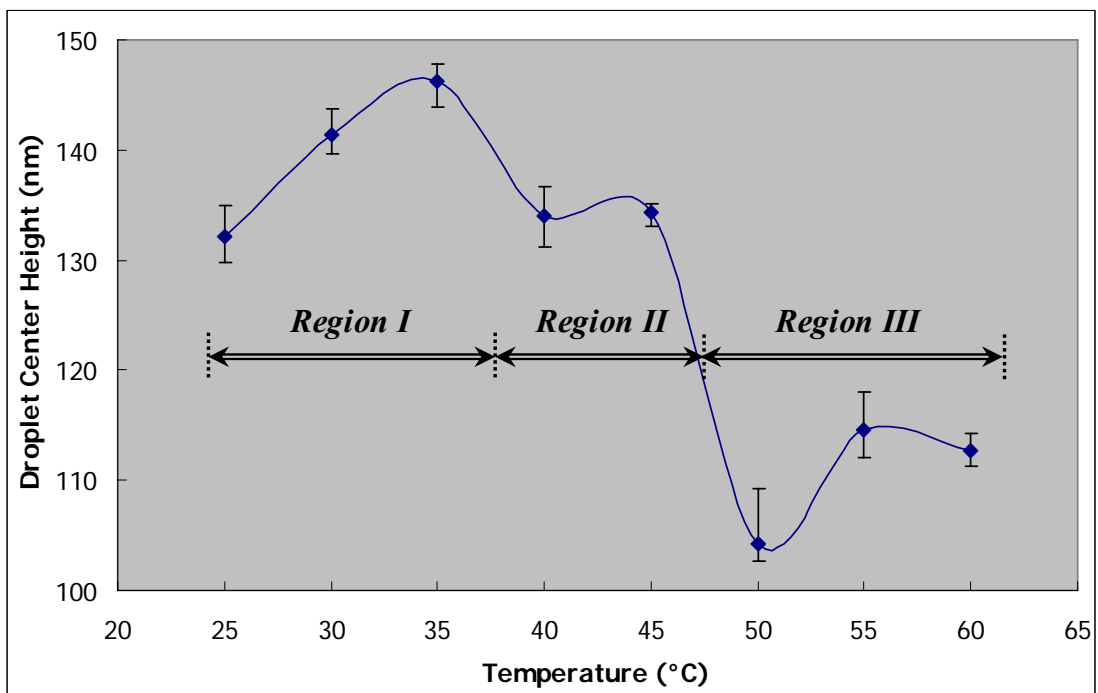


Figure 5.17: Variation of droplet center height with substrate temperature.

In Figure 5.17, we see the variation of droplet center height with respect to substrate

temperature. Droplet center height is basically the height of a droplet from its middle point. It may not be the highest point within the droplet.

From the graph, there seems to be no discernable trend. However, as we have stated before and also indicated in the figure, these droplets can be divided into three temperature regions corresponding to three types of droplet profiles. For the first three temperatures in Region I, heights are generally higher than those in the other two regions. This could be due to the better spread and formed droplets and lower evaporation rates, i.e. lower drying rate, that do not result in the formation of ring-like structures as stated in the previous section. Hence, there is almost no mass accumulated at the edge and then the measured heights are generally larger. In this region, the center height increases with an increase in temperature due to the decrease of width for the same dried droplet volume. The next two temperatures in Region II give a lower center height as droplets start to transit into the ring-like profile and some center materials accumulate towards the edge. This resulted in a decrease of droplet center height. In Region III, the splashing process is dominant with the formation of ring-like shape. This results in more materials from the droplet center being distributed to the droplet edge. At low temperature materials accumulated at the edge will flow back towards the center during the spreading after splashing. However, at such a high temperature region, rapid drying rate prevents the droplet from spreading and “freezes” the droplet during the splashing. Therefore, in Region III, droplet center height is decreased sharply and keeps the lowest.

5.4.2.3 Variation of Droplet Edge Angle

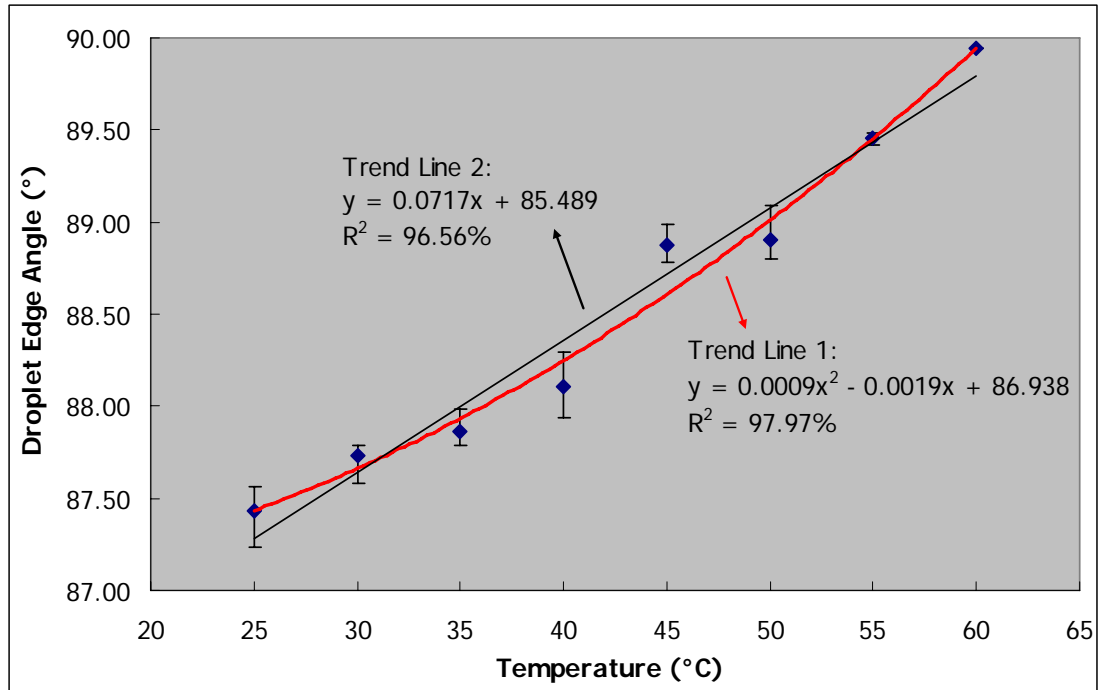


Figure 5.18: Variation of droplet edge angle with substrate temperature.

Variation of droplet edge angle with respect to substrate temperature is as shown in Figure 5.18. The edge angle is just the approximated internal angle that one side of the profile makes with the horizontal, i.e. the substrate. This is similar to the gradient of sides of a droplet. In our results, we have converted droplet edge angle into the angle that we see on the profile plots to make graphical representation easier. They are not actual angles that droplet edge makes with the substrate. However, the trend that they follow will be the same. The droplet edge angle (θ) with substrate temperature (T) fits in accordance with second order polynomial equation as:

$$\theta = 0.0009T^2 - 0.0019T + 86.938 \quad (5.9)$$

and $R^2 = 97.97\%$, which is close to one, representing a good fit. However, we still found the coefficient of the second order term is relatively close to 0 and thus a linear

fitting was also done as a comparison, given as:

$$\theta = 0.0717T + 85.489 \quad (5.10)$$

and $R^2 = 96.56\%$, which is also close to one, representing a good fit. Hence, we may consider droplet edge angle varies in a rough linear relation with drying temperature.

From the figure, we can see that the gradient of droplet side increases with substrate temperature. As discussed previously, as temperature increases, evaporation and drying take place faster. Therefore, this trend could be due to the fact that droplet does not have sufficient time to spread to its final equilibrium shape before drying. The liquid front that is still spreading and moving outwards from the center ‘freezes’ in mid motion, producing steep walls and hence a higher gradient. For drops that dried immediately upon impact at higher temperatures, their walls are almost vertical.

5.4.3 Drop Dispensing

The three drop dispensing stages may be used for varying the width and height of the dried drops according to the classification and analysis of droplet profiles addressed in previous sections. These three stages are named as: (1) Gaussian stage, (2) transition stage, and (3) ring-like stage, corresponding to the temperature regions I to III respectively mentioned in Section 5.4.2.2 (see Figure 5.17). They may fabricate dried drops with varying dimensions for various applications in potential.

(1) Gaussian Stage

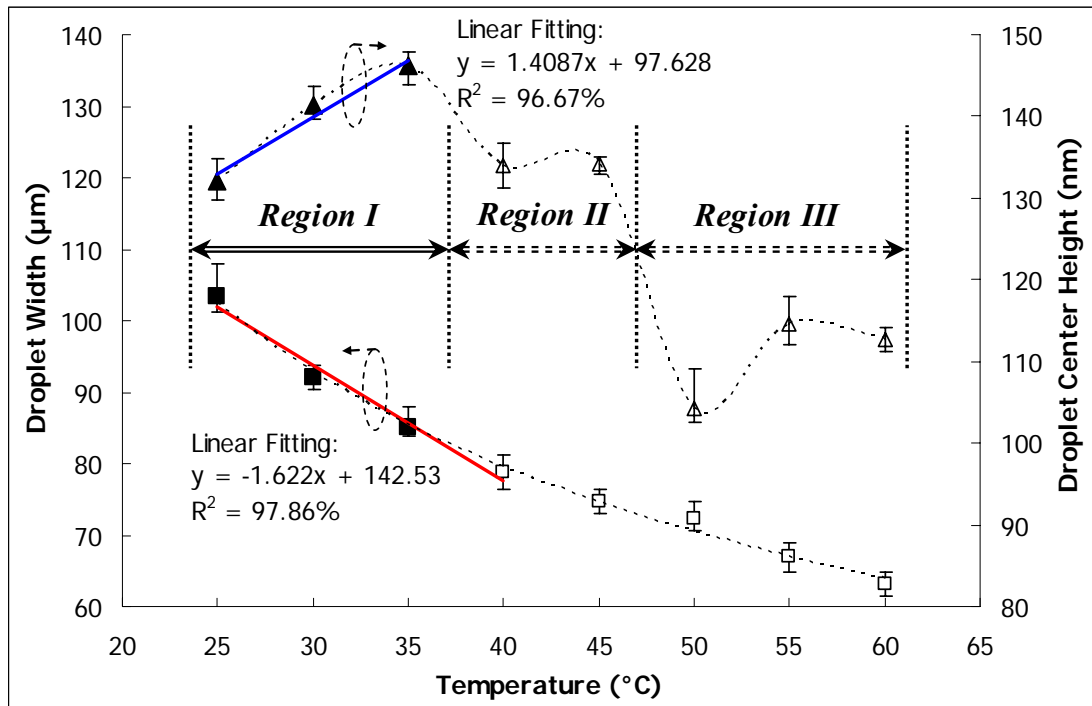


Figure 5.19: Linear fittings of the droplet width and height with substrate temperature after drying in Gaussian Stage.

In the Gaussian stage (Region I) as shown in Figure 5.19, with the same print-head nozzle size, the width of the dried droplets is nearly in a negative linear relation to the substrate temperature. Although the relationship between the droplet width and temperature is given by Equation (5.8) with more accuracy ($R^2 = 99.4\%$), we still use linear fitting here for the purpose of simplification. In contrast, the center height of dried drops has a positive linear relation with substrate temperature. Using their empirical equations, the maximum diameter of the dispensed drops can be controlled as desired after drying in this stage. Apparently the drops of Gaussian shape have a great influence on the surface morphology of uneven thin films that are formed by these printed drops. Such influences will in turn affect the final device performance

due to the variation of effective surface contact area, as discussed in Chapter 4.

(2) Transition Stage

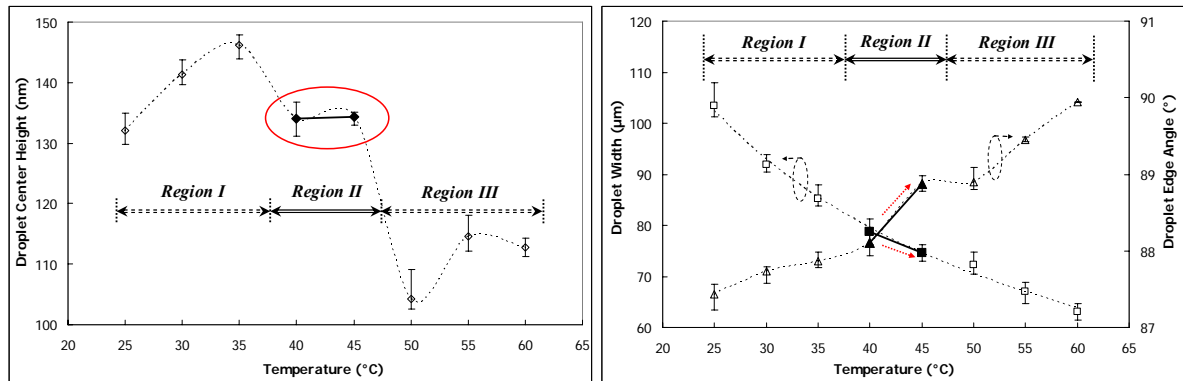


Figure 5.20: Variations of dried droplet properties in Transition Stage: (a) Drops keep similar height after drying; (b) Droplet width and edge angle vary in the inverse direction.

Under the transition stage (Region II in Figure 5.20) the width of the dried droplets can be varied without significant change in the height of the droplets as indicated in Figure 5.20 (a). With the increase of the droplet width, the droplet edge becomes sharper and sharper as shown in Figure 5.20 (b). As a result, a line with well-defined sharp edge may be obtained as well in this stage. Figure 5.21 shows such an example.

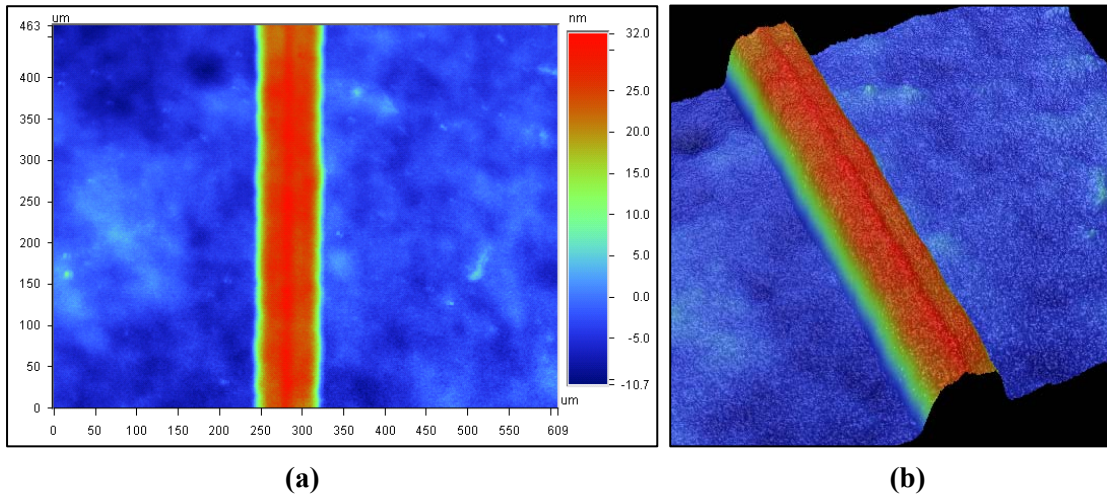


Figure 5.21: An example of dried single line with sharp edge at 45°C in Transition Stage:
(a) Top-down view; **(b)** 3D image.

(3) Ring-Like Stage

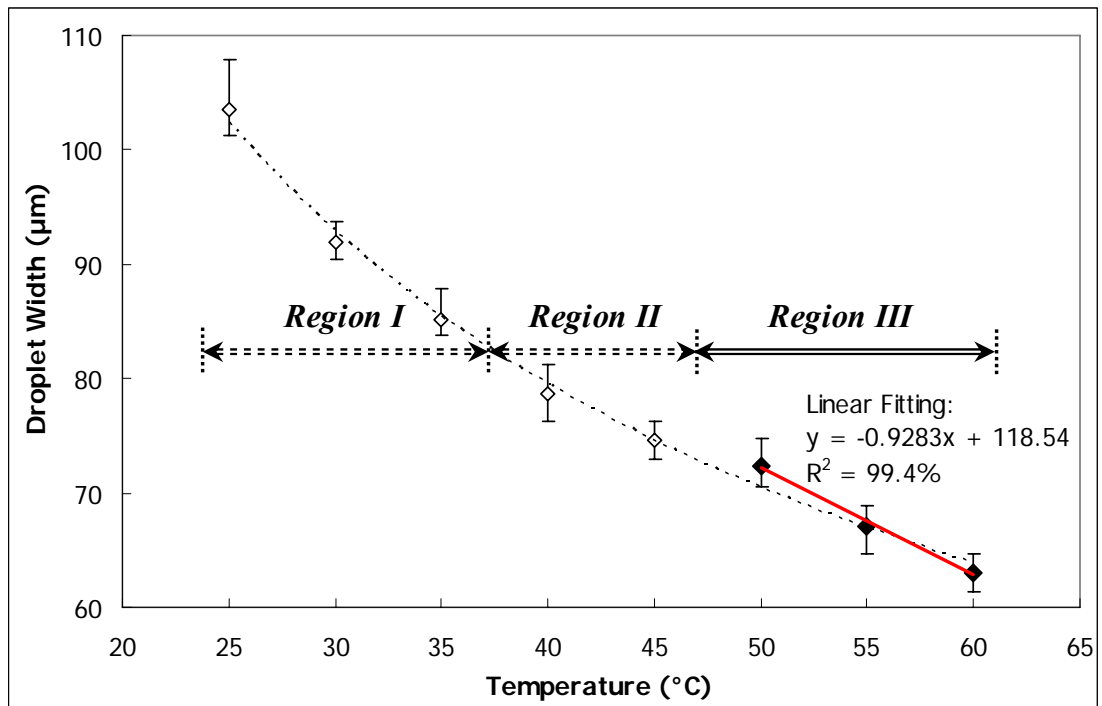


Figure 5.22: Linear relation of the droplet width with temperature in Ring-Like Stage.

The ring-like stage was indicated as Region III in Figure 5.22. From the figure, it can be seen that it has a good linear relationship between the droplet width and the substrate temperature ($R^2 = 99.4\%$). In this stage, drops are dried immediately upon

impact on the substrate. Thus it is difficult to control the droplet height, but dried drops usually have very sharp edges. We may take advantage of the hollow central base of the dried drop with the size control to print another material inside it in potential for various applications, such as micro-ring wells for cell culture and micro-ring scaffolds for tissue growth. An example of P-OLEDs based on micro-rings was employed by Khillan et al ^[160]. However, the existing problem is that it is difficult to obtain a uniform luminance from such OLED devices, especially in the low resolution case.

5.5 Conclusion

(1) Drop Drying Behavior

For super fine droplets, such as those less than 10pL, due to their very large surface-to-volume ratio, the drying rate is extremely high and drying behavior is extremely sensitive to substrate temperature. Under different range of temperatures, dried droplet shapes that are achievable can be categorized into three types: Gaussian shape, transition shape, and ring-like shape corresponding to low temperatures (<40°C), medium temperatures, and high temperatures (>50°C) respectively. The formation of ring-like structures at high temperatures is not from the coffee-stain effect, but from the splashing effect upon impact. During the change of droplet shapes, there exists an appropriate range of temperatures to obtain a good dried inkjet printed droplet shape with sharp edges and flat surface. Results from this experiment would

serve as a reference to achieve uniform film with a flat surface and a well-defined edge after droplet drying and has potential to be applied in the modeling of drop drying behavior.

(2) Drop Dispensing

In accordance with the classification of droplet profiles after drying, three stages of drop dispensing are named as: Gaussian stage, transition stage, and ring-like stage. In the Gaussian stage, linear relations of the droplet width and height with the substrate temperature are found. The former is negative and the latter positive. In the transition stage, the droplet width may be varied without significant change in the height and with a sharp edge formed. In the ring-like stage, the droplet width can be still controlled in the linear variation with temperature. Micro-rings formed by dried drops may have various applications in different fields such as the fabrication of cell culture plates and tissue scaffolds.

CHAPTER 6

REPRESENTATION AND MAPPING OF DRIED DROPLET PROFILES

6.1 Introduction

As discussed in Chapter 5, substrate temperature has a great influence on the formation of droplet shapes during drying. Different drying temperature will result in a series of various dried droplet profiles. These variations will have an effect on the surface morphology of printed thin films formed by dried drops. It will in turn affect the performance of final products to various extents. Hence examination of the profiles for printed drops after drying would be giving us an understanding of how the product performance is affected. With successful characterization, it would enable future research to set desirable printing parameters for the required drop shape forms.

In this chapter, *normalized* profiles of dried drops are of interest to us due to the fact that normalized data are independent of units of measurement, thus allowing underlying characteristics of actual dried droplet shapes to be compared. Shape representation and mapping of these profiles with substrate temperature were investigated using a method based on classical radial basis function network (introduced in Section 6.2). Two types of radial basis functions were carried out in order to conduct a comparison. The effectiveness of the models were evaluated and

discussed at the end.

6.2 Model of Radial Basis Function Networks

6.2.1 Basic Theory

The model of *radial basis function network* (RBFN) was first introduced in the solution of the real multivariate interpolation problem ^[161]. It takes a different approach by viewing the design of an *artificial neural network* as a curve fitting (i.e. approximation) problem in a high dimensional space. Currently it is still one of the main fields of research in numerical analysis. RBFN can be treated as a universal approximation in that any continuous function on a compact interval can in principle be well approximated or interpolated with arbitrary accuracy by a sum of the form of *radial basis functions* (RBF), if a sufficiently large number of RBFs are selected ^[162-165]. However, it may not always be desirable to obtain an exact interpolation as it may give rise to an over-fitting problem. In this section, we shall motivate the use of RBFs from the viewpoint of function approximation.

RBFN is a simple single hidden layer type of neural network, with the RBFs taking on the role of the activation functions of the network. RBF is a real-valued function whose value depends only on the radial distance from some point $\boldsymbol{\mu}$, called a *center*, so that the form of RBF (φ) can be written as:

$$\varphi(\mathbf{x}) = h(\|\mathbf{x} - \boldsymbol{\mu}\|) \quad (6.1)$$

where \mathbf{x} is the input vector variable, $h(\cdot)$ is the basis function used. The radial distance is usually Euclidean distant, although other distance functions are also possible. The typical architecture of a generalized RBFN is shown in Figure 6.1.

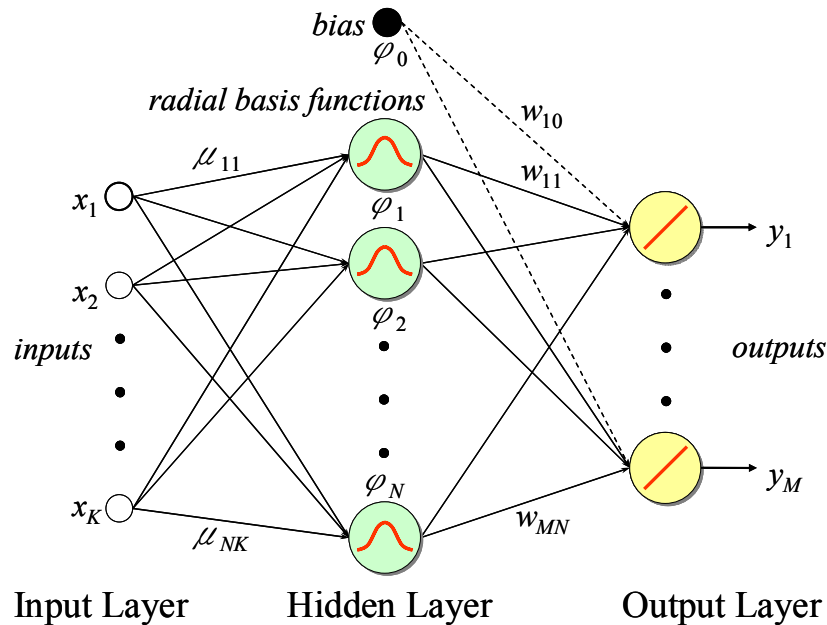


Figure 6.1: Architecture of a generalized radial basis function network. Each radial basis function φ_n ($n = 1, 2, \dots, N$) acts like a hidden unit. The line connecting the input x_k ($k = 1, 2, \dots, K$) to φ_n represents the corresponding element μ_{nk} of the center with the vector μ_n . The line connecting φ_n to the output unit y_m ($m = 1, 2, \dots, M$) represent the weight w_{mn} . An extra bias unit is shown with a constant activation function φ_0 (typically $\varphi_0 = 1$) to connect the outputs.

It can be seen that there are three layers in such an RBFN in its basic form, named as input layer, hidden layer, and output layer, respectively. The input layer consists of all source units to connect network to the ‘environment’. The only hidden layer in the network is made up of the RBF units with radial activation functions, which apply a nonlinear transformation from the input space to the hidden space. The dimension of the hidden space is directly related to the network capacity to approximate a smooth mapping between input and output; the higher the dimension of the hidden space, the

more accurate the approximation will be ^[162]. Often an extra bias unit with constant activation function (typically $\varphi_0 = 1$) is introduced in the hidden layer to improve network performance. The output layer supplies the response of the network to the input. It is fully connected to the hidden layer. It is the linear combination of RBFs with the *weights* (w_{mn}) as activation function coefficients.

In accordance with the network construction as shown in Figure 6.1, we shall write the RBFN mapping to build up function approximation in the form as:

$$y_m(\mathbf{x}) = \sum_{n=1}^N w_{mn} \varphi_n(\mathbf{x}) + w_{m0}, \quad (m = 1, 2, \dots, M) \quad (6.2)$$

where \mathbf{x} is the K -dimensional input vector, the φ_n 's are the radial basis functions, and the w_{mn} 's are the output layer weights connecting to the hidden layer. It is often to absorb the bias weights w_{m0} into the summation by assigning an extra basis function φ_0 with a constant value of 1, yielding:

$$y_m(\mathbf{x}) = \sum_{n=0}^N w_{mn} \varphi_n(\mathbf{x}), \quad (m = 1, 2, \dots, M) \quad (6.3)$$

Recall that RBFs are a class of functions whose key feature is that the distance from a center determines their response as implied by Equation (6.1), rewritten as below with a minor modification to coincide with Equation (6.2) and (6.3):

$$\varphi_n(\mathbf{x}) = h(\|\mathbf{x} - \boldsymbol{\mu}_n\|) \quad (6.4)$$

where $\boldsymbol{\mu}_n$ is the vector of the centers corresponding to the RBF φ_n in the hidden layer.

Most commonly used RBF is the Gaussian basis function, which has a form in the

RBFN as follows:

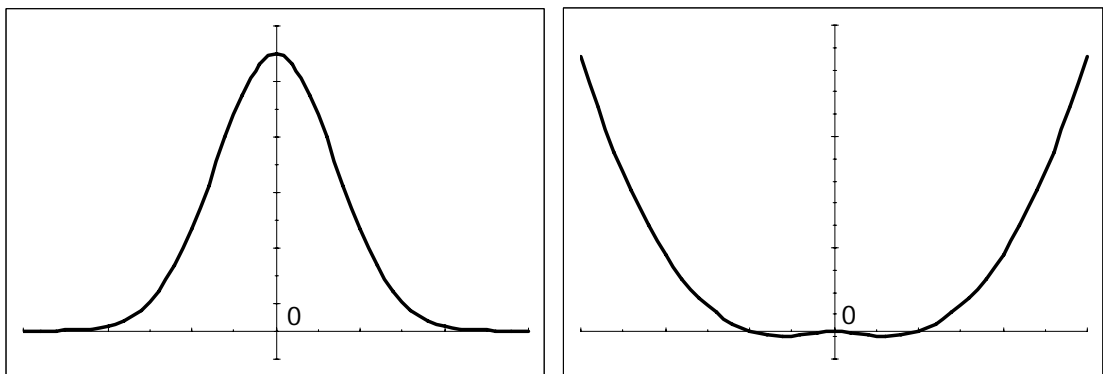
$$\varphi_n^G(\mathbf{x}) = h^G(\|\mathbf{x} - \boldsymbol{\mu}_n\|) = \exp\left(\frac{-\|\mathbf{x} - \boldsymbol{\mu}_n\|^2}{2\boldsymbol{\sigma}_n^2}\right) \quad (6.5)$$

where the vector $\boldsymbol{\sigma}_n$ is the *width* parameter (i.e. the standard deviation) for Gaussian basis function φ_n whose value can control the smoothness property of the approximation. Gaussian basis function provides an example of *local* RBF that gives significant response only in a neighborhood of its centre, as illustrated in Figure 6.2

(a). Another possible RBF choice is the thin-plate spline (TPS) function, derived from the theory of function interpolation [165]. It is an unbounded function with the form as:

$$\varphi_n^{\text{TPS}}(\mathbf{x}) = h^{\text{TPS}}(\|\mathbf{x} - \boldsymbol{\mu}_n\|) = \|\mathbf{x} - \boldsymbol{\mu}_n\|^2 \ln(\|\mathbf{x} - \boldsymbol{\mu}_n\|) \quad (6.6)$$

If the radial distance is close to zero, the corresponding function value will be approaching to zero. In contrast with Gaussian, TPS provides an example of *global* RBF whose response increases monotonically with distance from the centre even if at the position of infinity, as illustrated in Figure 6.2 (b).



(a) Gaussian

(b) Thin-plate spline

Figure 6.2: Schematic of function profiles for Gaussian and thin-plate spline.

Different types of RBFs are motivated from different points of view and each may be

shown to be optimal under some applied conditions ^[166]. The abovementioned two basis functions are very different: Gaussian RBF is positive and compact; TPS RBF is global and diverges at infinity. In the thesis, these two types of RBF are selected to conduct shape representation and mapping of dried droplet profiles with a comparison.

6.2.2 Training of Radial Basis Function Networks

The purpose of training an RBFN is to determine network parameters. In RBFN as shown in Figure 6.1, network parameters include the first and second layers of connectors, which are the basis function centers μ_{nk} (where appropriate, widths σ_{nk} for Gaussian RBFs), and weights w_{mn} for the output layer. This may lead to a two-stage training procedure for the determination of network parameters. In this chapter, neural network toolbox - NETLAB developed by Nabney and Bishop ^[167] was used for training RBFN. Two-stage processing used in NETLAB for the network training was briefly described in the follow.

(1) Parameters Determination of Radial Basis Functions

In the first stage only, the input data set is used to determine the parameters of the RBFs. For Gaussian RBFs, the parameters of centers and widths are required to be chosen. However, for TPS RBFs, only the centers are required to be obtained. Centers positions are adjusted by means of the *expectation-maximization* (EM) algorithm. EM

algorithm was referred to and discussed in detail in the references [163, 165, 168-169]. Here, we skip a detailed exposition of the EM algorithm due to the direct implementation of NETLAB software. In practice, a sufficient number of iterations of EM algorithm should be set in order to make the errors stabilize (discussed later in Section 6.4.1.1). If Gaussian basis functions are used, the widths of the RBFs are then set to the largest distance between determined centers. TPS basis functions do not have a width parameter and only the centers are required to be determined.

(2) Output Weights Determination

After determination of the structure (centers and widths, if any) of the RBFs in the first stage, it is then kept fixed to determine weights for the output layer in the second stage of training. This problem can be solved using *least squares* method. We shall rewrite Equation (6.3) in the system of equations as:

$$\begin{cases} y_1(\mathbf{x}) = \sum_{n=0}^N w_{1n} \varphi_n(\mathbf{x}) = \Phi \mathbf{w}_1 \\ y_2(\mathbf{x}) = \sum_{n=0}^N w_{2n} \varphi_n(\mathbf{x}) = \Phi \mathbf{w}_2 \\ \vdots \\ y_M(\mathbf{x}) = \sum_{n=0}^N w_{Mn} \varphi_n(\mathbf{x}) = \Phi \mathbf{w}_M \end{cases} \quad (6.7)$$

Thus the corresponding matrix form can be represented as:

$$\mathbf{y} = \Phi \mathbf{W} \quad (6.8)$$

where all the symbols have the following expressions, consistent with the network structure shown in Figure 6.1:

$$\mathbf{x} = \begin{bmatrix} x_1 \\ x_2 \\ \vdots \\ x_K \end{bmatrix};$$

$$\mathbf{y} = [y_1(\mathbf{x}), y_2(\mathbf{x}), \dots, y_M(\mathbf{x})] = \begin{bmatrix} y_1(x_1) & y_2(x_1) & \cdots & y_M(x_1) \\ y_1(x_2) & y_2(x_2) & \cdots & y_M(x_2) \\ \dots & \dots & \dots & \dots \\ y_1(x_K) & y_2(x_K) & \cdots & y_M(x_K) \end{bmatrix}_{K \times M};$$

$$\Phi = [\varphi_0(\mathbf{x}), \varphi_1(\mathbf{x}), \dots, \varphi_N(\mathbf{x})] = \begin{bmatrix} \varphi_0(x_1) & \varphi_1(x_1) & \cdots & \varphi_N(x_1) \\ \varphi_0(x_2) & \varphi_1(x_2) & \cdots & \varphi_N(x_2) \\ \dots & \dots & \dots & \dots \\ \varphi_0(x_K) & \varphi_1(x_K) & \cdots & \varphi_N(x_K) \end{bmatrix}_{K \times (N+1)};$$

$$\mathbf{w}_m = \begin{bmatrix} w_{m0} \\ w_{m1} \\ \vdots \\ w_{mN} \end{bmatrix}, (m = 1, 2, \dots, M);$$

$$\mathbf{W} = [\mathbf{w}_1, \mathbf{w}_2, \dots, \mathbf{w}_M] = \begin{bmatrix} w_{10} & w_{20} & \cdots & w_{M0} \\ w_{11} & w_{21} & \cdots & w_{M1} \\ \dots & \dots & \dots & \dots \\ w_{1N} & w_{2N} & \cdots & w_{MN} \end{bmatrix}_{(N+1) \times M}.$$

Now we consider the following target values $t_m(x_k)$ ($m = 1, 2, \dots, M; k = 1, 2, \dots, K$) in the $K \times M$ matrix form \mathbf{t} , which are the desired values we would like to obtain from the network model corresponding to the input vector \mathbf{x} :

$$\mathbf{t} = [t_1(\mathbf{x}), t_2(\mathbf{x}), \dots, t_M(\mathbf{x})] = \begin{bmatrix} t_1(x_1) & t_2(x_1) & \cdots & t_M(x_1) \\ t_1(x_2) & t_2(x_2) & \cdots & t_M(x_2) \\ \dots & \dots & \dots & \dots \\ t_1(x_K) & t_2(x_K) & \cdots & t_M(x_K) \end{bmatrix}_{K \times M}.$$

In comparison with the network estimated output \mathbf{y} ($K \times M$ matrix), the error for the

network can be evaluated by root mean square error (RMSE) expressed as:

$$\text{RMSE} = \sqrt{\frac{\sum_{m=1}^M \sum_{k=1}^K (\mathbf{y}_{km} - \mathbf{t}_{km})^2}{(K \times M)}} = \|\mathbf{y} - \mathbf{t}\| / \sqrt{K \times M} \quad (6.9)$$

where $\mathbf{y}_{km} = y_m(x_k)$ and $\mathbf{t}_{km} = t_m(x_k)$. Substituting \mathbf{y} using Equation (6.8), we can obtain:

$$\text{RMSE} = \|\Phi \mathbf{W} - \mathbf{t}\| / \sqrt{K \times M} \quad (6.10)$$

Therefore, the determination of the weights matrix \mathbf{W} can be considered as the problem of minimizing the value of the network RMSE. This is a general least squares problem ^[170] and results in a least squares solution below:

$$\mathbf{W} = (\Phi^T \Phi)^{-1} \Phi^T \mathbf{t} \quad (6.11)$$

If the symbol Φ^\dagger is used to denote

$$\Phi^\dagger = (\Phi^T \Phi)^{-1} \Phi^T \quad (6.12)$$

then we have the final form of the formula:

$$\mathbf{W} = \Phi^\dagger \mathbf{t} \quad (6.13)$$

where Φ is also called a *design matrix*, and Φ^\dagger is known as the *Moore-Penrose pseudo-inverse* of the matrix Φ , which can be computed efficiently using methods from linear algebra. In our case of shape representation and mapping of dried droplet profiles, only one output vector unit is required (i.e. $M = 1$) and target values are the experimental data sets of dried droplet profiles.

6.3 Normalization of Experimental Data

In order to obtain a more convincing analysis results for general purpose, the first thing is often to initialize the experimental data obtained. This step aims to eliminate

the negative influence of data ‘noise’ during the measurement. Normalization methods are said to be invariant to changes in measurement unit of the data when they provide the same normalized values. In our experimental data, extreme values could be unreliable outliers and thus we try to avoid having extreme values overly dominate the results in the subsequent analysis. *Rescaling normalization* method is then used to conduct the preprocessing of experimental data on dried droplet profiles. The formula is written as:

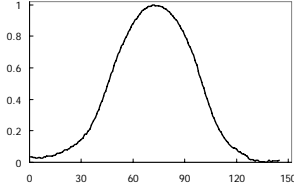
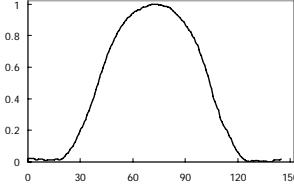
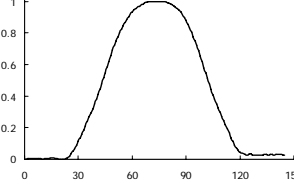
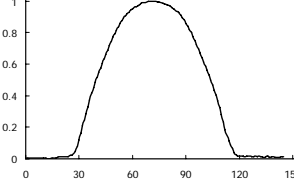
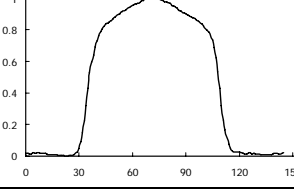
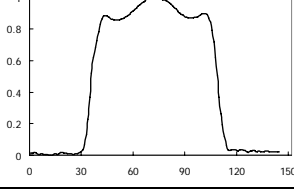
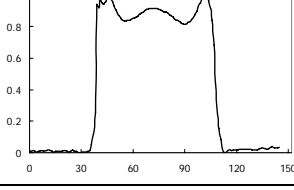
$$Z_i^N = \frac{Z_i - \min(\mathbf{Z})}{\max(\mathbf{Z}) - \min(\mathbf{Z})}, i = 1, 2, \dots \quad (6.14)$$

where \mathbf{Z} denotes the data set collected, whose elements are given by Z_i ($i = 1, 2, \dots$), such that $\mathbf{Z} = \{Z_1, Z_2, \dots\}$, and Z_i^N denotes the normalized data corresponding to Z_i . All normalized data have identical range from 0 to 1.

Equipment (drop-on-demand inkjet printing system and white light interferometer) and materials (PEDOT:PSS) used for data collection of actual dried droplet profiles are the same as described in Chapter 5. Table 6.1 and Table 6.2 summarize the normalized profiles of drying drops with the substrate temperature varying from 25°C to 60°C. Note that 60°C is the maximum temperature available from the inkjet printing system used. All 8 data sets of normalized profiles (T1 ~ T8) shown in Table 6.1 were selected for training RBF network in order to generate 8 types of typical drop drying shape representatives relating to different temperatures. Their temperature intervals cover the temperatures listed in Table 6.2. NETLAB^[167] software is used for the purpose of the network training. All 7 data sets of normalized profiles (E1 ~ E7)

shown in Table 6.2 were then used for the evaluation of the RBFN model generated.

Table 6.1: Summary of dried droplet profiles with temperature used for training RBFN.

No.	Substrate Temperature	Dried Droplet Profile (Normalized)
T1	25°C	
T2	30°C	
T3	35°C	
T4	40°C	
T5	45°C	
T6	50°C	
T7	55°C	

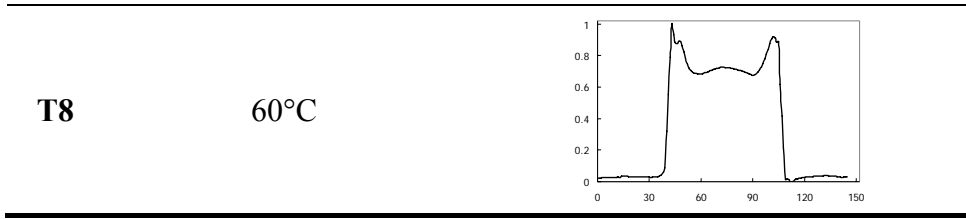
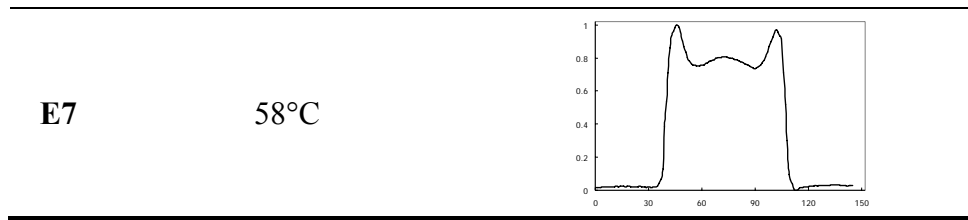


Table 6.2: Summary of dried droplet profiles with temperature used for evaluating RBFN.

No.	Substrate Temperature	Dried Droplet Profile (Normalized)
E1	28°C	
E2	32°C	
E3	38°C	
E4	42°C	
E5	48°C	
E6	52°C	



All dried droplet profile data after normalization are plotted together in Figure 6.3. It still shows that more materials will accumulate at the droplet boundary flowing from the center at higher temperature. This results in the decrease of droplet center height and the increase of the edge. The reason has been discussed at length in Section 5.4 of Chapter 5. In this chapter, shape representation and mapping are of our concern.

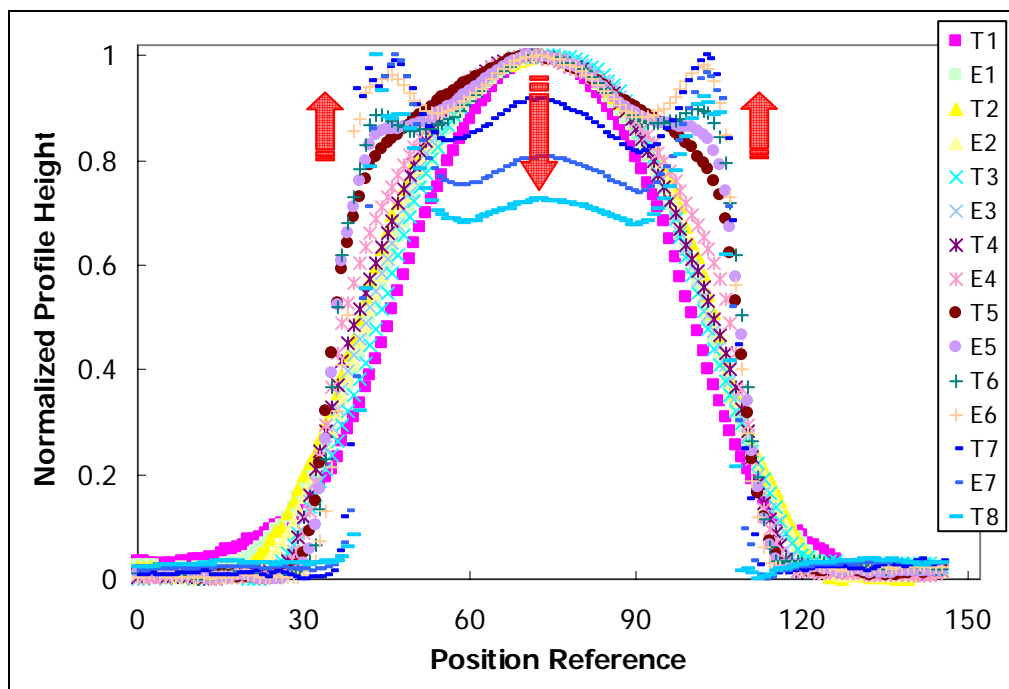


Figure 6.3: Plot of all normalized dried droplet Profiles. With the increase of drying temperature, droplet center height decreases and the edge increases.

6.4 Results and Discussion

In this section, we will focus our attention only on the analysis of *normalized* data to

show the results on the shape representation and mapping of dried droplet profiles with their drying temperatures. The profile data sets T1 ~ T8 in Table 6.1 were used for training RBF network to generate typical dried drop shapes. We trained each RBFN with its own training set. The profile data sets E1 ~ E7 in Table 6.2 were then used for evaluating the trained RBFN model.

6.4.1 Representation and Mapping of Dried Droplet Profiles

6.4.1.1 Selection of the Number of Iterations of EM Algorithm

In NETLAB toolbox, the EM algorithm is applied to estimate the structure parameters of radial basis functions in the network training. In practice we need to set a threshold to end the training. Figure 6.4 provides an example for one training data set T7. It shows the obtained generalization errors for the various numbers of iterations of EM algorithm. Error values are negative log likelihood of data. The result indicates that the EM algorithm converges quickly. In our case, no more than 30 iterations of EM algorithm were enough for errors to stabilize.

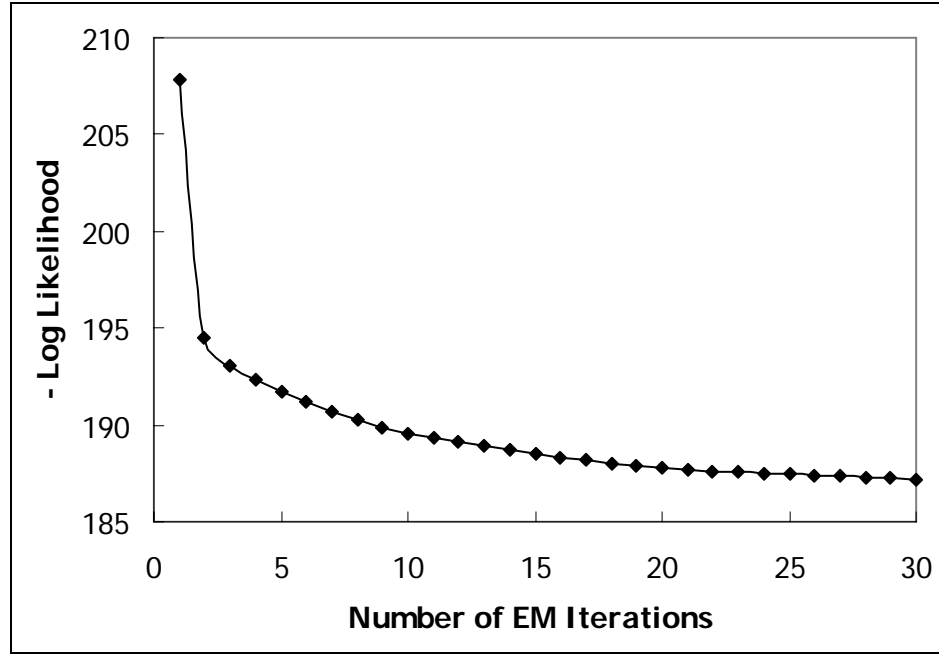


Figure 6.4: Convergence of EM algorithm for RBFN training from data set T7.

6.4.1.2 Selection of the Number of Radial Basis Functions

As mentioned in Section 6.2.1, a sum of RBFs can in principle approximate any continuous function on a compact interval with arbitrary accuracy, if a sufficiently large number of RBFs are selected. However, with the increase of the number of RBFs, approximation accuracy may not increase much but dramatic increase in time and space for computation will be expended. Therefore, we checked the variation of RMSE of network with the number of RBFs in order to give a reference of selecting the appropriate number of basis functions. Here RMSE can be simply calculated by:

$$\text{RMSE} = \sqrt{\frac{\sum_{i=1}^K (y_i - t_i)^2}{K}} \quad (6.15)$$

where K is the number of target values in one set, y_i and t_i ($i = 1, 2, \dots, K$) are the model output and target value, respectively. Each data set (T1 ~ T8) for training

network will have one RMSE obtained. The summation of these 8 RMSE values is considered as a global RMSE, whose variation with the number of RBFs is given in Figure 6.5.

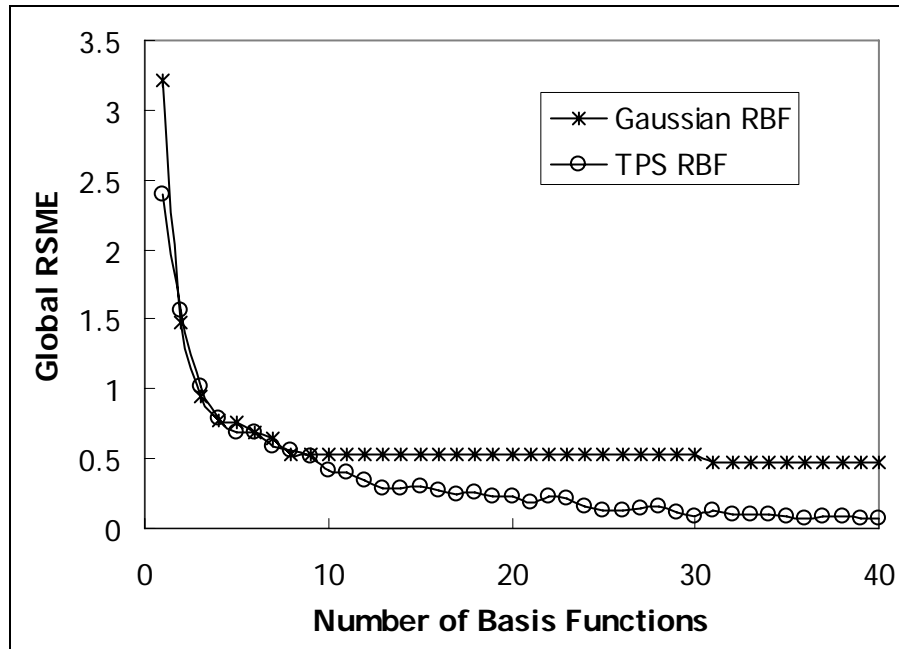
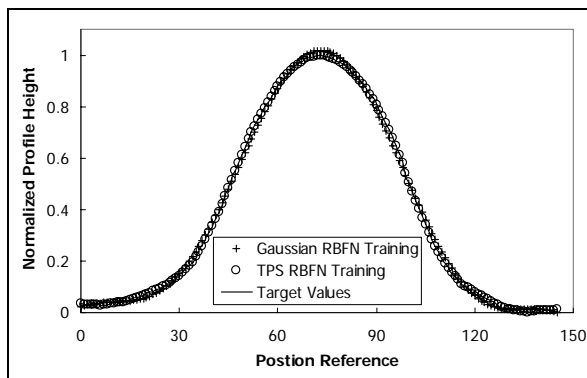


Figure 6.5: RMSE of the network with different number of RBFs.

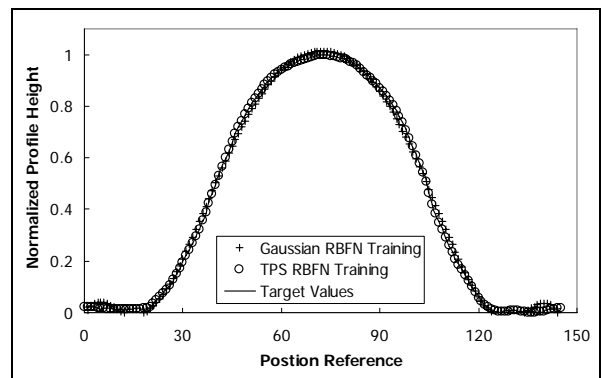
Observed from Figure 6.5, RMSE of network decreases with the increase of the number of RBFs for both Gaussian and TPS RBFN. For small number of RBFs (<10 for example), these two types of network show a similar approximation error. However, with further enlargement of RBFs, TPS RBFN exhibits a better mapping performance than Gaussian RBFN. Compared to TPS, Gaussian networks arrive more rapidly at a constant state where their RMSE remain nearly unchanged regardless of the number of basis functions. In our case, it is evident that 40 function units are sufficient for both Gaussian and TPS RBFN to stabilize the network RMSE in all the training data sets.

6.4.1.3 Shape Representation and Mapping Using RBFN

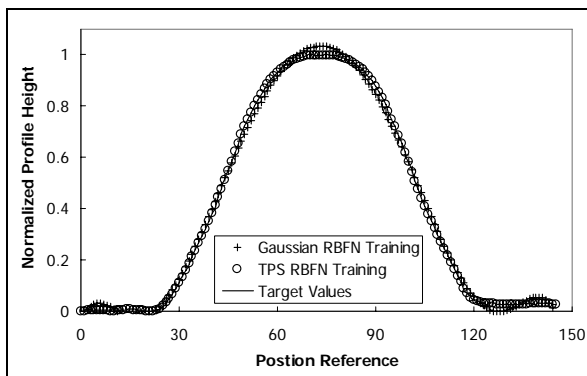
Under the above selected number of EM iterations and radial basis functions, the results of RBFN mapping for all the training data sets T1 ~ T8 are shown as below in Figure 6.6 (a) ~ (h), respectively. It can be seen that TPS RBFN exhibits an excellent approximation performance as compared to Gaussian RBFN. Gaussian RBFN tends to result in large deviations from the training data sets at high temperature as shown in Figure 6.6 (f) ~ (h).



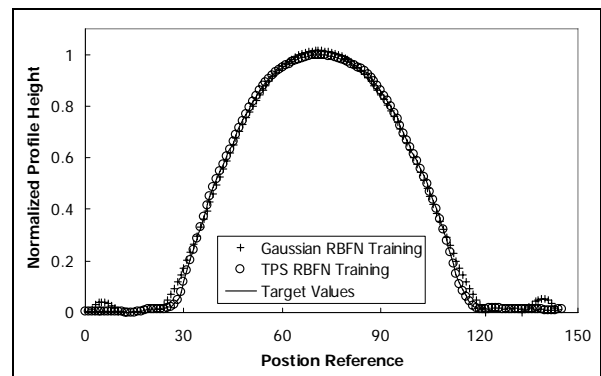
(a) Training data set T1 (25°C).



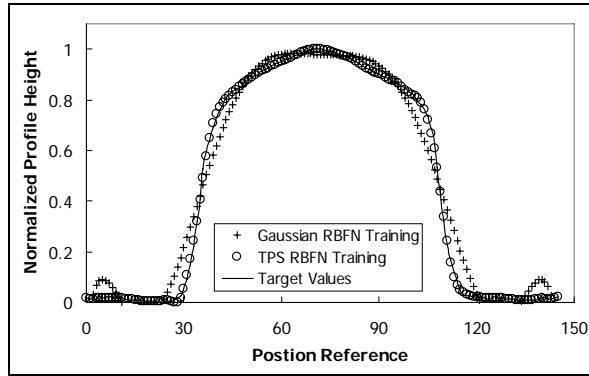
(b) Training data set T2 (30°C).



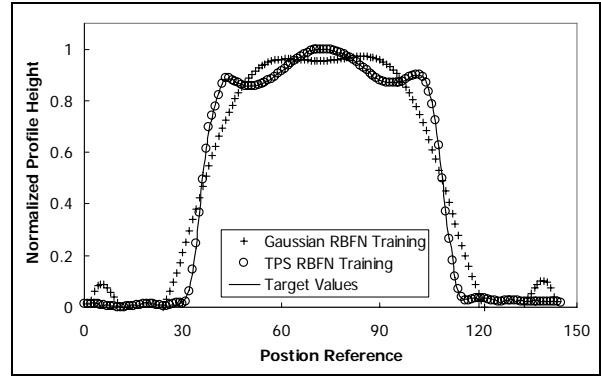
(c) Training data set T3 (35°C).



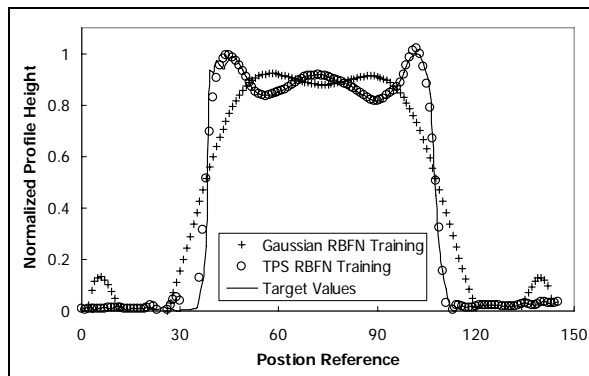
(d) Training data set T4 (40°C).



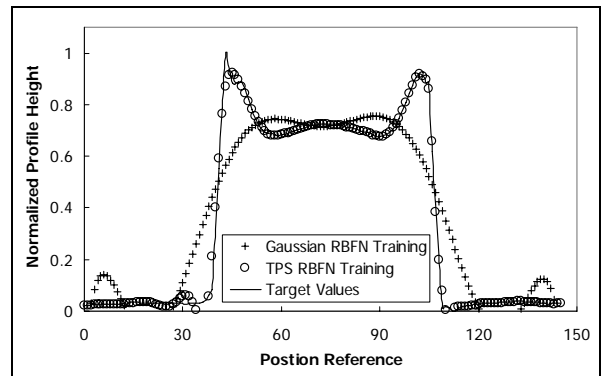
(e) Training data set T5 (45°C).



(f) Training data set T6 (50°C).



(g) Training data set T7 (55°C).



(h) Training data set T8 (60°C).

Figure 6.6: Shape representation and mapping using both Gaussian and TPS RBFN.

Table 6.3: Characteristics and comparison of Gaussian and TPS RBFN training.

Data Set No.	Drying Temperature	Gaussian RBFN Training		TPS RBFN Training	
		RMSE	R^2	RMSE	R^2
T1	25°C	0.0149	99.84%	0.0019	~100%
T2	30°C	0.0185	99.78%	0.0020	~100%
T3	35°C	0.0203	99.73%	0.0014	~100%
T4	40°C	0.0278	99.52%	0.0019	~100%
T5	45°C	0.0693	97.37%	0.0071	99.97%
T6	50°C	0.0920	95.43%	0.0048	99.99%
T7	55°C	0.1458	88.68%	0.0402	99.14%
T8	60°C	0.1444	83.88%	0.0221	99.62%

Note: R^2 less than 95% may give an unsatisfactory result.

The related RMSE and R^2 values between the trained RBFN outputs and target values are listed in Table 6.3. R^2 is the coefficient of determination which is a statistic that measures the goodness of fit of a model. It is given by the formulae below:

$$R^2 = 1 - \frac{SS_{error}}{SS_{total}},$$

$$SS_{error} = \sum_{i=1}^K (y_i - t_i)^2, \quad (6.16)$$

$$SS_{total} = \sum_{i=1}^K (t_i - \bar{t})^2, \text{ with } \bar{t} = \frac{1}{K} \sum_{i=1}^K t_i.$$

where SS_{total} is the total sum of squares, SS_{error} is the sum of square errors, and \bar{t} is the mean of the target values.

Consistent with the direct visualization from Figure 6.6, Table 6.3 shows that TPS RBFN has better mapping performance with smaller network RSME and higher statistical model accuracy than Gaussian RBFN for all the training data sets. At low temperature ($<40^\circ\text{C}$), dried droplet profile appears in the simplex Gaussian shape. Both Gaussian and TPS RBF networks can return excellent mapping accuracy in terms of R^2 statistic giving values greater than 99%. However, at high temperature ($>50^\circ\text{C}$) a rather complex profile arises for dried drops. Both types of network start to show different mapping behaviors and only the TPS RBFN gives fairly good shape representation. Judging from Figure 6.6 and Table 6.3, network mapping output is highly convincing when the corresponding R^2 reaches the value greater than 95%. If R^2 is around 95%, network output may provide a passable but not outstanding mapping, such as Gaussian RBFN mapping result shown in Figure 6.6 (f). It is evident that Gaussian RBFN exhibits poor mapping results with R^2 values of only

89% and 84% as shown in Figure 6.6 (g) and Figure 6.6 (h), respectively.

6.4.2 Evaluation of Generated RBFN Models

In this section, we used profile data sets E1 ~ E7 in Table 6.2 to evaluate the RBFN models trained in the previous section. Evaluation is implemented in two aspects: (1) At a given temperature listed in Table 6.2, compare its profile estimated by the network model with the corresponding experimental profile; (2) At a given profile shown in Table 6.2, compare its drying temperature estimated by the network model with the corresponding experimental temperature.

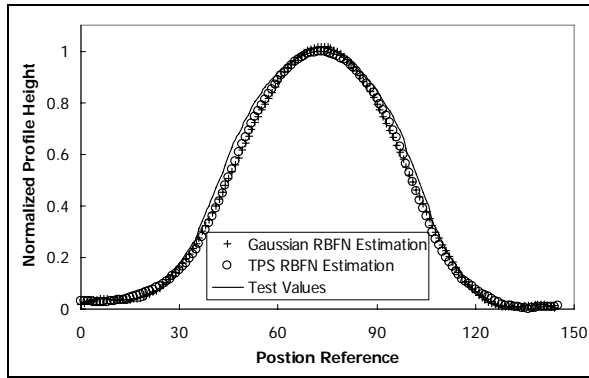
6.4.2.1 Estimation of Dried Droplet Profile at Given Temperature

From the training of RBFN, we have obtained 8 distinct sets of shape mapped to different temperature (T1 ~ T8). In order to estimate dried droplet profile at a given temperature, we shall first determine which interval of two adjacent mapped temperatures involves the given temperature. We are then able to estimate profile by linear interpolation using the profile data sets of determined two mapped temperatures. Table 6.4 illustrates the procedure of the proposed algorithm.

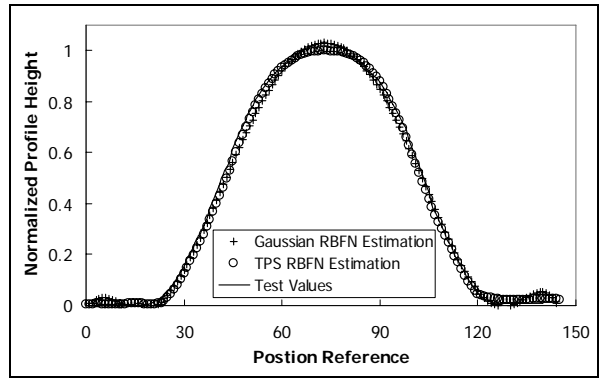
Table 6.4: Procedure for estimation of dried droplet profile at given temperature.

-
- (0). Let the vector set $\{\mathbf{P}_1, \mathbf{P}_2, \dots, \mathbf{P}_8\}$ denotes mapped profiles consisting of all 8 sets of RBFN training outputs in correspondence with the ascending temperatures T_1, T_2, \dots, T_8 . Assume temperature T is given to estimate its corresponding profile \mathbf{P} .
- (1). Compare T with the element in the temperature set $\{T_1, T_2, \dots, T_8\}$ to determine its location in the set. Assign counter $i \leftarrow 1, 2, \dots, 8$:
- If $T = T_i$, then $\mathbf{P} = \mathbf{P}_i$ and go to Step (3). Otherwise, continue to Step (2).
- (2). If else $T_i < T < T_{i+1}$, then do the following linear interpolation:
- $$\mathbf{P} = (T_{i+1} - T) \cdot \mathbf{P}_i + (T - T_i) \cdot \mathbf{P}_{i+1}.$$
- (3). Output the profile \mathbf{P} as the estimation result and calculate RMSE and R^2 as quality characteristics.
-

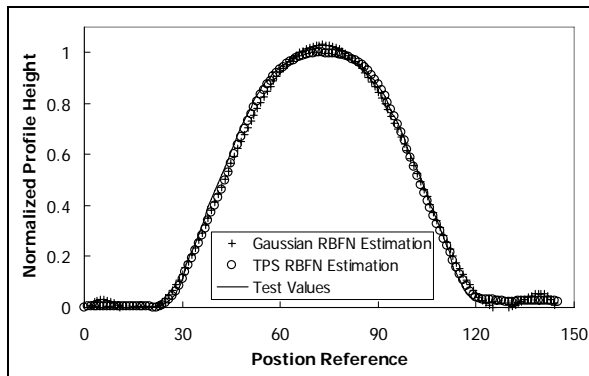
Results of the estimated shape from RBFN in comparison with the shape from data sets E1 ~ E7 are shown in Figure 6.7 (a) ~ (g), respectively. Compared to Gaussian RBFN, TPS RBFN exhibits a more effective performance for estimation. This is also demonstrated by the error data (RMSE and R^2) tabulated in Table 6.5.



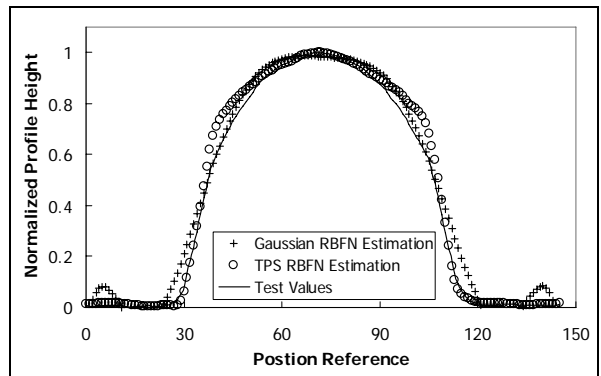
(a) Evaluation data set E1 (28°C).



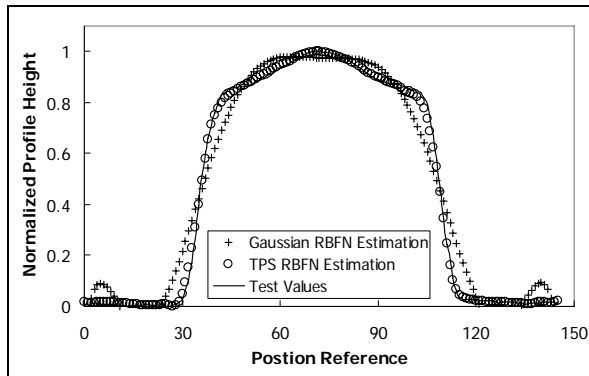
(b) Evaluation data set E2 (32°C).



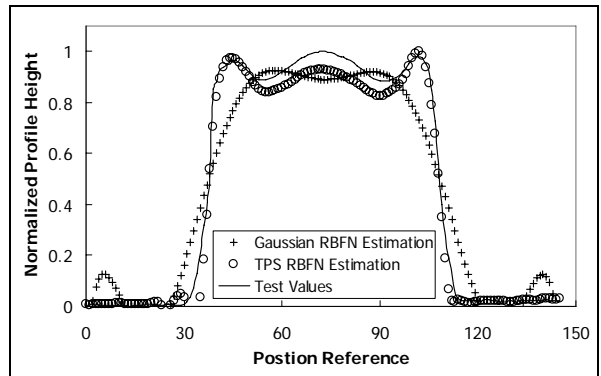
(c) Evaluation data set E3 (38°C).



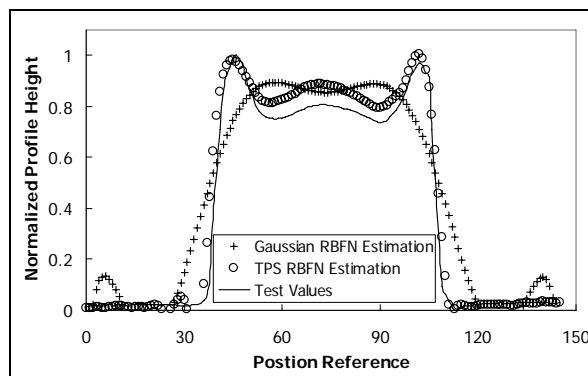
(d) Evaluation data set E4 (42°C).



(e) Evaluation data set E5 (48°C).



(f) Evaluation data set E6 (52°C).



(g) Evaluation data set E7 (58°C).

Figure 6.7: Shape estimation using both Gaussian and TPS RBFN.

Table 6.5: Characteristics and comparison of Gaussian and TPS RBFN estimation.

Data Set No.	Substrate Temperature	Gaussian RBFN Estimation		TPS RBFN Estimation	
		RMSE	R^2	RMSE	R^2
E1	28°C	0.0390	98.96%	0.0360	99.11%
E2	32°C	0.0264	99.55%	0.0197	99.75%
E3	38°C	0.0285	99.49%	0.0192	99.77%
E4	42°C	0.0546	98.24%	0.0401	99.05%
E5	48°C	0.0814	96.43%	0.0156	99.87%
E6	52°C	0.1211	92.69%	0.0499	98.76%
E7	58°C	0.1497	85.45%	0.0650	97.26%

Note: R^2 less than 95% may give an unsatisfactory result.

Table 6.5 provides RMSE and R^2 values as estimation quality characteristics for the comparison between RBFN estimation and experimental data. TPS RBFN shows a better estimation performance than Gaussian RBFN. It is evident that the estimation with R^2 of above 97% can be achieved for TPS RBF networks. Therefore, the approach based on TPS RBFN proposed is highly effective for the dried droplet shape estimation. As for the Gaussian RBF network, it works well only at low and medium given temperature (<50°C). For high temperature (>50°C), with R^2 of less than 95%, it is not suitable to conduct shape estimation. This result is also anticipated due to the poor training output of Gaussian RBFN at such a high temperature region.

6.4.2.2 Estimation of Temperature at Given Dried Droplet Profile

In this section, we shall estimate the corresponding temperature if a certain droplet profile is given. By analogy with the problem solution in the previous section, the first thing here is to find the corresponding ‘profile interval’ to ‘bracket’ such a given droplet profile. The two mapped profiles that are closest to the given profile take the role of ‘profile interval’. The decision of the ‘closest’ is based on the similarity measurement of all mapped profiles with the given profile. The given profile is then able to be represented by the two closest mapped profiles through least squares method. Such a least squares solution will return two linear coefficients. The estimation of temperature is given by linear interpolation via applying these two coefficients to the temperatures corresponding to the two closest mapped profiles determined. The procedure of the proposed algorithm is illustrated in Table 6.6.

Table 6.6: Procedure for estimation of temperature at given dried droplet profile.

(0). Let the vector set $\{\mathbf{P}_1, \mathbf{P}_2, \dots, \mathbf{P}_8\}$ denotes mapped profile consisting of all 8 sets of RBFN training outputs in correspondence with the ascending temperatures T_1, T_2, \dots, T_8 . Assume profile \mathbf{P} is given to estimate its corresponding temperature T .

(1). Calculate the Euclidean distance between \mathbf{P} and the element in the mapped profile set $\{\mathbf{P}_1, \mathbf{P}_2, \dots, \mathbf{P}_8\}$ to determine the degree of shape similarity, denoted by $\{d_1, d_2, \dots, d_8\}$. Assign counter $i \leftarrow 1, 2, \dots, 8$:

$$d_i = \|\mathbf{P} - \mathbf{P}_i\|.$$

(2). Obtain the two minimum distances from the set $\{d_1, d_2, \dots, d_8\}$. Assume d_m is minimum and d_n sub-minimum. In our case, it is often found that m and n are two contiguous indices (i.e. $|m - n| = 1$).

(3). Let $\mathbf{P} = w_1 \cdot \mathbf{P}_m + w_2 \cdot \mathbf{P}_n$, where w_1 and w_2 are linear coefficients. w_1 and w_2 are then determined using Equation (6.11) as a least squares solution, given by \hat{w}_1 and \hat{w}_2 , respectively:

$$\begin{bmatrix} \hat{w}_1 \\ \hat{w}_2 \end{bmatrix} = \left(\begin{bmatrix} \mathbf{P}_m & \mathbf{P}_n \end{bmatrix}^T \begin{bmatrix} \mathbf{P}_m & \mathbf{P}_n \end{bmatrix} \right)^{-1} \begin{bmatrix} \mathbf{P}_m & \mathbf{P}_n \end{bmatrix}^T \mathbf{P}.$$

(4). Do the following linear interpolation:

$$T = \hat{w}_1 \cdot T_m + \hat{w}_2 \cdot T_n.$$

(5). Output the temperature T as the estimation result and calculate δ as quality characteristic.

Note:

*. δ is the relative error, which is given by:

$$\delta = \left| \frac{T_{estimated} - T_{actual}}{T_{actual}} \right| \times 100\% \quad (6.17)$$

where $T_{estimated}$ and T_{actual} are the estimated and actual temperatures, respectively.

Table 6.7: Characteristics and comparison of Gaussian and TPS RBFN estimation.

Data Set No.	Substrate Temperature	Gaussian RBFN Estimation		TPS RBFN Estimation	
		Temperature	δ	Temperature	δ
E1	28°C	28.073	0.26%	28.073	0.26%
E2	32°C	32.217	0.68%	32.204	0.64%
E3	38°C	37.883	0.31%	37.887	0.30%
E4	42°C	41.987	0.03%	41.998	0.01%
E5	48°C	47.487	1.07%	47.680	0.67%
E6	52°C	56.397	8.46%	54.457	4.72%
E7	58°C	59.336	2.30%	60.612	4.50%

Note: δ is the relative error, which is calculated by Equation (6.17) in Table 6.6.

Results for the temperature estimation from both RBFNs are summarized and tabulated in Table 6.7, with the percentage values of the relative error between the estimated and experimental temperatures. Gaussian RBF networks work well for the estimation of the low and medium temperature, say $<50^{\circ}\text{C}$, with the error of below 5%. However, as Gaussian RBFN cannot return satisfactory mapping for droplet profiles at high temperature, its estimation performance will also be adversely affected. Hence, its estimation result may not be convincing for high temperature. For instance, sample E6 got an 8.5% error from the estimation based on Gaussian RBFN. One exception of an estimation error as low as 2.3% took place for data set E7, but this is most likely a mere coincidence. As for the TPS RBF networks, the estimation errors are below 5% for all test temperatures. Therefore, the approach based on TPS RBFN proposed is effective in estimating the drying temperature at a given droplet profile.

6.5 Conclusion

Both Gaussian and thin-plate spline (TPS) radial basis function network (RBFN) have been used for shape representation and mapping of dried droplet profiles with corresponding drying temperature. In our case, not more than 40 basis function units in the network are sufficient for error stabilization. TPS RBFN shows better representation and mapping performance than Gaussian RBFN in terms of smaller root mean square error and higher statistical goodness of model indicated by R^2 statistic. At low drying temperature ($<40^\circ\text{C}$), both Gaussian and TPS RBF networks can return excellent mapping accuracy in statistics of R^2 greater than 99%. At high temperature ($>50^\circ\text{C}$), TPS RBFN still possesses fairly good shape representation, but Gaussian RBFN exhibits poor mapping results with R^2 values significantly less than 95%. The effectiveness of both types of RBFN model has also been evaluated from the two aspects - estimation of dried droplet profile and estimation of drying temperature. Evaluation data results demonstrate that Gaussian RBFN is only effective for estimation of the characteristics at low and medium temperature ($<50^\circ\text{C}$). As for the TPS RBFN, it can achieve very high R^2 value of greater than 97% for the estimation of dried droplet profile, and low relative error of less than 5% for the estimation of drying temperature. Therefore, the approach based on the proposed TPS RBFN is effective to carry out the related estimations. Especially for estimating the dried droplet profile, TPS RBFN shows better estimation than Gaussian RBFN across the whole range of drying temperature. Successful profile representation and mapping enables drop printing parameters to be selected for the droplet shape required.

CHAPTER 7

CONCLUSIONS AND FUTURE WORK

7.1 Conclusions

The main objective of this study is to further investigate the application of drop-on-demand (DoD) inkjet printing technology in the fabrication of organic light emitting diode (OLED) devices. The main research contributions are reflected in the four aspects:

- i) Provide a systematic study on the effect of surface modification techniques. This work shows that dry surface treatments remove hydrocarbon contamination and achieve surface wettability more efficiently than wet surface treatments. It further concludes that Oxygen-Plasma dry treatment possesses slower surface degradation than UV-Ozone treatment. The results achieved better the existing results reported by other researchers.
- ii) Concern fabrication and characterization of polymer-based OLEDs using inkjet printing and spin-coating as a comparison. The results are interpreted and explained from the point of view of film surface morphology, as it is found that inkjet printed functional film has more surface contact area than spin-coated functional film. Different effective surface contact may eventually affect device performance at various degrees.
- iii) Develop understanding of droplet formation with respect to the drying

temperature. This work makes significant findings on the droplet morphology after drying - Gaussian shape, transition shape, and ring-like shape. The results also imply that the droplet morphology can be controlled for the selected drop dispensing by the substrate temperature.

- iv) Deal with mathematical modeling of dried droplet profiles. This work is the first to employ radial basis function network (RBFN) to map the droplet shape. It evaluates both Gaussian and thin-plate spline (TPS) RBFN methods. It concludes that the former works well only for a lower temperature range less than 50°C, and the latter gives a better estimation for the entire temperature range.

In the following, the major achievements of the research are presented in detail.

(1) Indium-Tin-Oxide (ITO) Substrate Surface Treatment

Different surface treatment processes for ITO substrate have been investigated and compared, including two dry treatments (UV-Ozone and Oxygen-Plasma) and three wet treatments (Alkaline, Neutral and Organic). Surface properties on various contact angles (i.e. sessile, receding and advancing contact angle), surface energy and contact angle hysteresis have been characterized. Experiments conducted showed that dry surface treatment is always more efficient than wet surface treatment for removing hydrocarbon contamination and making the surface wettable. Dry treatment produces surfaces fully hydrophilic and fairly uniform. Uniform wettability of the substrate is a key performance attribute because uniform wetting behavior of the deposited droplets

may result in a uniform deposited film on the substrate.

On the other hand, freshly modified ITO surfaces after dry treatment can be re-contaminated quickly by atmospheric hydrocarbon molecules. The surface degradation (ageing effect) has then been characterized with respect to time individually for UV-Ozone and Oxygen-Plasma dry surface treatment. Their behaviors of surface degradation follow a similar trend. Re-contamination occurs very quickly and within 5 minutes, leading to the contact angle rising around 6.5° and 3.5° for UV-Ozone and Oxygen-Plasma treatment, respectively. However, Oxygen-Plasma process seems to be a better dry treatment process. Other than the excellent surface wettability achieved, its surface also degrades slower than UV-Ozone treated surface. From the results of our experiments, with the proper experimental control, achieved surface wettability is generally better than those reported by other researchers.

(2) Drop-on-Demand Inkjet Printing in Fabrication of Polymeric OLED

Polymeric OLED (P-OLED) devices with PEDOT:PSS hole transport layer at two different inkjet printing resolutions (450dpi and 720dpi, dpi stands for drop per inch) have been fabricated in order to investigate the influence of different printing parameters on device performance. They have also been compared with P-OLED of spin-coated PEDOT:PSS layer in the performance of current-voltage-luminance characteristic, luminous efficiency and luminous power efficiency. Better P-OLED device performance has been achieved by inkjet printing than spin-coating under

some controlled conditions.

The difference of the P-OLED performance for inkjet printing from spin-coating can be interpreted and explained using the surface morphology of inkjet printed features. In the case of a spin-coated film, a two dimensional surface structure tends to be formed. However, inkjet printed droplets have greater freedom of mass transport during the drying process and this yields a more three dimensional surface structure. Therefore, inkjet printed film forms more surface contact area for adjacent layers, which may balance and enhance interactions between hole and electron charge carriers and thus may produce more light. At the different inkjet printing resolutions, 720dpi for P-OLED fabrication exhibits better device performance than 450dpi as 720dpi may form more effective surface contact. Hence surface structure of inkjet printed thin films can be optimized to significantly improve the device performance. In this thesis, the 720dpi inkjet printing gives a good example although it may not be optimized.

(3) Characterization of Single Microdroplet Drying Behavior

Due to the large surface-to-volume ratio, the drying behavior of super fine droplets is extremely sensitive to substrate temperature. Drying shapes and dispensing of inkjet printed microdroplets with around 10 pico-liter volume have been investigated and characterized. With varying substrate temperature, dried droplet shapes achieved can be categorized into three distinctive types: Gaussian shape, transition shape, and

ring-like shape corresponding to low temperature ($<40^{\circ}\text{C}$), medium temperature, and high temperature ($>50^{\circ}\text{C}$) respectively. Therein, the formation of ring-like structures at high temperature is not suggested from the coffee-stain effect, but from the splashing upon impact. Owing to the small size of microdroplets, the drying rate at high temperature is so rapid that fine droplets simply solidify during splashing, resulting in a ring-like shape left.

In accordance with the classification of droplet shapes after drying, three stages of drop dispensing may be used for varying the width and height of the dried drops, namely: Gaussian stage, transition stage, and ring-like stage. In the Gaussian stage, the droplet width and height are inversely and directly proportional to the substrate temperature, respectively. In the transition stage, the droplet width can be varied with no significant change in its height, along with the formation of well-defined sharp edge. In the ring-like stage, the droplet width still varies with temperature in a negative linear relationship. The dried droplet possesses a hollow central base. The investigation on drop dispensing yields practical drop drying information that may be used to obtain dried drops with varying dimensions for various potential applications.

(4) Shape Representation and Mapping of Dried Droplet Profiles

Radial basis function network (RBFN) has been used to solve the approximation problem on curve fitting. Both Gaussian and thin-plate spline (TPS) RBFN have been applied in shape representation and mapping of dried droplet profiles with respect to

drying temperature. In general, TPS RBFN shows better approximation performance than Gaussian RBFN. Gaussian RBFN can obtain good mapping results only for a low to medium drying temperature range ($<50^{\circ}\text{C}$). However, TPS RBFN always returns the smaller network error and better statistical goodness of fit across the overall range of drying temperature.

The effectiveness of Gaussian and TPS RBFN model has also been evaluated. Two aspects, namely the dried droplet profile and drying temperatures, are estimated for the purpose of model evaluation. Evaluation results demonstrate that Gaussian RBFN is only effective for the estimation of the characteristics at low to medium temperatures ($<50^{\circ}\text{C}$). In contrast, the approaches based on the proposed TPS RBFN are effective in carrying out all the estimations for the entire temperature range, especially to estimate the dried droplet profile at a given temperature. The successful shape representation and mapping would enable future researches to set desirable drop printing parameters for the droplet shape required in practice.

7.2 Future Work

From the research in this thesis, the following areas are considered as recommendations for the future work:

(1) Indium-Tin-Oxide (ITO) Substrate Surface Treatment

Investigation can be done using more different surface treatment processes in order to build up a database on ITO surface cleaning and modification as a reference. Surface topology and surface chemical composition investigation can be examined on the modified substrates. This would give us a better understanding of what is actually happening to the ITO surface and their possible effects on the performance of final products.

(2) Drop-on-Demand Inkjet Printing Technology

As the performance of P-OLED devices can be easily manipulated by using different operating parameters of a DoD inkjet printing system such as printing resolution, further studies are needed to understand the more detailed mechanism behind the changes in device performance characteristics. Investigations should be done on the various printing parameters that are involved in the printing of lines and thin films to obtain the required properties for a specific application.

(3) Characterization of Single Microdroplet Drying Behavior

An in-depth study of the forming process of the dried droplet profile can be carried out with possible simulation modeling or high speed photography. This can serve as a reference for any subsequent printing work that may be carried out to obtain desired specific features. Future work can also include the exploration of the formation of printed lines or complete thin films produced drop by drop.

At high temperature, printed drop will form a ring structure (i.e. micro-ring). The depressed center of such a structure can be exploited to print another material inside it for various potential applications, such as micro-ring wells for cell culture and micro-ring scaffolds for tissue growth.

(4) Shape Representation and Mapping of Dried Droplet Profiles

In our case of shape representation and mapping, Gaussian RBFN appears to be less effective than TPS RBFN. One of possible reasons is due to the determination of the width parameter for Gaussian basis functions. In the training stage, the width parameter is fixed for all Gaussian functions. Hence, all Gaussian RBFs in one network have the same shape with different position of centers only. This may result in lack of flexibility for such a network. Future work may be done on the adaptive determination of width parameter for each Gaussian function in order to improve its network performance on shape approximation.

During the determination of the RBF parameters in the first stage of network training, our method used is the unsupervised technique, which uses only the network input data and not the target data (desired values for the output corresponding to the input). In general, unsupervised training is not an optimal procedure but a considerably fast training procedure. Its goal may be used to discover clusters or other structures in the data. In order to set the RBF parameters to give optimal performance (global optimization) in obtaining the required network outputs, the target data should be

included during the network training. That is, *supervised training* rather than unsupervised training can be performed in the future work. It is worth pointing out that the determination of the RBF parameters by supervised training is a non-linear optimization problem. Typically it will be computationally intensive, and there is no guarantee that supervised training will remain localized. Moreover, if supervised training is adopted, RBFN may be losing its fast two-stage training. As a good compromise, the RBF parameters can be initialized using unsupervised techniques, after which they can be fine tuned under supervised procedures.

BIBLIOGRAPHY

1. "ELECTRONIC PAPER: organic light emitting diodes", website cited:
<http://komar.cs.stthomas.edu/qm425/01s/Tollefsrud2.htm>
2. "Organic light emitting diodes", website cited:
http://en.wikipedia.org/wiki/Organic_light-emitting_diode
3. O. Prache, "Active matrix molecular OLED microdisplays", *Displays*, v 22, n 2, 2001, pp. 49-56
4. W. Herfrich and W. G. Schneider, "Recombination radiation in anthracene crystals", *Physical Review Letters*, v 14, n 7, 1965, pp. 229-231
5. C. W. Tang and S. A. Van Slyke, "Organic electroluminescent diodes", *Applied Physics Letters*, 51, 1987, pp. 913-915
6. J. H. Burroughes, D. D. C. Bradley, A. R. Brown, R. N. Marks, K. Mackay, R. H. Friend, P. L. Burns and A. B. Holmes, "Light-emitting diodes based on conjugated polymers", *Nature*, 347, 1990, pp. 539-541
7. J. M. Shaw and P. F. Seidler, "Organic electronics: introduction", *IBM Journal of Research and Development*, v 45, n 1, 2001, pp. 3-9
8. D. A. Pardo, G. E. Jabbour and N. Peyghambarian, "Application of screen printing in the fabrication of organic light-emitting devices", *Advanced Materials*, v 12, n 17, 2000, pp. 1249-1252
9. G. E. Jabbour, R. Radspinner and N. Peyghambarian, "Screen printing for the fabrication of organic light-emitting devices", *IEEE Journal of Selected Topics*

- in *Quantum Electronics*, v 7, n 5, 2001, pp. 769-773
10. T. R. Hebner, C. C. Wu, D. Marcy, M. H. Lu and J. C. Sturm, "Ink-jet printing of doped polymers for organic light emitting devices", *Applied Physics Letters*, 72, 1998, pp. 519-521
 11. Y. Yang, S. Chang, J. Bharathan and J. Liu, "Organic/polymeric electroluminescent devices processed by hybrid ink jet printing", *Journal of Materials Science: Materials in Electronics*, v 11, n 2, 2000, pp. 89-96
 12. J. Bharathan and Y. Yang, "Polymer electroluminescent devices processed by inkjet printing: I. Polymer light-emitting logo", *Applied Physics Letters*, 72, 1998, pp. 2660-2662
 13. H. Kobayashi, S. Kanabe, S. Seki, H. Kiguchi, M. Kimura, I. Yudasaka, S. Miyashita, T. Shimoda, C. R. Towns, J. H. Burroughes and R. H. Friend, "A novel RGB multicolor light-emitting polymer display", *Synthetic Metals*, v 111-112, 2000, pp. 125-128
 14. M. Shibusawa, M. Kobayashi, J. Hanari, K. Sunohara and N. Ibaraki, "A 17-inch WXGA full-color OLED display using the polymer ink-jet technology", *IEICE Trans Electron*, v E86-C, n 11, 2003, pp. 2269-2274
 15. K. F. Teng and R. W. Vest, "Application of ink jet technology on photovoltaic metallization", *IEEE Electron Device Letters*, v 9, n 11, 1998, pp. 591-595
 16. D. Wallace, D. Hayes, T. Chen, V. Shah, D. Radulescu, P. Cooley, K. Wachtler and A. Nallani, "Think additive: ink-jet deposition of materials for MEMS packaging", *The 6th Topical Workshop on Packaging of MEMS and Related*

- Micro-Nano-Bio Integrated Systems, Long Beach, CA, Nov. 18-20, 2004
17. P. Calvert, "Inkjet printing for materials and devices", *Chemistry of Materials*, v 13, n 10, 2001, pp. 3299-3305
 18. B. J. De Gans, E. Kazancioglu, W. Meyer and U. S. Schubert, "Ink-jet printing polymers and polymer libraries using micropipettes", *Macromolecular Rapid Communications*, v 25, n 1, 2004, pp. 292-296
 19. J. R. Sheats, H. Antoniadis, M. Hueschen, W. Leonard, J. Miller, R. Moon, D. Roitman and A. Stocking, "Organic electroluminescent devices", *Science*, 273, 1996, pp. 884-888
 20. E. I. Haskal, M. Biichel, P. C. Duineveld and P. van de Weijer, "Passive-matrix polymer light-emitting displays", *MRS Bulletin*, v 27, 2002, pp. 864-869
 21. K. Leo, "Organic light emitting diodes: display and lighting technology of the future", website cited:
http://www.nanotechnology.de/ntforum/download/11_Leo_Novaled_TU_Dresden.pdf
 22. C. Freudenrich, "How OLEDs work", website cited:
<http://science.howstuffworks.com/oled1.htm>
 23. A. Dodabalapur, "Organic light emitting diodes", *Solid State Communications*, v 102, n 2-3, 1997, pp. 259-267
 24. K. Leo, "Organic light-emitting diodes: new opportunities for displays and lighting", website cited:
<http://www.messe-duesseldorf.de/glasstec06/pdf/scripte/Leo.pdf>

25. S. Vaidya, "Organic light emitting diodes", website cited:
<http://www.tulane.edu/~schmehl/Srivathsa%20Dept%20Seminar.ppt>
26. U. Lemmer, "Physics of nanostructures optoelectronics", website cited:
http://www.lti.uni-karlsruhe.de/rd_download/polymer2004/Plastic_Electronics_WS0405_Introduction.pdf
27. L. S. Hung and C. H. Chen, "Recent progress of molecular organic electroluminescent materials and devices", *Materials Science and Engineering*, R39, 2000, pp. 143-222
28. J. Kalinowski, "Electroluminescence in organics", *Journal of Physics D: Applied Physics*, v 32, 1999, pp. R179-R250
29. U. Mitshke and P. Bauerle, "The electroluminescence of organic materials", *Journal of Materials Chemistry*, v 10, 2000, pp. 1471-1507
30. R. H. Friend, "Conjugated polymers: new materials for optoelectronic devices", *Pure and Applied Chemistry*, v 73, 2001, pp. 425-430
31. I. D. Rees, K. L. Robinson, A. Holmes, C. R. Towns and R. O'Dell, "Recent development in light-emitting polymers", *MRS Bulletin*, v 27, 2002, pp. 451-455
32. M. Pope, H. P. Kallmann and P. Magnante, "Electroluminescence in organic crystals", *Journal of Chemical Physics*, v 38, 1963, pp. 2042-2043
33. S. A. Van Slyke, C. H. Chen and C. W. Tang, "Organic electroluminescent devices with improved stability", *Applied Physics Letters*, 69, 1996, pp. 2160-2162

34. J. Shinar (ed.), "Organic light-emitting devices: a survey", New York: Springer-Verlag, 2004, pp. 14-20
35. C. H. Chen and J. Shi, "Metal chelates as emitting materials for organic electroluminescence", *Coordination Chemistry Reviews*, v 171, 1998, pp. 161-174
36. Y. Hamada, "The development of chelate metal complexes as an organic electroluminescent materials", *IEEE Transactions on Electron Devices*, v 44, n 8, 1997, pp. 1208-1217
37. C. W. Tang, S. A. VanSlyke and C. H. Chen, "Electroluminescence of doped organic thin films", *Journal of Applied Physics*, 65, 1989, pp. 3615-3616
38. M. Angelopoulos, "Conducting polymers in microelectronics", *IBM Journal Research & Development*, v 45, n 1, 2001, pp. 57-75
39. C. K. Chiang, C. R. Fincher, Jr., Y. W. Park, and A. J. Heeger, H. Shirakawa, E. J. Louis, S. C. Gau and A. G. MacDiarmid, "Electrical conductivity in doped polyacetylene", *Physical Review Letters*, v 39, 1977, pp. 1098-1101
40. L. W. Shacklette, R. R. Chance, D. M. Ivory, G. G. Miller and R. H. Baughman, "Electrical and optical properties of highly conducting charge-transfer complexes of poly(*p*-phenylene)", *Synthetic Metals*, v 1, n3, 1980, pp.307-320
41. R. H. Friend, R. W. Gymer, A. B. Holmes, J. H. Burroughes, R. N. Marks, C. Taliani, D. D. C. Bradley, D. A. DosSantos, J. L. Bredas, M. Logdlung and W. R. Salaneck, "Electroluminescence in conjugated polymers", *Nature*, 397, 1999, pp. 121-128

42. S. Forero, P. H. Nguyen, W. Brutting and M. Schwoerer, "Charge carrier transport in poly(*p*-phenylenevinylene) light-emitting devices", *Physical Chemistry Chemical Physics*, v 1, 1999, pp. 1769-1776
43. L. Dai, B. Winkler, L. Dong and A. W. H. Mau, "Conjugated polymers for light emitting applications", *Advanced Materials*, v 13, 2001, pp. 915-925
44. C. H. Tan, A. R. Inigo, W. S. Fann, P. K. Wei, Y. S. Huang, G. Y. Perng and S. A. Chen, "The morphological dependence of charge transport in a soluble luminescent conjugated polymer", *Organic Electronics*, v 3, n 2, 2002, pp. 81-88
45. A. R. Inigo, C. H. Tan, W. S. Fann, Y. S. Huang, G. Y. Perng and S. A. Chen, "Non-dispersive hole transport in a soluble poly(*p*-phenylene vinylene)", *Advanced Materials*, v 13, 2001, pp. 504-508
46. H. Muller, F. Salhi and B. Blohorn, "Bis(arylidene)tetrathiapentalenes - novel building blocks for extended tetrathiafulvalenes and conducting polymers", *Synthetic Metals*, v 84, 1997, pp. 455-446
47. S. Shaked, S. Tal, Y. Roichman, A. Razin, S. Xiao, Y. Eichen and N. Tessler, "Charge density and film morphology dependence of charge mobility in polymer field-effect transistors", *Advanced Materials*, v 15, 2003, pp. 913-916
48. Y. Shi, J. Liu and Y. Yang, "Device performance and polymer morphology in polymer light emitting diodes: the control of thin film morphology and device quantum efficiency", *Journal of Applied Physics*, 87, 2000, pp. 4254-4263
49. J. Liu, Y. Shi, L. Ma and Y. Yang, "Device performance and polymer

- morphology in polymer light emitting diodes: the control of device electrical properties and metal/polymer contact”, *Journal of Applied Physics*, 88, 2000, pp. 605-609
50. T. Q. Nguyen, R. C. Kwong, M. E. Thompson and B. J. Schwartz, “Improving the performance of conjugated polymer-based devices by control of interchain interactions and polymer film morphology”, *Applied Physics Letters*, 76, 2000, pp. 2454-2456
51. T. Q. Nguyen, I. B. Martini, J. Liu and B. J. Schwartz, “Controlling interchain interactions in conjugated polymers: the effects of chain morphology on exciton annihilation and aggregation in MEH-PPV films”, *Journal of Physical Chemistry B*, 104, 2000, pp. 237-255
52. H. F. M. Schoo and R. J. C. E. Demandt, “Materials for polymer light emitting diodes”, *Philips Journal of Research*, v 51, n 4, 1998, pp. 527-533
53. D. Braun and A. J. Heeger, “Visible light emission from semiconducting polymer diodes”, *Applied Physics Letters*, 58, 1991, pp. 1982-1984
54. Y. Yang, E. Westerweele, C. Zhang, P. Smith and A. J. Heeger, “Enhanced performance of polymer light-emitting diodes using high-surface area polyaniline network electrodes”, *Journal of Applied Physics*, 77, 1995, pp. 694-698
55. S. Karg, J. C. Scott, J. R. Salem and M. Angelopoulos, “Increased brightness and lifetime of polymer light-emitting diodes with polyaniline anodes”, *Synthetic Metals*, v 80, 1996, pp. 111-117

56. Y. Yang and A. J. Heeger, "Polyaniline as a transparent electrode for polymer light-emitting diodes: lower operating voltage and higher efficiency", *Applied Physics Letters*, 64, 1994, pp.1245-1247
57. J. E. de Albuquerque, L. H. C. Mattosob, R. M. Fariac, J. G. Masters and A. G. MacDiarmid, "Study of the interconversion of polyaniline oxidation states by optical absorption spectroscopy", *Synthetic Metals*, v 146, n 1, 2004, pp. 1-10
58. F. Jonas and L. Schrader, "Conductive modification of polymers with polypyrroles and polythiophenes", *Synthetic Metals*, v 41-43, 1991, pp. 831-836
59. L. B. Groenendaal, F. Jonas, D. Freitag, H. Pielartzik and J. R. Reynolds, "Poly(3,4-ethylenedioxythiophene) and its derivatives: past, present, and future", *Advanced Materials*, v 12, 2000, pp. 481-494
60. J. C. Scott, S. A. Carter, S. Karg and M. Angelopoulos, "Polymeric anodes for organic light-emitting diodes", *Synthetic Metals*, v 85, 1997, pp. 1197-1200
61. J. S. Kim, M. Granstrom, R. H. Friend, N. Johansson, W. R. Salaneck, R. Daik, W. J. Feast and F. Cacialli, "Indium-tin oxide treatments for single- and double-layer polymeric light-emitting diodes: the relation between the anode physical, chemical, and morphological properties and the device performance", *Journal of Applied Physics*, 84, 1998, pp. 6859-6870
62. T. M. Brown, J. S. Kim, R. H. Friend, F. Cacialli, R. Daik and W. J. Feast, "Built-in field electroabsorption spectroscopy of polymer light-emitting diodes incorporating a doped poly(3,4-ethylene dioxythiophene) hole injection layer", *Applied Physics Letters*, 75, 1999, pp. 1679-1861

63. M. B. Khalifa, D. Vaufrey, A. Bouazizi, J. Tardy and H. Maaref, "Hole injection and transport in ITO/PEDOT/PVK/Al diodes", *Materials Science and Engineering: C*, v 21, 2002, pp. 277-282
64. W. H. Kim, A. J. Makinen, N. Nikolov, R. Shashindhar, H. Kim and Z. H. Kafafi, "Molecular organic light-emitting diodes using highly conducting polymers", *Applied Physics Letters*, 80, 2002, pp. 3844-3846
65. W. H. Kim, G. P. Kushto, H. Kim and Z. H. Kafafi, "Effect of annealing on the electrical properties and morphology of a conducting polymer used as an anode in organic light-emitting devices", *Journal of Polymer Science Part B: Polymer Physics*, v 41, 2003, pp. 2522-2528
66. "CLEVIOS™ P", website cited: http://www.clevios.com/index.php?page_id=995&prod_service_id=317&anw_id=0&operate=&suchstart=938&prodselect_5=317%7C&suchstart=938&anwselect_14=0&suchfeld=, February 2009
67. M. P. de Jong, L. V. van IJzendoorn and M. J. A. de Voigt, "Stability of the interface between indium-tin-oxide and poly(3,4-ethylene dioxythiophene)/poly(styrene sulfonate) in polymer light-emitting diodes", *Applied Physics Letters*, 77, 2000, pp. 2255-2257
68. A. Elschner, F. Jonas, S. Kirchmeyer and K. Wussow, "High-resistivity PEDT/PSS for reduced crosstalk in passive matrix OELs", *Asia Display/IDW'01*, October 2001, Nagoya, Japan, pp. 1427-1430
69. "CLEVIOS™ P VP AI 4083", website cited:

- http://www.clevios.com/index.php?page_id=995&prod_service_id=322&anw_id=0&operate=&suchstart=938&prodselect_5=322%7C&suchstart=938&anwselect_14=0&suchfeld=, February 2009
70. “CLEVIOS™ P VP CH 8000”, website cited: http://www.clevios.com/index.php?page_id=995&prod_service_id=325&anw_id=0&operate=&suchstart=938&prodselect_5=325%7C&suchstart=938&anwselect_14=0&suchfeld=, February 2009
71. J. Y. Kim, J. H. Jung D. E. Lee and J. Joo, “Enhancement of electrical conductivity of poly(3,4-ethylenedioxythiophene)/poly(4-styrenesulfonate) by a change of solvents”, *Synthetic Metals*, v 126, 2002, pp. 311-316
72. H. C. Starck Inc., “Baytron P VP Al 4083 and Baytron P VP CH 8000 product information for electronic grades designed for use as hole-injection material in OLEDs”
73. G. Heywang and F. Jonas, “Poly(alkylenedioxythiophene)s: new, very stable conducting polymers”, *Advanced Materials*, v 4, 1992, pp. 116-118
74. M. Dietrich, J. Heinze, G. Heywang and F. Jonas, “Electrochemical and spectroscopic characterization of polyalkylenedioxythiophenes”, *Journal of Electroanalytical Chemistry*, v 369, 1994, pp. 87-92
75. Q. Pei, G. Zuccarello, M. Ahlskog and O. Inganäs, “Electrochromic and highly stable poly(3,4-ethylenedioxythiophene) switches between opaque blue-black and transparent sky blue”, *Polymer*, v 35, n 7, 1994, pp. 1347-1351
76. R. Kiebooms, A. Aleshin, K. Hutchison, F. Wudl and A. Heeger, “Doped

- poly(3,4-ethylenedioxythiophene) films: thermal, electromagnetical and morphological analysis”, *Synthetic Metals*, v 101, 1999, pp. 436-437
77. F. Jonas, W. Krafft and B. Muys, “Poly(3,4-ethylenedioxythiophene): conductive coatings, technical applications and properties”, *Macromolecular Symposia*, v 100, 1995, pp. 167-173
78. A. N. Aleshin, S. R. Williams and A. J. Heeger, “Transport properties of poly(3,4-ethylenedioxythiophene)/poly(styrenesulfonate)”, *Synthetic Metals*, v 94, 1998, pp. 173-177
79. J. F. Rubinson, “Biology to engineering: the present status of conducting polymers”, *Conducting Polymers and Polymer Electrolytes: From Biology to Photovoltaics*, ACS Symposium Series No. 832, New York: Oxford University Press, 2003, pp. 2-15
80. J. C. Gustafsson, B. Leidberg and O. Inganas, “In situ spectroscopic investigation of electrochromism and ion transport in a poly(3,4-ethylenedioxythiophene)electrode in a solid state electrochemical cell”, *Solid State Ionics*, v 69, 1994, pp. 145-152
81. H. W. Heuer, R. Wehrmann and S. Kirchmeyer, “Electrochromic window based on conducting poly(3,4-ethylenedioxythiophene)-poly(styrene sulfonate)”, *Advanced Functional Materials*, v 12, 2002, pp. 89-94
82. P. Andersson, D. Nilsson, P. O. Svensson, M. Chen, A. Malmstrom, T. Remonen, T. Kugler and M. Berggren, “Active matrix displays based on all-organic electrochemical smart pixels printed on paper”, *Advanced Materials*, v 14, 2002,

pp. 1460-1464

83. A. A. Argun, A. Cirpan and J. R. Reynolds, "The first truly all-polymer electrochromic devices", *Advanced Materials*, v 15, 2003, pp. 1338-1341
84. S. A. Sapp, G. A. Sotzing, J. L. Reddinger and J. R. Reynolds, "Rapid switching solid state electrochromic devices based on complementary conducting polymer films", *Advanced Materials*, v 8, 1996, pp. 808-811
85. H. Sirringhaus, T. Kawase, R. H. Friend, T. Shimoda, M. Inbasekaran, W. Wu and E. P. Woo, "High-resolution inkjet printing of all-polymer transistor circuits", *Science*, 290, 2000, pp.2123-2126
86. N. Stutzmann, R. H. Friend and H. Sirringhaus, "Self-aligned, vertical-channel, polymer field-effect transistors", *Science*, 299, 2003, pp. 1881-1884
87. T. Kawase, H. Sirringhaus, R. H. Friend and T. Shimoda, "Inkjet printed via-hole interconnections and resistors for all-polymer transistor circuits", *Advanced Materials*, v 13, 2001, pp. 1601-1605
88. B. Chen, T. Cui, Y. Liu and K. Varahramyan, "All-polymer RC filter circuits fabricated with inkjet printing technology", *Solid-State Electronics*, v 47, 2003, pp. 841-847
89. D. Nilsson, T. Kugler, P. O. Svensson and M. Berggren, "An all-organic sensor-transistor based on a novel electrochemical sensors on paper", *Sensors and Actuators B: Chemical*, v 86, 2002, pp. 193-197
90. Y. Liu, T. Cui and K. Varahramyan, "All-polymer capacitor fabricated with inkjet printing technique", *Solid-State Electronics*, v 47, 2003, pp. 1543-1548

91. L. S. Roman, W. Mammo, L. A. A. Pettersson, M. R. Andersson and O. Inganas, "High quantum efficiency polythiophene/C₆₀ photodiodes", *Advanced Materials*, v 10, 1998, pp. 774-777
92. A. C. Arias, M. Granstrom, D. S. Thomas, K. Petritsch and R. H. Friend, "Doped conducting-polymer-semiconducting-polymer interfaces: their use in organic photovoltaic devices", *Physical Review E*, v 60, 1999, pp. 1854-1860
93. F. Zhang, M. Johansson, M. R. Andersson, J. C. Hummelen and O. Inganas, "Polymer photovoltaic cells with conducting polymer anodes", *Advanced Materials*, v 14, 2002, pp. 662-665
94. G. Greczynski, Th. Kugler, M. Keil, W. Osikowicz, M. Fahlman and W. R. Salaneck, "Photoelectron spectroscopy of thin films of PEDOT-PSS conjugated polymer blend: a mini-review and some new results", *Journal of Electron Spectroscopy and Related Phenomena*, v 121, 2001, pp. 1-17
95. S. Ghosh and O. Inganas, "Nano-structured conducting polymer network based on PEDOT-PSS", *Synthetic Metals*, v 121, 2001, pp.1321-1322
96. S. L. Lai, M. Y. Chen, M. K. Fung, C. S. Lee and S. T. Lee, "Concentration effect of glycerol on the conductivity of PEDOT film and the device performance", *Materials Science and Engineering: B*, v 104, 2003, pp. 26-30
97. T. Granlund, L. A. A. Pettersson and O. Inganas, "Determination of the emission zone in a single-layer polymer light-emitting diode through optical measurements", *Journal of Applied Physics*, v 89, n11, 2001, pp. 5897-5902
98. F. Louwet, L. Groenendaal, J. Dhaen, J. Manca, J. Van Luppen, E. Verdonck and

- L. Leenders, "PEDOT/PSS: synthesis, characterization, properties and applications", *Synthetic Metals*, v 135-136, 2003, pp. 115-117
99. J. Huang, P. F. Milelr, J. C. de Mello, A. J. de Mello and D. D. C. Bradley, "Influence of thermal treatment on the conductivity and morphology of PEDOT/PSS films", *Synthetic Metals*, v 139, 2003, pp. 569-572
100. S. K. M. Jonsson, J. Birgeron, X. Crispin, G. Greczynski, W. Osikowicz, A. W. Denier van der Gon, W. R. Salaneck and M. Fahlman, "The effects of solvents on the morphology and sheet resistance in poly(3,4-ethylenedioxythiophene)-polystyrenesulfonic acid (PEDOT-PSS) films", *Synthetic Metals*, v 139, 2003, pp. 1-10
101. I. G. Hill, D. Milliron, J. Schwartz and A. Kahn, "Organic semiconductor interfaces: electronic structure and transport properties", *Applied Surface Science*, v 166, n 1-4, 2000, pp. 354-362
102. K. Sugiyama, H. Ishii, Y. Ouchi and K. Seki, "Dependence of indium-tin-oxide work function on surface cleaning method as studied by ultraviolet and X-ray photoemission spectroscopies", *Journal of Applied Physics*, v 87, 2000, pp. 295-298
103. J. S. Kim, F. Cacialli, A. Cola, G. Gigli and R. Cingolani, "Increase of charge carriers density and reduction of Hall mobilities in oxygen-plasma treated indium-tin-oxide anodes", *Applied Physics Letters*, v 75, n 1, 1999, pp. 9-21
104. J. S. Kim, F. Cacialli and R. Friend, "Surface conditioning of indium-tin oxide anodes for organic light-emitting diodes", *Thin Solid Films*, v 445, n 2, 2003, pp.

358-366

105. F. Li, H. Tang, J. Shinar, O. Resto and S. Z. Weisz, "Effects of aquaregia treatment of indium-tin-oxide substrates on the behavior of double layered organic light-emitting diodes", *Applied Physics Letters*, 70, 1997, pp. 2741-2743
106. M. Ishii, T. Mori, H. Fujikawa, S. Tokito and Y. Taga, "Improvement of organic electroluminescent device performance by in situ plasma treatment of indium-tin-oxide surface", *Journal of Luminescence*, v 87-89, 2000, pp. 1165-1167
107. G. Gustafsson, Y. Cao, G. M. Treacy, F. Klavetter, N. Colaneri and A. J. Heeger, "Flexible light-emitting diodes made from soluble conducting polymers", *Nature*, 357, 1992, pp. 477-479
108. M. Stöbel, J. Staudigel, F. Steuber, J. Blassing, J. Simmerer, A. Winnacker, H. Neuner, D. Metzdorf, H. -H. Johannes and W. Kowalsky, "Electron injection and transport in 8-hydroxyquinoline aluminum", *Synthetic metals*, v 111-112, 2000, pp. 19-24
109. L. S. Hung, C. W. Tang and M. G. Mason, "Enhanced electron injection in organic electroluminescence devices using an Al/LiF electrode", *Applied Physics Letters*, 70, 1997, pp. 152-154
110. G. E. Jabbour, Y. Kawabe, S. E. Shaheen, J. F. Wang, M. M. Morrell, B. Kippelen and N. Peyghambarian, "Highly efficient and bright organic electroluminescent devices with an aluminum cathode", *Applied Physics Letters*,

- 71, 1997, pp. 1762-1764
111. G. E. Jabbour, B. Kippelen, N. R. Armstrong and N. Peyghambarian, "Aluminum based cathode structure for enhanced electron injection in electroluminescent organic devices", *Applied Physics Letters*, 73, 1998, pp. 1185-1187
112. B. Geffroy, P. le Roy and C. Prat, "Organic light-emitting diode (OLED) technology: materials, devices and display technologies", *Polymer International*, v 55, 2006, pp. 572-582
113. P. Broms, J. Birgersson, N. Johansson, M. Logdlund and W. R. Salaneck, "Calcium electrodes in polymer LEDs", *Synthetic Metals*, v 74, n 2, 1995, pp. 179-181
114. F. Li, H. Tang, J. Anderegg and J. Shinar, "Fabrication and electroluminescence of double-layered organic light-emitting diodes with the Al₂O₃/Al cathode", *Applied Physics Letters*, 70, 1997, pp. 1233-1235
115. H. W. Schmidt, C. Schmitz, P. Posch and M. Thelakkat, "Combinatorial methods for screening and optimization of materials and device parameters in organic light emitting diodes", *Proceedings of the SPIE - The International Society for Optical Engineering*, v 3797, 1999, pp. 58-65
116. C. Schmitz, P. Posch, M. Thelakkat and H. W. Schmidt, "Efficient screening of electron transport material in multilayer organic light emitting diodes by combinatorial methods", *Proceedings of the SPIE - The International Society for Optical Engineering*, v 3797, 1999, pp. 423-431

117. L. Zou, V. Savvate'ev, J. Booher, C. H. Kim and J. Shinar, "Combinatorial fabrication and studies of intense efficient ultraviolet-violet organic light-emitting device arrays", *Applied Physics Letters*, 79, 2001, pp. 2282-2284
118. J. Liu, T. -F. Guo, Y. Shi and Y. Yang, "Solvation induced morphological effects on the polymer/metal contacts", *Journal of Applied Physics*, 89, 2001, pp. 3668-3673
119. J. Ouyang, T. -F. Guo, Y. Yang, H. Higuchi, M. Yoshioka and T. Nagatsuka, "High-performance, flexible polymer light-emitting diodes fabricated by a continuous polymer coating process", *Advanced Materials*, v 14, 2002, pp. 915-918
120. Z. -G. Li and H. Meng (ed.), "Organic light-emitting materials and devices", Boca Raton: CRC Press by Taylor & Francis Group, LLC, 2006, pp. 567-580
121. J. Birnstock, J. Blässing, A. Hunze, M. Scheffel, M. Stöbel, K. Heuser, G. Wittmann, J. Wörle and A. Winnacker, "Screen-printed passive matrix displays based on light-emitting polymers", *Applied Physics Letters*, 78, 2001, pp. 3905-3907
122. D. B. Wallace, "Ink-jet deposition of materials for electronics manufacturing", MicroFab Technologies Inc., SIMTech Public Lectures, Aug 2005
123. H. P. Le, "Progress and trends in ink-jet printing technology", *Journal of Imaging Science and Technology*, v 42, n 1, 1998, pp. 49-62
124. H. J. Trost, S. Ayers, T. Chen, W. R. Cox, M. E. Grove and R. Hoenigman, "Using drop-on-demand technology for manufacturing grin lenses", *Proceeding*

- 2001 Annual Manufacturing ASPE, 10-15 Nov. 2001 (ASPE Raleigh NC 2001), pp. 533-536
125. B. Praveen, "Computational modeling and analysis of drop formation for piezo-actuated microdispenser based on drop on demand system", Industrial Project Report, Thesis for the Degree of Master of Science (Mechatronics), 2005, National University of Singapore
126. Y. Liu, K. Varahramyan and T. Cui, "Low-voltage all-polymer field-effect transistor fabricated using an inkjet printing technique", *Macromolecular Rapid Communications*, v 26, 2005, pp. 1955-1959
127. G. Perrin, T. S. Lundgren and B. T. Khuri-Yakub, "Controlled ink-jet printing and deposition of organic polymers and solid particles", *Applied Physics Letters*, 73, 1998, pp. 2375-2377
128. H. Fan, Y. Lu, A. Stump, S. T. Reed, T. Baer, R. Schunk, V. Perez-Luna, G. P. Lopez and C. J. Brinker, "Rapid prototyping of patterned functional nanostructures", *Nature*, 405, 2000, pp. 56-60
129. P. Kumar, A. Metha, M. D. Dadmun, J. Zheng, L. Peyser, A. P. Bartko, R. M. Dickson, T. Thundat, B. G. Sumpter, D. W. Noid and M. D. Barnes, "Narrow-bandwidth spontaneous luminescence from oriented semiconducting polymer nanostructures", *The Journal of Physical Chemistry B*, v 107, n 26, 2003, pp. 6252-6257
130. S. Magdassi and M. B. Moshe, "Patterning of organic nanoparticles by ink-jet printing of microemulsions", *Langmuir*, 19, 2003, pp. 939-942

131. E. Garnett and D. Ginley, "Electrical and morphological properties of inkjet printed pedot/pss films", *Journal of Undergraduate Research*, v 5, 2005, pp. 24-29
132. T. Kawase, T. Shimoda, C. Newsome, H. Sirringhaus and R. H. Friend, "Inkjet printing of polymer thin film transistors", *Thin Solid Films*, v 438, 2003, pp. 279-287
133. M. Plötner, T. Wegener, S. Richter, S. Howitz, and W-J. Fischer, "Investigation of ink-jet printing of poly-3-octylthiophene for organic field-effect transistors from different solutions", *Synthetic Metals*, v 147, 2004, pp. 299-303
134. Y. Yoshioka, P. D. Calvert and G. E. Jabbour, "Simple modification of sheet resistivity of conducting polymeric anodes via combinatorial ink-jet printing techniques", *Macromolecular Rapid Communications*, v 26, 2005, pp. 238-246
135. Y. Yoshioka and G. E. Jabbour, "Desktop inkjet printer as a tool to print conducting polymers", *Synthetic Metals*, v 156, 2006, pp. 779-783
136. C. Sele, T. von Werne, R. H. Friend and H. Sirringhaus, "Lithography-free, self-aligned inkjet printing with sub-hundred-nanometer resolution", *Advanced Materials*, v 17, n 8, 2005, pp. 997-1001
137. S. Besbes, H. B. Ouada, J. Davenas, L. Ponsonnet, N. Jaffrezic and P. Alcouffe, "Effect of surface treatment and functionalization on the ITO properties for OLEDs", *Materials Science and Engineering C: Materials for Biological Applications*, v 26, 2006, pp. 505-510
138. Z. Y. Zhong and Y. D. Jiang, "Surface modification and characterization of

- indium-tin oxide for organic light-emitting devices”, *Journal of Colloid and Interface Science*, v 302, 2006, pp. 613-619
139. J. S. Kim, F. Cacialli and R. Friend, “Surface conditioning of indium-tin oxide anodes for organic light-emitting diodes”, *Thin Solid Films*, v 445, 2003, pp. 358-366
140. J. S. Kim, P. K. H. Ho, D. S. Thomas, R. H. Friend, F. Cacialli, G. W. Bao and S. F. Y. Li, “X-ray photoelectron spectroscopy of surface-treated indium-tin oxide thin films”, *Chemical Physics Letters*, v 315, 1999, pp. 307-312
141. Z. Y. Zhong, Y. X. Zhong, C. Liu, S. Yin, W. X. Zhang and D. F. Shi, “Study on the surface wetting properties of treated indium-tin-oxide anodes for polymer electroluminescent devices”, *Physica Status Solidi (A)*, v 198, n 1, 2003, pp. 197-203
142. J. S. Kim, R. H. Friend and F. Cacialli, “Surface energy and polarity of treated indium-tin-oxide anodes for polymer light-emitting diodes studied by contact-angle measurements”, *Journal of Applied Physics*, v 86, n 5, 1999, pp. 2774-2778
143. W. Birch, “Introduction to wettability”, *Lecture Notes on Surface Wettability for One-Day Short Course*, Singapore: Institute of Materials Research and Engineering, 2006
144. J. N. Israelachvili, “*Intermolecular and surface forces*”, 2nd Edition, San Diego: Academic Press, 1998, pp. 149-151
145. P. C. Hiemenz and R. Rajagopalan, “*Principles of colloid and surface*

- chemistry”, 3rd Edition, New York: Marcel Dekker Inc., 1997, pp. 248-291
146. J. D. Andrade (ed.), “Surface and interfacial aspects of biomedical polymers, volume 1: surface chemistry and physics”, New York: Plenum Press, 1985, pp. 249-292
147. D. Y. Kwok and A. W. Neumann, “Contact angle measurement and contact angle interpretation”, *Advances in Colloid and Interface Science*, v 81, 1999, pp. 167-249
148. Litrex Co., “Litrex 80.L industrial ink-jet system for LEP display research: operator manual”, Revision C, 10 Jan. 2003
149. Fujifilm Dimatix Inc., “Spectra SX3 128-channel jetting assembly”, PDS00053 Rev. 01, 26 Jun. 2009, website cited: <http://www.dimatix.com>
150. Y. S. Ng, J. X. Zhou, Jerry Y. H. Fuh, H. T. Loh, Y. S. Wong, J. J. Gray and Chua S. J., “Influence of piezoelectric pulse profile on forming accuracy of inkjet printed PEDOT:PSS droplets for OLED fabrication”, *Proceedings of the International Conference on Manufacturing Automation (ICMA)*, Singapore, May 2007
151. K. Müllen and U. Scherf (ed.), “Organic light emitting devices: synthesis, properties and applications”, Weinheim: Wiley-VCH, 2006, pp 154-158
152. T. Shimoda, K. Morii, S. Seki and H. Kiguchi, “Inkjet printing of light-emitting polymer displays”, *MRS Bulletin*, v 28, n 11, 2003, pp. 821-827
153. M. Ikegawa and H. Azuma, “Droplet behaviors on substrates in thin-film formation using ink-jet printing”, *JSME International Journal Series B*, v 47, n 3,

- 2004, pp. 490-496
154. R. D. Deegan, O. Bakajin, T. F. Dupont, G. Huber, S. R. Nagel and T. A. Witten, “Capillary flow as the cause of ring stains from dried liquid drops”, *Nature*, v 389, 1997, pp. 827-829
155. R. D. Deegan, “Pattern formation in drying drops”, *Physical Review E*, v 61, n 1, 2000, pp. 475-485
156. R. D. Deegan, O. Bakajin, T. F. Dupont, G. Huber, S. R. Nagel and T. A. Witten, “Contact line deposits in an evaporating drop”, *Physical Review E*, v 62, n 1, 2000, pp. 756-765
157. M. Toivakka, “Numerical investigation of droplet impact spreading in spray coating of paper”, *Proceedings of 2003 TAPPI 8th Advanced Coating Fundamentals Symposium*, Atlanta: TAPPI Press, 2003
158. P. C. Duineveld, M. M. de Kok, M. Buechel, A. H. Sempel, K. A. H. Mutsaers, P. Weijer, I. G. J. Camps and E. I. Haskai, “Ink-jet printing of polymer light-emitting devices”, *Proceedings of SPIE*, v 4464, 2002, pp. 59-67
159. K. Murata, “Full research of the super-fine inkjet: A nanoscale function-adding tool aimed at industrialization”, *AIST Today International Edition*, n 22, 2006, pp. 18-19
160. R. K. Khillan, Y. Su and K. Varahramyan, “High resolution polymer LEDs fabricated by drop-on-demand inkjet printing and reactive ion etching”, *Proceedings of SPIE - The International Society for Optical Engineering*, v 5729, 2005, pp. 59-65

161. M. J. D. Powell, "Radial basis functions for multivariable interpolation: a review", In *Algorithms for Approximation (Clarendon Press Institute Of Mathematics And Its Applications Conference Series)*, Edited by J. C. Mason and M. G. Cox, New York: Oxford University Press, 1987, pp. 143-167
162. S. Haykin, "Neural networks: a comprehensive foundation", 2nd Edition, Upper Saddle River: Prentice Hall, 1999, pp. 278-339
163. C. M. Bishop, "Neural networks for pattern recognition", New York: Oxford University Press, 1995, pp. 33-76, 164-193
164. C. M. Bishop, "Pattern recognition and machine learning", New York: Springer-Verlag, 2006, pp. 78-113, 225-324
165. I. Nabney, "NETLAB: algorithms for pattern recognition", 2nd Printing with Corrections, London: Springer-Verlag, 2003, pp. 79-116, 191-224
166. A. R. Webb and S. Shannon, "Shape-adaptive radial basis functions", *IEEE Transactions on Neural Networks*, v 9, n 6, 1998, pp. 1155-1166
167. I. Nabney and C. M. Bishop, "NETLAB toolbox for MATLAB[®]", NETLAB neural network software available from the website cited: <http://www.ncrg.aston.ac.uk/netlab/index.php>
168. A. P. Dempster, N. M. Laird and D. B. Rubin, "Maximum likelihood from incomplete data via the EM algorithm", *Journal of the Royal Statistical Society Series B (Methodological)*, v 39, n 1, 1977, pp. 1-38
169. S. Borman, "The expectation maximization algorithm: a short tutorial", website cited: http://www.seanborman.com/publications/EM_algorithm.pdf

170. C. D. Meyer, "Matrix analysis and applied linear algebra", Philadelphia: Society for Industrial and Applied Mathematics, 2000, pp. 210-237, 411-449

PUBLICATIONS

Journal Paper

1. Zhou J.X.✉, Jerry Fuh Y.H., Loh H.T., Wong Y.S., Ng Y.S., Jeffrey Gray J. and Chua S.J., “Characterization of Drop-on-Demand Microdroplet Printing”, *International Journal of Advanced Manufacturing Technology*, v48, 2010, pp.243-250
2. Zhou J.X.✉, Jerry Fuh Y.H., Loh H.T., Wong Y.S., Ng Y.S., Jeffrey Gray J. and Chua S.J., “Study on the Wetting Properties of Modified Indium-Tin-Oxide (ITO) Substrate Surface by Contact Angle Measurement”, *Journal of Colloid and Interface Science*, 2010. (In Preparation)
3. Zhou J.X.✉, Jerry Fuh Y.H., Loh H.T., Wong Y.S., Ng Y.S. and Chua S.J., “Characteristics of Drop-on-Demand Inkjet Printing of PEDOT:PSS in the Fabrication of Polymer OLEDs”, *Thin Solid Films*, 2010. (In Preparation)
4. Zhou J.X.✉, Jerry Fuh Y.H., Loh H.T., Wong Y.S. and Chua S.J., “Study of Shape Representation and Mapping for Drop-on-Demand Inkjet Printed PEDOT:PSS Droplet Drying Profiles”, *Physica Status Solidi (a)*, 2010. (In Preparation)

Conference Paper

1. Zhou J.X.✉, Jerry Fuh Y.H., Loh H.T., Wong Y.S., Ng Y.S., Jeffrey Gray J. and Chua S.J., “Characterization of Drop-on-Demand Micro Droplet Printing”, *International Conference on Product Design and Manufacturing Systems (PDMS 2007)*, Oct 2007, Chongqing, China.
2. Ng Y.S., Zhou J.X.✉, Jerry Fuh Y.H., Loh H.T., Wong Y.S., Jeffrey Gray J. and Chua S.J., “Influence of Piezoelectric Pulse Profile on Forming Accuracy of Inkjet Printed PEDOT:PSS Droplets for OLED Fabrication”, *International Conference on Manufacturing Automation (ICMA'07)*, May 2007, Singapore.
(2007 Highly Recommended Paper Award by Rapid Prototyping Journal)

APPENDIX

A. Taguchi Design of Experiments in Optimization of Inkjet Printing Drop Ejection Parameters

As introduced in Section 4.2.2.5 of Chapter 4, in order to reduce experimental errors, the printed drops from drop-on-demand (DoD) inkjet printing system should be consistent in drop volume, velocity and direction etc. under the same ejection condition. Hence it is worth optimizing drop ejection parameters to minimize the deviation of the drops coming out from different nozzles. Experiments of this preliminary work were guided and executed using *Taguchi design of experiments* for data collection.

1. Methodology Developed for Optimization

Before actual inkjet printing, the parameters that determine the voltage pulse signal used to control the ejection of droplets from the print-head need to be selected. As stated in Section 4.2.2.5 of Chapter 4, there were altogether 5 different drop ejection parameters set to determine the profile of voltage pulse signal. These main parameters (i.e. factors) were Channel I Pulse Amplitude (*CH1*), Channel II Pulse Amplitude (*CH2*), Pulse Width (*W*), Pulse Rise Time (*R*) and Pulse Fall Time (*F*), respectively. With these many factors, a methodology based on *Taguchi design of experiments* was developed for a systematic optimization.

The method of Taguchi design of experiments is widely used as a quality control tool in research and industries. From limited experimental data, it is a convenient method to achieve better processing conditions. In Taguchi experimental design, only interactions between two main factors (i.e. two-way interactions) are considered, since including high-order interactions between more than two main factors within the design may result in the experiment becoming very time consuming and expensive to carry out. In practice, interactions between more than two main factors are rarely present and normally of very small influence on the final experimental results. Figure A.1 illustrates the schematic layout for the flow of the entire experimental data collection and analysis. Referring to the Figure A.1, after designing the experiment involving the main factors and all the possible two-way interactions, the data could be collected accordingly for the analysis in the future.

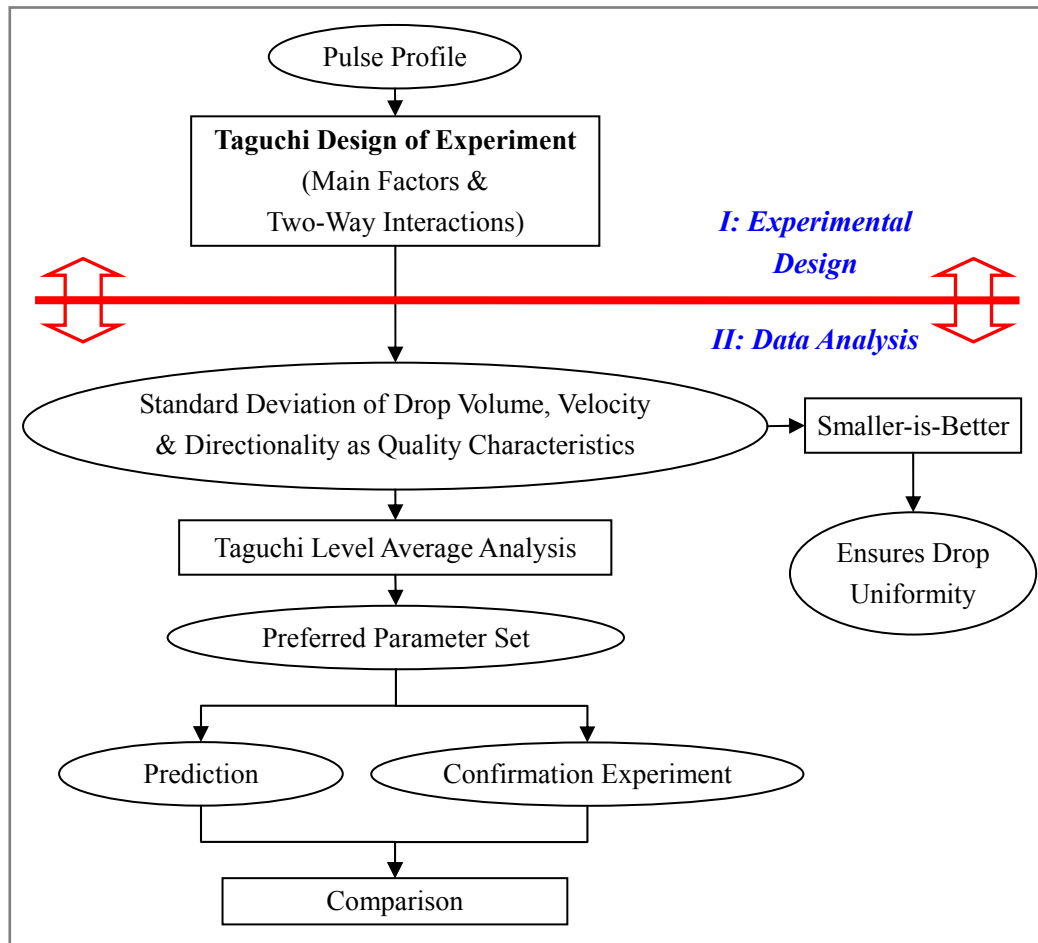


Figure A.1: Schematic flow of methodology based on Taguchi design of experiments for data collection and analysis.

2. Taguchi Design of Experiments

For 5 main factors, there were maximum 10 possible two-way interactions between any two main factors. The smallest *orthogonal array* in Taguchi design that can accommodate these 15 elements should be selected, which was an $L16(2^{15})$ array as shown in Table A.1. Two levels for each main factor were selected for the experiment as shown in Table A.2. We have selected these values with care to avoid the setting combination of the main factors that did not allow drops to be ejected and that were beyond the operating range of the inkjet printing system.

Table A.1: $L16(2^{15})$ array used for Taguchi design of experiments.

RUN No.	CHI	CH2	CHI*CH2	W	CHI*W	CH2*W	F*R	F	CHI*F	CH2*F	W*R	W*F	CH2*R	CHI*R	R
1	1	1	1	1	1	1	1	1	1	1	1	1	1	1	1
2	1	2	2	2	2	1	1	2	2	1	1	1	1	2	2
3	2	1	2	1	2	1	2	1	2	1	2	1	2	1	2
4	2	2	1	2	1	1	2	2	1	1	2	1	2	2	1
5	1	1	1	2	2	2	2	2	2	2	2	1	1	1	1
6	1	2	2	1	1	2	2	1	1	2	2	1	1	2	2
7	2	1	2	2	1	2	1	2	1	2	1	1	2	1	2
8	2	2	1	1	2	2	1	1	2	2	1	1	2	2	1
9	1	1	1	1	1	1	1	2	2	2	2	2	2	2	2
10	1	2	2	2	2	1	1	1	1	2	2	2	2	1	1
11	2	1	2	1	2	1	2	2	1	2	1	2	1	2	1
12	2	2	1	2	1	1	2	1	2	2	1	2	1	1	2
13	1	1	1	2	2	2	2	1	1	1	1	2	2	2	2
14	1	2	2	1	1	2	2	2	2	1	1	2	2	1	1
15	2	1	2	2	1	2	1	1	2	1	2	2	1	2	1
16	2	2	1	1	2	2	1	2	1	1	2	2	1	1	2

Note:

- (1) The 1's and 2's represent the level code for each factor and interaction.
- (2) CHI , $CH2$, W , F and R are known as main factors, controlled by inkjet printing system.
- (3) Interactions are identified by the "*" sign between two main factors.

Table A.2: Level settings of the main factors for Taguchi design of experiments.

Level Code	CHI (V)	CH2 (V)	W (μ s)	F (μ s)	R (μ s)
1	55	55	45	40	40
2	45	40	30	20	20

Note:

- (1) CHI and $CH2$ have units of voltage (V).
- (2) W , F , and R are not real time in units of microsecond (μ s), but in units defined by Litrex Co. W can be converted to real time in microsecond by multiplying a factor of 0.125. F and R can be converted to real time in microsecond by multiplying a factor of 0.1.

3. Randomization and Replication of Experiments

In practice, our experiment was conducted with randomization and replication. Using the randomization, all experimental runs inclusive of replications are mixed and each has an equal chance of being randomly chosen. Randomization can reduce systematic bias that is possible as a result of data generation and collection. It also reduces the effect of unrelated factors and other influences that are not considered during the experiments. Replication can prevent the data bias both between and within experiments. Using the replication, setup changes that results in errors can be more evenly distributed between the different collected data. Data collection errors due to human bias can also be reduced using replication.

For each drop ejection condition, our experiment from Taguchi design had 3 replications, giving a total of 48 experimental runs that were carried out in a completely randomized order. The 5 main factors with their relevant level settings and the sequence of complete randomization used for the replicated experiment were summarized and listed in Table A.3.

Table A.3: Taguchi design of experiments with 3 replications and randomization used.

RUN No.	CH1 (V)	CH2 (V)	W (μs)	F (μs)	R (μs)	Randomization Sequence with 3 Replications of Experiment		
<i>1</i>	55	55	45	40	40	(44)	(35)	(43)
<i>2</i>	55	40	30	20	20	(31)	(17)	(39)
<i>3</i>	45	55	45	40	20	(02)	(22)	(38)
<i>4</i>	45	40	30	20	40	(23)	(15)	(33)
<i>5</i>	55	55	30	20	40	(04)	(40)	(30)
<i>6</i>	55	40	45	40	20	(32)	(03)	(10)
<i>7</i>	45	55	30	20	20	(21)	(45)	(20)
<i>8</i>	45	40	45	40	40	(46)	(47)	(24)
<i>9</i>	55	55	45	20	20	(19)	(27)	(11)
<i>10</i>	55	40	30	40	40	(48)	(07)	(42)
<i>11</i>	45	55	45	20	40	(06)	(34)	(05)
<i>12</i>	45	40	30	40	20	(26)	(25)	(41)
<i>13</i>	55	55	30	40	20	(29)	(37)	(09)
<i>14</i>	55	40	30	20	40	(18)	(14)	(12)
<i>15</i>	45	55	30	40	40	(36)	(28)	(08)
<i>16</i>	45	40	45	20	20	(13)	(01)	(16)

Note:

- (1) The 5 main factors for drop ejection with their relevant level settings are summarized.
- (2) The randomization sequence is numbered from 1 to 48 enclosed in parentheses for all the experimental runs.

So far, Taguchi experimental design was completed, and subsequently experiments were carried out according to Table A.3 for data collection. As to data analysis for the purpose of optimization, my article [150] presented a more detailed explanation. For those interested in Taguchi design of experiments, the book “*Taguchi Methods: A Hands-On Approach*” (Addison-Wesley Publishing Company Inc., 1993) by Glen S. Peace provides an introductory theory. It illustrates Taguchi methods step by step with various examples. An in-depth and comprehensive study on the experimental design can be found in the book “*Design and Analysis of Experiments*” (John Wiley & Sons Inc., 6th Edition, 2005) by Douglas C. Montgomery.

